Synthesis of Two-Dimensional Hexagonal Boron Nitride and Tin-Derivative Dichalcogenides for Nanoelectronic Applications

---

Ren-Jie Chang

Supervised by Professor Jamie H. Warner



Hertford College

Department of Materials

University of Oxford

Submitted in conformity with the requirements

for the degree of DPhil in Materials Science

May 2019

Copyright © 2019 by Ren-Jie Chang

Declaration

The material contained within this thesis has not previously been submitted for a degree at the University of Oxford or any other university. The research reported within this thesis has been conducted by the author unless indicated otherwise.

Copyright Notice

The copyright of this thesis rests with the author. No quotation from it should be published without the prior written consent of the author, and any information derived from it should be acknowledged.

Abstract

The discovery of graphene (Gr) has so far drawn significant attention and expanded into the development of other two-dimensional (2D) materials with complementary electronic properties over the past few years. Molybdenum disulfide (MoS_2) and tungsten disulfide (WS_2) are examples of semiconducting transition metal dichalcogenides (TMDs), which have a direct band gap in the red spectral region (1.8−2.0 eV), making them promising candidates for the future flexible optoelectronic applications. However, exploiting other 2D materials with different bandgap values is still necessary for devices with comprehensive functionalities. This DPhil project aims to develop 2D insulating hexagonal boron nitride (hBN) and semiconducting tin-derivative dichalcogenides (e.g. tin sulfide SnS_2, Sn doped WS_2) using chemical vapour deposition (CVD) growth method, which possesses the advantages for mass production compared to the commonly-used exfoliation approach.

In the first part of growth of hBN, a new oxide-assisted CVD process was developed via the formation of thin oxide layer on Cu surface, which can passivate the nucleation sites of Cu surfaces before hBN growth. In the following hBN growth stage the oxide layer gradually decomposes in the reducing hydrogen atmosphere and only the limited fresh Cu surface is able to absorb the active species forming stable nuclei. This leads to increased domain sizes from 1 to 20 μm by reducing the nucleation density from 10^6 to 10^3 mm^{-2}.

In the second part of growth of SnS_2, a new precursor SnS was used for the growth and investigation for the photodetecting performance via combining them with Gr electrodes. The Gr-SnS_2-Gr transistors exhibit prominent photodetector response with high detectivity and photoresponsivity. The response of all 2D photodetectors depends upon charge trapping and the Schottky barrier modulation at the interface of SnS_2 and Gr. This indicates that SnS_2 has photosensing performance that is comparable to other 2D TMDs, such as MoS_2 and WS_2, in the green spectral region when combined with Gr electrodes.

For the traditional growth of SnS_2 on SiO_2 substrates, one of the drawbacks is the high percentage of crystals with vertical growth, which is detrimental for the device applications. To improve this, the CVD-grown WS_2 layers were utilised as the substrates for the growth of 2D SnS_2. In addition to the formation of type II van der Waals (vdW) heterostructures, the lateral growth of SnS_2 is stabilised with epitaxially aligned crystals on the basal planes whereas cluster growth appears on the edges of WS_2 layers. This is attributed to the lower energy barrier of migration for adsorbed active species on the defect-free surface, resulting in facilitated surface diffusion compared to the defect-rich surface.

Lastly, a post-growth doping strategy in monolayer and bilayer WS_2 crystals utilising a metal exchange mechanism was demonstrated, whereby Sn atoms become substitutional dopants in the W sites through energetically favourable replacement. This can be achieved by firstly growing WS_2 single crystals and then reacting with a SnS precursor. The Sn dopants exhibit an n-type doping behaviour in the WS_2 layers based on the decreased threshold voltage obtained from transistor device measurements. Annular dark field scanning transmission electron microscopy (ADF-STEM) shows that in bilayer WS_2 the Sn doping occurs only in the top layer, creating vertical heterostructures with atomic layer doping precision.

Acknowledgements

The great scientist Isaac Newton stated that if he had seen further it is only by standing on the shoulders of giants. In my case, I have completed this DPhil journey only because I was greatly supported by the very best individuals. First and foremost, I would like to profoundly thank my supervisor Professor Jamie Warner for his patience and guidance throughout the period of time of my study. His broad knowledge and keen observation have inspired me and sharpened my skills to become an independent researcher. Second, I would like to sincerely appreciate my examiners, Dr. Alexander Robertson and Professor Amalia Patane, for giving the intellectual stimulating and valuable suggestions during the viva, which greatly improve the thesis.

Similarly, I would also like to express my deep appreciation to Dr. Yuewen Sheng, Dr. Xiaochen Wang, Mr. Tongxin Chen, Mr. Yang Lu, who had been most helpful in providing their ideas in the synthesis of 2D materials. Developing synthesis routes for new types of materials is challenging and requires plenty of time. Through frequent brainstorming together on every predicament, I was made to have clearer scope and the Sn-derivative dichalcogenides have now been successfully grown.

This project involves several works that I could not accomplish without the assistance from my colleagues and collaborators. Their knowledge and expertise on certain facilities were indispensable for broadening aspects in this project. I acknowledge Dr. Haijie Tan, Dr. Ye Fan, Dr. Yingqiu Zhou, and Dr. Hefu Huang for their kind and generous experience sharing about the device fabrication and device measurement. I am thankful to Dr. Shanshan Wang, Dr. Jakyung Lee, Dr. Gyeonghee Ryu, and Ms. Jun Chen for their support on the use of TEM to characterise a variety of samples. I also appreciate Dr. Benjamin Porter, and Mr. Nhlakanipho Mkhize in Professor Harish Bhaskaran group for the help on AFM measurements.

I would also like to appreciate the rest of my colleagues, Dr. Viktoryia Shautsova, Dr. Thomas Samuels, Dr. Martin Tweedie, Dr. Wenshuo Xu, Dr. Sha Li, Dr. Qu Chen, Ms. Sapna Sinha, Ms. Yi Wen, Ms. Linlin Hou, Ms. Qianyang Zhang, and Mr. Peng Tang for their constructive viewpoints and opinions during the discussion, which improved my research work. I am also grateful for my peers, Wing Chung Liu, Shuqiu Wang, Yutian Wen, and Ghazi Sarwat for their invaluable discussions and advice. I thank many of my friends in Oxford, Yu-Jen, Bo-Shiuan, Kai-Sheng, Yujiro, Ayumi, Sewook, Yi-Sheng, Yung-Kang, Li-Yao, Jeff, Gu-Lung, Kun-Wei, and Mi-Jun for bringing me such an enjoyable and unforgettable memory during my 4-year stay in Oxford.

Last but not least, I would like to express my sincere gratitude to my parents for their unconditional support and endless encouragement no matter what decision I made for my path of life. I am more than happy to dedicate this achievement to them.

Publications

First-author:

(1) **Chang, R.-J.**; Tan, H.; Wang, X.; Porter, B.; Chen, T.; Sheng, Y.; Zhou, Y.; Huang, H.; Bhaskaran, H.; Warner, J. H., High-Performance All 2D-Layered Tin Disulfide: Graphene Photodetecting Transistors with Thickness-Controlled Interface Dynamics. *ACS Appl. Mater. Interfaces* **2018,** *10* (15), 13002-13010.

(2) **Chang, R.-J.**; Wang, X.; Wang, S.; Sheng, Y.; Porter, B.; Bhaskaran, H.; Warner, J. H., Growth of Large Single-Crystalline Monolayer Hexagonal Boron Nitride by Oxide-Assisted Chemical Vapor Deposition. *Chem. Mater.* **2017,** *29* (15), 6252-6260.

(3) **Chang, R.-J.**; Sheng, Y.; Chen, T.; Mkhize, N.; Lu, Y.; Bhaskaran, H.; Warner, J. H., Morphology Control of Two-Dimensional Tin Disulfide on Transition Metal Dichalcogenides Using Chemical Vapor Deposition. *ACS Appl. Nano Mater.* **2019,** *2* (7), 4222-4231.

(4) **Chang, R.-J.**; Sheng, Y.; Ryu, G. H.; Mkhize, N.; Chen, T.; Lu, Y.; Chen, J.; Lee, J. K.; Bhaskaran, H.; Warner, J. H., Metal Exchange Driven Post-Growth Substitutional Tin Doping of WS_2 2D Crystals Using Chemical Vapor Deposition. *ACS Appl. Mater. Interfaces* **2019,** *11* (27), 24279-24288.

Co-author:

(1) Sheng, Y.; Chen, T.; Lu, Y.; **Chang, R.-J.**; Sinha, S.; Warner, J. H., High-Performance WS_2 Monolayer Light-Emitting Tunneling Devices Using 2D Materials Grown by Chemical Vapor Deposition. *ACS Nano* **2019,** *13* (4), 4530-4537.

(2) Ryu, G. H.; Chen, J.; Wen, Y.; Zhou, S.; **Chang, R.-J.**; Warner, J. H., Atomic Structural Catalogue of Defects and Vertical Stacking in 2H/3R Mixed Polytype Multilayer WS_2 Pyramids. *Nanoscale* **2019,** *11* (22), 10859-10871.

(3) Chen, T.; Sheng, Y.; Zhou, Y.; **Chang, R.-J.**; Wang, X.; Huang, H.; Zhang, Q.; Hou, L.; Warner, J. H., High Photoresponsivity in Ultrathin 2D Lateral Graphene:WS_2:Graphene Photodetectors Using Direct CVD Growth. *ACS Appl. Mater. Interfaces* **2019,** *11* (6), 6421-6430.

(4) Lu, Y.; Chen, T.; Ryu, G. H.; Huang, H.; Sheng, Y.; **Chang, R.-J.**; Warner, J. H., Self-Limiting Growth of High-Quality 2D Monolayer MoS_2 by Direct Sulfurization Using Precursor-Soluble Substrates for Advanced Field-Effect Transistors and Photodetectors. *ACS Appl. Nano Mater.* **2019,** *2* (1), 369-378.

(5) Huang, H.; Xu, W.; Chen, T.; **Chang, R.-J.**; Sheng, Y.; Zhang, Q.; Hou, L.; Warner, J. H., High-Performance Two-Dimensional Schottky Diodes Utilizing Chemical Vapour Deposition-Grown Graphene–MoS_2 Heterojunctions. *ACS Appl. Mater. Interfaces* **2018,** *10* (43), 37258-37266.

(6) Huang, H.; Sheng, Y.; Zhou, Y.; Zhang, Q.; Hou, L.; Chen, T.; **Chang, R.-J.**; Warner, J. H., 2D-Layer-Dependent Behavior in Lateral Au/WS_2/Graphene Photodiode Devices with Optical Modulation of Schottky Barriers. *ACS Appl. Nano Mater.* **2018,** *1* (12), 6874-6881.

(7) Wang, X.; Sheng, Y.; **Chang, R.-J.**; Lee, J. K.; Zhou, Y.; Li, S.; Chen, T.; Huang, H.; Porter, B. F.; Bhaskaran, H.; Warner, J. H., Chemical Vapor Deposition Growth of Two-Dimensional Monolayer Gallium Sulfide Crystals Using Hydrogen Reduction of Ga_2S_3. *ACS Omega* **2018,** *3* (7), 7897-7903.

(8) Chen, J.; Jung, G. S.; Ryu, G. H.; **Chang, R.-J.**; Zhou, S.; Wen, Y.; Buehler, M. J.; Warner, J. H., Atomically Sharp Dual Grain Boundaries in 2D WS_2 Bilayers. *Small* **2019,** Just Accepted.

(9) Chen, T.; Lu, Y.; Sheng, Y.; Shu, Y.; Li, X.; **Chang, R.-J.**; Bhaskaran, H.; Warner, J. H., Ultrathin All-2D Lateral Graphene:GaS:Graphene UV Photodetectors by Direct CVD Growth. *ACS Appl. Mater. Interfaces* **2019,** Under Review.

Table of contents

Chapter 1 Introduction……...1

1.1 Project Aims……....1

1.2 The Scope of this Thesis……..1

Chapter 2 Literature Review…….3

2.1 Introduction…….3

2.2 Overview of 2D Materials……...5

2.2.1 Crystal Structure……...…6

2.2.2 Band Structure…….9

2.2.3 Hexagonal Boron Nitride…….11

2.2.4 Tin Disulfide……....11

2.3 Optoelectronics Based on 2D Materials……....12

2.3.1 Phototransistors- Photoconductive Effect……....13

2.3.2 Photodiodes- Photovoltaic Effect…….16

2.3.3 Contact Engineering……19

2.4 Chemical Vapour Deposition Synthesis of 2D Materials……...23

2.4.1 Layer Number……..23

2.4.2 Domain Size……28

2.4.3 Morphology……33

2.4.4 Orientation……...37

2.5 Chemical Vapour Deposition Synthesis of Hybrid 2D Materials……...42

2.5.1 Doping of 2D Materials……....42

2.5.2 Lateral Heterostructures……...46

2.5.3 Vertical Heterostructures (van der Waals Heterostructures)…….....51

2.6 Conclusion……59

2.7 Reference……..60

Chapter 3 Methodology……....82

3.1 Introduction……...82

3.2 Chemical Vapour Deposition Synthesis of 2D Materials……...82

3.2.1 Synthesis of Hexagonal Boron Nitride (hBN)……..82
3.2.2 Synthesis of Tin Disulfide (SnS_2)…….....84
3.2.3 Synthesis of Graphene……85
3.2.4 Synthesis of Tungsten Disulfide (WS_2)……86
3.2.5 Synthesis of Molybdenum Disulfide (MoS_2)……...87
3.2.6 Thermal Doping of Tin in TMDs……88
3.3 Transfer of 2D Materials……....88
3.3.1 2D Materials on Cu substrates……..88
3.3.2 2D Materials on SiO_2 substrates……...89
3.4 Microscopy Characterisation……89
3.4.1 Optical Microscopy……..89
3.4.2 Scanning Electron Microscopy……....90
3.4.3 Transmission Electron Microscopy……91
3.4.4 Annular Dark Field Scanning Transmission Electron Microscopy……..92
3.4.5 Atomic Force Microscopy……...93
3.5 Spectroscopy Characterisation……..93
3.5.1 Raman Spectroscopy……....94
3.5.2 Photoluminescence Spectroscopy……....96
3.6 Device Measurement……....97
3.6.1 Fabrication Process……..97
3.6.2 Electrical and Opto-Electrical Measurement……100
3.7 Reference……....101

Chapter 4 Growth of Large Single-Crystalline Monolayer Hexagonal Boron Nitride by Oxide-Assisted Chemical Vapour Deposition……...102

4.1 Introduction……102
4.2 Results and Discussions……...104
4.2.1 Oxide-Assisted CVD growth of hBN……104
4.2.2 Characterisation and Orientation Analysis of hBN……....112
4.2.3 Employing hBN for the Growth of MoS_2/hBN Vertical Heterostructures…….....119
4.3 Conclusion……..122
4.4 Reference……123

Chapter 5 Chemical Vapour Deposition Growth of 2D Layered SnS_2 and its Optoelectronic Characteristics with Graphene Electrodes……...128

5.1 Introduction……128

5.2 Results and Discussions……...130

5.2.1 Synthesis and Characterisation of SnS_2 crystals……....130

5.2.2 Photodetecting Transistors Based on Gr-SnS_2-Gr……..137

5.2.3 Effect of SnS_2 Channel Thickness on Device Characteristics……....147

5.3 Conclusion……..150

5.4 Reference……151

Chapter 6 Morphology Control of Two-Dimensional Tin Disulfide on Transition Metal Dichalcogenides using Chemical Vapour Deposition……..155

6.1 Introduction……155

6.2 Results and Discussions……...156

6.2.1 CVD Growth of SnS_2 on WS_2 Monolayers……....156

6.2.2 Growth Mechanism……....164

6.2.3 CVD Growth of SnS_2 on Other 2D Materials……....170

6.3 Conclusion……..197

6.4 Reference……176

Chapter 7 Metal Exchange Driven Post-Growth Substitutional Tin Doping of 2D WS_2 Crystals using Chemical Vapour Deposition……....179

7.1 Introduction……179

7.2 Results and Discussions……...181

7.2.1 Thermal Doping of Sn in the CVD-Grown WS_2 Layers……....181

7.2.2 ADF-STEM Characterisation of Sn Doped WS_2 Layers……....186

7.2.3 Electrical Properties of Sn Doped WS_2 Monolayers……..195

7.3 Conclusion……..197

7.4 Reference……....198

Chapter 8 Conclusion and Future Outlook……...200

8.1 Thesis Summary……..200

8.2 Future Outlook……....202

Chapter 1

Introduction

1.1 Project Aims

This doctorate project aims to develop 2D insulating hexagonal boron nitride (hBN) and semiconducting tin-derivative dichalcogenides (e.g., tin sulfide SnS_2, SnS_2/WS_2 heterostructures, and Sn-doped WS_2) using chemical vapour deposition (CVD) growth method, which is advantageous for large-scale manufacturing and compatibility with current semiconductor processes. It involves the investigation of underlying mechanism, and a variety of characterisation techniques.

1.2 The Scope of this Thesis

The thesis covers the research that has been performed over the time span of four years of DPhil degree at Department of Materials and Hertford College, University of Oxford. It unfolds with a literature review in Chapter 2 that summarises the recent advances in the nanoelectronic applications based on 2D materials and their synthesis as well as structural control using CVD technique. Methodology in Chapter 3 describes the experimental details on CVD setup and the characterisation of 2D materials, as well as the fabrication techniques that are exploited in device manufacturing.

Chapter 4 demonstrates the work of hBN synthesis using a new modified growth route by means of introducing an oxide passivating layer on the Cu surface before the growth. This brings to a reduced nucleation density and an increased domain size, reducing the density of

defects such as domain boundaries. Chapter 5 explores the new 2D layered semiconductors SnS_2 to realise the all-2D optoelectronics to expand the wavelength response and interface physics. The SnS_2 is grown by CVD and then assembled layer by layer into lateral ultrathin transistors with graphene electrodes. The Gr-SnS_2-Gr transistors exhibit excellent photodetector response and are comparable to other 2D transition metal dichalcogenides of MoS_2 and WS_2. Chapter 6 reports the synthesis of SnS_2/WS_2 vertical heterojunctions and provides detailed characterisation of the properties of the material to understand the charge transfer and type II vertical heterojunction that is formed. The edges and basal plane of WS_2 is shown to be a critical factor in determining the growth kinetics of SnS_2 and influence the final 2D vertical stack. Chapter 7 introduces a new chemistry approach for doping 2D materials post-growth utilising the metal exchange mechanism and the Sn-doped WS_2 layers are successfully obtained. The metal exchange mechanism is only restricted to the top layer and this creates a vertical bilayer with pristine bottom layer and doped top layer, realizing novel atomically precise monolayer control of heterojunctions. This opens new chemical pathways to achieving controlled modification of 2D semiconductors.

The last chapter gives a brief summary and conclusion for the whole thesis. Several aspects and challenges of the future works as extension to this thesis are also discussed.

Chapter 2

Literature Review

2.1 Introduction

Transistors made up of a semiconductor channel, source, drain and gate electrodes are the basis of modern microelectronic and integrated circuit industry. Over the past few decades, transistors based on Si semiconductors have facilitated the development of devices including computers, the Internet, mobile displays, and much more. The progress in the development of semiconductors was well predicted by Moore's Law, where the density of transistors in a chip doubles every couple of years.[1] This mainly relies on the shrinkage of the geometrical dimensions of the transistors and leads to the channel length reaching to sub-10 nm scale. Despite these advances, fundamental physical limits for the minimum size of Si transistors are now being approached due to the short-channel effect.[2] Additional new materials and device architectures are required to address the challenges of the transistor scaling in the next decades.

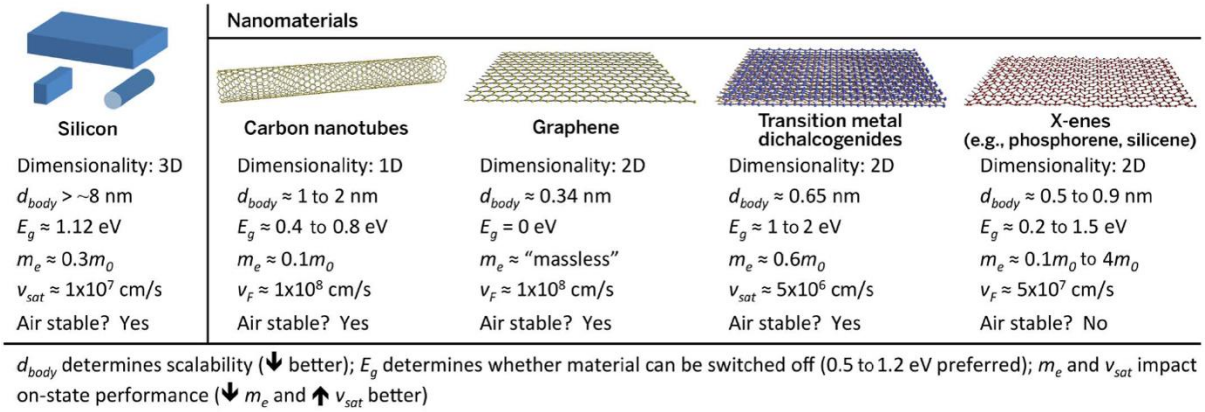


Figure 2.1. Physical properties of nanomaterials for the application in transistors. d_{body} is the channel or body thickness; E_g is the band gap of the nanomaterials; m_e is the effective mass of electrons

in the nanomaterials; v_F is the Fermi velocity. Reproduced with permission from ref. [3]. © 2015 American Association for the Advancement of Science.

Two-dimensional (2D) materials are one of the potential material candidates with promising features to replace current Si transistors in the next generation of electronic devices. The natural length of planar transistors, which indicates the smallest size of transistors that can be turned off, is given by $\lambda = \sqrt{d_{body} d_{ox} \varepsilon_s / \varepsilon_{ox}}$, where λ is the natural length, d_{body} and d_{ox} are the thickness of the semiconducting channel and oxidation dielectric layer, and ε_s and ε_{ox} are their corresponding dielectric constants. For transistors based on Si semiconductors, the natural length is calculated to be around 4 nm. In contrast, when utilising 2D MoS_2 as the semiconducting channel for the transistors, the natural length can bring down to 0.66 nm because of the reduced dimensionality and d_{body} (**Figure 2.1**).[3]

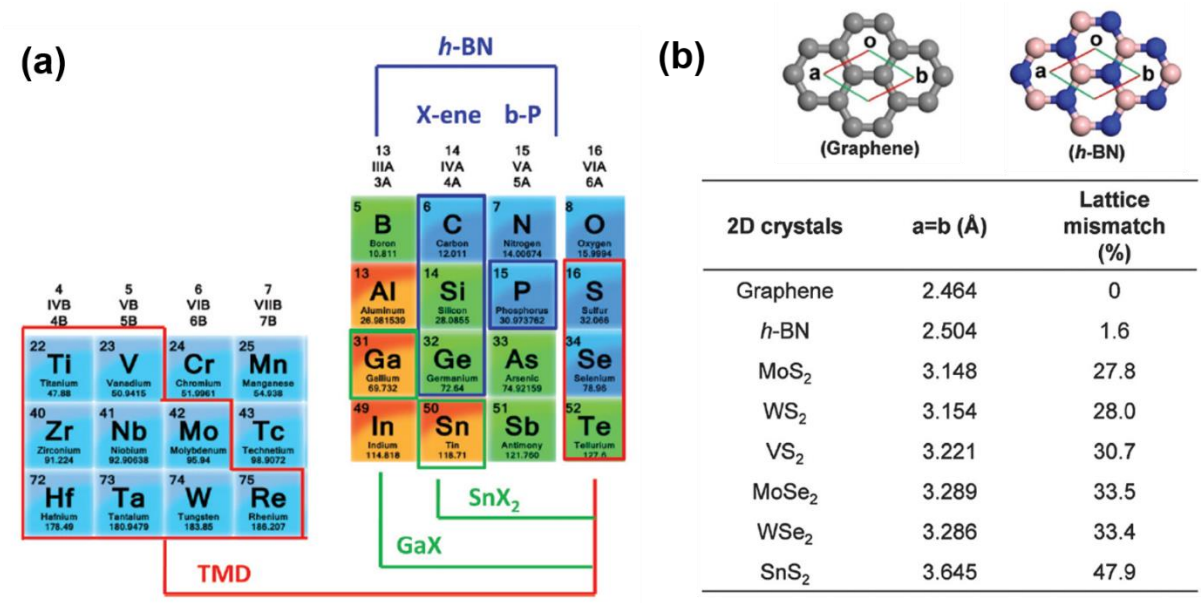
Graphene is the first 2D material discovered in 2004 by the two scientists in University of Manchester,[4] Andre Geim and Kostya Novoselov, who were awarded the Nobel Prize in Physics later in 2010. Since then, the enormous success of graphene research has sparked immense interest and stimulated the development of a wide range of 2D materials with complementary electronic properties,[5-8] particularly on semiconducting metal chalcogenides (e.g., MoS_2 and WS_2) because of their chemical stability and the potential to dominate the new transistor era.[9-10] Other 2D materials such as hexagonal boron nitride (hBN), phosphorene and even metal oxides also draw significant attentions,[11-13] as combining these 2D materials with different properties provides the opportunities to build up an ultrathin smart device with various functionalities in the future.

This chapter is devoted to review the current advances in synthesis and nanoelectronic applications of 2D materials. Based on the thesis subject, it starts by introducing the fundamental overview of 2D materials, and their basic physical properties. This is then

followed by a review of nanoelectronics based on 2D semiconductors with a specific focus on their photoresponse properties, and the materials synthesis using chemical vapour deposition (CVD), which is advantageous for its compatibility with current semiconductor processes for large scale production. The CVD synthesis covers the growth of single components and the complex 2D materials, including the surface modification through doping strategies, and the fabrication of both lateral and vertical heterostructures. The review of these 2D materials is mainly based on insulating hBN and semiconducting MoS_2, WS_2 and SnS_2.

2.2 Overview of 2D Materials

The large family of 2D materials can be classified into several categories, as summarised by the periodic table in **Figure 2.2**(a).[14] These include (1) X-enes such as graphene and silicene, (2) metal carbides and nitrides (MX-enes), (3) black phosphorus or phosphorene (b-P), (4) hexagonal boron nitride (hBN), (5) metal chalcogenides including transition metal dichalcogenides (TMDs) such as MoS_2 and WS_2, group IVA dichalcogenides such as SnS_2 and $SnSe_2$, and group IIIA monochalcogenides such as GaS and GaSe. The 2D materials, in general, have a rhombus unit cell with a basis of two or three lattice sites depending on their chemical formula and crystal structure. The lattice constant of a selection of 2D materials are listed in **Figure 2.2**(b), demonstrating a high percentage of lattice mismatch between individual 2D materials.[15]



2D crystals	a=b (Å)	Lattice mismatch (%)
Graphene	2.464	0
h-BN	2.504	1.6
MoS_2	3.148	27.8
WS_2	3.154	28.0
VS_2	3.221	30.7
$MoSe_2$	3.289	33.5
WSe_2	3.286	33.4
SnS_2	3.645	47.9

Figure 2.2. A library of 2D materials beyond graphene. (a) Elemental constituents of 2D materials in periodic table. Reproduced with permission from ref. [14]. © 2015 The Royal Society of Chemistry. (b) Unit cell for the 2D materials and their in-plane lattice constants. Reproduced with permission from ref. [15]. © 2016 The Royal Society of Chemistry.

2.2.1 Crystal Structures

In general, 2D materials have a layered structure, with a covalently-bonded planar crystal and a weak van der Waals (vdW) force separating each layer. Graphene, a single layer crystal composed of sp^2-hybridised carbon atoms arranged in hexagonal honeycomb lattice, has the simplest configuration among various 2D materials. Monolayer hBN exhibits a similar hexagonal lattice form but with alternating B and N atoms sitting on different lattice sites. In contrast, semiconducting metal dichalcogenides have a slightly complex layered structure, with a metal layer sandwiched between two chalcogen atomic layers. According to the arrangement of metal atom and its six neighbouring chalcogen atoms, the monolayer structure of metal dichalcogenides can be categorised as trigonal prismatic (hexagonal, H) and octahedral (tetragonal, T) phase.[16] In H-phase metal dichalcogenides such as MoS_2 and WS_2, the metal

atom possesses trigonal prismatic coordination (D_{3h} point group) with the hexagonal symmetry from the top view (**Figure 2.3**(a)). In contrast, T-phase metal dichalcogenides such as SnS_2 have the octahedral coordination (D_{3d} point group) of metal atom surrounded by chalcogen atoms resulting in hexagonal arrangement of chalcogen atoms in the top view (**Figure 2.4**(a)).

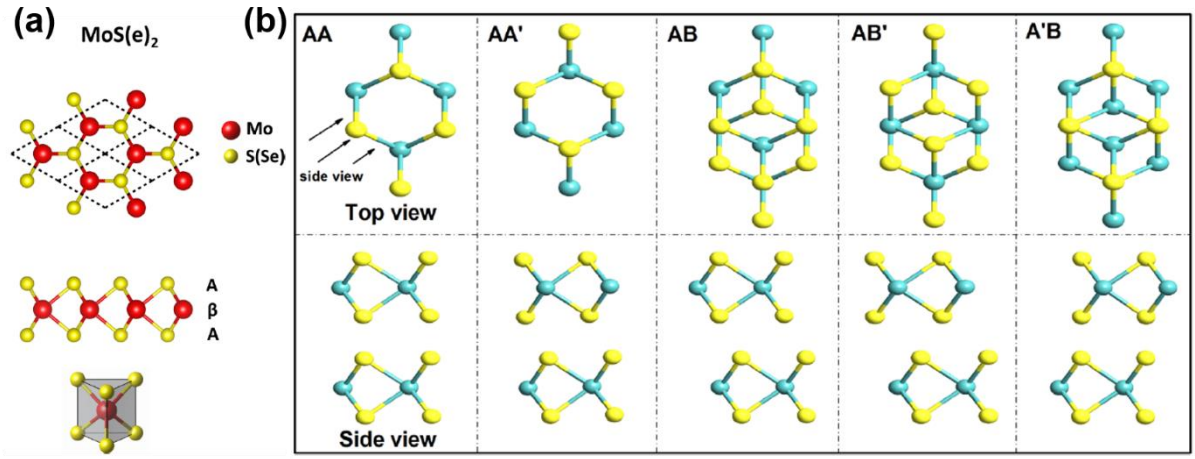


Figure 2.3. H phase monolayer and bilayer crystal structure of MoS_2. (a) Atomic structure for the monolayer MoS_2. Reproduced with permission from ref. [16]. © 2016 American Physical Society. (b) Stacking orders for bilayer MoS_2. Reproduced with permission from ref. [17]. © 2018 IOP Publishing.

In the bilayer H-phase MoS_2, there are five possible stacking orders which are depicted in **Figure 2.3**(b).[17] In the AA and AA' configurations, two MoS_2 monolayers are aligned. For the AA stacking, the Mo (S) atoms of the top layer are above the Mo (S) atoms of the bottom layer. In contrast, the AA' stacking has the Mo (S) atoms of the top layer eclipsed over S (Mo) atoms of the bottom layer, resulting in an inversion symmetry for two layers. For the AB stacking, the S atoms of the top layer are staggered over the Mo atoms of the bottom layer, with the Mo atoms of the top MoS_2 layer above the hexagon centres of the bottom MoS_2 layer. The AB' and A'B stacking configurations both have the top layer in a reversed sequence, with the Mo atoms from top and bottom layer overlaid for AB' stacking, and the S atoms from top and bottom layer overlaid for A'B stacking. In AB' stacking, the S atoms in the top MoS_2 layer

lie above the hexagon centres of the bottom MoS_2 layer, while the Mo atoms in the top MoS_2 layer lie above the hexagon centres of the bottom MoS_2 layer in A'B stacking.

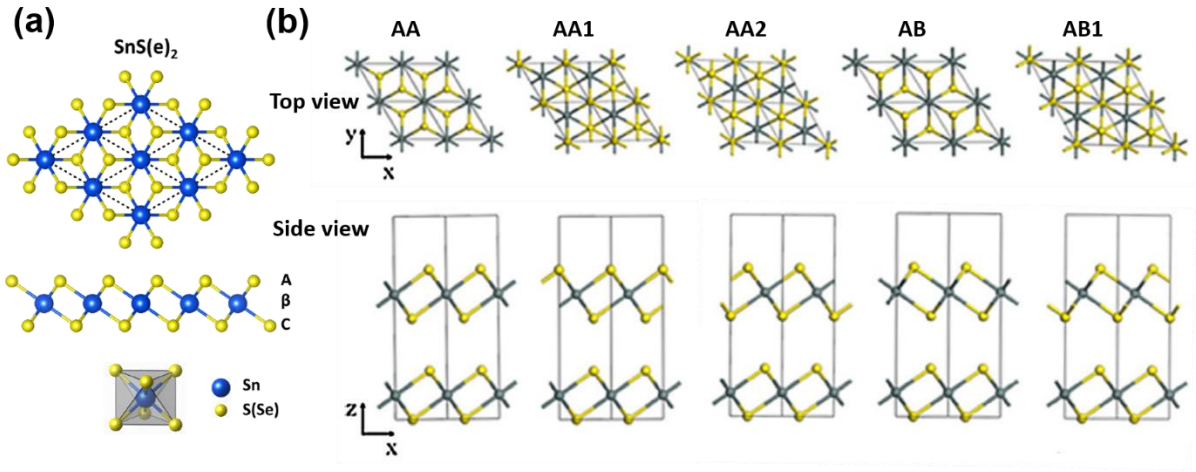


Figure 2.4. T phase monolayer and bilayer crystal structure of SnS_2. (a) Atomic structure of the monolayer SnS_2. Reproduced with permission from ref. [16]. © 2016 American Physical Society. (b) Stacking orders for bilayer SnS_2. Reproduced with permission from ref. [18]. © 2015 Elsevier B.V.

Similarly, T-phase SnS_2 in the form of bilayer also has five different stacking patterns recorded as AA, AA1, AA2, AB, and AB1 (**Figure 2.4**(b)).[18] The AA stacking configuration has an aligned sequence with all Sn (S) atoms of the top layer over the Sn (S) atoms of the bottom layer. The AA1 configuration is the stacking with the topmost S atoms over the Sn atoms of the bottom layer. In contrast, the AA2 configuration is the staggered stacking with the Sn atoms of the top layer over the upper S atoms of the bottom layer. For the both AB and AB1 stacking, the top layer has a reversed atom arrangement with respect to the bottom layer. In the AB stacking, the Sn atoms of the top layer and the Sn atoms of the bottom layer are overlaid. In the AB1 stacking, the Sn atoms of the top layer are over the lower S atoms of the bottom layer.

2.2.2 Band Structures

The variety of electronic properties from different 2D materials can be explained in terms of their band structures, shown in **Figure 2.5**. The band structures of 2D materials are calculated by density functional theory (DFT).[19] The band structure of graphene is characterised by conical valence and conduction bands that intersect across k-space in the Brillouin zone at two different Dirac points, denoted by *K* and *K'*, originating from the two lattice vectors of graphene in **Figure 2.2**(b). The energy of the crossing point is zero, indicating that graphene is gapless and semi-metallic. Besides, the linear energy dispersion of graphene results in the charge carriers behaving as though they have zero mass. The massless characteristic enables the carriers to travel over 100 times faster in graphene than in silicon, causing graphene with a high carrier mobility. In contrast, single layer of hBN presents a direct band gap of > 4.5 eV located at the *K* and *K'* points of the Brillouin zone. This makes hBN regarded as an insulator and a perfect dielectric layer to preserve the electronic properties of adjacent materials because of its atomic flatness and low concentration of trapped charges.

Semiconducting metal chalcogenides have an electronic band structure which strongly depends on the number of layer.[20] In the bulk and multilayer WS_2 samples, the valence band maximum is situated at the Γ point and the conduction band minimum is located at a midpoint along the Γ-*K* line of the Brillouin zone.[21] The indirect band gap of bulk WS_2 is calculated to be ~ 1.2 eV and increases gradually when decreasing the layer thickness. When the WS_2 thickness is reduced to monolayer, both the valence band maximum and the conduction band minimum shift to *K* point of the Brillouin zone and results in the transition from indirect band gap to direct band gap of ~2.0 eV.[22] The direct band gap allows the recombination of electron-hole pairs without the involvement of phonons and makes the monolayer WS_2 exhibit strong photoluminescence signal under the optical excitation. In contrast, in the case of SnS_2 it remains an indirect band gap semiconductor even in monolayer form. For the bulk SnS_2 crystals,

the valence band maximum is situated at an intermediate point between *Γ* and *M* point and the conduction band minimum is located at *L* point of the Brillouin zone.[16] Similar to the bulk form, the few-layer and monolayer SnS_2 possess the valence band maximum located along the *Γ*-*K* line of the Brillouin zone, but with the conduction band minimum shifted to the *M* point. The indirect band gaps are calculated to be 2.18 eV for the bulk crystals and 2.41 eV for the monolayer with intermediate values for the few-layer systems. For the semiconducting metal chalcogenides, the increase of the band gaps with the reduction of layer number can be imputed to the effective reduction of electrostatic interactions and the quantum confinement of electrons within the layered materials with finite thickness.[23-25]

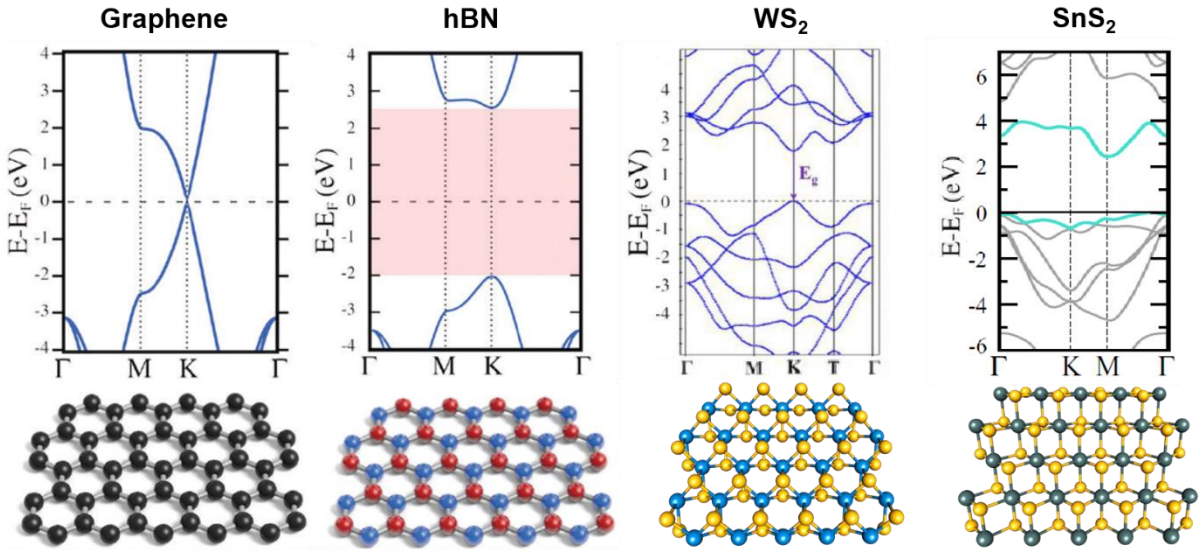


Figure 2.5. Band structure of 2D materials varying from semi-metallic to insulating and semiconducting properties. Graphene is semi-metallic 2D materials with zero band gap, while monolayer hBN is stable insulator with a large band gap of > 4.5 eV. Monolayer WS_2 and SnS_2 are both semiconductors with a direct band gap of ~ 1.9 eV and an indirect band gap of ~ 2.4 eV, respectively. Reproduced with permission from ref. [19]. © 2017 The Royal Society of Chemistry, ref. [21]. © 2013 American Chemical Society and ref. [16]. © 2016 American Physical Society.

2.2.3 Hexagonal Boron Nitride

Two-dimensional hexagonal boron nitride (hBN) is similar to graphene in its structure but with alternating B and N atoms arranged in its monolayer honeycomb structure, and is the thinnest insulating material with an electrical bandgap of 5.9 eV.[26] It exhibits not only superior mechanical flexibility, chemical and temperature stability, but also high thermal conductivity.[27-30] These fascinating properties make hBN a good candidate for various applications such as membranes for strong oxidation resistance,[31] deep ultraviolet emitters,[32] quantum photonic emitters,[33] encapsulation layers,[34-35] passivating dielectric layer in electronic devices and tunnelling barriers in field effect tunnelling transistors.[36] In addition, hBN is also considered as a promising insulating substrate for semi-metallic graphene and semiconducting metal dichalcogenides growth to construct van der Waals (vdW) heterostructures for electronic and photovoltaic devices that exhibit unique characteristics and are unobtainable from single-component 2D materials.[37-38] These extensive applications of hBN require high quality and uniformity. Elimination of defects and precise control of layer number are therefore highly demanded.

2.2.4 Tin Disulfide

Monolayer molybdenum disulfide (MoS_2) and tungsten disulfide (WS_2) are examples of semiconducting TMDs, which have a bandgap in the red spectral region (1.8~2.0 eV) and several fascinating physical properties including piezoelectricity,[39] spin-orbit interaction and valley Hall effect.[40-41] Additionally, the direct bandgap,[20] high absorption coefficient and 2D structural form make them promising candidates for flexible optoelectronic applications such as phototransistors,[42] light emitting diodes (LED),[43] memory devices and logic circuits.[44-45]

Tin disulfide (SnS_2) is another 2D semiconductor other than MoS_2 and WS_2 and is particularly of great interest among the layered materials because of its earth-abundant and environmentally-friendly constituents with prominent chemical stability. The bandgap of SnS_2 is located in the green spectral region (2.2 eV), providing greater selectivity in wavelength for the future optoelectronic devices. Similar to MoS_2, SnS_2 exhibits n-type characteristics and possesses a layered structure, crystallising in a CdI_2-type lattice structure, in which S-Sn-S trilayers with internal covalent bondings are held together by van der Waals forces. The S-Sn-S trilayers are stacked with a periodicity of one layer and a global D_{3d} space group symmetry. Recent studies have also demonstrated the great potential of SnS_2 in various applications including field effect transistors with high carrier mobility and on-off ratio,[46] gas sensors with high sensitivity and selectivity,[47] thermoelectric devices with high conversion efficiency,[48] and anodes with high charge storage capacity for Na/Li ion batteries.[49] It is also predicted that SnS_2 could be a potential stabilizer for the metallic phase in monolayer MoS_2 and WS_2 through alloying,[50] which is beneficial for better catalytic activity in electrochemistry and energy storage. In addition, it is observed that the removal of sulfur atoms under the electron irradiation of SnS_2 results in phase transformation into p-type SnS semiconductor,[51] which could enable the direct synthesis of lateral p-n junction with sharp interface simply by using tin chalcogenides components.[52]

2.3 Optoelectronics Based on 2D Materials

For the application in optoelectronic devices, photodetectors which convert light signals into electrical signals are the fundamental building blocks for the development of many innovative technologies such as video imaging, remote sensing, environmental monitoring, security checks and night vision devices.[53-55] For many years, traditional semiconductor films like Si, InGaAs and HgCdTe have dominated the commercial photodetector market because of their

high performance as well as mature large-scale production and integration technologies (**Figure 2.6**(a)).[56-58] However, they usually suffer from several drawbacks, including thick materials usage, strictly controlled fabrication conditions and rigorous operation demands. In comparison, 2D semiconductors with different band gap values listed in **Figure 2.6**(b) have been considered as promising candidates for the next generation optoelectronic systems because of their high transparency, atomically thickness and strong light-matter interaction.[59]

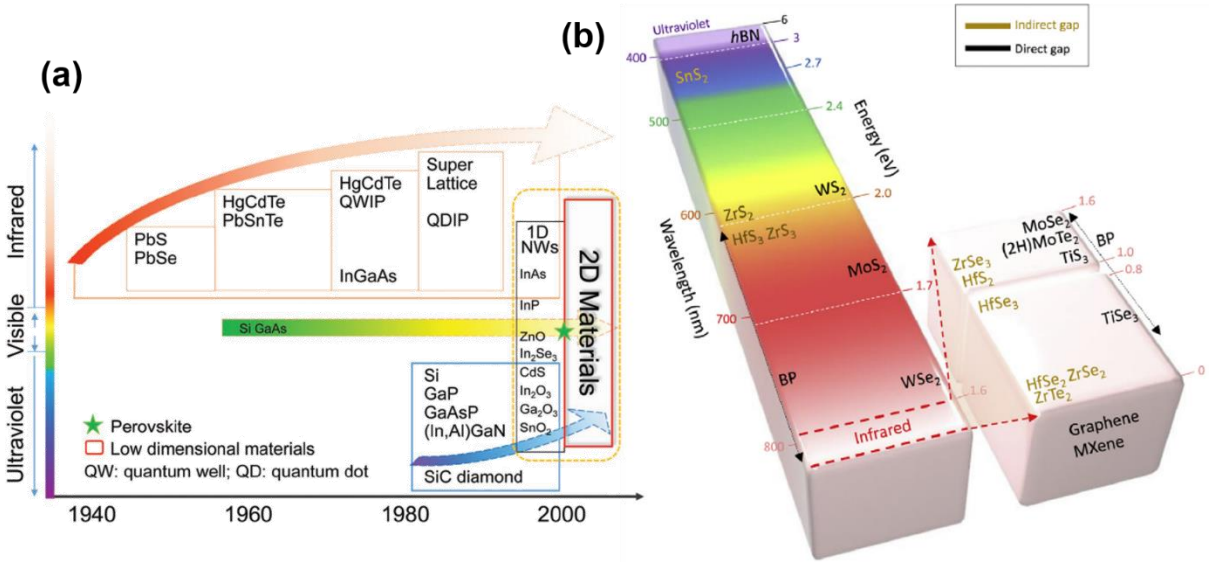


Figure 2.6. Materials candidate for optoelectronic devices. (a) A brief chronology demonstrating the timeline of thin film photodetectors for different spectral ranges. Reproduced with permission from ref. [55]. © 2017 Wiley-VCH. (b) Electromagnetic spectrum showing the bandgap of 2D materials varying from visible to infrared region. Reproduced with permission from ref. [59]. © 2017 Elsevier B.V.

2.3.1 Phototransistors- Photoconductive Effect

A phototransistor is the simplest form of the photodetector.[60] **Figure 2.7**(a) shows a typical configuration of a phototransistor based on 2D semiconductors such as MoS_2, which consists of a semiconducting 2D materials channel with two contacts affixed to the opposite ends of the channel that serve as source and drain electrodes on dielectric layers. In dark state,

the channel only allows a small current flow between the two electrodes. When the channel is under the illumination using a focused laser beam, the device current increases for all values of the gate voltage shown in **Figure 2.7**(b). This is ascribed to the photoconductive effect, where the excess free carriers including electrons and holes are generated after the photon absorption and results in an increase in conductivity. The amount of photogenerated carriers is dependent on the intensity of laser illumination. As shown in **Figure 2.7**(c), the output current increases gradually when raising the intensity of the illumination power from 0.015 μW to 15 μW, even if the applied bias in less than 1 V.

The photoresponsivity (R), defined as the photocurrent divided by the incident illumination power, is one of the important parameters to compare the detection performance of photodetectors that are constructed with different materials and geometries. It is an indication of how the detector system responds to illumination. In general, the photocurrent increases sublinearly with the incident excitation power, resulting in a reduction in photoresponsivity when increasing the incident excitation power (**Figure 2.7**(d)). This is attributed to the increasing carrier recombination and trap state saturation at higher illumination intensities.[61] These electrical characteristics can be explained by the energy band diagram illustrated in **Figure 2.7**(e).[62] According to the transfer curves shown in **Figure 2.7**(b), the MoS_2 channel exhibits an n-type semiconductor behaviour, where the Fermi level is closed to the conduction band edge and is usually higher than that of metals. This results in a Schottky barrier, an energy barrier for charge carriers to cross the metal-semiconductor junction, at the interface between Au (metal) and MoS_2 (semiconductor) when reaching the equilibrium state (**Figure 2.7**(e)-I). Illuminating the MoS_2 channel triggers the light absorption and generation of electron-hole pairs, which can be extracted conversely from source and drain electrodes by applying a bias (**Figure 2.7**(e)-II). When the device is operated under negative gate voltage, the Fermi level shifts downwards leading to a larger Schottky barrier. The photogenerated

carriers are more difficult to drift to the external circuit and results in a reduction of photocurrent (**Figure 2.7**(e)-III). By contrast, applying a positive gate voltage can make the Fermi level approach closer to the conduction band, bringing about the lower Schottky barrier and an increased extraction of photogenerated carriers (**Figure 2.7**(e)-IV).

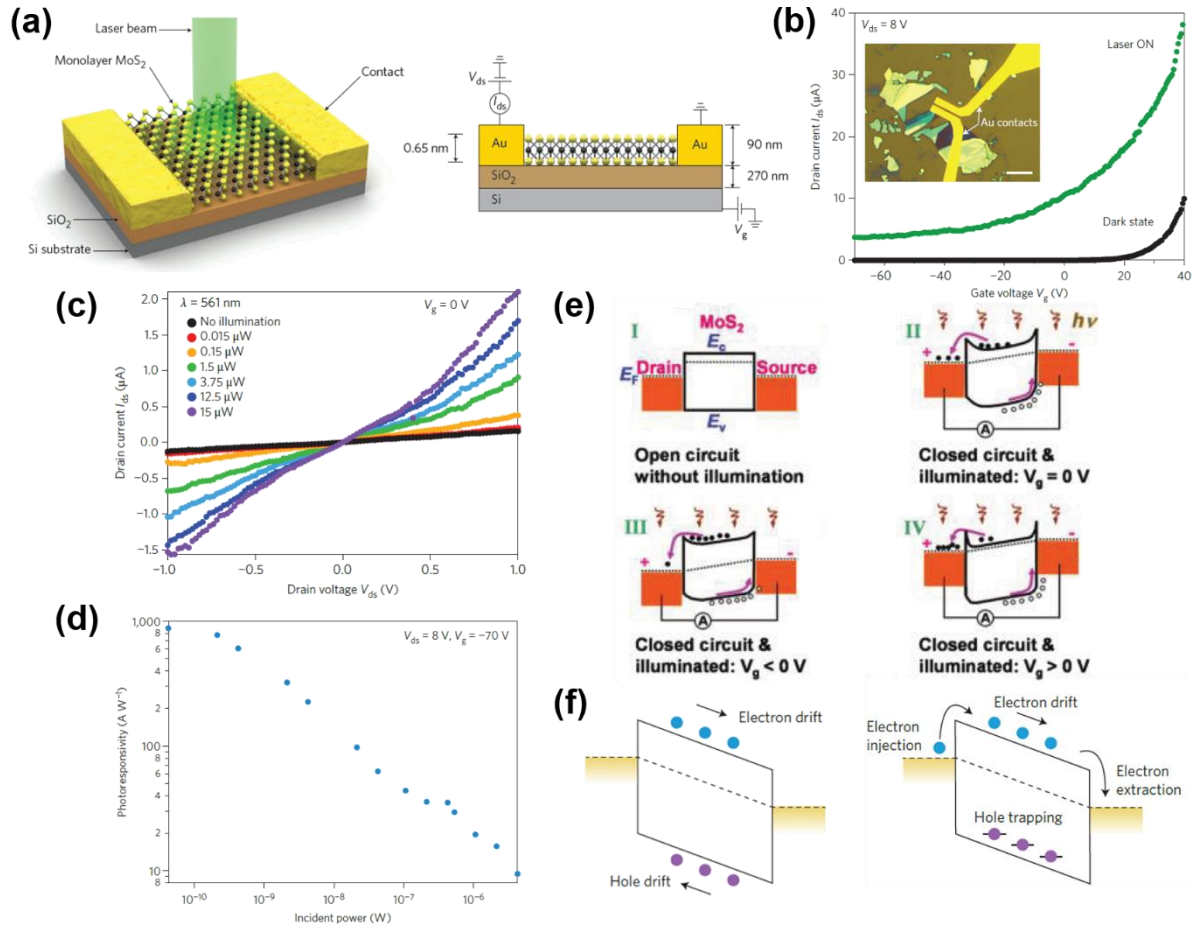


Figure 2.7. Photoconductive effect in phototransistors. (a) Schematic illustrations of the top view and side view of a monolayer MoS_2 phototransistor. (b) Gating response of the monolayer MoS_2 photransistor in dark and illuminated state. The inset shows the optical image of the as-fabricated device. (c) I-V characteristics of the monolayer MoS_2 phototransistor in the dark and under different illumination intensities. (d) Power-dependent photoresponsivity of the MoS_2 phototransistor. (a-d) Reproduced with permission from ref. [60]. © 2013 Nature Publishing Group. (e) Band diagrams of the MoS_2 phototransistor under the illumination and different gate biases. Reproduced with permission from ref. [62]. © 2012 American Chemical Society. (f) Band diagrams of the MoS_2 phototransistor

explaining the effect of charge trapping on photogenerated carriers. Reproduced with permission from ref. [64]. © 2014 Nature Publishing Group.

Photogating is a particular example of the photoconductive effect.[63] This is ascribed to the localised trap states such as structural disorder and surface adsorbates. When electron-hole pairs are generated in the semiconductor under illumination, one of the two carrier types is trapped in the localised states and acts as a local gate modulating the resistance effectively. Take **Figure 2.7**(f) for example, when the holes are trapped in the localised states near the valence band edge, the local gate of the trapped holes can shift the Fermi level based on the electric field effect, thus inducing more electrons and enhancing the photoresponse.[64] This often results in a high internal gain, which is defined as the ratio between the number of charge carriers that contribute to the photocurrent and the number of incident photons. However, this also brings the drawback of slower response time during the photo-switching testing because of the large time constant for carriers to escape from the traps. It may also be responsible for the hysteresis in the output I-V characteristics. In reality, when phototransistors based on 2D semiconductors are under illumination, both the photogating and photoconductive effects occur on the same device and contribute to the photocurrent simultaneously because of the unavoidable intrinsic defects in the 2D semiconductors, such as sulphur vacancies and domain boundaries in the MoS_2 layers.

2.3.2 Photodiodes- Photovoltaic Effect

Other than relying on the external electric field through applying a bias between the source and drain electrodes, a photodiode is another common photodetector.[65] It is usually operated by means of the photovoltaic effect, where the photogenerated electron-hole pairs are separated by a built-in electric field at the junction interface and extracted towards opposite

directions. The built-in electric field is often generated by connecting p-type semiconductors and n-type semiconductors together forming a 2D p-n junction, which is one of the most important building blocks in modern electronics. Due to the ultrathin thickness of 2D semiconductors, the weak screening effect makes 2D p-n junctions different from traditional bulk p-n junction and can be effectively tuned by an external gate voltage.[66]

In 2D semiconductors, MoS_2 is the one of the most commonly-used n-type semiconductor,[67-68] while WSe_2 is one of the well-investigated semiconductor with p-type characteristics.[69-70] As shown in **Figure 2.8**(a), stacking these two individual materials creates a simple p-n junction in the vertical heterostructure. The Al and Pd metal contacts in **Figure 2.8**(a) are chosen to enhance the n-type and p-type characteristics, facilitating the injection of electrons into n-type MoS_2 and holes into p-type WSe_2. In the dark state, the I-V characteristic curves of the junction shown in **Figure 2.8**(b) exhibit rectifying behaviour and can be modulated by gate voltages. Under illumination, the heterostructrure exhibits a gate-dependent photovoltaic response (**Figure 2.8**(c)), which can be related to the interlayer tunnelling-mediated recombination of the majority carriers across the junction of the heterostructure. The spatial photocurrent map in the inset of **Figure 2.8**(c) further indicates that the photovoltaic response primarily originates at the junction area between the MoS_2 and WSe_2 layers. This can be attributed to the rapid separation of photocarriers at the interface of the MoS_2 and WSe_2 layers, and the negligible potential barriers in the lateral transport direction, as illustrated by the lateral band profile in **Figure 2.8**(d). Besides, the photoresponsivity can be enhanced from 2 mA/W to 10 mA/W when employing additional graphene layers to connect each 2D semiconductor to metal electrodes (**Figure 2.8**(e)). This is due to the increasing collection rate of the photogenerated carriers through reducing the loss from interlayer recombination. However, this also brings about linear I-V characteristic curves and the disappearance of

rectifying behaviour both in the dark and illumination states, shown in **Figure 2.8**(f), because the currents are primarily dominated by the direct tunnelling between the two graphene layers.

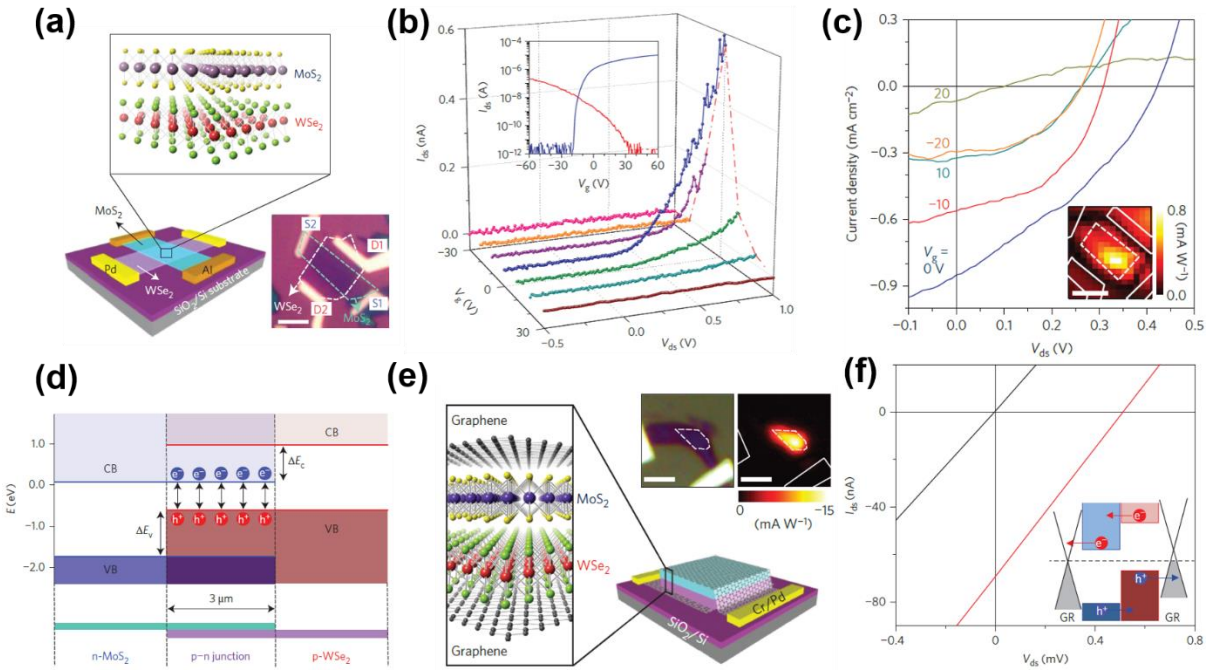


Figure 2.8. Photovoltaic effect in photodiodes. (a) Schematic and optical images of the photodiode based on the van der Waals stacked MoS_2/WSe_2 heterostructure. (b) I-V characteristics of the photodiode at different gate voltages. The inset shows the individual transfer curves of monolayer MoS_2 and WSe_2. (c) Photoresponse characteristics of the photodiode at different gate voltages under white light illumination. The inset shows the photocurrent map of the MoS_2/WSe_2 heterostructure without applying the bias. (d) Energy band diagram of the individual MoS_2, WSe_2 and their junction area. (e) Schematic and the optical as well as photocurrent map image of the MoS_2/WSe_2 heterostructure sandwiched between graphene electrodes. (f) I-V output characteristics of the graphene-sandwiched MoS_2/WSe_2 heterostructure in both the dark state and illumination state. (a-f) Reproduced with permission from ref. [65]. © 2014 Nature Publishing Group.

2.3.3 Contact Engineering

With the reduced channel length in transistors, the contact resistance at the interface between the semiconductor and the metal electrodes ultimately dominates the device performance.[71-73] Low contact resistance in devices based on 2D semiconductors is required for achieving high on-state current and large photoresponse. One of the most important figure-of-merits that determines the contact resistance and charge transport efficiency is the Schottky barrier height at the metal-semiconductor junction. The larger the Schottky barrier height is, the larger energy is required for thermionic emission to overcome the barrier.

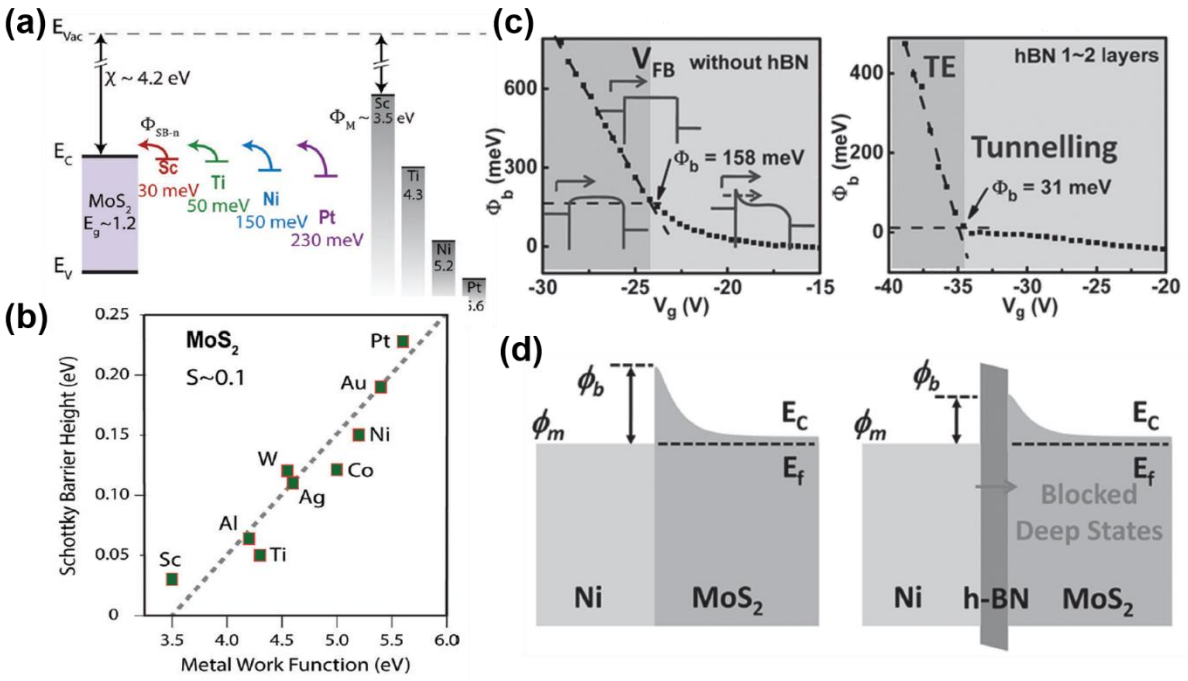


Figure 2.9. Fermi level pinning at the contacts between metal and 2D semiconductors. (a) Schematic band diagram demonstrating the expected and actual band alignment between 2D MoS_2 and other metal electrodes. (b) The relationship between Schottky barrier height extracted from experimental results and the various work functions of contact metals. (a, b) Reproduced with permission from ref. [78]. © 2018 The Royal Society of Chemistry. (c) The plots of Schottky barrier height for different gate voltages with and without the hBN tunnelling layer. (d) Schematic band

diagram showing the reduced Schottky barrier with the hBN layer insertion. (c, d) Reproduced with permission from ref. [81]. © 2016 Wiley-VCH.

In an ideal metal-semiconductor junction, the Schottky barrier height is well predicted by the Schottky-Mott rule and can be expressed as the energy difference between the energy work function and the semiconductor electron affinity.[74-75] Selecting different metals with various work functions for a semiconductor channel results in the modulation of Schottky barrier height and can greatly influence the device performance. However, in reality the experimental studies reveal that the metal-2D semiconductor contacts is strongly influenced by Fermi level pinning,[76-77] where the Schottky barrier heights are almost independent of the metal work functions and leading to a relative small range that the barrier can be adjusted. As shown in **Figure 2.9**(a), adopting Sc and Pt as the metal electrodes for the transistors based on MoS_2, a negative Schottky barrier height of -0.7 eV and positive Schottky barrier height of 1.4 eV, respectively, is calculated under the Schottky-Mott condition. Instead, the effective Schottky barrier height extracted from the transistor electrical measurement is only 0.03 eV for Sc and 0.23 eV for Pt.[78] **Figure 2.9**(b) further plots the extracted Schottky barrier heights for a variety of metals, indicating a pinning factor S of around 0.1. The pinning factor S is defined as $\partial\Phi_{SB}/\partial\Phi_M$, where Φ_{SB} is the Schottky barrier height and Φ_M is the metal work function, and is equal to 1 when achieving the Schottky-Mott condition.

When the metal is directly in contact with the semiconductor, the wave function of the metal electron penetrates to nanometre depth into the semiconductor and charges the interface states of the semiconductor. This results in the formation of metal-induced gap states (MIGS) inside the semiconductor bandgap and the increase of the contact resistance at the metal-semiconductor junction.[79-80] Inserting a thin tunnelling layer into the contact interface to separate metal and semiconductor is found to be advantageous for alleviating the MIGS and

improving the contact performance.[81-84] As shown in **Figure 2.9**(c), the initial Schottky barrier height for MoS_2/Ni contacts can be reduced from 158 meV to 31 meV with the use of hBN as interfacial layers. This is ascribed to the attenuation of metal electron wave function and the weakened filling of MIGS at the semiconductor. The effective Schottky barrier height can therefore be reduced with small tunnelling resistance, as illustrated in **Figure 2.9**(d). Besides, benefiting from the atomically thin layer of hBN, the thickness of the tunnelling layer can be precisely controlled to optimise the resistance from the Schottky barrier and carrier tunnelling.

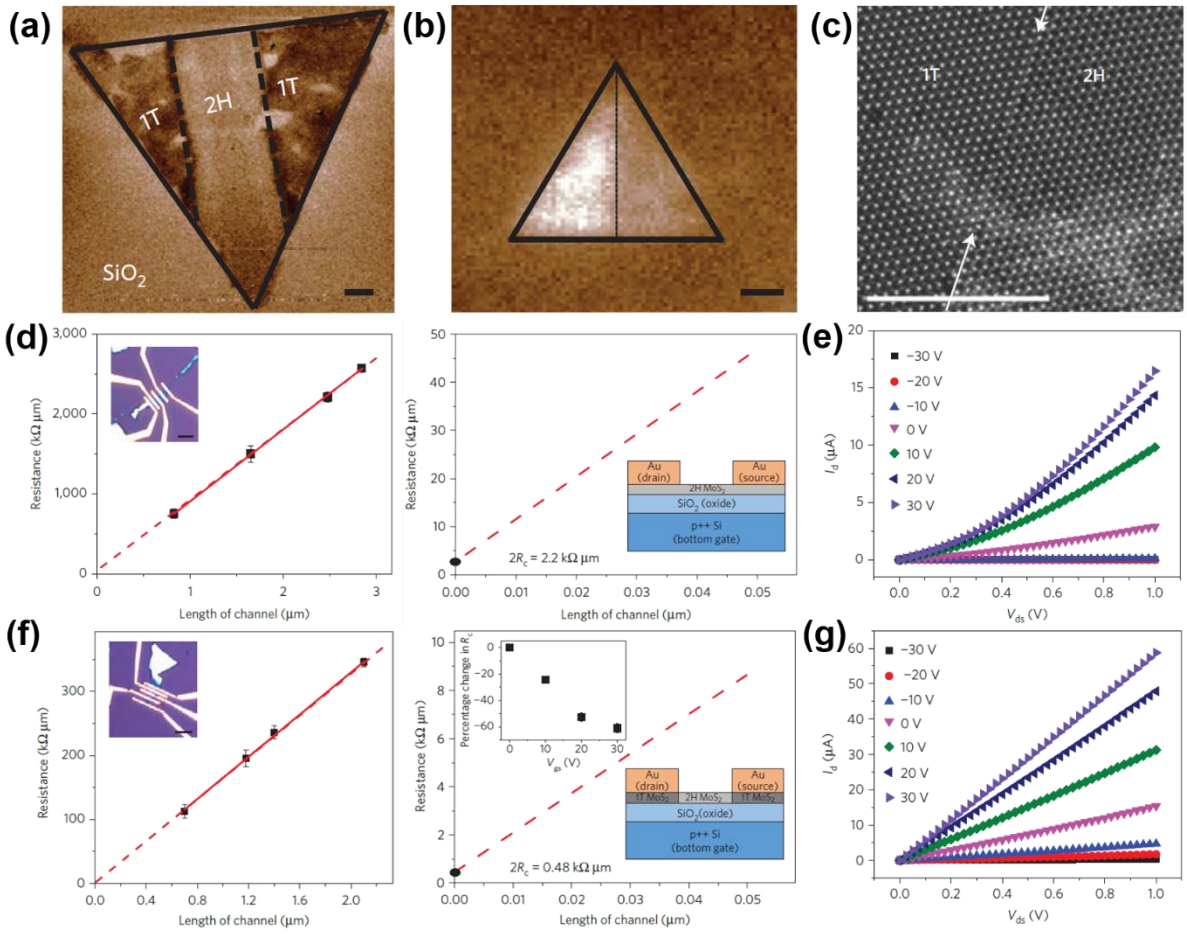


Figure 2.10. Phase engineered homojunction contact. (a) Electrostatic force microscopy phase image of a triangular MoS_2 monolayer demonstrating the locally patterned 1T-2H-1T phases. (b) PL map of a monolayer MoS_2 single crystal. The 2H phase (left) exhibits stronger PL signal than the 1T phase (right). (c) High resolution TEM image of the phase boundary between 2H and 1T phase MoS_2 monolayer. (d) The relationship between the contact resistance for the MoS_2 channel and the channel

length with Au electrodes deposited on the 2H phase. (e) I-V characteristic curves of the MoS_2 channel with 2H phase contacted to the Au electrodes under different gate voltages. (f) The relationship between the contact resistance for the MoS_2 channel and the channel length with Au electrodes deposited on the 1T phase. (g) I-V characteristic curves of the MoS_2 channel with 2H phase contacted to the Au electrodes under different gate voltages. (a-g) Reproduced with permission from ref. [89]. © 2014 Nature Publishing Group.

An alternative method to improve the contact performance is the realisation of an edge contact to eliminate the resistance stemming from the van der Waals gap and tunnelling barrier.[85-86] This can be achieved by combining the encapsulation and etching techniques to make the device topology where metal electrodes are connected to 2D materials along their atomic edges.[87] Similar concept can also be adopted using phase engineering of 2D materials. In the example of MoS_2, the most stable 2H phase exhibits semiconducting behaviour while it can be converted to the metastable 1T phase with metallic characteristics by organolithium chemical treatment.[88] It is viable to achieve a seamless edge contact with 1T-2H MoS_2 through the covalent bonding. To fabricate this, the 2H MoS_2 layers are partially covered by PMMA and then immersed into *n*-butyl lithium. Lithium ions are then intercalated into the interlayer on the exposed area and donate electrons, leading to a local transformation and structural change into 1T MoS_2, which remains after the removal of the *n*-butyl lithium.[89] **Figure 2.10**(a) shows the electrostatic force microscopy image of a resulted 1T-2H-1T MoS_2 triangle, demonstrating that the 1T and 2H phases can coexist in the same crystal. The PL intensity map in **Figure 2.10**(b) further indicates the quenching of the characteristic peak within the 1T phase and exhibits a clear boundary between 1T and 2H phases, which is further confirmed by the high resolution TEM (**Figure2.10**(c)). The device based on original 2H MoS_2 shows a contact resistance of 1.1 kΩ μm (**Figure2.10**(d)) and nonlinear feature of the I-V curve (**Figure2.10**(e)), indicating the existence of the Schottky barrier. With the aids of these phase

engineering and local patterning skills, the contact resistance decreases to 0.2 kΩ μm (**Figure2.10**(f)) and the I-V curves exhibit linear features (**Figure2.10**(g)) when the 1T phase is used as the contact for the 2H MoS_2 channel, showing an enhanced contact performance.

2.4 CVD Synthesis of 2D Materials

In comparison to the traditional top-down exfoliation methods, chemical vapour deposition (CVD) growth has been proven to be scalable and compatible with current semiconductor processes.[90] There are several elementary steps during the whole growth process: (1) sublimation and transport of the precursors by a forced flow of a carrier gas, (2) diffusion of the precursors from the gas phase to the growth substrate surface, (3) adsorption and reaction of the precursors on the substrate, (4) surface diffusion of the adsorbed species to the growth sites, (5) incorporation of the adsorbed species into the crystalline lattices, (6) desorption and sublimation of the remaining species on the substrate surface. The growth parameters in these sequential steps plays a vital role in controlling the film structure including layer number, domain size, morphology and orientation.

2.4.1 Layer Number

The majority of 2D materials have layer-dependent physical properties. The band gap of MoS_2 and WS_2, for example, decreases with the increase of layer number.[20, 22] On the other hand, the thickness of hBN plays a critical role in field effect transistors when serving as a tunnelling barrier.[36] The precise control of layer number for 2D materials during the synthesis therefore becomes desirable for its practical applications in electronic devices. This could be achieved with the aid of understanding their growth mechanisms.

Similar to the growth of graphene on Cu, the decomposition of the precursor mainly occurs on the catalytic metal surface. To explore the fundamental mechanisms underlying the CVD of hBN on catalytic Cu, Park *et al.* evaluated the structural stability of B-N intermediates on a Cu substrate using first-principals calculations (**Figure 2.11**(a)).[91] It is found that the dehydrogenation of ammonia borane (H_3B-NH_3) precursors firstly occurs on the substrate surface, as this reaction is more energetic favourable than the dissociation of the B-N bond. After which they start to incorporate with each other for the formation of cyclic-BN ring through polymerization, and finally achieve stable hBN layers. Kidambi *et al.* utilized a combination of complementary in-situ X-ray photoelectron spectroscopy and X-ray diffraction to reveal the surface states at different growth stages.[92] They discovered that the B and N supply routes are different during growth of hBN. As shown in **Figure 2.11**(b), B is found to be incorporated into the Cu bulk under the exposure of borazine precursors, resulting in a Cu lattice expansion and B precipitation from Cu upon cooling. In contrast, the N incorporation is not observed due to the much lower solubility on the Cu substrate. As a consequence, the supply of B can be either from the Cu bulk or surface, while N is fed only via the Cu catalytic surface. They also suggested that additional layers nucleated and grew only at the interface between the catalyst and the first hBN layer.

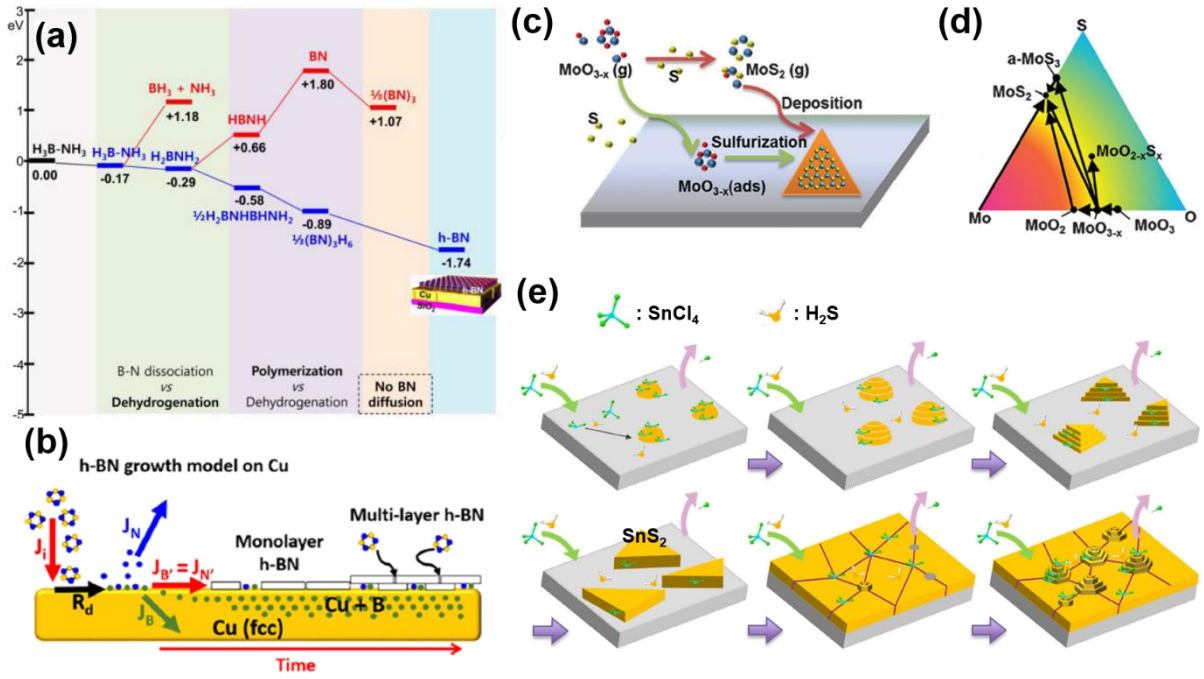


Figure 2.11. Growth mechanisms of 2D materials. (a) Reaction energy diagram for hBN layer growth on Cu substrate. Reproduced with permission from ref. [91]. © 2015 American Chemical Society. (b) Schematic diagram explaining the growth of monolayer and multilayer hBN. Reproduced with permission from ref. [92]. © 2014 American Chemical Society. (c) Schematic diagram showing two possible growth processes of MoS_2 using MoO_3 and S precursors. (d) Ternary phase diagram of Mo-O-S with the labelled arrows indicating the reaction pathways of MoS_2. (c, d) Reproduced with permission from ref. [93]. © 2015 The Royal Society of Chemistry. (e) Schematic diagram showing the nucleation and growth mode of SnS_2 on SiO_2 substrate using $SnCl_4$ and H_2S precursors. Reproduced with permission from ref. [94]. © 2018 IOP Publishing.

The growth of 2D semiconducting metal chalcogenides on SiO_2 substrate is non-catalytic and much more complicated than hBN. In general, the growth follows the layer-by-layer mode and there are two possible routes for the surface growth. Take MoS_2 using MoO_3 and S precursor powders for example, the MoO_3 is first partially reduced by S to form a volatile MoO_{3-x} species.[93] As shown in **Figure 2.11**(c), the MoO_{3-x} species could (a) adsorb and diffuse on the substrate, reacting with S to form MoS_2; or (b) directly react with S in the gas phase,

and the resulting MoS_2 clusters deposit and grow on the substrate. These two different routes are highly dependent on the adsorption/desorption of both MoO_{3-x} species and MoS_2 clusters, which could be adjusted by changing the substrate temperature and precursor-substrate distance. Besides, the ratio of MoO_3 and S precursor supply is also of great importance to ensure 2D growth of MoS_2. The S-poor environment could lead to the formation of oxide or oxysulfide nanoparticles while an excess of S may yield amorphous non-volatile MoS_3 (**Figure 2.11**(d)). The growth mechanism of SnS_2 is different from classic layer-by-layer mode. Zhang *et al.* reported that the initial nuclei could be several monolayers high and determine the eventual thickness of 2D SnS_2 crystals (**Figure 2.11**(e)).[94] This may be due to the appearance of other SnS_x phases prior to the growth stage.

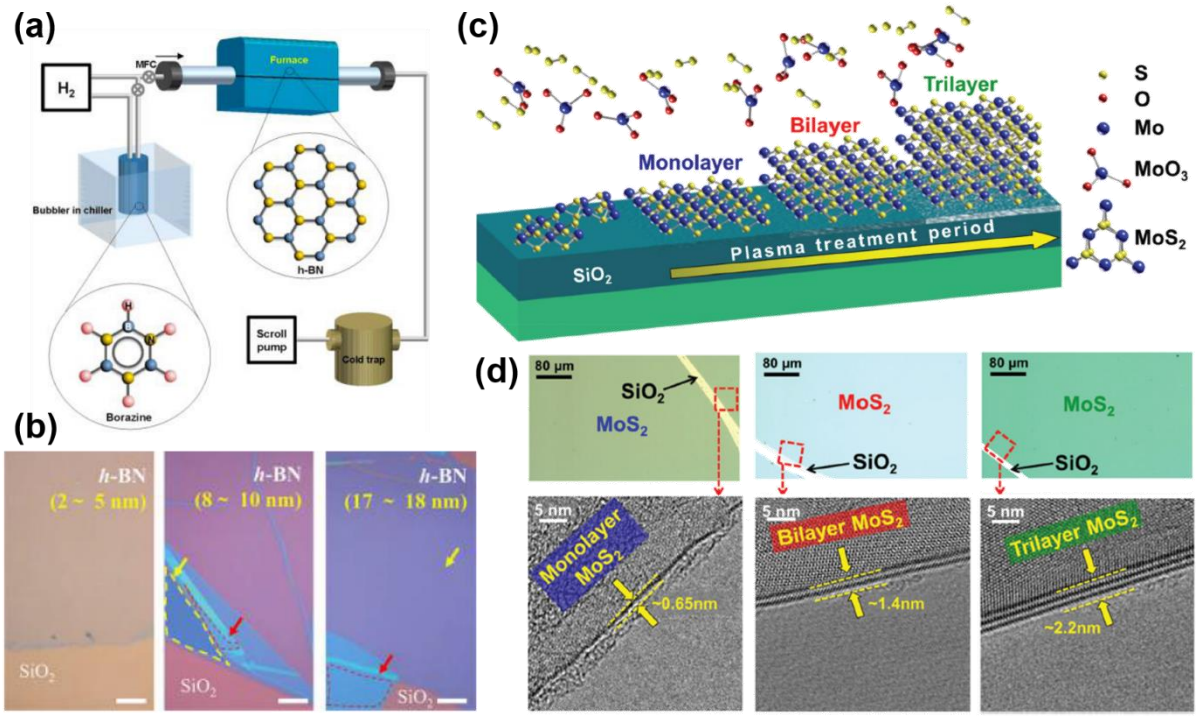


Figure 2.12. Controlling the number of layers in 2D materials during CVD growth. (a) Schematic diagram of the low pressure CVD setup for the growth of hBN. Reproduced with permission from ref. [95]. © 2014 American Chemical Society. (b) Optical images of hBN films with different thicknesses on SiO_2 substrate. Reproduced with permission from ref. [100]. © 2012 American Chemical Society. (c) Schematic diagram of the layer control for CVD MoS_2 films with different plasma treatment time.

(d) Optical images with the corresponding high resolution TEM images showing the uniform monolayer, bilayer and trilayer MoS_2 films. (c, d) Reproduced with permission from ref. [102]. © 2015 The Royal Society of Chemistry.

During the CVD growth, the control of hBN layers is highly pressure-sensitive. When using a Pt growth substrate, the monolayer hBN was obtained under low-pressure regime (**Figure 2.12**(a)), while at high pressure a thick film was grown on Pt (111) and a thin film was grown on Pt (100).[95] The possible explanation for this is that the catalytic effect of the Pt (111) surface is higher than that of the Pt (100) surface because of the higher density of the Pt atoms, and Pt (111) surface is also known to be an epitaxial surface for the graphene and hBN growth.[96-97] This leads to a more efficient decomposition of the precursors. Similarly, monolayer hBN is prone to be obtained under the low pressure CVD on Cu substrate, while ambient pressure CVD growth results in few layer growth.[98] The possible explanation for this is that the surface-mediated growth is promoted and less affected by the gas-flow effect at low pressure conditions. Koepke *et al.* also found that at ambient pressure growth, the resulted hBN is more amorphous, disordered and sp^3-bonded.[99] Kim *et al.* reported that under ambient pressure the growth rate of hBN at a constant temperature is strongly affected by the concentration of the precursor and the carrier gas condition.[100] As shown in **Figure 2.12**(b), different thicknesses of hBN films ranging from 2 to 20 nm can be achieved by controlling the growth time and the carrier gas ratio of hydrogen and nitrogen.

The number of layers in 2D semiconducting metal chalcogenides could be effectively controlled by altering the growth temperature. He *et al.* reported that growth at 750°C would yield $MoSe_2$ dominated by monolayer, while 825 and 900°C leads to the formation of bilayer and trilayer to tetralayer $MoSe_2$.[101] In addition, oxygen plasma treatment is also found to be influential in layer control, demonstrated in **Figure 2.12**(c).[102] The optical and TEM images in

Figure 2.12(d) display the MoS_2 films with monolayer, bilayer and trilayer obtained by varying the period of oxygen plasma treatment time. This is because of higher surface reactivity with the increase of plasma treatment time, therefore facilitating the heterogeneous nucleation during the growth.

2.4.2 Domain size

The improvement for the quality of CVD-grown 2D materials is still imperative for practical applications because of the inevitable existence of its domain boundaries.[103-104] These domain boundaries will disrupt the structural continuity, resulting in degradation of its extraordinary physical properties. Although the grain size of the hBN has been significantly enlarged through delicate control of relevant parameters, it is still much smaller than that of graphene grown on Cu foils, whose domain size can reach to inch-scale.[105] This may be attributed to the greater chemical affinity of N-containing intermediates for the Cu surface than carbon intermediates. Density function theory (DFT) calculations suggest that the adsorption energy of a pair of graphene carbon atoms on Cu surface is around 0.06 eV and the activation energy for graphene nucleation is measured to be about 3 eV, suggesting that the critical nuclei size for graphene is about 50 carbon pairs.[106] In comparison, the adsorption energies of the B-N pair in hBN on the Cu surface is around 0.25 eV and the activation energy for hBN nucleation is estimated to be around 5 eV, suggesting that the critical nuclei size is about 20 BN pairs, which is significantly lower than that for graphene.[107] As a consequence, the nucleation density of hBN on Cu can be achieved with much lower surface supersaturations of precursors. The domain sizes of CVD grown hBN were typically in the order of micrometre.

Similar to the optimised graphene growth parameters, increasing the growth temperature and reducing the precursor feeding rate and suppressing the initial nucleation density are proven to be an efficient route to increase the domain size and enhance the film

quality. Several strategies have been developed to enhance the domain size by means of decreasing the initial nucleation density. Tay *et al.* found that the nucleation density and domain sizes are highly dependent on the surface morphology of the Cu substrate.[108] The domain size of hBN grown on electropolished Cu substrate is an order of magnitude larger than unpolished Cu substrate. By achieving larger hBN domains, the grain boundaries-induced defects are effectively reduced, leading to the formation of hBN films with smoother and higher quality. Wu *et al.* demonstrated that the large hBN domain size with uniform crystalline orientation can be obtained by increasing the hydrogen gas flow during the growth stage.[109] Song *et al.* proposed that the feeding rate of ammonia borane precursor is the key factor in controlling the nucleation density.[110] As demonstrated in **Figure 2.13**(a), when heating above the temperature of 60 °C, ammonia borane starts to decompose into hydrogen, borazine and aminoborane.[111] Through optimizing the decomposition temperature and the growth time, the nucleation density is greatly suppressed and results in an increased domain size (**Figure 2.13**(b)). Khan *et al.* used the melted Cu as substrate to grow hBN and showed that the domain size can increase to more than 5 μm because the melted Cu has a very smooth surface morphology with no rolling features comprising of parallel uneven grooves, therefore reducing the nucleation sites.[112] Similarly, Tay *et al.* reported that the hBN domain size can be grown up to 10 μm using resolidified Cu substrates.[113] Later on, Ji *et al.* combined using Cu enclosure with high pressure H_2 annealing, successfully obtaining single-crystalline monolayer hBN domains with a lateral size up to ~300 μm (**Figure 2.13**(c)).[114] The evaporative loss of Cu atoms at the inner surface was consequently supressed by a re-deposition effect that occurred because of the limited volume of the enclosure, making the inner surface have a lower surface roughness and leading to the reduction of hBN nucleation density.

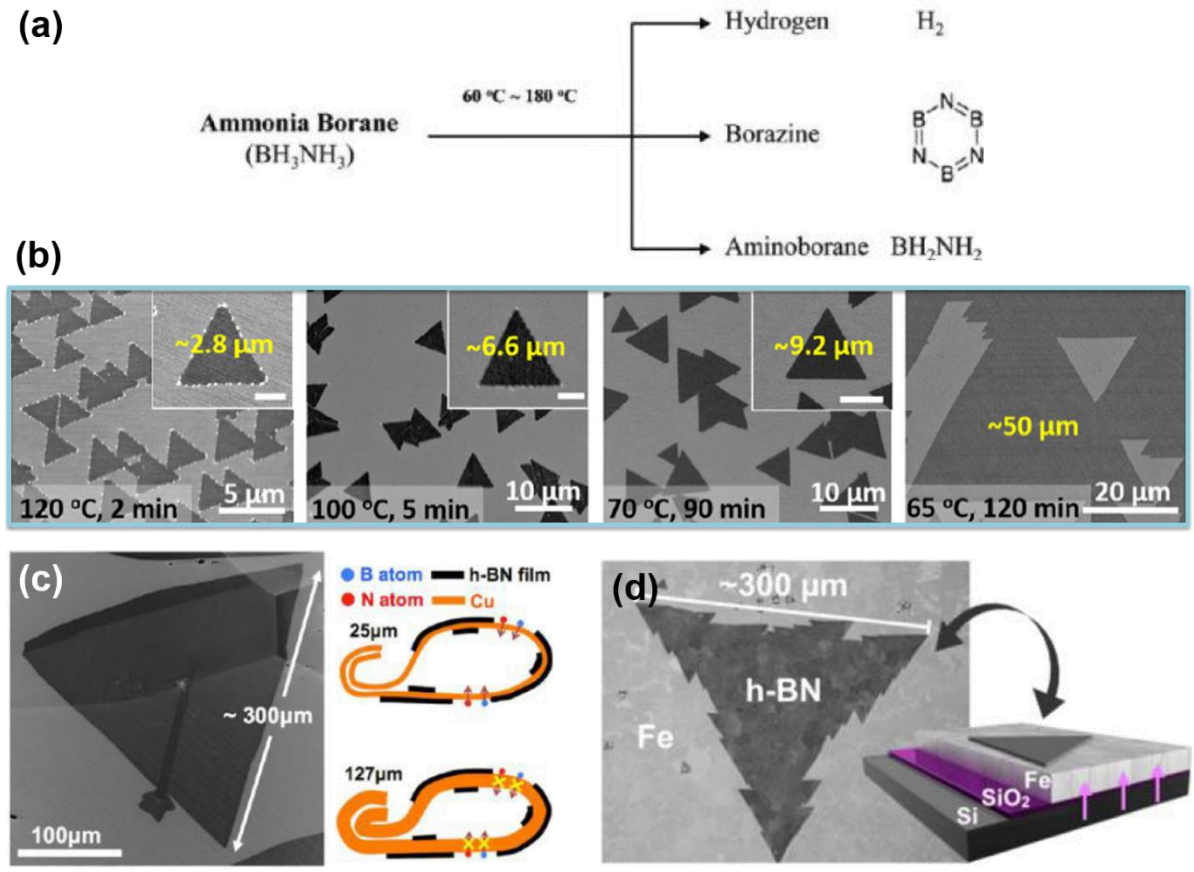


Figure 2.13. Domain size enhancement of hBN crystals. (a) The thermally decomposition of commonly used ammonia borane precursor for hBN growth into hydrogen, borazine and aminoborane at 60~180°C. Reproduced with permission from ref. [111]. © 2012 American Chemical Society. (b) SEM images of hBN triangles grown at different ammonia borane precursor decomposition temperatures and growth time. Reproduced with permission from ref. [110]. © 2015 Springer International Publishing AG. (c) SEM image showing the hBN with lateral size up to 300 μm grown on Cu enclosure. Reproduced with permission from ref. [114]. © 2017 American Chemical Society. (d) Schematic of catalyst system composed of $Fe/SiO_2/Si$ and the SEM image of obtained large hBN domain. Reproduced with permission from ref. [116]. © 2015 American Chemical Society.

Besides the commonly used Cu substrate for hBN growth, designing novel substrates is another strategy for growing hBN with large domains. Lu *et al.* demonstrated that the nucleation density can be greatly reduced to 60 per mm^2 by introducing Ni into the Cu

substrates, and single-crystal hBN domains can grow up to 7500 μm^2 under the optimised condition.[115] They attributed this to the different growth mechanism based on solid-gas reaction involving surface chemistry of Ni-B and Ni-N. Caneva *et al.* took a simple thin film Fe/SiO_2/Si catalyst system and successfully grew monolayer hBN single crystal with lateral dimensions of about 0.3 mm (**Figure 2.13**(d)).[116] In this approach, controlled Si diffusion into the Fe catalyst allows exclusive nucleation of monolayer hBN with very low nucleation densities.

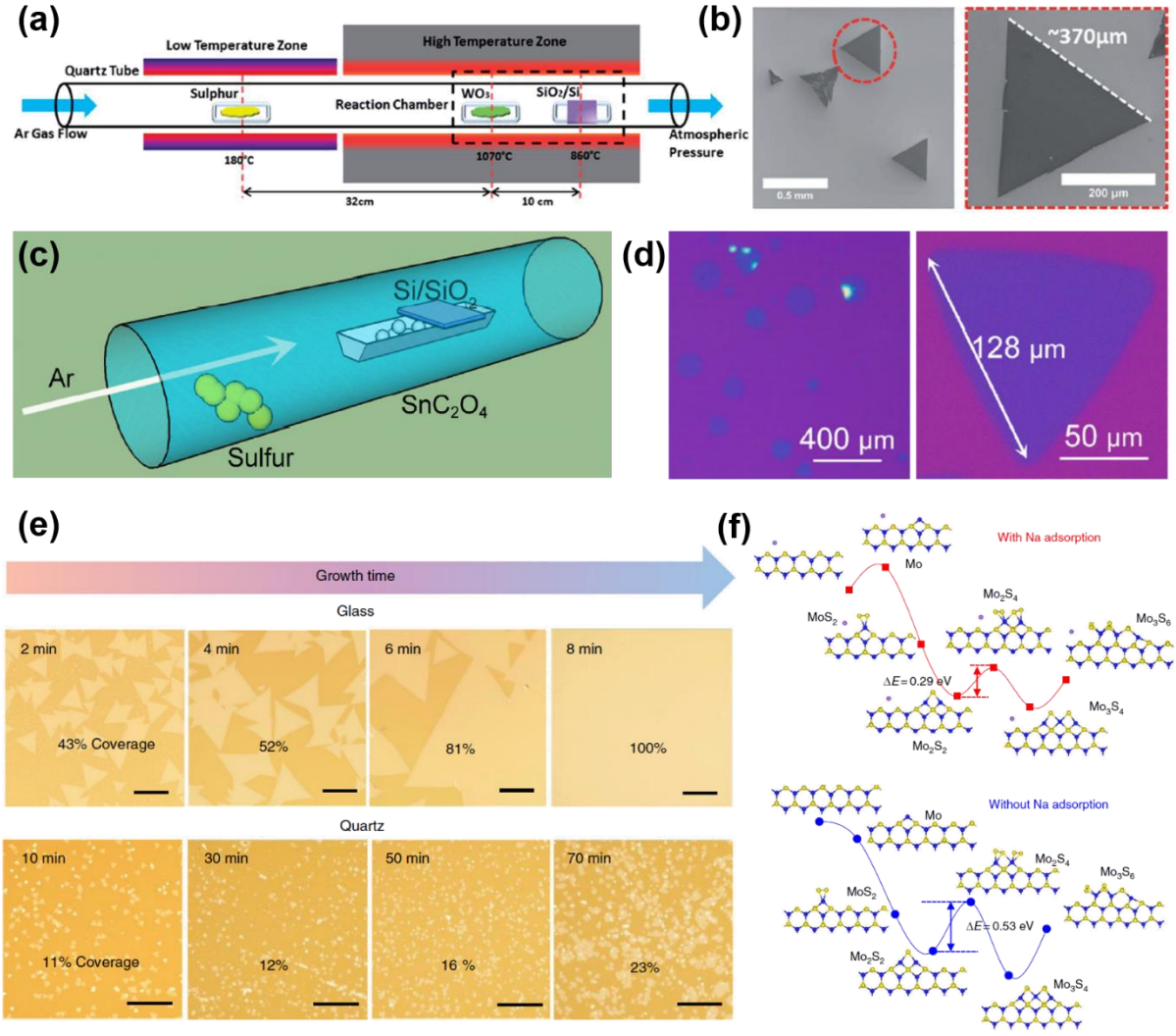


Figure 2.14. Growing large single crystal 2D semiconductors. (a) Schematic illustration for the CVD experimental setup for the growth of large single crystal WS_2. (b) SEM images of the resulted as-grown WS_2 crystals. (a, b) Reproduced with permission from ref. [117]. © 2014 The Royal Society of Chemistry. (c) Schematic illustration for the CVD experimental setup for the growth of large single

crystal SnS_2. (d) Optical images of the resulted as-grown SnS_2 crystals. (c, d) Reproduced with permission from ref. [118]. © 2017 Springer International Publishing AG. (e) Growth-time-dependent optical images of MoS_2 synthesized on a soda-lime glass and quartz glass. (f) The energy diagrams for MoS_2 growth along the S-terminated edges with and without the aids of Na adsorption. (e, f) Reproduced with permission from ref. [124]. © 2018 Nature Publishing Group.

In the growth of 2D semiconducting metal chalcogenides, Rong *et al.* firstly adopted two furnace system illustrated in **Figure 2.14**(a) to accurately control the introduction time and the amount of S vapour during the growth of WS_2, enabling the formation of triangular WS_2 domain with the lateral size up to 370 μm (**Figure 2.14**(b)).[117] Ye *et al.* reported a facile CVD method utilising tin oxalate precursor for the synthesis of the 2D atomic-layer SnS_2 (**Figure 2.14**(c)).[118] Compared to traditional tin oxide precursors, tin oxalate has medium vapour pressure at the reaction temperature. This provides a better control of the Sn supply and the size of the resultant SnS_2 single crystal domains can be as large as 128 μm (**Figure 2.14**(d)). Switching the growth substrate from conventional insulating SiO_2 or sapphire to catalytic Au or soda-lime glass is demonstrated to be another effective way for obtaining 2D semiconductors with large domain.[119-124] **Figure 2.14**(e) shows the comparison between the MoS_2 grown on soda-lime glass and quartz surfaces, where the growth rate is much faster on soda-lime glass. This is because of the existence of the Na element in the soda-lime glass. With the incorporation of Na, the highest energy barrier during the MoS_2 step growth reduces from 0.53 to 0.29 eV (**Figure 2.14**(f)), leading to the ultrafast growth of MoS_2.[124] In addition, carrier gas is another factor in determining the domain size. Introducing a small amount of oxygen is found to be beneficial for decreasing the MoS_2 nucleation density through etching off the unstable nuclei on sapphire and SiO_2 substrate surfaces.[125]

2.4.3 Morphology

Due to the binary elements of hBN, there are greater morphology variation for hBN domains resulting from different termination patterns. For most of the CVD-grown sample, hBN domains usually adopt triangular shape, instead of hexagonal shape observed in graphene growth. This is attributed to the asymmetric N and B terminated edge energies. Based on the theoretical calculation showing the lower energy for N-terminated zigzag edges compared to B-terminated zigzag edges, the triangular hBN domains are mostly with the N-terminated zigzag edges.[126]

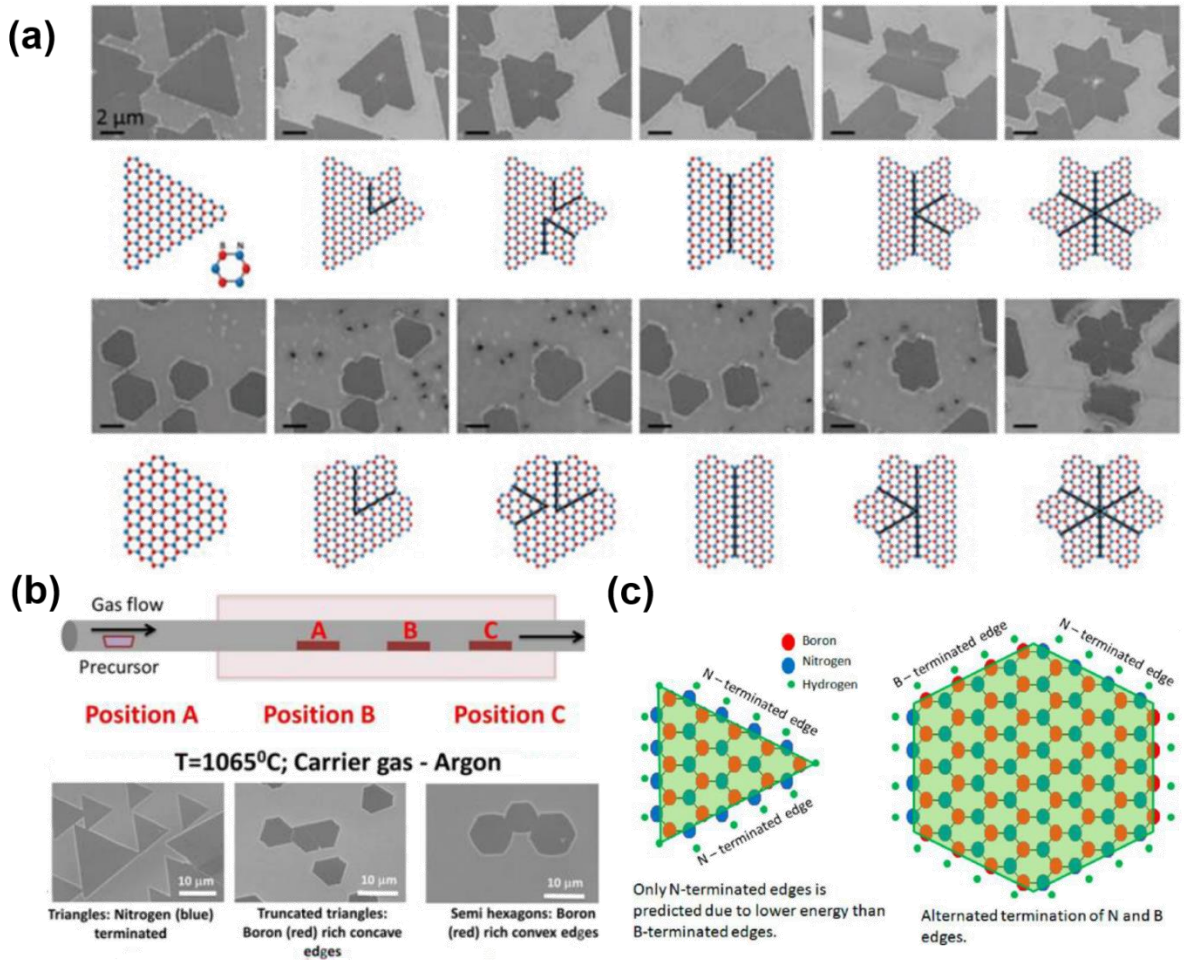


Figure 2.15. Morphology control of hBN crystals. (a) SEM images paired with their interpreted atomic configurations of various multifaceted shape of hBN crystals. Reproduced with permission from ref. [113]. © 2016 The Royal Society of Chemistry. (b) CVD experimental setup for the hBN growth

and the corresponding SEM images for different positions within the furnace. Reproduced with permission from ref. [107]. © 2015 American Chemical Society. (c) Triangular hBN structure with all sides of N-terminated edges and hexagonal hBN structure with alternating N-terminated and B-terminated edges. Reproduced with permission from ref. [108]. © 2014 American Chemical Society.

In addition to the conventional triangles, several complex morphologies of hBN have also been investigated. Kim *et al.* observed an asymmetric diamond shape with one side of equilateral triangle for the diamond when increasing the heating temperature of the ammonia borane precursor.[111] Tay *et al.* reported a variety of multifaceted hBN shapes with well-defined edges such as rhombus or butterfly shapes formed by the coalescence of two mirroring domains and other complex shapes (**Figure 2.15**(a)).[113] Recent work conducted by Zhang *et al.* revealed that shape variation of hBN domains can be manipulated by adjusting the chemical balance between boron and nitrogen.[127] This can be simply realized by placing Cu substrate at different positions in the CVD chamber. As shown in **Figure 2.15**(b), the morphology of single hBN domain changes from triangular to truncate triangular and finally to pseudo hexagonal shape as the substrate position moves away from the precursor inlet.[107] This shape variation is affected by the ratio of boron and nitrogen active species concentrations on the Cu surface. When moving away from the precursor inlet, the deficiency of nitrogen active species results in the alternated termination of N and B edges, shown in **Figure 2.15**(c).[108] After changing the carrier gas from argon to nitrogen, all Cu substrates in the CVD chamber exhibited exclusively triangular shapes of hBN crystals. This drastic difference can be explained by an additional source of active nitrogen resulting in nitrogen terminated triangular domain shape. Similarly, Yin *et al.* designed a wedge-shaped Cu pocket with two open ends as the substrate for hBN growth.[128] They found that the triangular hBN domain truncated more significantly from the bending end to the crimping end and the shape of hBN domains finally evolve into a hexagon. They proposed that the enhanced Cu vapor pressure may play an important role here.

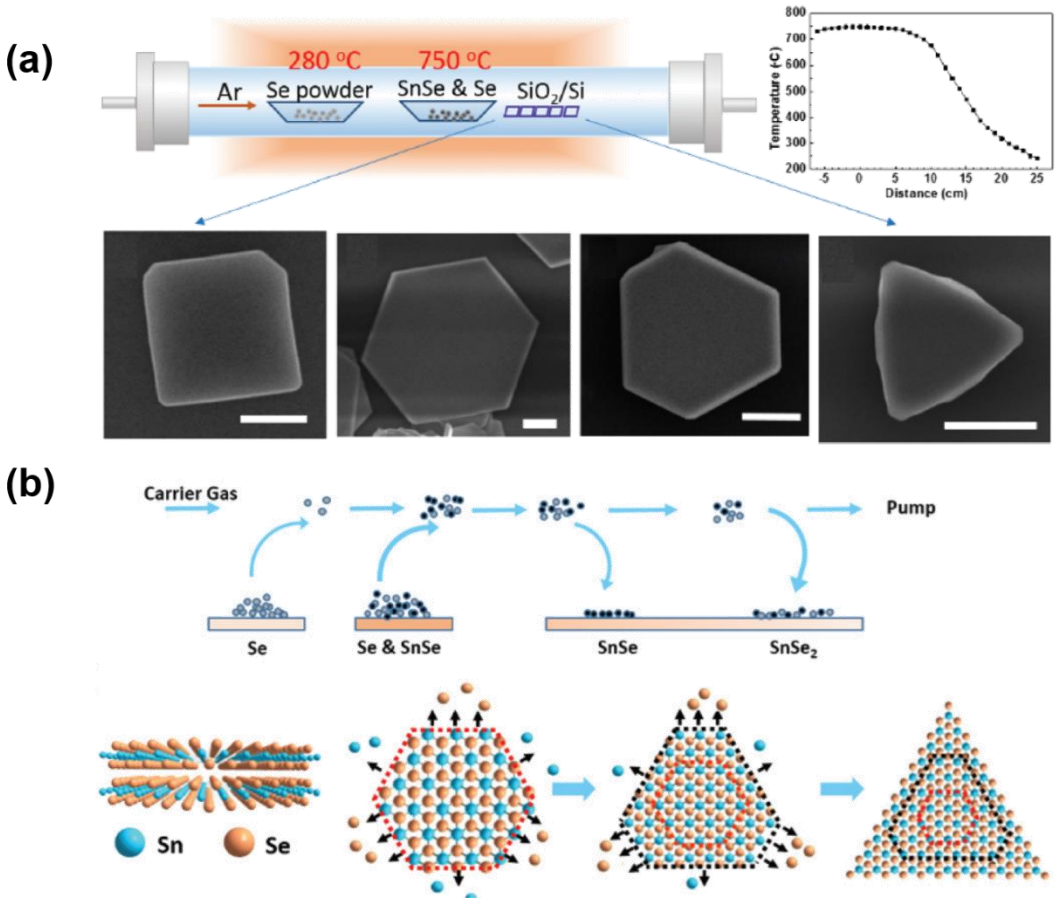


Figure 2.16. Morphology and composition control of SnSe and $SnSe_2$. (a) SEM images of different SnSe and $SnSe_2$ morphologies obtained from the temperature gradient in the furnace. (b) Schematic illustration and the atomic model to expound the shape evolution. (a, b) Reproduced with permission from ref. [129]. © 2015 The Royal Society of Chemistry.

Morphology management for tailoring the properties of 2D semiconductors has attracted great interest in the applications of electrocatalysis and optoelectronics. Huang *et al.* developed a facile CVD method to synthesize the diverse shaped $SnSe_2$ and SnSe on SiO_2 substrate placing at the downstream of the furnace.[129] As displayed in **Figure 2.16**(a), the shape of the deposited crystals resembles square, hexagonal, truncated triangular and triangular in sequence as the temperature of substrate declines. They proposed that the supply of selenium atoms has a great impact on determining the morphology. On substrates of higher temperature,

adsorbed selenium atoms inclined to quickly desorb into the carrier gas, resulting in the square SnSe nuclei because of their orthorhombic crystal structure. As the temperature of substrate decreases, there are more Se atoms deposited on the substrate surface and bond with Sn zigzag terminated edges (**Figure 2.16**(b)). The Sn zigzag terminated edges hence disappear gradually, resulting in the shape evolution from truncated triangles to triangles. In contrast to the Sn chalcogenides, the morphology of MoS_2 shown in **Figure 2.17**(a-d) is found to evolve from compact shape to dendritic structure with the increase of S/Mo stoichiometry ratio from gaseous precursor via adjusting position of the substrate.[130] This brings about the decreasing fractal dimension and turns the growth process from thermodynamic regime to kinetic regime because of the increasing growth rate (**Figure 2.17**(e)). The dendritic thorns, illustrated in **Figure 2.17**(f), arise from the much faster growth rate of Mo zigzag terminated edges compared to that of S zigzag terminated edges because of the excess S vapour.[131]

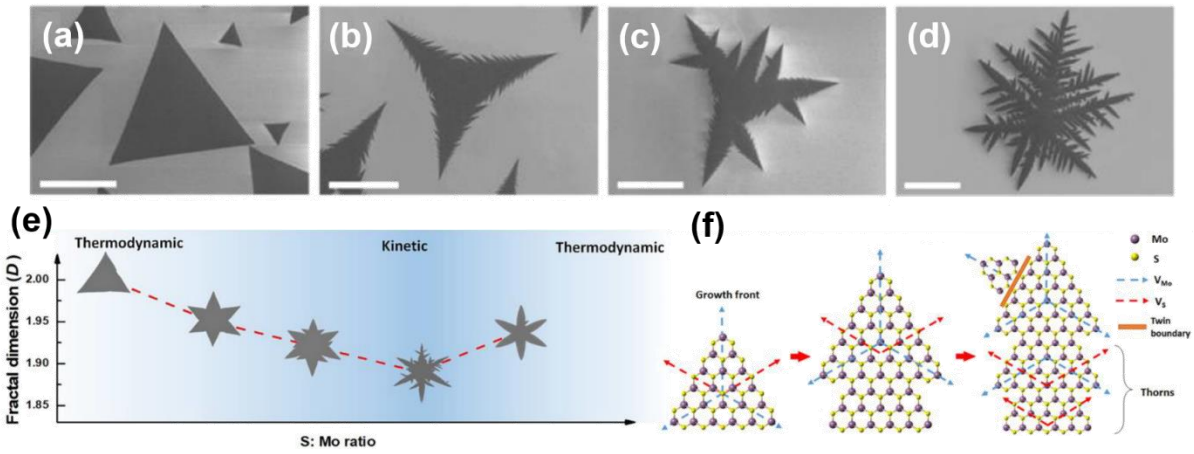


Figure 2.17. Shape evolution of MoS_2 crystals from triangles to dendrites. (a-d) SEM images of the resulting monolayer MoS_2 under different S:Mo vapour concentration ratio. Reproduced with permission from ref. [130]. © 2018 American Chemical Society. (e) The evolution of fractal dimension with the different S:Mo vapour concentration ratio. (f) Schematic atomic model explaining the thorns generation along the branches of MoS_2. (e, f) Reproduced with permission from ref. [131]. © 2018 American Chemical Society.

2.4.4 Orientation

When two adjacent domains coalesce during the growth of 2D materials, misoriented lattice growth may lead to the formation of defects and domain boundaries, which often have negative effects on their intrinsic properties.[132-133] Controlling the domain orientation to obtain alignment of 2D materials is therefore imperative. This could realise the production of wafer-scale single crystalline 2D materials for the fabrication of large-scale device arrays with high and uniform performance.

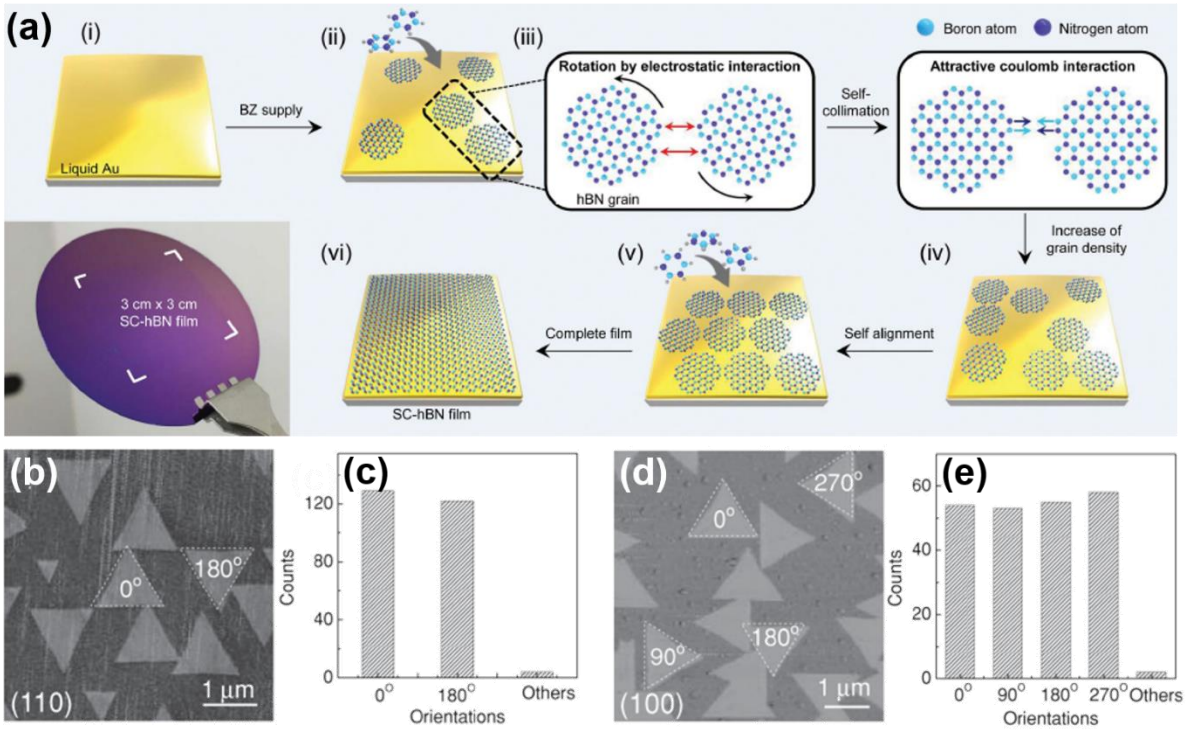


Figure 2.18. Orientation control of hBN crystals. (a) Schematic illustration for the growth of single crystalline hBN film by means of self-collimated circular hBN grains on liquid Au surface. Reproduced with permission from ref. [134]. © 2018 American Association for the Advancement of Science. (b) Friction force image of hBN domains grown on Ge (110). (c) Statistical distribution of the orientations of the hBN domains grown on Ge (110). (d) Friction force image of hBN domains grown on Ge (100). (e) Statistical distribution of the orientations of the hBN domains grown on Ge (110). (b-e) Reproduced with permission from ref. [135]. © 2015 Wiley-VCH.

To obtain the hBN with well alignment during the CVD growth, a variety of growth substrates have been investigated over the past few years. Lee *et al.* reported a method of synthesising the single crystalline hBN film on a wafer scale using liquid Au (**Figure 2.18**(a)).[134] The key step is the facile rotation of hBN domains by means of the Coulomb interaction between B and N atoms at the perimeter of each domain. This results in the seamless stitching when the self-collimated domains merge. Yin *et al.* showed that highly aligned hBN can be epitaxially grown on (100) and (110) facets of Ge substrates.[135] The number of primary orientations of the hBN domains reveals strong dependence on the crystal plane of underlying Ge. As shown in **Figure 2.18**(b), the Ge (110) surface preserves twofold symmetry, where the hBN triangles are of mirror symmetry and opposite to each other (**Figure 2.18**(c)). In comparison, the fourfold symmetry of Ge (100) surfaces showed in **Figure 2.18**(d) exhibits four equivalent preferred orientations of the hBN triangles with edges perpendicular to each other (**Figure 2.18**(e)).

Hite *et al.* examined the dependence of the hBN growth behaviour on different crystalline facets of Cu substrate by utilising electron backscatter diffraction mapping (EBSD) combined with SEM analysis.[136] They found that the growth of hBN is most stable with the most rapid growth rate on Cu (111) because of the lower surface energy compared to the Cu (100) and Cu (110). The proposed atomic arrangements of hBN triangles on the most common facets including Cu (100), Cu (110) and Cu (111) are illustrated in **Figure 2.19**(a-c).[137] It can be seen that at least one edge of the hBN domains is parallel to the close-packing direction of the Cu surface, which is beneficial for passivating the edge of the hBN domains. Similar to Ge substrate, there are two preferred orientation for hBN triangles with mirror symmetry on Cu (111) (**Figure 2.19**(a)) and Cu (110) (**Figure 2.19**(b)), while four hBN triangles with the rotation of 90° from one another are observed on Cu (100) (**Figure 2.19**(c)). In comparison, hBN triangles grown on Cu (102) and Cu (103) only share a unique lattice orientation with one

of their edges aligned perpendicular to the symmetric axis of the Cu substrate (**Figure 2.19**(d-e)).[138] This is attributed to the minimum stacking energy at 60° for both Cu (102) and Cu (103) but there are two minimum values at 30° and 90° on Cu (111) on the basis of DFT calculations (**Figure 2.19**(f)).

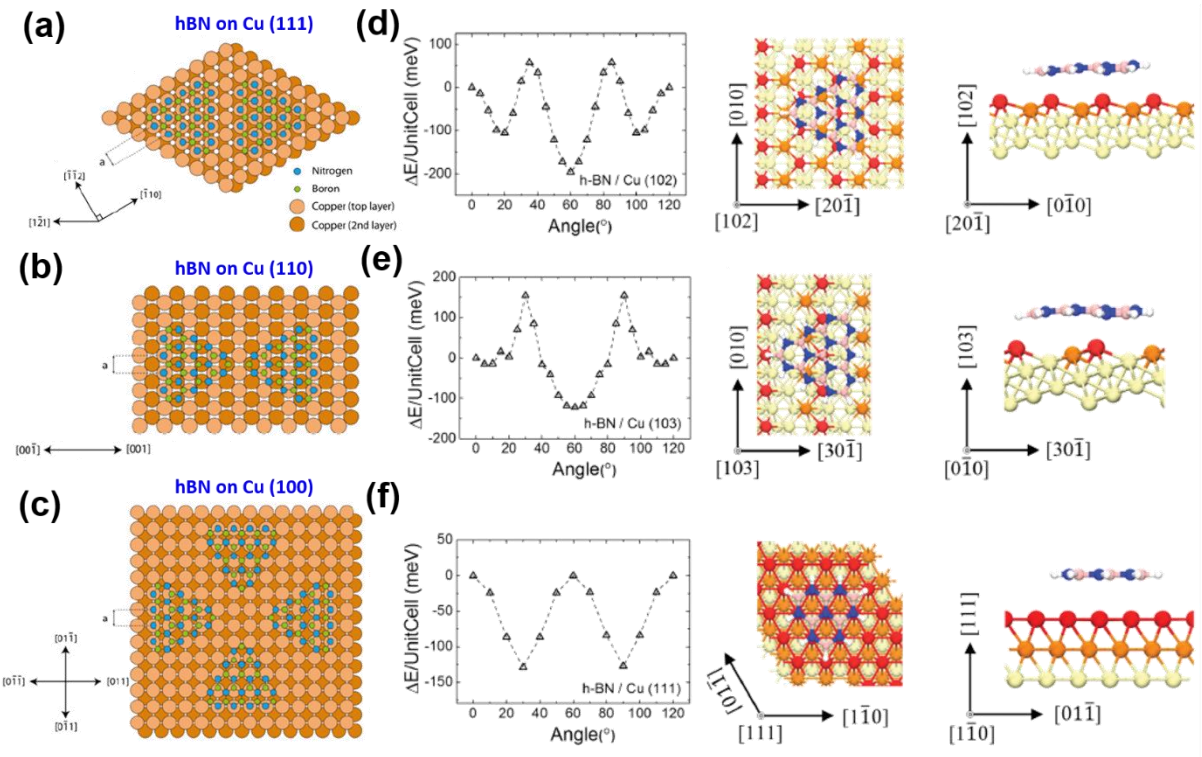


Figure 2.19. Orientation dependence for stacking energies and the optimised structures based of DFT calculation. (a-c) Atomic structure of monolayer hBN on different orientations of Cu surfaces: (a) Cu (111), (b) Cu (110), and (c) Cu (100), respectively. (a-c) Reproduced with permission from ref. [137]. © 2015 IOP Publishing. (d) Energy corrugations of hBN rotating on Cu (102) and the optimised stacking structure. (e) Energy corrugations of hBN rotating on Cu (103) and the optimised stacking structure. (f) Energy corrugations of hBN rotating on Cu (111) and the optimised stacking structure. (d-f) Reproduced with permission from ref. [138]. © 2016 Wiley-VCH.

In the growth of 2D semiconducting metal chalcogenides, SiO_2 is the most widely used substrate. This inevitably results in a large concentration of domain boundaries because of its

amorphous nature. Sapphire has been considered as an alternative substrate for controlling the crystallographic orientations of 2D semiconductors layers because of their similar lattice structure. In light of this, Dumcenco *et al.* firstly reported the achievement of MoS_2 epitaxial growth on sapphire with centimetre-scale uniformity.[139] The atomically smooth terraces on the sapphire surface is found to be critical in the control of MoS_2 orientation. Aljarb *et al.* further discovered that the position of sapphire growth substrate plays a crucial role in controlling the orientation of the MoS_2 domain (**Figure 2.20**(a)).[140] They ascribed this to the different ratio between the S and MoO_3 precursor shown in **Figure 2.20**(b). The higher the S/Mo ratio goes, the easier it is to reduce the MoO_3 and form small MoS_2 crystalline seeds that are able to align with the lattice structure to the substrate (**Figure 2.20**(c)). Besides, the effect of carrier gas on the orientation of the 2D semiconductors has also been investigated. It is observed that the highly misaligned WS_2 domains grown in pure Ar showed linear arrays of distorted atomic rings along the boundaries between merged WS_2 domains (**Figure 2.20**(d-g)).[141] In contrast, introducing H_2 carrier gas assist the alignment of WS_2 triangles with low misorientation angles between merged domains (**Figure 2.20**(h-k)).

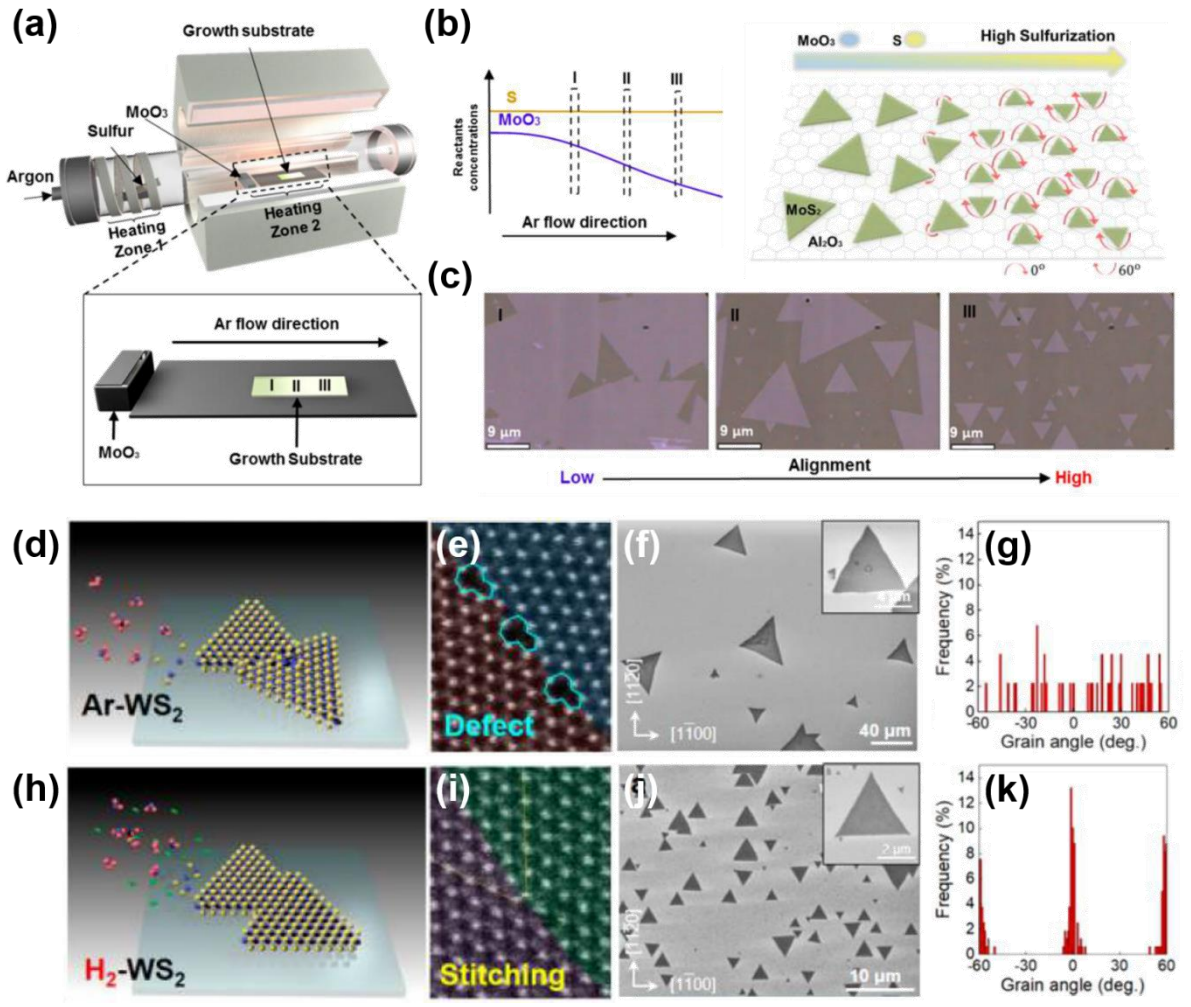


Figure 2.20. Controlling the domain orientations of 2D semiconductors during CVD growth. (a) Schematic illustration of the CVD setup for the growth of MoS_2 on sapphire. (b) The temperature profile inside the CVD furnace. (c) The corresponding optical images of the MoS_2 grown on sapphire placing at the position indicated in (a). (a-c) Reproduced with permission from ref. [140]. © 2017 American Chemical Society. (d) Schematic illustration showing the growth of WS_2 on sapphire under the pure Ar gas (Ar-WS_2). (e) ADF-STEM image demonstrating the Ar-WS_2 domain boundary composed of pentagons and heptagons. (f) SEM image of the as-grown Ar-WS_2. (g) Statistical angle distribution of Ar-WS_2. (h) Schematic illustration showing the growth of WS_2 on sapphire under the pure H_2-Ar mixture gas (H_2-WS_2). (i) ADF-STEM image demonstrating the seamless stitching of H_2-WS_2. (j) SEM image of the as-grown H_2-WS_2. (k) Statistical angle distribution of H_2-WS_2. (d-k) Reproduced with permission from ref. [141]. © 2018 American Chemical Society.

2.5 CVD Synthesis of Hybrid 2D Materials

The diversity of 2D materials provides possibilities to exploit structural tuning and accomplish artificial hybrid 2D structures that possess novel functions beyond the reach of the existing materials. This gives additional ways to design and fabricate novel materials with more than one building block, and the obtained hybrid 2D structures with modulated properties can also be integrated with other materials to satisfy different application requirements and deliver improved performance of nanoelectronic devices.

2.5.1 Doping of 2D Materials

As a supplement to the restricted intrinsic properties of specific 2D materials, element doping is considered as the primary technique to effectively modify the physical properties and expand their functionalities.[142] Some metal dopants such as Mn and Fe are predicted to enable the induction of magnetism in the 2D semiconductors.[143-145] It is feasible to control the carrier type through substitution doping of specific metal in the 2D semiconductors. Nb doped MoS_2, for example, exhibits p-type characteristics,[146] whereas Re dopants act as electron donors resulting in n-type doping for MoS_2.[147] Tuneable bandgap can also be obtained by altering chemical composition in 2D transition metal chalcogenide alloys and has been accomplished in several cases via metal or chalcogen substitutional doping, including $Mo_xW_{(1-x)}S_2$,[148-149] $Mo_xW_{(1-x)}Se_2$,[150] $MoS_{2x}Se_{2(1-x)}$,[151-152] $WS_{2x}Se_{2(1-x)}$,[153-154] $SnS_{2x}Se_{2(1-x)}$,[155] and $ReS_{2x}Se_{2(1-x)}$.[156] In addition, it is viable to conduct phase transformation during the doping process of 2D materials. H phase is reported to be the most stable phase at room temperature for MoS_2 and WS_2, but the co-existence of both H phase and T phase was observed in monolayer $Mo_xW_{(1-x)}S_2$ alloy.[157] Yang *et al.* also demonstrated that stable T-phase MoS_2 could be acquired when alloying with Re through substitutional doping.[158] Similarly, $MoTe_2$ was experimentally shown to undergo a

transition of properties from semiconducting to semi-metallic as the chemical composition is varied with the W substitution.[159]

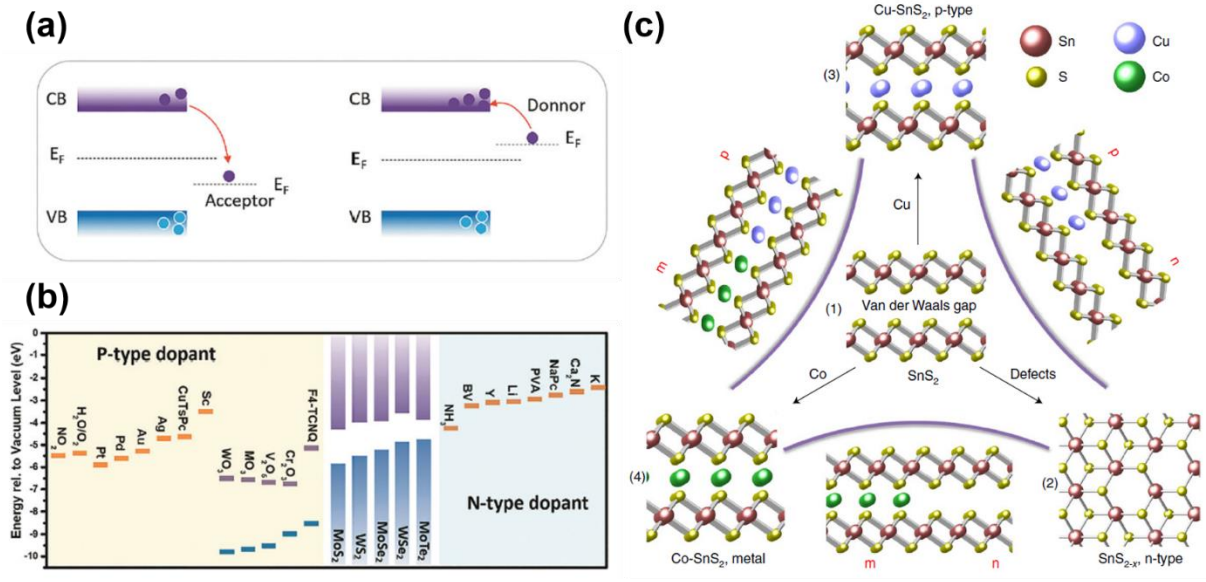


Figure 2.21. Doping of 2D materials through charge transfer. (a) Schematic band diagram for acceptor and donor charge transfer behaviour based on the difference of Fermi level. (b) Energy band diagram summarising the p-type and n-type dopants in 2D semiconductors. (a, b) Reproduced with permission from ref. [162]. © 2019 The Royal Society of Chemistry. (c) Schematic illustration showing the change of properties for SnS_2 layers through intercalation doping with different elements. Reproduced with permission from ref. [161]. © 2018 Nature Publishing Group.

Doping of 2D semiconductors is generally categorised into two types: surface chemical doping and substitutional doping. In the case of surface chemical doping, dopants are placed in contact with the 2D semiconductors by physical or chemical interaction without the structural damage. This is usually achieved by chemical treatment or solvent-based intercalation approach.[160-161] The dopant types are classified as acceptor and donor which is determined by the Fermi level difference to the host semiconductors and the charge transfer direction.[162] As shown in **Figure 2.21**(a), when the dopants exhibit a lower Fermi level they accept electrons from the host semiconductors, leaving holes on the host semiconductors and

causing p-type doping. On the contrary, the electrons are donated to host semiconductors when the dopants have a higher Fermi level, resulting in n-type doping. A variety of dopant sources ranging from small molecules to ions and particles have been investigated when adsorbed on the surface of 2D semiconductors (**Figure 2.21**(b)). Some popular doping species include 2,3,5,6-tetrafluoro-7,7,8,8-tetracyano quinodimethane (F4-TCNQ) and Au nanoparticles,[163-164] which exhibits the p-type behaviour, as well as benzyl viologen (BV) and polyvinyl alcohol (PVA) with the n-type characteristics.[165-166] Recently, Gong *et al.* demonstrated an intercalation doping method to effectively tune the properties of SnS_2.[161] As illustrated in **Figure 2.21**(c), CVD-grown SnS_2 intrinsically exhibits n-type semiconducting behaviour because of the existence of sulfur vacancies, but can be transformed into a p-type semiconductor and a highly conductive metal when intercalated with Cu and Co, respectively. This enables the construction of p-n junction with a direct chemically-bonded metal-semiconductor interface when combined with the lithography technique, improving the device performance.

The modified 2D structure through surface charge transfer doping, however, lacks covalent surface bonding between the dopants and host 2D semiconductors, which may be in a metastable state and unable to maintain the modulated properties eternally. Substitutional doping where part of the lattice sites in the original 2D lattice are exchanged by foreign atoms, in comparison, has been widely adopted for band structure engineering and phase engineering.[167-169] This type of doping is usually achieved by using co-evaporation CVD approach and introducing all material precursors together during the growth phase of crystals (**Figure 2.22**(a)).[147] For example, employing the sulfur and selenium powder in the typical experimental setup for MoS_2 growth results in the doping of MoS_2 by Se and the formation of $MoS_{2x}Se_{2(1-x)}$. The stoichiometry between chalcogen atoms can be adjusted through altering the spatial separation between the precursors and growth substrate. This substitution of

chalcogenides in the lattice gives rise to the changes in the energy band gap which is evidenced by the tuneable photoluminescence characteristic peak displayed in **Figure 2.22**(b).[151]

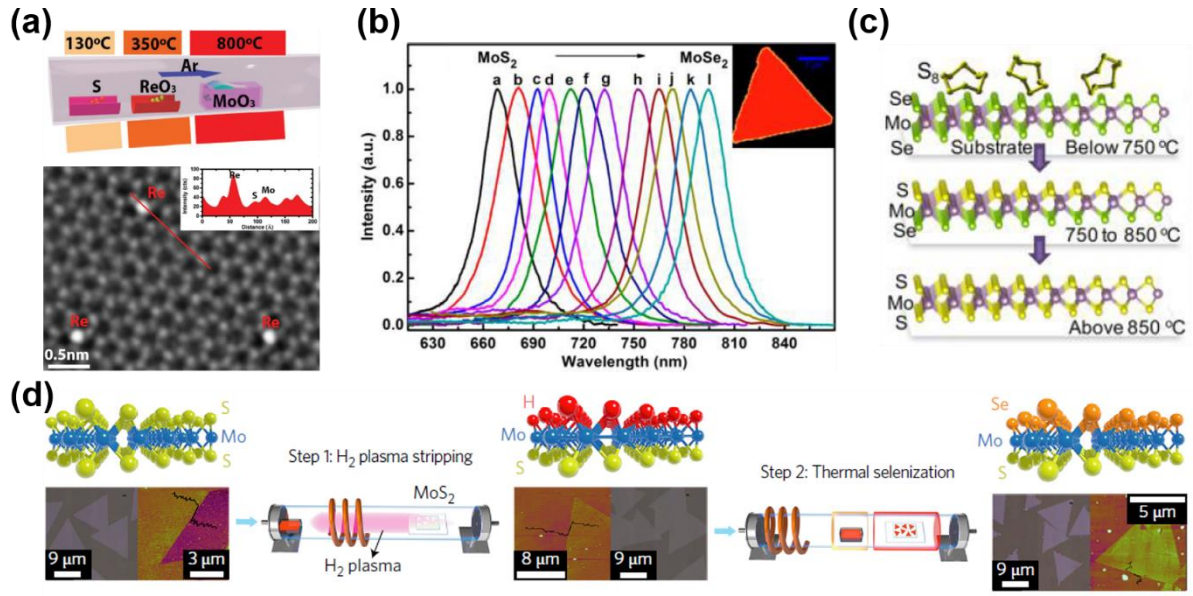


Figure 2.22. Substitutional doping of 2D semiconductors. (a) Schematic illustration of the CVD experimental setup for the synthesis of Re doped MoS_2 and the resulted STEM image. Reproduced with permission from ref. [147]. © 2018 Wiley-VCH. (b) Photoluminescence spectra of a series of composition tuneable $MoS_{2x}Se_{2(1-x)}$ monolayers. Reproduced with permission from ref. [151]. © 2014 American Chemical Society. (c) Schematic illustration demonstrating the mechanism for the synthesis of the Janus SMoSe. Reproduced with permission from ref. [171]. © 2017 American Chemical Society. (d) Synthesis of the Janus SeMoS monolayers through H_2 plasma-assisted process. Reproduced with permission from ref. [172]. © 2017 Nature Publishing Group.

Another way to synthesise the substitutional doped 2D semiconductors is to separate the growth of pristine 2D semiconductors and the doping of foreign atoms. In this method, the host 2D semiconductors are firstly synthesised with high quality and followed by gentle post treatments. This is more promising to integrate different 2D elements together and obtain controllable properties compared to the one-step synthesis because of the better control of

dopants distribution. Take the same case of $MoS_{2x}Se_{2(1-x)}$ for example, this could also be achieved by thermal annealing of CVD-grown MoS_2 under the Se atmosphere.[170] In addition, this two-step strategy further increases the degree of controllability. When anneal the $MoSe_2$ under the S atmosphere, the Se atoms in the top layer are in direct contact with the gaseous molecules and are easier to be replaced with S atoms. This allows the formation of Janus SMoSe structure with different chalcogen atoms in the top and bottom layer through the subtle control of doping temperature (**Figure 2.22**(c)).[171] Likewise, such surface modification can also be carried out by first stripping off the top S atoms from MoS_2 using H_2 plasma treatment, followed by thermal selenization process as indicated in **Figure 2.22**(d).[172]

2.5.2 Lateral Heterostructures

Heterostructures based on 2D materials are hybrid structures that incorporate at least two different 2D materials through lateral or vertical stacking. This provides nearly infinite combinations for tuning the structural and electronic properties to fulfil the demands on device functionalities. Understanding the band structure and band alignments between different 2D materials is therefore imperative for the device design and materials selection in each segment, because the different band alignments can trigger diverse interactions and affect the mobile charge carriers flow.

Figure 2.23(a) displays an example of band offsets between various Mo-based and W-based TMDs.[173] According to the discontinuities produced by band alignments at the interface, heterostructures can be categorised into straddling gap (type I), staggered gap (type II) or broken gap (type III), as described in **Figure 2.23**(b).[174] Each of these band alignments has particular applications to meet the requirement from different varieties of devices (**Figure 2.23**(c)).[175] Type I band alignments are most widely exploited in devices that generate light such as laser and light emitting diodes because of their capabilities of spatially confining the

carriers. Type II band alignments are commonly utilised in high electron mobility transistors, solar cells and devices for harnessing interlayer excitons. In contrast, Type III band alignments enable the band-to-band tunnelling and are generally adopted in tunnelling field effect transistors for low power consumption in electronics.

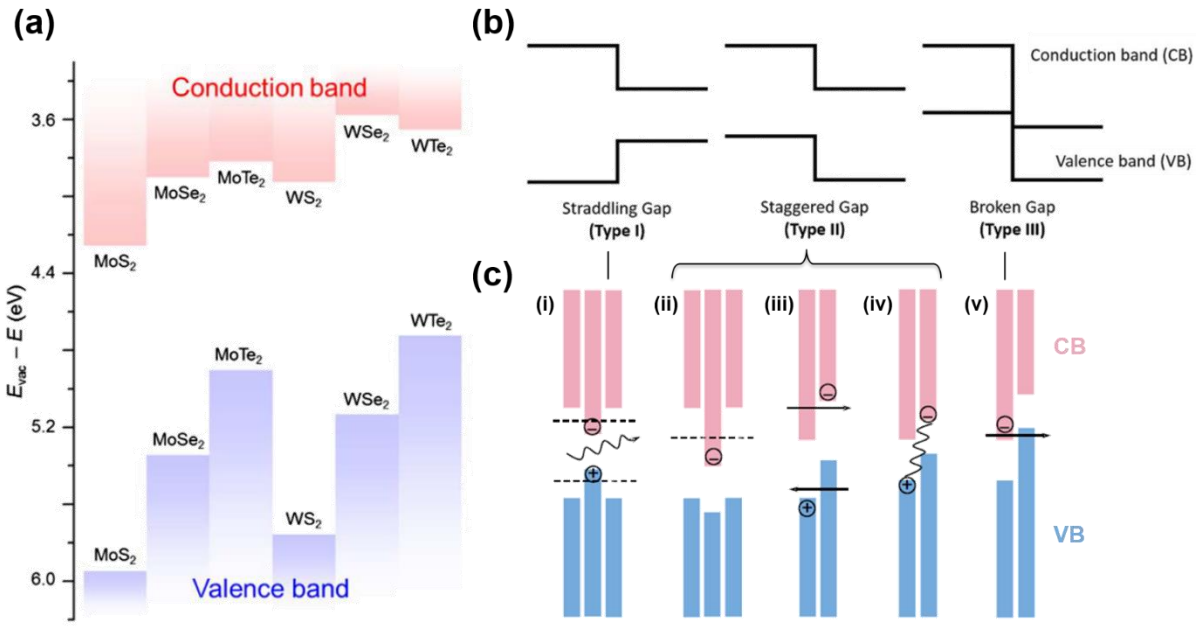


Figure 2.23. Heterostructures based on 2D materials and their band alignments. (a) Band alignment for Mo-based and W-based dichalcogenides. Reproduced with permission from ref. [173]. © 2016 American Association for the Advancement of Science. (b) Schematic illustration of three types of band alignment for semiconductor heterojunction. Reproduced with permission from ref. [174]. © 2016 The Royal Society of Chemistry. (c) Schematic illustration of different band alignments from type I, type II and type III heterojunctions utilised in semiconductor devices. Reproduced with permission from ref. [175]. © 2016 American Physical Society.

Lateral heterostrctures are mostly produced by vapour phase growth methods such as CVD as it is challenging to atomically stitch different 2D crystals using traditional techniques such as mechanical exfoliation. To grow the lateral heterostructure, it is important to take the lattice constant difference into consideration as the in-built strain at the interface may affect

the structural stability. The earliest study of heterostructures adopted graphene and hBN as the building blocks because of their structure similarity. It is expected that they can form a seamless interface when merged through proper interface control because of their lattice coherence. In recent works, theoretical calculations predicted that an obvious bandgap opening could be realized in the in-plane hBN and graphene heterostructures together with a relatively high carrier mobilities.[176] This makes hBN-Gr a promising 2D material for graphene-based nanoelectronics. By employing an atmospheric pressure CVD system, Han *et al.* developed two-step continued growth method for achieving lateral hBN-Gr films on easily available Cu substrates.[177] With this method, direct nucleation and growth of hBN ribbons from the existing edges of graphene were realised. The key point in this growth process was to keep the edges of the existing graphene domain fresh and sharp. Liu *et al.* subsequently introduced a hydrogen etching step and a designed lateral epitaxial growth pathway (**Figure 2.24**(a)).[178] Monolayer graphene was first grown on Cu foils, and then etched by hydrogen to form hexagonal holes down to the Cu substrate. Then, hBN was patched onto the bare Cu regions, leading to lateral hBN-Gr heterostructures with sharp interfaces. Recently, Sutter *et al.* also reported a nanoscale integration of hBN and graphene into striped patterns by using a similar lateral heteroepitaxy method (**Figure 2.24**(b)).[179] This was realized by alternating the streams of precursor species, and the width of the graphene and hBN were controlled below 100 nm (**Figure 2.24**(c)).

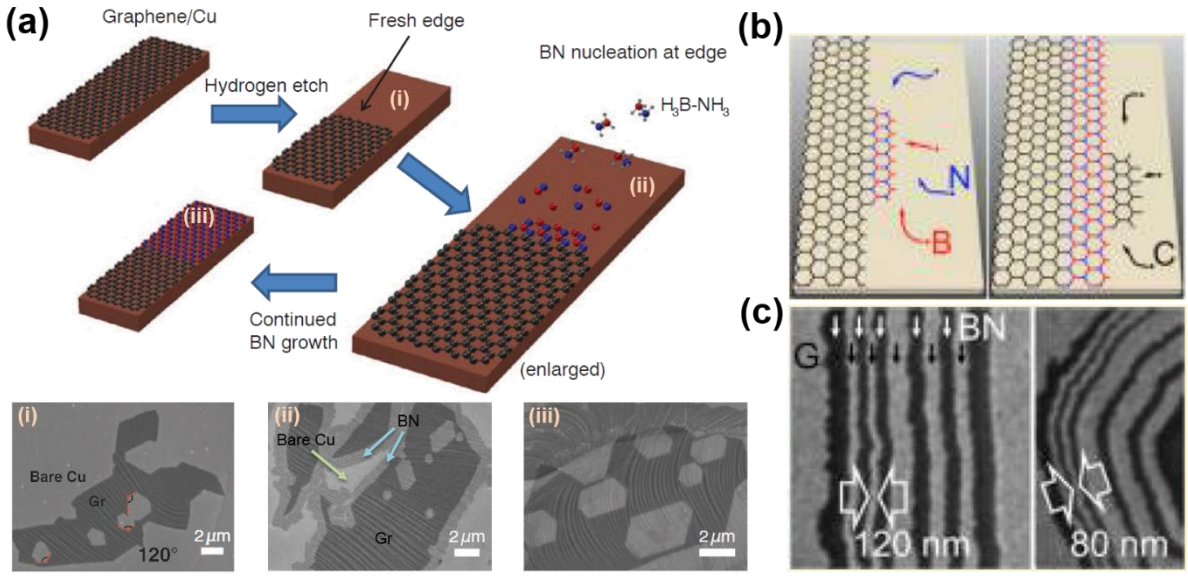


Figure 2.24. CVD growth of graphene-hBN lateral heterostructures. (a) Schematic illustration of epitaxial growth of hBN on fresh graphene edges with the aids of hydrogen etching and the resulted SEM images in each step. Reproduced with permission from ref. [178]. © 2014 American Association for the Advancement of Science. (b) Schematics showing the sequential growth of hBN and graphene by lateral hetero-epitaxy. (c) SEM images of the strip-patterned hBN-graphene lateral heterostructures. (b, c) Reproduced with permission from ref. [179]. © 2014 American Chemical Society.

Lateral heterostructures between 2D semiconductors is another structure of great interest as they provide an atomically sharp interface and narrow active region at the junction. To design the synthesis route of lateral heterostructures based on 2D semiconductors, the most straightforward strategy is growing individual component sequentially with multistep. This has so for been successfully employed on several lateral heterostructures cases including MoS_2-WS_2,[180-183] $MoSe_2$-WSe_2,[184-186] WSe_2-WS_2,[187] MoS_2-$MoSe_2$,[187] and WSe_2-MoS_2.[188-189] The biggest challenge is to extend this to the multi-heterostructures or superlattices because of the random nucleation during the temperature swing between growth steps. Besides, most of the 2D materials are of single or few atomic layer thickness and have no tolerance to any slight thermal degradation.

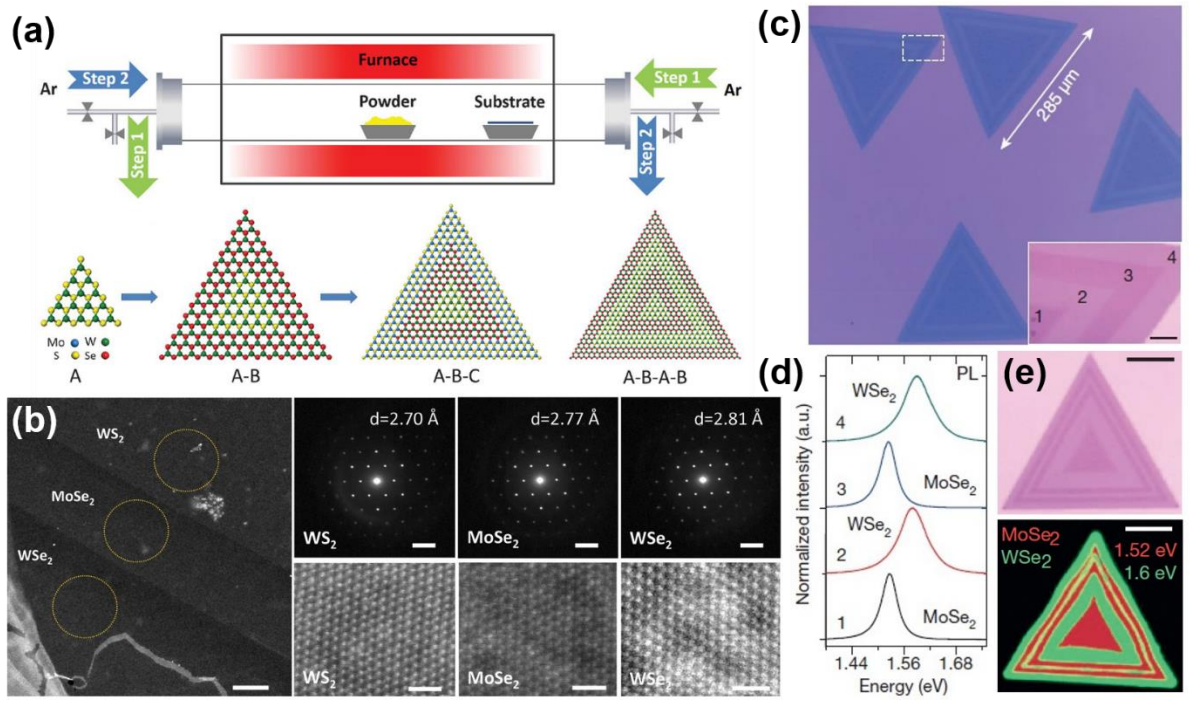


Figure 2.25. CVD growth of semiconductor-semiconductor lateral heterostructures. (a) Schematic illustration of the step-by-step CVD system for the lateral heterostructure obtained via robust epitaxial growth. (b) High resolution ADF-STEM images of individual WS_2, $MoSe_2$ and WSe_2 region within the lateral WS_2-$MoSe_2$-WSe_2 multiheterostructure. (a, b) Reproduced with permission from ref. [190]. © 2017 American Association for the Advancement of Science. (c) Optical image of multi-junction lateral heterostructures. The inset shows the zoomed in optical image of the region within the dashed box. (d) PL spectra measured on the four points in (c). (e) Optical image of five-junction lateral heterostructures and the corresponding composite PL mapping showing that the regions of dark-contrast and bright-contrast are $MoSe_2$ and WSe_2, respectively. (c-e) Reproduced with permission from ref. [191]. © 2018 Nature Publishing Group.

In recently years, a modified step-by-step thermal CVD system was designed to overcome this and realise the epitaxial growth of lateral multi-heterostructures and superlattices.[190] As shown in **Figure 2.25**(a), a reverse Ar flow from the substrate to precursor was introduced additionally during the temperature swing between the sequential growth stages. This can not only prevent the existing 2D materials from exposure under high

temperature through a continuous flush by cold Ar gas, but stop the vapour supply of precursors to eliminate the undesired nucleation. With this improved controllability, the quality and integrity of individual layers can be well preserved and the junction between each component could be atomically sharp as evidenced by the ADF-STEM images in **Figure 2.25**(b). Similarly, Sahoo *et al.* demonstrated a one-pot synthesis method for the growth of growth of large-area monolayer 2D superlattices via sequential edge epitaxy.[191] This sequential edge epitaxy is accomplished by the controlled selective growth of each 2D component through switching different carrier gases. The growth of MoS_2 and $MoSe_2$ undergoes when using N_2 and H_2O as the carrier gas, whereas switching the carrier gas to Ar with 5% H_2 the growth of WS_2 and WSe_2 is promoted. This enables the *in situ* sequential growth of multiple junctions through alternating the carrier gas cyclically and the domain size of the resulted lateral heterostructure crystals can be up to nearly 300 μm, shown in **Figure 2.25**(c). Through the analysis of photoluminescence spectroscopy demonstrated in **Figure 2.25**(d) and (e), the as-synthesised multi-heterostructures are of high spatial uniformity. These synthetic improvements are beneficial for the assembly of planar multi-junctions and allow the design of complex structures for device applications.

2.5.3 Vertical Heterostructures (van der Waals Heterostructures)

Similar to lateral heterostructures, the simplest case of vertical heterostructures is based on graphene and hBN. The vertical Gr/hBN heterostructure is coupled by interlayer van der Waals interactions. Some unique physical phenomena and interfacial properties such as the emergence of the superlattice Dirac cone and the Hofstadter butterfly effect have been discovered.[192-195] Moreover, graphene on an hBN substrate opens the bandgap because of the local potential variation for bond distortion and moiré periodicity.[196] The Gr-hBN heterostructures have been exploited to fabricate high performance graphene-based transistors

because of the atomic flatness and charge homogeneity nature of the dielectric hBN substrate.[197] As compared with traditional graphene-based transistors fabricated on SiO_2/Si substrates, the intrinsic property of graphene was largely maintained,[198] and the electronic scattering effects from charged surface states or impurities on SiO_2 substrates were greatly suppressed.[199] The carrier mobility was measured as high as 60,000 cm^2/Vs in exfoliated graphene and 37,000 cm^2/Vs in CVD grown graphene on hBN substrates.[197, 200] Moreover, graphene and hBN films were also assembled into Gr/hBN/Gr sandwiched architectures and served as field-effect tunnelling transistors, which displayed ultrahigh on-off ratios > 10^4.[201] So far, most of the vertically Gr/hBN heterostructures have been fabricated by mechanical cleavage methods or layer-by-layer transfer techniques, which are obviously not suitable for industrial-scale applications.[197, 202-203] It is therefore imperative to develop a new route for the direct growth of high quality vertical heterostructures. To achieve these ends, it is crucial to engineer the CVD growth process, such as the selection of precursor molecules, the optimisation of the growth parameters, and the design of special chemical reactions during the CVD processes.

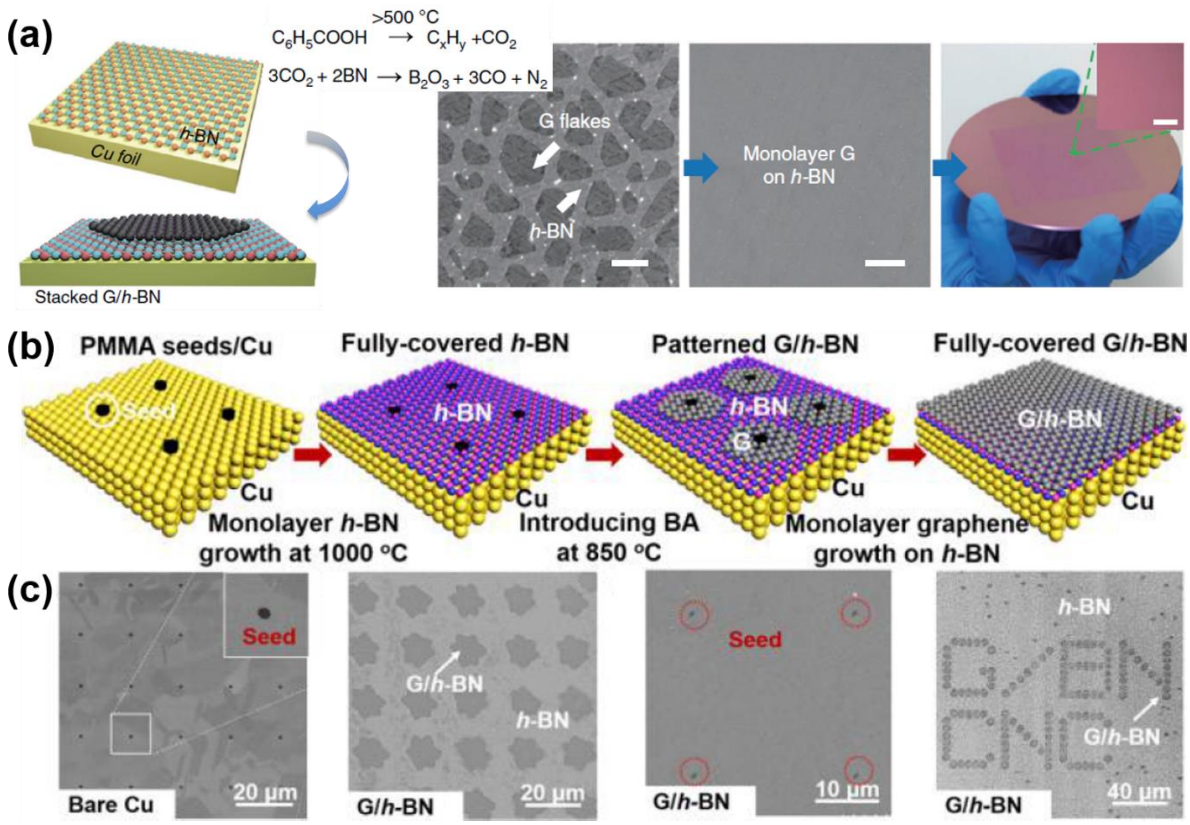


Figure 2.26. CVD growth of graphene/hBN vertical heterostructures. (a) Growth of graphene on the hBN surface using benzoic acid as the carbon precursor and the SEM and optical images of the resulted stacked graphene/hBN heterostructures. Reproduced with permission from ref. [204]. © 2015 Nature Publishing Group. (b) Schematic diagrams demonstrating the growth of patterned graphene/hBN heterostructures using PMMA seeds on Cu foils as nucleation sites. (c) SEM images of the patterned PMMA arrays and the as-grown graphene/hBN heterostructures. (b, c) Reproduced with permission from ref. [205]. © 2016 American Chemical Society.

Using the hBN domains or continuous hBN films as the graphene growth substrate, it is straightforward to control the synthesis of lateral or vertical Gr/hBN heterostructures because of a significant difference in the growth rate of graphene on hBN and metal substrate. Nevertheless, the main challenge for the direct CVD growth of Gr/hBN heterostructures is that the catalytic ability of hBN is too weak to assist the carbon precursor decomposition. Kim *et al.* obtained vertically stacked regions of graphene on hBN by using low-pressure CVD with

methane as carbon source, where graphene nucleated on Cu foils and extended to overlap on hBN flakes.[37] Gao *et al.* developed another temperature-triggered chemical reaction route to control the selective growth of lateral and vertical Gr/hBN heterostructures.[204] In this process, a complete monolayer hBN was firstly grown on Cu substrate by CVD. The subsequent graphene growth was achieved by using benzoic acid as precursor, which could enable the graphene growth on hBN at relatively low temperature (< 900°C) and circumvent the etching of the underlying hBN film. The resulted graphene with partially and fully coverage on hBN surface could be therefore realized with wafer-scale by controlling the growth parameters such as deposition time and carbon feeding rate (**Figure 2.26**(a)). Song *et al.* developed a seed-assisted growth by using predefined poly(methyl methacrylate) (PMMA) seeds on Cu substrate via electron-beam lithography (EBL) that act as nucleation sites in the following CVD growth process (**Figure 2.26**(b)).[205] The advantage of this approach is to effectively control the nucleation density and locations of monolayer graphene domain (**Figure 2.26**(c)), which facilitates the construction of patterned graphene devices with similar electronic performance. The direct grown graphene on hBN showed higher carrier mobility than that of graphene/h-BN obtained by layer-by-layer transfer methods.

Being a chemically inert and electrically insulating 2D template without dangling bonds and charged impurities, hBN is also considered as the ideal pre-growth substrate for the growth of 2D semiconductors. Okada *et al.* reported the growth of WS_2 onto mechanical exfoliated hBN through a three-furnace CVD process.[206] They observed that the nucleation density at the edge of the hBN flake is much higher than that of the middle part shown in **Figure 2.27**(a). This is attributed to the high density of dangling bonds accommodated at the edge of the hBN crystal, presumably providing the nucleation site during the growth of WS_2 atomic layers. Through the characterisation of low-energy electron microscopy (LEEM), the crystalline orientation of as-grown WS_2 was found to be strictly associated with the underlying hBN,

which was caused by the Coulomb interaction and the van der Waals force between neighbouring layers (**Figure 2.27**(b)). Later on, Zhang *et al.* demonstrated that the similar method could be applied to the growth of WSe_2.[207] They proposed that the single-atom vacancies on the hBN surface could trap the W atoms during the nucleation stage, leading to a reduced formation energy for one orientation of WSe_2 domain. As shown in **Figure 2.27**(c), the WSe_2 triangular domains grown on the mechanically exfoliated hBN surface exhibit only two orientations mirroring to each other. The ADF-STEM images in **Figure 2.27**(d) further demonstrate the area with two types of merging domains. A continuous WSe_2 lattice on hBN stitches seamlessly at the boundary of two WSe_2 domains with identical orientation. In contrast, for the two mirroring domains the formation of inversion domain boundary is clearly observed at the interface.

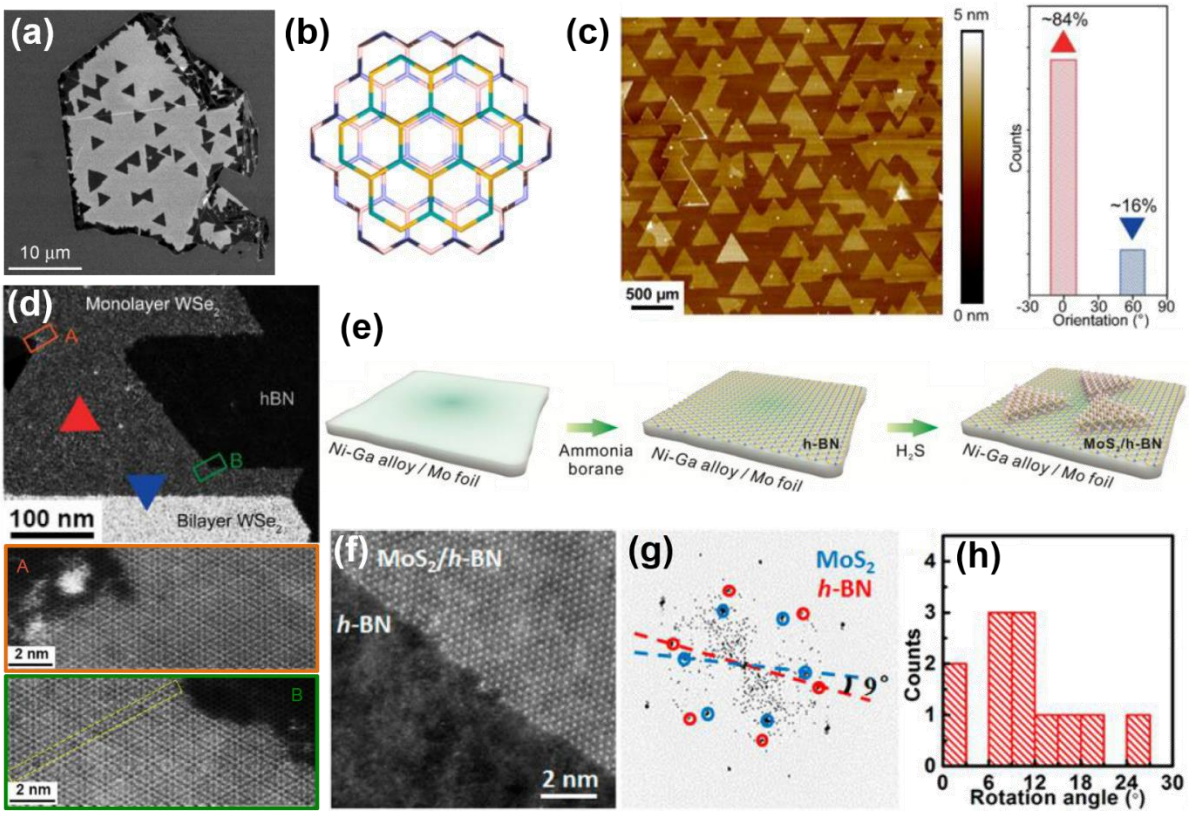


Figure 2.27. CVD growth of semiconductor/hBN vertical heterostructures. (a) SEM image of triangular WS_2 crystals grown onto hBN flakes. (b) Atomic structural model of the WS_2/hBN

heterostructures with the bottom hBN layer and top WS_2 layer. (a, b) Reproduced with permission from ref. [206]. © 2014 American Chemical Society. (c) AFM image of the epitaxial WSe_2 domains on hBN and their orientation histogram. (d) ADF-STEM images showing the merging of two domains with same orientation and with inverse orientation. (c, d) Reproduced with permission from ref. [207]. © 2019 American Chemical Society. (e) Schematic illustration showing the growth of MoS_2/hBN heterostructures through a sulphide-resistant Ni-Ga alloy substrate. Reproduced with permission from ref. [209]. © 2016 American Chemical Society. (f) ADF-STEM image resolving the lattice atoms of the MoS_2/hBN heterostructures. (g) Corresponding FFT pattern of the area in (f) displaying two sets of six-fold symmetric spots and their relative rotation angle. (h) Statistical distribution for the relative rotation angle of MoS_2 grown on hBN. (f-h) Reproduced with permission from ref. [210]. © 2017 American Chemical Society.

For the purpose of realising large scale production, it is still essential to synthesise 2D heterostructures based on scalable methods. Wang *et al.* demonstrated a direct all-CVD process for the fabrication of monolayer MoS_2/hBN vertical heterostructure films.[208] It was found that using 2 to 4 layers h-BN films was the most ideal because the films were most robust against etching from residual oxygen and degradation at high temperature during the growth. The 2D MoS_2 crystals grown on the hBN films exhibit a higher nucleation density and smaller domain size, compared to those grown on the SiO_2, which may result from the higher roughness of the transferred hBN film on SiO_2. Because during the MoS_2 growth sulphur will react with Cu, the hBN grown on Cu by CVD needs to be transferred to an alternative substrate. This transfer step can introduce the unwanted polymer residual in the interface, which will degrade the layer-layer interactions and heterostructure quality. To resolve this problem, sulphide-resistant catalyst such as Ni-Ga alloy (**Figure 2.27**(e)) and Au substrate have been developed for the direct growth of MoS_2/hBN heterostructures.[209-210] These substrates have high catalytic activity for the first-step growth of hBN and avoid the reaction with sulfur during the second-step

growth of MoS_2, hence removing the requirement of the intermediate transfer process. The as-grown single crystal MoS_2 domains could be improved with the lateral size up to 20 μm on hBN, which is around 10 times larger than those synthesis with additional transfer steps. The ADF-STEM image shown in **Figure 2.27**(f) demonstrates that the synthesised heterostructure is of high crystalline quality with no obvious defects. Besides, through extracting the FFT pattern from the heterostructure area in the image (**Figure 2.27**(g)), a low angle (6~18°) is found to be the most dominant on the basis of the statistical histogram for specific relative rotation angles between the as-grown MoS_2 and hBN (**Figure 2.27**(h)).

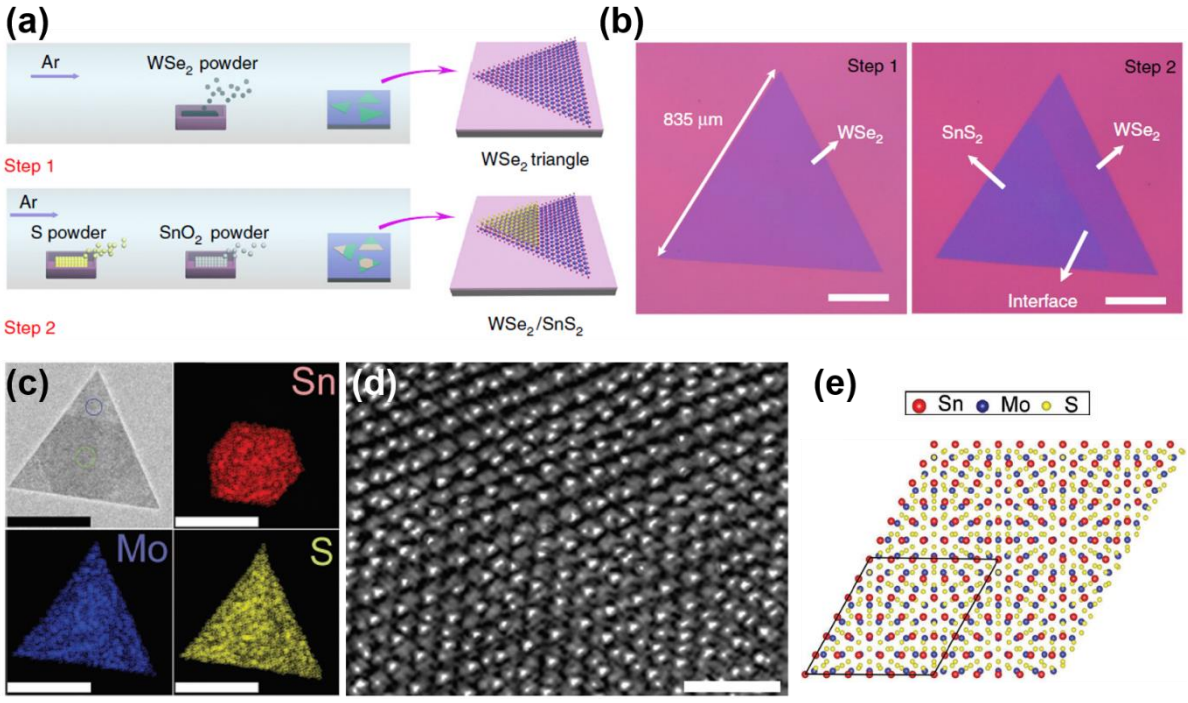


Figure 2.28. CVD growth of semiconductor/semiconductor vertical heterostructures. (a) Schematic diagram illustrating the two-step vapour epitaxy growth of SnS_2/WSe_2 heterostructures. (b) Optical images of the as-grown monolayer WSe_2 after step 1 and the vertically stacked SnS_2/WSe_2 after step 2. The scale bars are 200 μm. (a, b) Reproduced with permission from ref. [224]. © 2017 Nature Publishing Group. (c) Low magnification TEM image of a SnS_2/MoS_2 heterostructure and corresponding energy dispersive X-ray (EDX) elemental mapping images. The scale bars are 1 μm. (d) High resolution TEM image of SnS_2/MoS_2 bilayers showing the moiré pattern from the heterostructure.

The scale bar is 2 nm. (e) Atomic structural model of the corresponding SnS_2/MoS_2 heterostructure. (c-e) Reproduced with permission from ref. [226]. © 2016 Wiley-VCH.

The vertical heterostructures based on 2D semiconductors brings a series of fascinating physical properties including spin valley polarization,[211] anti-ambipolar behaviour,[212] superior rectification ratio,[213] tuneable interlayer interaction,[214] ultrafast charge transfer and efficient photocurrent generation.[215-216] Some of which are even unable to obtain from the single component of 2D layered semiconductors. Most of the modulated electrical and optical properties by interlayer coupling result from the effective charge transfer, which has a great potential in a variety of applications such as tunnelling diodes,[217-219] photodetectors,[220] light emitting diodes,[221] photovoltaic cells,[222] and spin valleytronic devices.[223]

In light of this, abundant efforts are applied in synthesizing the 2D semiconductor vertical heterostructures using direct CVD growth to avoid trapped impurities or transfer residue at the interface. Gong *et al.* demonstrated a single-step controlled CVD synthesis of heterostructures based on MoS_2 and WS_2.[180] A mixed powder of tungsten and tellurium, MoO_3, and sulphur powders were used as the source materials and put in the different places of the furnace during the synthesis. The different nucleation and growth rate of MoS_2 and WS_2 determine the growth sequence and the structure of the final product. At low temperature of 650°C, in-plane lateral WS_2-MoS_2 heterostructures are formed, whereas the vertical WS_2/MoS_2 bilayer heterostructures dominate when increasing the temperature to 850°C. This one-step growth, however, lacks the spatial and size control of the heterostructures and it is difficult to obtain atomically abrupt interface because of the cross-contamination of different 2D materials.

To compensate for this flaw, two-step or multistep growth strategies are further developed. Yang *et al.* reported a two-step van der Waals epitaxial growth SnS_2/WSe_2 heterostructures (**Figure 2.28**(a)), where the large band offset can lead to efficient interlayer

charge transfer according to the theoretical calculation.[224] The size of the vertical heterostructure can be well controlled by the growth time and the lateral size could reach nearly to millimetre scale, as demonstrated by the optical images in **Figure 2.28**(b). Likewise, Zhou *et al.* used the similar method to construct the $SnSe_2/MoS_2$ heterostructures.[225] They further demonstrated that photodetectors based on the $SnSe_2/MoS_2$ vdW heterostructures have an enhanced photoresponsivity of up to 9100 A/W, which is higher by two orders of magnitude than those devices with single MoS_2 channels. Similarly, Li *et al.* utilized high resolution TEM to characterize the SnS_2/MoS_2 heterostructures grown by direct CVD method (**Figure 2.28**(c)).[226] They observed that the heterostructures exhibit well-aligned lattice orientation between the bottom MoS_2 layer and top SnS_2 layer (**Figure 2.28**(d)), forming a periodic moiré superlattice pattern, which is consistent with the atomic model shown in **Figure 2.28**(e).

2.6 Conclusion

The post-Moore's law era excites the growing research and exploration of 2D materials to fulfil the requirements of nanoelectronic devices in next generation. Compared with graphene comprising single layer of carbon atoms, 2D semiconductors and hBN are with more complex structures and provide the increasing diversity of property tuning. Great efforts have been made using scalable CVD approach to realise the industrial-scale production. In addition to the single component 2D materials, promising progress has also been achieved in the development of 2D hybrid structures with tailoring properties, including the techniques of doping and heterostructure design. Despite the great success of graphene and TMDs research that has brought to a variety of applications in recent years, large-scale manufacturing of other 2D materials is still at its infancy. Besides, owing to the complex processes involved in the CVD growth, a thorough understanding of the various aspects of the growth is still essential to ensure the reproducibility and precise control for the property tuning of 2D materials.

2.7 Reference

(1) Moore, G. E., Cramming More Components Onto Integrated Circuits. *Electronics* **1965,** *38*, 114-117.

(2) Ferain, I.; Colinge, C. A.; Colinge, J.-P., Multigate Transistors as the Future of Classical Metal–Oxide–Semiconductor Field-Effect Transistors. *Nature* **2011,** *479*, 310.

(3) Franklin, A. D., Nanomaterials in Transistors: From High-Performance to Thin-Film Applications. *Science* **2015,** *349* (6249), aab2750.

(4) Novoselov, K. S.; Geim, A. K.; Morozov, S. V.; Jiang, D.; Zhang, Y.; Dubonos, S. V.; Grigorieva, I. V.; Firsov, A. A., Electric Field Effect in Atomically Thin Carbon Films. *Science* **2004,** *306* (5696), 666-669.

(5) Novoselov, K. S.; Jiang, D.; Schedin, F.; Booth, T. J.; Khotkevich, V. V.; Morozov, S. V.; Geim, A. K., Two-Dimensional Atomic Crystals. *Proc. Natl. Acad. Sci. U.S.A.* **2005,** *102* (30), 10451-10453.

(6) Butler, S. Z.; Hollen, S. M.; Cao, L.; Cui, Y.; Gupta, J. A.; Gutiérrez, H. R.; Heinz, T. F.; Hong, S. S.; Huang, J.; Ismach, A. F.; Johnston-Halperin, E.; Kuno, M.; Plashnitsa, V. V.; Robinson, R. D.; Ruoff, R. S.; Salahuddin, S.; Shan, J.; Shi, L.; Spencer, M. G.; Terrones, M.; Windl, W.; Goldberger, J. E., Progress, Challenges, and Opportunities in Two-Dimensional Materials Beyond Graphene. *ACS Nano* **2013,** *7* (4), 2898-2926.

(7) Bhimanapati, G. R.; Lin, Z.; Meunier, V.; Jung, Y.; Cha, J.; Das, S.; Xiao, D.; Son, Y.; Strano, M. S.; Cooper, V. R.; Liang, L.; Louie, S. G.; Ringe, E.; Zhou, W.; Kim, S. S.; Naik, R. R.; Sumpter, B. G.; Terrones, H.; Xia, F.; Wang, Y.; Zhu, J.; Akinwande, D.; Alem, N.; Schuller, J. A.; Schaak, R. E.; Terrones, M.; Robinson, J. A., Recent Advances in Two-Dimensional Materials beyond Graphene. *ACS Nano* **2015**.

(8) Novoselov, K. S.; Mishchenko, A.; Carvalho, A.; Castro Neto, A. H., 2D Materials and van der Waals Heterostructures. *Science* **2016,** *353* (6298), 9439.

(9) Manzeli, S.; Ovchinnikov, D.; Pasquier, D.; Yazyev, O. V.; Kis, A., 2D Transition Metal Dichalcogenides. *Nat. Rev. Mater.* **2017,** *2*, 17033.

(10) Chhowalla, M.; Jena, D.; Zhang, H., Two-Dimensional Semiconductors for Transistors. *Nat. Rev. Mater.* **2016,** *1*, 16052.

(11) Pacilé, D.; Meyer, J. C.; Girit, Ç. Ö.; Zettl, A., The Two-Dimensional Phase of Boron Nitride: Few-Atomic-Layer Sheets and Suspended Membranes. *Appl. Phys. Lett.* **2008,** *92* (13), 133107.

(12) Liu, H.; Neal, A. T.; Zhu, Z.; Luo, Z.; Xu, X.; Tománek, D.; Ye, P. D., Phosphorene: An Unexplored 2D Semiconductor with a High Hole Mobility. *ACS Nano* **2014,** *8* (4), 4033-4041.

(13) Ma, R.; Sasaki, T., Nanosheets of Oxides and Hydroxides: Ultimate 2D Charge-Bearing Functional Crystallites. *Adv. Mater.* **2010,** *22* (45), 5082-5104.

(14) Xie, L. M., Two-Dimensional Transition Metal Dichalcogenide Alloys: Preparation, Characterization and Applications. *Nanoscale* **2015,** *7* (44), 18392-18401.

(15) Wang, X.; Weng, Q.; Yang, Y.; Bando, Y.; Golberg, D., Hybrid Two-Dimensional Materials in Rechargeable Battery Applications and Their Microscopic Mechanisms. *Chem. Soc. Rev.* **2016,** *45* (15), 4042-4073.

(16) Gonzalez, J. M.; Oleynik, I. I., Layer-Dependent Properties of SnS_2 and $SnSe_2$ Two-Dimensional Materials. *Phys. Rev. B* **2016,** *94* (12), 125443.

(17) Dong, Y.; Zeng, B.; Xiao, J.; Zhang, X.; Li, D.; Li, M.; He, J.; Long, M., Effect of Sulphur Vacancy and Interlayer Interaction on the Electronic Structure and Spin Splitting of Bilayer MoS_2. *J. Phys. Condens. Matter* **2018,** *30* (12), 125302.

(18) Zhang, H.; Xia, C.; Zhao, X.; Wang, T.; Li, J., Tunable Electronic Structures in the Two-Dimension SnX_2 (X=S and Se) Nanosheets by Stacking Effects. *Appl. Surf. Sci.* **2015,** *356*, 1200-1206.

(19) Roldán, R.; Chirolli, L.; Prada, E.; Silva-Guillén, J. A.; San-Jose, P.; Guinea, F., Theory of 2D Crystals: Graphene and Beyond. *Chem. Soc. Rev.* **2017,** *46* (15), 4387-4399.

(20) Splendiani, A.; Sun, L.; Zhang, Y.; Li, T.; Kim, J.; Chim, C.-Y.; Galli, G.; Wang, F., Emerging Photoluminescence in Monolayer MoS_2. *Nano Lett.* **2010,** *10* (4), 1271-1275.

(21) Gutiérrez, H. R.; Perea-López, N.; Elías, A. L.; Berkdemir, A.; Wang, B.; Lv, R.; López-Urías, F.; Crespi, V. H.; Terrones, H.; Terrones, M., Extraordinary Room-Temperature Photoluminescence in Triangular WS_2 Monolayers. *Nano Lett.* **2013,** *13* (8), 3447-3454.

(22) Kuc, A.; Zibouche, N.; Heine, T., Influence of Quantum Confinement on the Electronic Structure of the Transition Metal Sulfide TS_2. *Phys. Rev. B* **2011,** *83* (24), 245213.

(23) Cheiwchanchamnangij, T.; Lambrecht, W. R. L., Quasiparticle Band Structure Calculation of Monolayer, Bilayer, and Bulk MoS_2. *Phys. Rev. B* **2012,** *85* (20), 205302.

(24) Hüser, F.; Olsen, T.; Thygesen, K. S., How Dielectric Screening in Two-Dimensional Crystals Affects the Convergence of Excited-State Calculations: Monolayer MoS_2. *Phys. Rev. B* **2013,** *88* (24), 245309.

(25) Latini, S.; Olsen, T.; Thygesen, K. S., Excitons in van der Waals Heterostructures: The Important Role of Dielectric Screening. *Phys. Rev. B* **2015,** *92* (24), 245123.

(26) Watanabe, K.; Taniguchi, T.; Kanda, H., Direct-Bandgap Properties and Evidence for Ultraviolet Lasing of Hexagonal Boron Nitride Single Crystal. *Nat. Mater.* **2004,** *3* (6), 404-409.

(27) Song, L.; Ci, L.; Lu, H.; Sorokin, P. B.; Jin, C.; Ni, J.; Kvashnin, A. G.; Kvashnin, D. G.; Lou, J.; Yakobson, B. I.; Ajayan, P. M., Large Scale Growth and Characterization of Atomic Hexagonal Boron Nitride Layers. *Nano Lett.* **2010,** *10* (8), 3209-3215.

(28) Li, L. H.; Cervenka, J.; Watanabe, K.; Taniguchi, T.; Chen, Y., Strong Oxidation Resistance of Atomically Thin Boron Nitride Nanosheets. *ACS Nano* **2014,** *8* (2), 1457-1462.

(29) Kho, J.-G.; Moon, K.-T.; Kim, J.-H.; Kim, D.-P., Properties of Boron Nitride (B_xN_y) Films Produced by the Spin-Coating Process of Polyborazine. *J. Am. Ceram. Soc.* **2000,** *83* (11), 2681-2683.

(30) Tao, O.; Yuanping, C.; Yuee, X.; Kaike, Y.; Zhigang, B.; Jianxin, Z., Thermal Transport in Hexagonal Boron Nitride Nanoribbons. *Nanotechnology* **2010,** *21* (24), 245701.

(31) Liu, Z.; Gong, Y.; Zhou, W.; Ma, L.; Yu, J.; Idrobo, J. C.; Jung, J.; MacDonald, A. H.; Vajtai, R.; Lou, J.; Ajayan, P. M., Ultrathin High-Temperature Oxidation-Resistant Coatings of Hexagonal Boron Nitride. *Nat. Commun.* **2013,** *4*, 2541.

(32) Kubota, Y.; Watanabe, K.; Tsuda, O.; Taniguchi, T., Deep Ultraviolet Light-Emitting Hexagonal Boron Nitride Synthesized at Atmospheric Pressure. *Science* **2007,** *317* (5840), 932-934.

(33) Tran, T. T.; Bray, K.; Ford, M. J.; Toth, M.; Aharonovich, I., Quantum Emission from Hexagonal Boron Nitride Monolayers. *Nat. Nanotechnol.* **2016,** *11* (1), 37-41.

(34) Lee, G.-H.; Cui, X.; Kim, Y. D.; Arefe, G.; Zhang, X.; Lee, C.-H.; Ye, F.; Watanabe, K.; Taniguchi, T.; Kim, P.; Hone, J., Highly Stable, Dual-Gated MoS_2 Transistors Encapsulated by Hexagonal Boron Nitride with Gate-Controllable Contact, Resistance, and Threshold Voltage. *ACS Nano* **2015,** *9* (7), 7019-7026.

(35) Sheng, Y.; Xu, W.; Wang, X.; He, Z.; Rong, Y.; Warner, J. H., Mixed Multilayered Vertical Heterostructures Utilizing Strained Monolayer WS_2. *Nanoscale* **2016,** *8* (5), 2639-2647.

(36) Britnell, L.; Gorbachev, R. V.; Jalil, R.; Belle, B. D.; Schedin, F.; Katsnelson, M. I.; Eaves, L.; Morozov, S. V.; Mayorov, A. S.; Peres, N. M. R.; Castro Neto, A. H.; Leist,

J.; Geim, A. K.; Ponomarenko, L. A.; Novoselov, K. S., Electron Tunneling through Ultrathin Boron Nitride Crystalline Barriers. *Nano Lett.* **2012,** *12* (3), 1707-1710.

(37) Kim, S. M.; Hsu, A.; Araujo, P. T.; Lee, Y.-H.; Palacios, T.; Dresselhaus, M.; Idrobo, J.-C.; Kim, K. K.; Kong, J., Synthesis of Patched or Stacked Graphene and hBN Flakes: A Route to Hybrid Structure Discovery. *Nano Lett.* **2013,** *13* (3), 933-941.

(38) Wang, M.; Jang, S. K.; Jang, W.-J.; Kim, M.; Park, S.-Y.; Kim, S.-W.; Kahng, S.-J.; Choi, J.-Y.; Ruoff, R. S.; Song, Y. J.; Lee, S., A Platform for Large-Scale Graphene Electronics – CVD Growth of Single-Layer Graphene on CVD-Grown Hexagonal Boron Nitride. *Adv. Mater.* **2013,** *25* (19), 2746-2752.

(39) Wu, W.; Wang, L.; Li, Y.; Zhang, F.; Lin, L.; Niu, S.; Chenet, D.; Zhang, X.; Hao, Y.; Heinz, T. F.; Hone, J.; Wang, Z. L., Piezoelectricity of Single-Atomic-Layer MoS_2 for Energy Conversion and Piezotronics. *Nature* **2014,** *514*, 470.

(40) Schaibley, J. R.; Yu, H.; Clark, G.; Rivera, P.; Ross, J. S.; Seyler, K. L.; Yao, W.; Xu, X., Valleytronics in 2D materials. *Nat. Rev. Mater.* **2016,** *1*, 16055.

(41) Mak, K. F.; McGill, K. L.; Park, J.; McEuen, P. L., The Valley Hall Effect in MoS_2 Transistors. *Science* **2014,** *344* (6191), 1489-1492.

(42) Kufer, D.; Konstantatos, G., Photo-FETs: Phototransistors Enabled by 2D and 0D Nanomaterials. *ACS Photonics* **2016,** *3* (12), 2197-2210.

(43) Withers, F.; Del Pozo-Zamudio, O.; Mishchenko, A.; Rooney, A. P.; Gholinia, A.; Watanabe, K.; Taniguchi, T.; Haigh, S. J.; Geim, A. K.; Tartakovskii, A. I.; Novoselov, K. S., Light-Emitting Diodes by Band-Structure Engineering in van der Waals Heterostructures. *Nat. Mater.* **2015,** *14* (3), 301-306.

(44) Lei, S.; Wen, F.; Li, B.; Wang, Q.; Huang, Y.; Gong, Y.; He, Y.; Dong, P.; Bellah, J.; George, A.; Ge, L.; Lou, J.; Halas, N. J.; Vajtai, R.; Ajayan, P. M., Optoelectronic Memory Using Two-Dimensional Materials. *Nano Lett.* **2015,** *15* (1), 259-265.

(45) Wang, H.; Yu, L.; Lee, Y.-H.; Shi, Y.; Hsu, A.; Chin, M. L.; Li, L.-J.; Dubey, M.; Kong, J.; Palacios, T., Integrated Circuits Based on Bilayer MoS_2 Transistors. *Nano Lett.* **2012,** *12* (9), 4674-4680.

(46) Debtanu, D.; John, M.; Sean, S.; Vincent, Z.; Arnold, G.; Haibing, P., High on/off Ratio Field Effect Transistors Based on Exfoliated Crystalline SnS_2 Nano-Membranes. *Nanotechnology* **2013,** *24* (2), 025202.

(47) Ou, J. Z.; Ge, W.; Carey, B.; Daeneke, T.; Rotbart, A.; Shan, W.; Wang, Y.; Fu, Z.; Chrimes, A. F.; Wlodarski, W.; Russo, S. P.; Li, Y. X.; Kalantar-zadeh, K.,

Physisorption-Based Charge Transfer in Two-Dimensional SnS_2 for Selective and Reversible NO_2 Gas Sensing. *ACS Nano* **2015,** *9* (10), 10313-10323.

(48) Lee, M.-J.; Ahn, J.-H.; Sung, J. H.; Heo, H.; Jeon, S. G.; Lee, W.; Song, J. Y.; Hong, K.-H.; Choi, B.; Lee, S.-H.; Jo, M.-H., Thermoelectric Materials by Using Two-Dimensional Materials with Negative Correlation Between Electrical and Thermal Conductivity. *Nat. Commun.* **2016,** *7*, 12011.

(49) Chao, D.; Liang, P.; Chen, Z.; Bai, L.; Shen, H.; Liu, X.; Xia, X.; Zhao, Y.; Savilov, S. V.; Lin, J.; Shen, Z. X., Pseudocapacitive Na-Ion Storage Boosts High Rate and Areal Capacity of Self-Branched 2D Layered Metal Chalcogenide Nanoarrays. *ACS Nano* **2016,** *10* (11), 10211-10219.

(50) Raffone, F.; Ataca, C.; Grossman, J. C.; Cicero, G., MoS_2 Enhanced T-Phase Stabilization and Tunability Through Alloying. *J. Phys. Chem. Lett.* **2016,** *7* (13), 2304-2309.

(51) Sutter, E.; Huang, Y.; Komsa, H. P.; Ghorbani-Asl, M.; Krasheninnikov, A. V.; Sutter, P., Electron-Beam Induced Transformations of Layered Tin Dichalcogenides. *Nano Lett.* **2016,** *16* (7), 4410-4416.

(52) Ahn, J.-H.; Lee, M.-J.; Heo, H.; Sung, J. H.; Kim, K.; Hwang, H.; Jo, M.-H., Deterministic Two-Dimensional Polymorphism Growth of Hexagonal n-Type SnS_2 and Orthorhombic p-Type SnS Crystals. *Nano Lett.* **2015,** *15* (6), 3703-3708.

(53) Buscema, M.; Island, J. O.; Groenendijk, D. J.; Blanter, S. I.; Steele, G. A.; van der Zant, H. S. J.; Castellanos-Gomez, A., Photocurrent Generation with Two-Dimensional van der Waals Semiconductors. *Chem. Soc. Rev.* **2015,** *44* (11), 3691-3718.

(54) Xie, C.; Mak, C.; Tao, X.; Yan, F., Photodetectors Based on Two-Dimensional Layered Materials Beyond Graphene. *Adv. Funct. Mater.* **2017,** *27* (19), 1603886.

(55) Wang, J.; Fang, H.; Wang, X.; Chen, X.; Lu, W.; Hu, W., Recent Progress on Localized Field Enhanced Two-Dimensional Material Photodetectors from Ultraviolet—Visible to Infrared. *Small* **2017,** *13* (35), 1700894.

(56) Soref, R. A., Silicon-Based Optoelectronics. *Proc. IEEE* **1993,** *81* (12), 1687-1706.

(57) Smith, D. L.; Mailhiot, C., Proposal for Strained Type II Superlattice Infrared Detectors. *J. Appl. Phys.* **1987,** *62* (6), 2545-2548.

(58) Rogalski, A., HgCdTe Infrared Detector Material: History, Status and Outlook. *Rep. Prog. Phys.* **2005,** *68* (10), 2267-2336.

(59) Choi, W.; Choudhary, N.; Han, G. H.; Park, J.; Akinwande, D.; Lee, Y. H., Recent Development of Two-Dimensional Transition Metal Dichalcogenides and Their Applications. *Mater. Today* **2017,** *20* (3), 116-130.

(60) Lopez-Sanchez, O.; Lembke, D.; Kayci, M.; Radenovic, A.; Kis, A., Ultrasensitive Photodetectors Based on Monolayer MoS_2. *Nat. Nanotechnol.* **2013,** *8* (7), 497-501.

(61) Ghatak, S.; Pal, A. N.; Ghosh, A., Nature of Electronic States in Atomically Thin MoS_2 Field-Effect Transistors. *ACS Nano* **2011,** *5* (10), 7707-7712.

(62) Yin, Z.; Li, H.; Li, H.; Jiang, L.; Shi, Y.; Sun, Y.; Lu, G.; Zhang, Q.; Chen, X.; Zhang, H., Single-Layer MoS_2 Phototransistors. *ACS Nano* **2012,** *6* (1), 74-80.

(63) Fang, H.; Hu, W., Photogating in Low Dimensional Photodetectors. *Adv. Sci.* **2017,** *4* (12), 1700323.

(64) Koppens, F. H. L.; Mueller, T.; Avouris, P.; Ferrari, A. C.; Vitiello, M. S.; Polini, M., Photodetectors Based on Graphene, Other Two-Dimensional Materials and Hybrid Systems. *Nat. Nanotechnol.* **2014,** *9* (10), 780-793.

(65) Lee, C.-H.; Lee, G.-H.; van der Zande, A. M.; Chen, W.; Li, Y.; Han, M.; Cui, X.; Arefe, G.; Nuckolls, C.; Heinz, T. F.; Guo, J.; Hone, J.; Kim, P., Atomically Thin p–n Junctions with van der Waals Heterointerfaces. *Nat. Nanotechnol.* **2014,** *9* (9), 676-681.

(66) Frisenda, R.; Molina-Mendoza, A. J.; Mueller, T.; Castellanos-Gomez, A.; van der Zant, H. S. J., Atomically Thin p–n Junctions Based on Two-Dimensional Materials. *Chem. Soc. Rev.* **2018,** *47* (9), 3339-3358.

(67) Zhang, W.; Huang, J.-K.; Chen, C.-H.; Chang, Y.-H.; Cheng, Y.-J.; Li, L.-J., High-Gain Phototransistors Based on a CVD MoS_2 Monolayer. *Adv. Mater.* **2013,** *25* (25), 3456-3461.

(68) Ganatra, R.; Zhang, Q., Few-Layer MoS_2: A Promising Layered Semiconductor. *ACS Nano* **2014,** *8* (5), 4074-4099.

(69) Huang, J.-K.; Pu, J.; Hsu, C.-L.; Chiu, M.-H.; Juang, Z.-Y.; Chang, Y.-H.; Chang, W.-H.; Iwasa, Y.; Takenobu, T.; Li, L.-J., Large-Area Synthesis of Highly Crystalline WSe_2 Monolayers and Device Applications. *ACS Nano* **2014,** *8* (1), 923-930.

(70) Zhang, W.; Chiu, M.-H.; Chen, C.-H.; Chen, W.; Li, L.-J.; Wee, A. T. S., Role of Metal Contacts in High-Performance Phototransistors Based on WSe_2 Monolayers. *ACS Nano* **2014,** *8* (8), 8653-8661.

(71) Allain, A.; Kang, J.; Banerjee, K.; Kis, A., Electrical Contacts to Two-Dimensional Semiconductors. *Nat. Mater.* **2015,** *14* (12), 1195-1205.

(72) Xu, Y.; Cheng, C.; Du, S.; Yang, J.; Yu, B.; Luo, J.; Yin, W.; Li, E.; Dong, S.; Ye, P.; Duan, X., Contacts between Two- and Three-Dimensional Materials: Ohmic, Schottky, and p–n Heterojunctions. *ACS Nano* **2016,** *10* (5), 4895-4919.

(73) Somvanshi, D.; Kallatt, S.; Venkatesh, C.; Nair, S.; Gupta, G.; Anthony, J. K.; Karmakar, D.; Majumdar, K., Nature of Carrier Injection in Metal/2D-Semiconductor Interface and its Implications for the Limits of Contact Resistance. *Phys. Rev. B* **2017,** *96* (20), 205423.

(74) Tung, R. T., The Physics and Chemistry of the Schottky Barrier Height. *Appl. Phys. Rev.* **2014,** *1* (1), 011304.

(75) Liu, Y.; Guo, J.; Zhu, E.; Liao, L.; Lee, S.-J.; Ding, M.; Shakir, I.; Gambin, V.; Huang, Y.; Duan, X., Approaching the Schottky–Mott Limit in van der Waals Metal–Semiconductor Junctions. *Nature* **2018,** *557* (7707), 696-700.

(76) Das, S.; Chen, H.-Y.; Penumatcha, A. V.; Appenzeller, J., High Performance Multilayer MoS_2 Transistors with Scandium Contacts. *Nano Lett.* **2013,** *13* (1), 100-105.

(77) Kim, C.; Moon, I.; Lee, D.; Choi, M. S.; Ahmed, F.; Nam, S.; Cho, Y.; Shin, H.-J.; Park, S.; Yoo, W. J., Fermi Level Pinning at Electrical Metal Contacts of Monolayer Molybdenum Dichalcogenides. *ACS Nano* **2017,** *11* (2), 1588-1596.

(78) Schulman, D. S.; Arnold, A. J.; Das, S., Contact Engineering for 2D Materials and Devices. *Chem. Soc. Rev.* **2018,** *47* (9), 3037-3058.

(79) Monch, W., On the Physics of Metal-Semiconductor Interfaces. *Rep. Prog. Phys.* **1990,** *53* (3), 221-278.

(80) Kerelsky, A.; Nipane, A.; Edelberg, D.; Wang, D.; Zhou, X.; Motmaendadgar, A.; Gao, H.; Xie, S.; Kang, K.; Park, J.; Teherani, J.; Pasupathy, A., Absence of a Band Gap at the Interface of a Metal and Highly Doped Monolayer MoS_2. *Nano Lett.* **2017,** *17* (10), 5962-5968.

(81) Wang, J.; Yao, Q.; Huang, C.-W.; Zou, X.; Liao, L.; Chen, S.; Fan, Z.; Zhang, K.; Wu, W.; Xiao, X.; Jiang, C.; Wu, W.-W., High Mobility MoS_2 Transistor with Low Schottky Barrier Contact by Using Atomic Thick h-BN as a Tunneling Layer. *Adv. Mater.* **2016,** *28* (37), 8302-8308.

(82) Dankert, A.; Langouche, L.; Kamalakar, M. V.; Dash, S. P., High-Performance Molybdenum Disulfide Field-Effect Transistors with Spin Tunnel Contacts. *ACS Nano* **2014,** *8* (1), 476-482.

(83) Lee, S.; Tang, A.; Aloni, S.; Philip Wong, H. S., Statistical Study on the Schottky Barrier Reduction of Tunneling Contacts to CVD Synthesized MoS_2. *Nano Lett.* **2016,** *16* (1), 276-281.

(84) Cui, X.; Shih, E.-M.; Jauregui, L. A.; Chae, S. H.; Kim, Y. D.; Li, B.; Seo, D.; Pistunova, K.; Yin, J.; Park, J.-H.; Choi, H.-J.; Lee, Y. H.; Watanabe, K.; Taniguchi, T.; Kim, P.; Dean, C. R.; Hone, J. C., Low-Temperature Ohmic Contact to Monolayer MoS_2 by van der Waals Bonded Co/h-BN Electrodes. *Nano Lett.* **2017,** *17* (8), 4781-4786.

(85) Cui, X.; Lee, G.-H.; Kim, Y. D.; Arefe, G.; Huang, P. Y.; Lee, C.-H.; Chenet, D. A.; Zhang, X.; Wang, L.; Ye, F.; Pizzocchero, F.; Jessen, B. S.; Watanabe, K.; Taniguchi, T.; Muller, D. A.; Low, T.; Kim, P.; Hone, J., Multi-Terminal Transport Measurements of MoS_2 Using a van der Waals Heterostructure Device Platform. *Nature Nanotechnol.* **2015,** *10*, 534.

(86) Guimarães, M. H. D.; Gao, H.; Han, Y.; Kang, K.; Xie, S.; Kim, C.-J.; Muller, D. A.; Ralph, D. C.; Park, J., Atomically Thin Ohmic Edge Contacts Between Two-Dimensional Materials. *ACS Nano* **2016,** *10* (6), 6392-6399.

(87) Wang, L.; Meric, I.; Huang, P. Y.; Gao, Q.; Gao, Y.; Tran, H.; Taniguchi, T.; Watanabe, K.; Campos, L. M.; Muller, D. A.; Guo, J.; Kim, P.; Hone, J.; Shepard, K. L.; Dean, C. R. *Science* **2013,** *342* (6158), 614-617.

(88) Chhowalla, M.; Shin, H. S.; Eda, G.; Li, L.-J.; Loh, K. P.; Zhang, H., The Chemistry of Two-Dimensional Layered Transition Metal Dichalcogenide Nanosheets. *Nat. Chem.* **2013,** *5* (4), 263-275.

(89) Kappera, R.; Voiry, D.; Yalcin, S. E.; Branch, B.; Gupta, G.; Mohite, A. D.; Chhowalla, M., Phase-Engineered Low-Resistance Contacts for Ultrathin MoS_2 Transistors. *Nature Mater.* **2014,** *13*, 1128.

(90) Cai, Z.; Liu, B.; Zou, X.; Cheng, H.-M., Chemical Vapor Deposition Growth and Applications of Two-Dimensional Materials and Their Heterostructures. *Chem. Rev.* **2018,** *118* (13), 6091-6133.

(91) Park, S.; Lee, J.; Kim, H. S.; Park, J.-B.; Lee, K. H.; Han, S. A.; Hwang, S.; Kim, S.-W.; Shin, H.-J., Formation of Hexagonal Boron Nitride by Metal Atomic Vacancy-Assisted B–N Molecular Diffusion. *ACS Nano* **2015,** *9* (1), 633-638.

(92) Kidambi, P. R.; Blume, R.; Kling, J.; Wagner, J. B.; Baehtz, C.; Weatherup, R. S.; Schloegl, R.; Bayer, B. C.; Hofmann, S., In Situ Observations during Chemical Vapor

Deposition of Hexagonal Boron Nitride on Polycrystalline Copper. *Chem. Mater.* **2014,** *26* (22), 6380-6392.

(93) Ji, Q.; Zhang, Y.; Zhang, Y.; Liu, Z., Chemical Vapour Deposition of Group-VIB Metal Dichalcogenide Monolayers: Engineered Substrates from Amorphous to Single Crystalline. *Chem. Soc. Rev.* **2015,** *44* (9), 2587-2602.

(94) Haodong, Z.; Thomas van, P.; Ankit Nalin, M.; Hugo, B.; Iuliana, R.; Matty, C.; Wilfried, V.; Annelies, D., Nucleation and Growth Mechanism of 2D SnS_2 by Chemical Vapor Deposition: Initial 3D Growth Followed by 2D Lateral Growth. *2D Mater.* **2018,** *5* (3), 035006.

(95) Park, J.-H.; Park, J. C.; Yun, S. J.; Kim, H.; Luong, D. H.; Kim, S. M.; Choi, S. H.; Yang, W.; Kong, J.; Kim, K. K.; Lee, Y. H., Large-Area Monolayer Hexagonal Boron Nitride on Pt Foil. *ACS Nano* **2014,** *8* (8), 8520-8528.

(96) Sutter, P.; Sadowski, J. T.; Sutter, E., Graphene on Pt(111): Growth and Substrate Interaction. *Phys. Rev. B* **2009,** *80* (24), 245411.

(97) Müller, F.; Stöwe, K.; Sachdev, H., Symmetry versus Commensurability: Epitaxial Growth of Hexagonal Boron Nitride on Pt(111) From B-Trichloroborazine $(ClBNH)_3$. *Chem. Mater.* **2005,** *17* (13), 3464-3467.

(98) Lin, W.-H.; Brar, V. W.; Jariwala, D.; Sherrott, M. C.; Tseng, W.-S.; Wu, C.-I.; Yeh, N.-C.; Atwater, H. A., Atomic-Scale Structural and Chemical Characterization of Hexagonal Boron Nitride Layers Synthesized at the Wafer-Scale with Monolayer Thickness Control. *Chem. Mater.* **2017,** *29* (11), 4700-4707.

(99) Koepke, J. C.; Wood, J. D.; Chen, Y.; Schmucker, S. W.; Liu, X.; Chang, N. N.; Nienhaus, L.; Do, J. W.; Carrion, E. A.; Hewaparakrama, J.; Rangarajan, A.; Datye, I.; Mehta, R.; Haasch, R. T.; Gruebele, M.; Girolami, G. S.; Pop, E.; Lyding, J. W., Role of Pressure in the Growth of Hexagonal Boron Nitride Thin Films from Ammonia-Borane. *Chem. Mater.* **2016,** *28* (12), 4169-4179.

(100) Kim, K. K.; Hsu, A.; Jia, X.; Kim, S. M.; Shi, Y.; Dresselhaus, M.; Palacios, T.; Kong, J., Synthesis and Characterization of Hexagonal Boron Nitride Film as a Dielectric Layer for Graphene Devices. *ACS Nano* **2012,** *6* (10), 8583-8590.

(101) He, Y.; Sobhani, A.; Lei, S.; Zhang, Z.; Gong, Y.; Jin, Z.; Zhou, W.; Yang, Y.; Zhang, Y.; Wang, X.; Yakobson, B.; Vajtai, R.; Halas, N. J.; Li, B.; Xie, E.; Ajayan, P., Layer Engineering of 2D Semiconductor Junctions. *Adv. Mater.* **2016,** *28* (25), 5126-5132.

(102) Jeon, J.; Jang, S. K.; Jeon, S. M.; Yoo, G.; Jang, Y. H.; Park, J.-H.; Lee, S., Layer-Controlled CVD Growth of Large-Area Two-Dimensional MoS_2 Films. *Nanoscale* **2015,** *7* (5), 1688-1695.

(103) Gibb, A. L.; Alem, N.; Chen, J.-H.; Erickson, K. J.; Ciston, J.; Gautam, A.; Linck, M.; Zettl, A., Atomic Resolution Imaging of Grain Boundary Defects in Monolayer Chemical Vapor Deposition-Grown Hexagonal Boron Nitride. *J. Am. Chem. Soc.* **2013,** *135* (18), 6758-6761.

(104) Najmaei, S.; Liu, Z.; Zhou, W.; Zou, X.; Shi, G.; Lei, S.; Yakobson, B. I.; Idrobo, J.-C.; Ajayan, P. M.; Lou, J., Vapour Phase Growth and Grain Boundary Structure of Molybdenum Disulphide Atomic Layers. *Nat. Mater.* **2013,** *12* (8), 754-759.

(105) Wu, T.; Zhang, X.; Yuan, Q.; Xue, J.; Lu, G.; Liu, Z.; Wang, H.; Wang, H.; Ding, F.; Yu, Q.; Xie, X.; Jiang, M., Fast Growth of Inch-Sized Single-Crystalline Graphene from a Controlled Single Nucleus on Cu-Ni Alloys. *Nat. Mater.* **2016,** *15* (1), 43-47.

(106) Kim, H.; Mattevi, C.; Calvo, M. R.; Oberg, J. C.; Artiglia, L.; Agnoli, S.; Hirjibehedin, C. F.; Chhowalla, M.; Saiz, E., Activation Energy Paths for Graphene Nucleation and Growth on Cu. *ACS Nano* **2012,** *6* (4), 3614-3623.

(107) Stehle, Y.; Meyer, H. M.; Unocic, R. R.; Kidder, M.; Polizos, G.; Datskos, P. G.; Jackson, R.; Smirnov, S. N.; Vlassiouk, I. V., Synthesis of Hexagonal Boron Nitride Monolayer: Control of Nucleation and Crystal Morphology. *Chem. Mater.* **2015,** *27* (23), 8041-8047.

(108) Tay, R. Y.; Griep, M. H.; Mallick, G.; Tsang, S. H.; Singh, R. S.; Tumlin, T.; Teo, E. H. T.; Karna, S. P., Growth of Large Single-Crystalline Two-Dimensional Boron Nitride Hexagons on Electropolished Copper. *Nano Lett.* **2014,** *14* (2), 839-846.

(109) Wu, Q.; Park, J.-H.; Park, S.; Jung, S. J.; Suh, H.; Park, N.; Wongwiriyapan, W.; Lee, S.; Lee, Y. H.; Song, Y. J., Single Crystalline Film of Hexagonal Boron Nitride Atomic Monolayer by Controlling Nucleation Seeds and Domains. *Sci. Rep.* **2015,** *5*, 16159.

(110) Song, X.; Gao, J.; Nie, Y.; Gao, T.; Sun, J.; Ma, D.; Li, Q.; Chen, Y.; Jin, C.; Bachmatiuk, A.; Rümmeli, M. H.; Ding, F.; Zhang, Y.; Liu, Z., Chemical Vapor Deposition Growth of Large-Scale Hexagonal Boron Nitride with Controllable Orientation. *Nano Res.* **2015,** *8* (10), 3164-3176.

(111) Kim, K. K.; Hsu, A.; Jia, X.; Kim, S. M.; Shi, Y.; Hofmann, M.; Nezich, D.; Rodriguez-Nieva, J. F.; Dresselhaus, M.; Palacios, T.; Kong, J., Synthesis of Monolayer Hexagonal Boron Nitride on Cu Foil Using Chemical Vapor Deposition. *Nano Lett.* **2012,** *12* (1), 161-166.

(112) Khan, M. H.; Huang, Z.; Xiao, F.; Casillas, G.; Chen, Z.; Molino, P. J.; Liu, H. K., Synthesis of Large and Few Atomic Layers of Hexagonal Boron Nitride on Melted Copper. *Sci. Rep.* **2015,** *5*, 7743.

(113) Tay, R. Y.; Park, H. J.; Ryu, G. H.; Tan, D.; Tsang, S. H.; Li, H.; Liu, W.; Teo, E. H. T.; Lee, Z.; Lifshitz, Y.; Ruoff, R. S., Synthesis of Aligned Symmetrical Multifaceted Monolayer Hexagonal Boron Nitride Single Crystals on Resolidified Copper. *Nanoscale* **2016,** *8* (4), 2434-2444.

(114) Ji, Y.; Calderon, B.; Han, Y.; Cueva, P.; Jungwirth, N. R.; Alsalman, H. A.; Hwang, J.; Fuchs, G. D.; Muller, D. A.; Spencer, M. G., Chemical Vapor Deposition Growth of Large Single-Crystal Mono-, Bi-, Tri-Layer Hexagonal Boron Nitride and Their Interlayer Stacking. *ACS Nano* **2017,** *11* (12), 12057-12066.

(115) Lu, G.; Wu, T.; Yuan, Q.; Wang, H.; Wang, H.; Ding, F.; Xie, X.; Jiang, M., Synthesis of Large Single-Crystal Hexagonal Boron Nitride Grains on Cu–Ni Alloy. *Nat. Commun.* **2015,** *6*, 6160.

(116) Caneva, S.; Weatherup, R. S.; Bayer, B. C.; Brennan, B.; Spencer, S. J.; Mingard, K.; Cabrero-Vilatela, A.; Baehtz, C.; Pollard, A. J.; Hofmann, S., Nucleation Control for Large, Single Crystalline Domains of Monolayer Hexagonal Boron Nitride via Si-Doped Fe Catalysts. *Nano Lett.* **2015,** *15* (3), 1867-1875.

(117) Rong, Y.; Fan, Y.; Leen Koh, A.; Robertson, A. W.; He, K.; Wang, S.; Tan, H.; Sinclair, R.; Warner, J. H., Controlling Sulphur Precursor Addition for Large Single Crystal Domains of WS_2. *Nanoscale* **2014,** *6* (20), 12096-12103.

(118) Ye, G.; Gong, Y.; Lei, S.; He, Y.; Li, B.; Zhang, X.; Jin, Z.; Dong, L.; Lou, J.; Vajtai, R.; Zhou, W.; Ajayan, P. M., Synthesis of Large-Scale Atomic-layer SnS_2 through Chemical Vapor Deposition. *Nano Res.* **2017,** *10* (7), 2386-2394.

(119) Shi, J.; Ma, D.; Han, G.-F.; Zhang, Y.; Ji, Q.; Gao, T.; Sun, J.; Song, X.; Li, C.; Zhang, Y.; Lang, X.-Y.; Zhang, Y.; Liu, Z., Controllable Growth and Transfer of Monolayer MoS_2 on Au Foils and Its Potential Application in Hydrogen Evolution Reaction. *ACS Nano* **2014,** *8* (10), 10196-10204.

(120) Shi, J.; Zhang, X.; Ma, D.; Zhu, J.; Zhang, Y.; Guo, Z.; Yao, Y.; Ji, Q.; Song, X.; Zhang, Y.; Li, C.; Liu, Z.; Zhu, W.; Zhang, Y., Substrate Facet Effect on the Growth of Monolayer MoS_2 on Au Foils. *ACS Nano* **2015,** *9* (4), 4017-4025.

(121) Gao, Y.; Liu, Z.; Sun, D.-M.; Huang, L.; Ma, L.-P.; Yin, L.-C.; Ma, T.; Zhang, Z.; Ma, X.-L.; Peng, L.-M.; Cheng, H.-M.; Ren, W., Large-Area Synthesis of High-Quality and Uniform Monolayer WS_2 on Reusable Au Foils. *Nat. Commun.* **2015,** *6*, 8569.

(122) Yun, S. J.; Chae, S. H.; Kim, H.; Park, J. C.; Park, J.-H.; Han, G. H.; Lee, J. S.; Kim, S. M.; Oh, H. M.; Seok, J.; Jeong, M. S.; Kim, K. K.; Lee, Y. H., Synthesis of Centimeter-Scale Monolayer Tungsten Disulfide Film on Gold Foils. *ACS Nano* **2015,** *9* (5), 5510-5519.

(123) Chen, J.; Zhao, X.; Tan, S. J. R.; Xu, H.; Wu, B.; Liu, B.; Fu, D.; Fu, W.; Geng, D.; Liu, Y.; Liu, W.; Tang, W.; Li, L.; Zhou, W.; Sum, T. C.; Loh, K. P., Chemical Vapor Deposition of Large-Size Monolayer $MoSe_2$ Crystals on Molten Glass. *J. Am. Chem. Soc.* **2017,** *139* (3), 1073-1076.

(124) Yang, P.; Zou, X.; Zhang, Z.; Hong, M.; Shi, J.; Chen, S.; Shu, J.; Zhao, L.; Jiang, S.; Zhou, X.; Huan, Y.; Xie, C.; Gao, P.; Chen, Q.; Zhang, Q.; Liu, Z.; Zhang, Y., Batch Production of 6-Inch Uniform Monolayer Molybdenum Disulfide Catalyzed by Sodium in Glass. *Nat. Commun.* **2018,** *9* (1), 979.

(125) Chen, W.; Zhao, J.; Zhang, J.; Gu, L.; Yang, Z.; Li, X.; Yu, H.; Zhu, X.; Yang, R.; Shi, D.; Lin, X.; Guo, J.; Bai, X.; Zhang, G., Oxygen-Assisted Chemical Vapor Deposition Growth of Large Single-Crystal and High-Quality Monolayer MoS_2. *J. Am. Chem. Soc.* **2015,** *137* (50), 15632-15635.

(126) Liu, Y.; Bhowmick, S.; Yakobson, B. I., BN White Graphene with "Colorful" Edges: The Energies and Morphology. *Nano Lett.* **2011,** *11* (8), 3113-3116.

(127) Zhang, Z.; Liu, Y.; Yang, Y.; Yakobson, B. I., Growth Mechanism and Morphology of Hexagonal Boron Nitride. *Nano Lett.* **2016,** *16* (2), 1398-1403.

(128) Yin, J.; Yu, J.; Li, X.; Li, J.; Zhou, J.; Zhang, Z.; Guo, W., Large Single-Crystal Hexagonal Boron Nitride Monolayer Domains with Controlled Morphology and Straight Merging Boundaries. *Small* **2015,** *11* (35), 4497-4502.

(129) Huang, Y.; Xu, K.; Wang, Z.; Shifa, T. A.; Wang, Q.; Wang, F.; Jiang, C.; He, J., Designing the Shape Evolution of $SnSe_2$ Nanosheets and Their Optoelectronic Properties. *Nanoscale* **2015,** *7* (41), 17375-17380.

(130) Xu, W.; Li, S.; Zhou, S.; Lee, J. K.; Wang, S.; Sarwat, S. G.; Wang, X.; Bhaskaran, H.; Pasta, M.; Warner, J. H., Large Dendritic Monolayer MoS_2 Grown by Atmospheric Pressure Chemical Vapor Deposition for Electrocatalysis. *ACS Appl. Mater. Interfaces* **2018,** *10* (5), 4630-4639.

(131) Wang, J.; Cai, X.; Shi, R.; Wu, Z.; Wang, W.; Long, G.; Tang, Y.; Cai, N.; Ouyang, W.; Geng, P.; Chandrashekar, B. N.; Amini, A.; Wang, N.; Cheng, C., Twin Defect Derived Growth of Atomically Thin MoS_2 Dendrites. *ACS Nano* **2018,** *12* (1), 635-643.

(132) van der Zande, A. M.; Huang, P. Y.; Chenet, D. A.; Berkelbach, T. C.; You, Y.; Lee, G.-H.; Heinz, T. F.; Reichman, D. R.; Muller, D. A.; Hone, J. C., Grains and Grain Boundaries in Highly Crystalline Monolayer Molybdenum Disulphide. *Nat. Mater.* **2013,** *12* (6), 554-561.

(133) Zhou, Y.; Sarwat, S. G.; Jung, G. S.; Buehler, M. J.; Bhaskaran, H.; Warner, J. H., Grain Boundaries as Electrical Conduction Channels in Polycrystalline Monolayer WS_2. *ACS Appl. Mater. Interfaces* **2019,** *11* (10), 10189-10197.

(134) Lee, J. S.; Choi, S. H.; Yun, S. J.; Kim, Y. I.; Boandoh, S.; Park, J.-H.; Shin, B. G.; Ko, H.; Lee, S. H.; Kim, Y.-M.; Lee, Y. H.; Kim, K. K.; Kim, S. M., Wafer-Scale Single-Crystal Hexagonal Boron Nitride Film via Self-Collimated Grain Formation. *Science* **2018,** *362* (6416), 817-821.

(135) Yin, J.; Liu, X.; Lu, W.; Li, J.; Cao, Y.; Li, Y.; Xu, Y.; Li, X.; Zhou, J.; Jin, C.; Guo, W., Aligned Growth of Hexagonal Boron Nitride Monolayer on Germanium. *Small* **2015,** *11* (40), 5375-5380.

(136) Hite, J. K.; Robinson, Z. R.; Eddy, C. R.; Feigelson, B. N., Electron Backscatter Diffraction Study of Hexagonal Boron Nitride Growth on Cu Single-Crystal Substrates. *ACS Appl. Mater. Interfaces* **2015,** *7* (28), 15200-15205.

(137) Grace, E. W.; Alexander, J. M.; James, J. M.; Marc, W.; Maria, A.; Jose, A.; Kai, C.; Gavin, R. B.; Neil, R. W., van der Waals Epitaxy of Monolayer Hexagonal Boron Nitride on Copper Foil: Growth, Crystallography and Electronic Band Structure. *2D Mater.* **2015,** *2* (2), 025003.

(138) Li, J.; Li, Y.; Yin, J.; Ren, X.; Liu, X.; Jin, C.; Guo, W., Growth of Polar Hexagonal Boron Nitride Monolayer on Nonpolar Copper with Unique Orientation. *Small* **2016,** *12* (27), 3645-3650.

(139) Dumcenco, D.; Ovchinnikov, D.; Marinov, K.; Lazić, P.; Gibertini, M.; Marzari, N.; Sanchez, O. L.; Kung, Y.-C.; Krasnozhon, D.; Chen, M.-W.; Bertolazzi, S.; Gillet, P.; Fontcuberta i Morral, A.; Radenovic, A.; Kis, A., Large-Area Epitaxial Monolayer MoS2. *ACS Nano* **2015,** *9* (4), 4611-4620.

(140) Aljarb, A.; Cao, Z.; Tang, H.-L.; Huang, J.-K.; Li, M.; Hu, W.; Cavallo, L.; Li, L.-J., Substrate Lattice-Guided Seed Formation Controls the Orientation of 2D Transition-Metal Dichalcogenides. *ACS Nano* **2017,** *11* (9), 9215-9222.

(141) Ji, H. G.; Lin, Y.-C.; Nagashio, K.; Maruyama, M.; Solís-Fernández, P.; Sukma Aji, A.; Panchal, V.; Okada, S.; Suenaga, K.; Ago, H., Hydrogen-Assisted Epitaxial Growth

of Monolayer Tungsten Disulfide and Seamless Grain Stitching. *Chem. Mater.* **2018,** *30* (2), 403-411.

(142) Pham, V. P.; Yeom, G. Y., Recent Advances in Doping of Molybdenum Disulfide: Industrial Applications and Future Prospects. *Adv. Mater.* **2016,** *28* (41), 9024-9059.

(143) Cheng, Y. C.; Zhu, Z. Y.; Mi, W. B.; Guo, Z. B.; Schwingenschlögl, U., Prediction of Two-Dimensional Diluted Magnetic Semiconductors: Doped Monolayer MoS_2 Systems. *Phys. Rev. B* **2013,** *87* (10), 100401.

(144) Zhang, K.; Feng, S.; Wang, J.; Azcatl, A.; Lu, N.; Addou, R.; Wang, N.; Zhou, C.; Lerach, J.; Bojan, V.; Kim, M. J.; Chen, L.-Q.; Wallace, R. M.; Terrones, M.; Zhu, J.; Robinson, J. A., Manganese Doping of Monolayer MoS_2: The Substrate Is Critical. *Nano Lett.* **2015,** *15* (10), 6586-6591.

(145) Li, B.; Xing, T.; Zhong, M.; Huang, L.; Lei, N.; Zhang, J.; Li, J.; Wei, Z., A Two-Dimensional Fe-Doped SnS_2 Magnetic Semiconductor. *Nat. Commun.* **2017,** *8* (1), 1958.

(146) Suh, J.; Park, T.-E.; Lin, D.-Y.; Fu, D.; Park, J.; Jung, H. J.; Chen, Y.; Ko, C.; Jang, C.; Sun, Y.; Sinclair, R.; Chang, J.; Tongay, S.; Wu, J., Doping against the Native Propensity of MoS_2: Degenerate Hole Doping by Cation Substitution. *Nano Lett.* **2014,** *14* (12), 6976-6982.

(147) Zhang, K.; Bersch, B. M.; Joshi, J.; Addou, R.; Cormier, C. R.; Zhang, C.; Xu, K.; Briggs, N. C.; Wang, K.; Subramanian, S.; Cho, K.; Fullerton-Shirey, S.; Wallace, R. M.; Vora, P. M.; Robinson, J. A., Tuning the Electronic and Photonic Properties of Monolayer MoS_2 via In Situ Rhenium Substitutional Doping. *Adv. Funct. Mater.* **2018,** *28* (16), 1706950.

(148) Chen, Y.; Xi, J.; Dumcenco, D. O.; Liu, Z.; Suenaga, K.; Wang, D.; Shuai, Z.; Huang, Y.-S.; Xie, L., Tunable Band Gap Photoluminescence from Atomically Thin Transition-Metal Dichalcogenide Alloys. *ACS Nano* **2013,** *7* (5), 4610-4616.

(149) Liu, X.; Wu, J.; Yu, W.; Chen, L.; Huang, Z.; Jiang, H.; He, J.; Liu, Q.; Lu, Y.; Zhu, D.; Liu, W.; Cao, P.; Han, S.; Xiong, X.; Xu, W.; Ao, J.-P.; Ang, K.-W.; He, Z., Monolayer $W_xMo_{1-x}S_2$ Grown by Atmospheric Pressure Chemical Vapor Deposition: Bandgap Engineering and Field Effect Transistors. *Adv. Funct. Mater.* **2017,** *27* (13), 1606469.

(150) Zhang, M.; Wu, J.; Zhu, Y.; Dumcenco, D. O.; Hong, J.; Mao, N.; Deng, S.; Chen, Y.; Yang, Y.; Jin, C.; Chaki, S. H.; Huang, Y.-S.; Zhang, J.; Xie, L., Two-Dimensional

Molybdenum Tungsten Diselenide Alloys: Photoluminescence, Raman Scattering, and Electrical Transport. *ACS Nano* **2014,** *8* (7), 7130-7137.

(151) Li, H.; Duan, X.; Wu, X.; Zhuang, X.; Zhou, H.; Zhang, Q.; Zhu, X.; Hu, W.; Ren, P.; Guo, P.; Ma, L.; Fan, X.; Wang, X.; Xu, J.; Pan, A.; Duan, X., Growth of Alloy $MoS_{2x}Se_{2(1-x)}$ Nanosheets with Fully Tunable Chemical Compositions and Optical Properties. *J. Am. Chem. Soc.* **2014,** *136* (10), 3756-3759.

(152) Li, H.; Zhang, Q.; Duan, X.; Wu, X.; Fan, X.; Zhu, X.; Zhuang, X.; Hu, W.; Zhou, H.; Pan, A.; Duan, X., Lateral Growth of Composition Graded Atomic Layer $MoS_{2(1-x)}Se_{2x}$ Nanosheets. *J. Am. Chem. Soc.* **2015,** *137* (16), 5284-5287.

(153) Duan, X.; Wang, C.; Fan, Z.; Hao, G.; Kou, L.; Halim, U.; Li, H.; Wu, X.; Wang, Y.; Jiang, J.; Pan, A.; Huang, Y.; Yu, R.; Duan, X., Synthesis of $WS_{2x}Se_{2-2x}$ Alloy Nanosheets with Composition-Tunable Electronic Properties. *Nano Lett.* **2016,** *16* (1), 264-269.

(154) Wu, X.; Li, H.; Liu, H.; Zhuang, X.; Wang, X.; Fan, X.; Duan, X.; Zhu, X.; Zhang, Q.; Meixner, A. J.; Duan, X.; Pan, A., Spatially Composition-Modulated Two-Dimensional $WS_{2x}Se_{2(1-x)}$ Nanosheets. *Nanoscale* **2017,** *9* (14), 4707-4712.

(155) Wang, Y.; Le, H.; Li, B.; Shang, J.; Xia, C.; Fan, C.; Deng, H.-X.; Wei, Z.; Li, J., Composition-Tunable 2D $SnSe_{2(1-x)}S_{2x}$ Alloys towards Efficient Bandgap Engineering and High Performance (Opto)Electronics. *J. Mater. Chem. C* **2017,** *5* (1), 84-90.

(156) Cui, F.; Feng, Q.; Hong, J.; Wang, R.; Bai, Y.; Li, X.; Liu, D.; Zhou, Y.; Liang, X.; He, X.; Zhang, Z.; Liu, S.; Lei, Z.; Liu, Z.; Zhai, T.; Xu, H., Synthesis of Large-Size 1T′ $ReS_{2x}Se_{2(1-x)}$ Alloy Monolayer with Tunable Bandgap and Carrier Type. *Adv. Mater.* **2017,** *29* (46), 1705015.

(157) Wang, Z.; Liu, P.; Ito, Y.; Ning, S.; Tan, Y.; Fujita, T.; Hirata, A.; Chen, M., Chemical Vapor Deposition of Monolayer $Mo_{1-x}W_xS_2$ Crystals with Tunable Band Gaps. *Sci. Rep.* **2016,** *6*, 21536.

(158) Yang, S.-Z.; Gong, Y.; Manchanda, P.; Zhang, Y.-Y.; Ye, G.; Chen, S.; Song, L.; Pantelides, S. T.; Ajayan, P. M.; Chisholm, M. F.; Zhou, W., Rhenium-Doped and Stabilized MoS_2 Atomic Layers with Basal-Plane Catalytic Activity. *Adv. Mater.* **2018,** *30* (51), 1803477.

(159) Rhodes, D.; Chenet, D. A.; Janicek, B. E.; Nyby, C.; Lin, Y.; Jin, W.; Edelberg, D.; Mannebach, E.; Finney, N.; Antony, A.; Schiros, T.; Klarr, T.; Mazzoni, A.; Chin, M.; Chiu, Y. c.; Zheng, W.; Zhang, Q. R.; Ernst, F.; Dadap, J. I.; Tong, X.; Ma, J.; Lou, R.;

Wang, S.; Qian, T.; Ding, H.; Osgood, R. M.; Paley, D. W.; Lindenberg, A. M.; Huang, P. Y.; Pasupathy, A. N.; Dubey, M.; Hone, J.; Balicas, L., Engineering the Structural and Electronic Phases of $MoTe_2$ through W Substitution. *Nano Lett.* **2017,** *17* (3), 1616-1622.

(160) Choi, M. S.; Qu, D.; Lee, D.; Liu, X.; Watanabe, K.; Taniguchi, T.; Yoo, W. J., Lateral MoS_2 p–n Junction Formed by Chemical Doping for Use in High-Performance Optoelectronics. *ACS Nano* **2014,** *8* (9), 9332-9340.

(161) Gong, Y.; Yuan, H.; Wu, C.-L.; Tang, P.; Yang, S.-Z.; Yang, A.; Li, G.; Liu, B.; van de Groep, J.; Brongersma, M. L.; Chisholm, M. F.; Zhang, S.-C.; Zhou, W.; Cui, Y., Spatially Controlled Doping of Two-Dimensional SnS_2 through Intercalation for Electronics. *Nat. Nanotechnol.* **2018,** *13*, 294-299.

(162) Luo, P.; Zhuge, F.; Zhang, Q.; Chen, Y.; Lv, L.; Huang, Y.; Li, H.; Zhai, T., Doping Engineering and Functionalization of Two-Dimensional Metal Chalcogenides. *Nanoscale Horizons* **2019,** *4* (1), 26-51.

(163) Mouri, S.; Miyauchi, Y.; Matsuda, K., Tunable Photoluminescence of Monolayer MoS_2 via Chemical Doping. *Nano Lett.* **2013,** *13* (12), 5944-5948.

(164) Chen, C.-H.; Wu, C.-L.; Pu, J.; Chiu, M.-H.; Kumar, P.; Takenobu, T.; Li, L.-J., Hole Mobility Enhancement and p-Doping in Monolayer WSe_2 by Gold Decoration. *2D Mater.* **2014,** *1* (3), 034001.

(165) Kiriya, D.; Tosun, M.; Zhao, P.; Kang, J. S.; Javey, A., Air-Stable Surface Charge Transfer Doping of MoS_2 by Benzyl Viologen. *J. Am. Chem. Soc.* **2014,** *136* (22), 7853-7856.

(166) Lockhart de la Rosa, C. J.; Nourbakhsh, A.; Heyne, M.; Asselberghs, I.; Huyghebaert, C.; Radu, I.; Heyns, M.; De Gendt, S., Highly Efficient and Stable MoS_2 FETs with Reversible n-Doping Using a Dehydrated Poly(vinyl-alcohol) Coating. *Nanoscale* **2017,** *9* (1), 258-265.

(167) Gong, Y.; Liu, Z.; Lupini, A. R.; Shi, G.; Lin, J.; Najmaei, S.; Lin, Z.; Elías, A. L.; Berkdemir, A.; You, G.; Terrones, H.; Terrones, M.; Vajtai, R.; Pantelides, S. T.; Pennycook, S. J.; Lou, J.; Zhou, W.; Ajayan, P. M., Band Gap Engineering and Layer-by-Layer Mapping of Selenium-Doped Molybdenum Disulfide. *Nano Lett.* **2014,** *14* (2), 442-449.

(168) Gao, J.; Kim, Y. D.; Liang, L.; Idrobo, J. C.; Chow, P.; Tan, J.; Li, B.; Li, L.; Sumpter, B. G.; Lu, T.-M.; Meunier, V.; Hone, J.; Koratkar, N., Transition-Metal Substitution

Doping in Synthetic Atomically Thin Semiconductors. *Adv. Mater.* **2016,** *28* (44), 9735-9743.

(169) Susarla, S.; Kochat, V.; Kutana, A.; Hachtel, J. A.; Idrobo, J. C.; Vajtai, R.; Yakobson, B. I.; Tiwary, C. S.; Ajayan, P. M., Phase Segregation Behavior of Two-Dimensional Transition Metal Dichalcogenide Binary Alloys Induced by Dissimilar Substitution. *Chem. Mater.* **2017,** *29* (17), 7431-7439.

(170) Li, H.; Wu, X.; Liu, H.; Zheng, B.; Zhang, Q.; Zhu, X.; Wei, Z.; Zhuang, X.; Zhou, H.; Tang, W.; Duan, X.; Pan, A., Composition-Modulated Two-Dimensional Semiconductor Lateral Heterostructures via Layer-Selected Atomic Substitution. *ACS Nano* **2017,** *11* (1), 961-967.

(171) Zhang, J.; Jia, S.; Kholmanov, I.; Dong, L.; Er, D.; Chen, W.; Guo, H.; Jin, Z.; Shenoy, V. B.; Shi, L.; Lou, J., Janus Monolayer Transition-Metal Dichalcogenides. *ACS Nano* **2017,** *11* (8), 8192-8198.

(172) Lu, A.-Y.; Zhu, H.; Xiao, J.; Chuu, C.-P.; Han, Y.; Chiu, M.-H.; Cheng, C.-C.; Yang, C.-W.; Wei, K.-H.; Yang, Y.; Wang, Y.; Sokaras, D.; Nordlund, D.; Yang, P.; Muller, D. A.; Chou, M.-Y.; Zhang, X.; Li, L.-J., Janus Monolayers of Transition Metal Dichalcogenides. *Nat. Nanotechnol.* **2017,** *12*, 744.

(173) Liu, Y.; Stradins, P.; Wei, S.-H., Van der Waals Metal-Semiconductor Junction: Weak Fermi Level Pinning Enables Effective Tuning of Schottky Barrier. *Sci. Adv.* **2016,** *2* (4), e1600069.

(174) Pant, A.; Mutlu, Z.; Wickramaratne, D.; Cai, H.; Lake, R. K.; Ozkan, C.; Tongay, S., Fundamentals of Lateral and Vertical Heterojunctions of Atomically Thin Materials. *Nanoscale* **2016,** *8* (7), 3870-3887.

(175) Özçelik, V. O.; Azadani, J. G.; Yang, C.; Koester, S. J.; Low, T., Band Alignment of Two-Dimensional Semiconductors for Designing Heterostructures with Momentum Space Matching. *Phys. Rev. B* **2016,** *94* (3), 035125.

(176) Zhao, R.; Wang, J.; Yang, M.; Liu, Z.; Liu, Z., BN-Embedded Graphene with a Ubiquitous Gap Opening. *J. Phys. Chem. C* **2012,** *116* (39), 21098-21103.

(177) Han, G. H.; Rodríguez-Manzo, J. A.; Lee, C.-W.; Kybert, N. J.; Lerner, M. B.; Qi, Z. J.; Dattoli, E. N.; Rappe, A. M.; Drndic, M.; Johnson, A. T. C., Continuous Growth of Hexagonal Graphene and Boron Nitride In-Plane Heterostructures by Atmospheric Pressure Chemical Vapor Deposition. *ACS Nano* **2013,** *7* (11), 10129-10138.

(178) Liu, L.; Park, J.; Siegel, D. A.; McCarty, K. F.; Clark, K. W.; Deng, W.; Basile, L.; Idrobo, J. C.; Li, A.-P.; Gu, G., Heteroepitaxial Growth of Two-Dimensional

Hexagonal Boron Nitride Templated by Graphene Edges. *Science* **2014,** *343* (6167), 163-167.

(179) Sutter, P.; Huang, Y.; Sutter, E., Nanoscale Integration of Two-Dimensional Materials by Lateral Heteroepitaxy. *Nano Lett.* **2014,** *14* (8), 4846-4851.

(180) Gong, Y.; Lin, J.; Wang, X.; Shi, G.; Lei, S.; Lin, Z.; Zou, X.; Ye, G.; Vajtai, R.; Yakobson, B. I.; Terrones, H.; Terrones, M.; Tay, Beng K.; Lou, J.; Pantelides, S. T.; Liu, Z.; Zhou, W.; Ajayan, P. M., Vertical and In-Plane Heterostructures from WS_2/MoS_2 Monolayers. *Nat. Mater.* **2014,** *13*, 1135.

(181) Yoo, Y.; Degregorio, Z. P.; Johns, J. E., Seed Crystal Homogeneity Controls Lateral and Vertical Heteroepitaxy of Monolayer MoS_2 and WS_2. *J. Am. Chem. Soc.* **2015,** *137* (45), 14281-14287.

(182) Chen, K.; Wan, X.; Wen, J.; Xie, W.; Kang, Z.; Zeng, X.; Chen, H.; Xu, J.-B., Electronic Properties of MoS_2–WS_2 Heterostructures Synthesized with Two-Step Lateral Epitaxial Strategy. *ACS Nano* **2015,** *9* (10), 9868-9876.

(183) Heo, H.; Sung, J. H.; Jin, G.; Ahn, J.-H.; Kim, K.; Lee, M.-J.; Cha, S.; Choi, H.; Jo, M.-H., Rotation-Misfit-Free Heteroepitaxial Stacking and Stitching Growth of Hexagonal Transition-Metal Dichalcogenide Monolayers by Nucleation Kinetics Controls. *Adv. Mater.* **2015,** *27* (25), 3803-3810.

(184) Huang, C.; Wu, S.; Sanchez, A. M.; Peters, J. J. P.; Beanland, R.; Ross, J. S.; Rivera, P.; Yao, W.; Cobden, D. H.; Xu, X., Lateral Heterojunctions within Monolayer $MoSe_2$–WSe_2 Semiconductors. *Nat. Mater.* **2014,** *13*, 1096.

(185) Gong, Y.; Lei, S.; Ye, G.; Li, B.; He, Y.; Keyshar, K.; Zhang, X.; Wang, Q.; Lou, J.; Liu, Z.; Vajtai, R.; Zhou, W.; Ajayan, P. M., Two-Step Growth of Two-Dimensional WSe_2/$MoSe_2$ Heterostructures. *Nano Lett.* **2015,** *15* (9), 6135-6141.

(186) Zhang, X.-Q.; Lin, C.-H.; Tseng, Y.-W.; Huang, K.-H.; Lee, Y.-H., Synthesis of Lateral Heterostructures of Semiconducting Atomic Layers. *Nano Lett.* **2015,** *15* (1), 410-415.

(187) Duan, X.; Wang, C.; Shaw, J. C.; Cheng, R.; Chen, Y.; Li, H.; Wu, X.; Tang, Y.; Zhang, Q.; Pan, A.; Jiang, J.; Yu, R.; Huang, Y.; Duan, X., Lateral Epitaxial Growth of Two-Dimensional Layered Semiconductor Heterojunctions. *Nat. Nanotechnol.* **2014,** *9*, 1024.

(188) Li, M.-Y.; Shi, Y.; Cheng, C.-C.; Lu, L.-S.; Lin, Y.-C.; Tang, H.-L.; Tsai, M.-L.; Chu, C.-W.; Wei, K.-H.; He, J.-H.; Chang, W.-H.; Suenaga, K.; Li, L.-J., Epitaxial Growth of a Monolayer WSe_2-MoS_2 Lateral p-n Junction with an Atomically Sharp Interface. *Science* **2015,** *349* (6247), 524-528.

(189) Li, M.-Y.; Pu, J.; Huang, J.-K.; Miyauchi, Y.; Matsuda, K.; Takenobu, T.; Li, L.-J., Self-Aligned and Scalable Growth of Monolayer WSe_2–MoS_2 Lateral Heterojunctions. *Adv. Funct. Mater.* **2018,** *28* (17), 1706860.

(190) Zhang, Z.; Chen, P.; Duan, X.; Zang, K.; Luo, J.; Duan, X., Robust Epitaxial Growth of Two-Dimensional Heterostructures, Multiheterostructures, and Superlattices. *Science* **2017,** *357* (6353), 788-792.

(191) Sahoo, P. K.; Memaran, S.; Xin, Y.; Balicas, L.; Gutiérrez, H. R., One-Pot Growth of Two-Dimensional Lateral Heterostructures via Sequential Edge-Epitaxy. *Nature* **2018,** *553*, 63-67.

(192) Yankowitz, M.; Xue, J.; Cormode, D.; Sanchez-Yamagishi, J. D.; Watanabe, K.; Taniguchi, T.; Jarillo-Herrero, P.; Jacquod, P.; LeRoy, B. J., Emergence of Superlattice Dirac Points in Graphene on Hexagonal Boron Nitride. *Nat. Phys.* **2012,** *8* (5), 382-386.

(193) Dean, C. R.; Wang, L.; Maher, P.; Forsythe, C.; Ghahari, F.; Gao, Y.; Katoch, J.; Ishigami, M.; Moon, P.; Koshino, M.; Taniguchi, T.; Watanabe, K.; Shepard, K. L.; Hone, J.; Kim, P., Hofstadter's Butterfly and the Fractal Quantum Hall Effect in Moiré Superlattices. *Nature* **2013,** *497* (7451), 598-602.

(194) Hunt, B.; Sanchez-Yamagishi, J. D.; Young, A. F.; Yankowitz, M.; LeRoy, B. J.; Watanabe, K.; Taniguchi, T.; Moon, P.; Koshino, M.; Jarillo-Herrero, P.; Ashoori, R. C., Massive Dirac Fermions and Hofstadter Butterfly in a van der Waals Heterostructure. *Science* **2013,** *340* (6139), 1427-1430.

(195) Ponomarenko, L. A.; Gorbachev, R. V.; Yu, G. L.; Elias, D. C.; Jalil, R.; Patel, A. A.; Mishchenko, A.; Mayorov, A. S.; Woods, C. R.; Wallbank, J. R.; Mucha-Kruczynski, M.; Piot, B. A.; Potemski, M.; Grigorieva, I. V.; Novoselov, K. S.; Guinea, F.; Fal'ko, V. I.; Geim, A. K., Cloning of Dirac Fermions in Graphene Superlattices. *Nature* **2013,** *497* (7451), 594-597.

(196) Decker, R.; Wang, Y.; Brar, V. W.; Regan, W.; Tsai, H.-Z.; Wu, Q.; Gannett, W.; Zettl, A.; Crommie, M. F., Local Electronic Properties of Graphene on a BN Substrate via Scanning Tunneling Microscopy. *Nano Lett.* **2011,** *11* (6), 2291-2295.

(197) Dean, C. R.; Young, A. F.; MericI; LeeC; WangL; SorgenfreiS; WatanabeK; TaniguchiT; KimP; Shepard, K. L.; HoneJ, Boron Nitride Substrates for High-Quality Graphene Electronics. *Nat. Nanotechnol.* **2010,** *5* (10), 722-726.

(198) Ponomarenko, L. A.; Geim, A. K.; Zhukov, A. A.; Jalil, R.; Morozov, S. V.; Novoselov, K. S.; Grigorieva, I. V.; Hill, E. H.; Cheianov, V. V.; Fal'ko, V. I.; Watanabe, K.;

Taniguchi, T.; Gorbachev, R. V., Tunable Metal-Insulator Transition in Double-Layer Graphene Heterostructures. *Nat. Phys.* **2011,** *7* (12), 958-961.

(199) Chen, J.-H.; Jang, C.; Xiao, S.; Ishigami, M.; Fuhrer, M. S., Intrinsic and Extrinsic Performance Limits of Graphene Devices on SiO_2. *Nat. Nanotechnol.* **2008,** *3* (4), 206-209.

(200) Gannett, W.; Regan, W.; Watanabe, K.; Taniguchi, T.; Crommie, M. F.; Zettl, A., Boron Nitride Substrates for High Mobility Chemical Vapor Deposited Graphene. *Appl. Phys. Lett.* **2011,** *98* (24), 242105.

(201) Britnell, L.; Gorbachev, R. V.; Jalil, R.; Belle, B. D.; Schedin, F.; Mishchenko, A.; Georgiou, T.; Katsnelson, M. I.; Eaves, L.; Morozov, S. V.; Peres, N. M. R.; Leist, J.; Geim, A. K.; Novoselov, K. S.; Ponomarenko, L. A., Field-Effect Tunneling Transistor Based on Vertical Graphene Heterostructures. *Science* **2012,** *335* (6071), 947-950.

(202) Haigh, S. J.; Gholinia, A.; Jalil, R.; Romani, S.; Britnell, L.; Elias, D. C.; Novoselov, K. S.; Ponomarenko, L. A.; Geim, A. K.; Gorbachev, R., Cross-Sectional Imaging of Individual Layers and Buried Interfaces of Graphene-Based Heterostructures and Superlattices. *Nat. Mater.* **2012,** *11* (9), 764-767.

(203) Lee, K. H.; Shin, H.-J.; Lee, J.; Lee, I.-y.; Kim, G.-H.; Choi, J.-Y.; Kim, S.-W., Large-Scale Synthesis of High-Quality Hexagonal Boron Nitride Nanosheets for Large-Area Graphene Electronics. *Nano Lett.* **2012,** *12* (2), 714-718.

(204) Gao, T.; Song, X.; Du, H.; Nie, Y.; Chen, Y.; Ji, Q.; Sun, J.; Yang, Y.; Zhang, Y.; Liu, Z., Temperature-Triggered Chemical Switching Growth of In-Plane and Vertically Stacked Graphene-Boron Nitride Heterostructures. *Nat. Commun.* **2015,** *6*, 6835.

(205) Song, X.; Gao, T.; Nie, Y.; Zhuang, J.; Sun, J.; Ma, D.; Shi, J.; Lin, Y.; Ding, F.; Zhang, Y.; Liu, Z., Seed-Assisted Growth of Single-Crystalline Patterned Graphene Domains on Hexagonal Boron Nitride by Chemical Vapor Deposition. *Nano Lett.* **2016,** *16* (10), 6109-6116.

(206) Okada, M.; Sawazaki, T.; Watanabe, K.; Taniguch, T.; Hibino, H.; Shinohara, H.; Kitaura, R., Direct Chemical Vapor Deposition Growth of WS_2 Atomic Layers on Hexagonal Boron Nitride. *ACS Nano* **2014,** *8* (8), 8273-8277.

(207) Zhang, X.; Zhang, F.; Wang, Y.; Schulman, D. S.; Zhang, T.; Bansal, A.; Alem, N.; Das, S.; Crespi, V. H.; Terrones, M.; Redwing, J. M., Defect-Controlled Nucleation and Orientation of WSe_2 on hBN: A Route to Single-Crystal Epitaxial Monolayers. *ACS Nano* **2019,** *13* (3), 3341-3352.

(208) Wang, S.; Wang, X.; Warner, J. H., All Chemical Vapor Deposition Growth of MoS_2:h-BN Vertical van der Waals Heterostructures. *ACS Nano* **2015,** *9* (5), 5246-5254.

(209) Fu, L.; Sun, Y.; Wu, N.; Mendes, R. G.; Chen, L.; Xu, Z.; Zhang, T.; Rümmeli, M. H.; Rellinghaus, B.; Pohl, D.; Zhuang, L.; Fu, L., Direct Growth of MoS_2/h-BN Heterostructures via a Sulfide-Resistant Alloy. *ACS Nano* **2016,** *10* (2), 2063-2070.

(210) Zhang, Z.; Ji, X.; Shi, J.; Zhou, X.; Zhang, S.; Hou, Y.; Qi, Y.; Fang, Q.; Ji, Q.; Zhang, Y.; Hong, M.; Yang, P.; Liu, X.; Zhang, Q.; Liao, L.; Jin, C.; Liu, Z.; Zhang, Y., Direct Chemical Vapor Deposition Growth and Band-Gap Characterization of MoS_2/h-BN van der Waals Heterostructures on Au Foils. *ACS Nano* **2017,** *11* (4), 4328-4336.

(211) Schaibley, J. R.; Rivera, P.; Yu, H.; Seyler, K. L.; Yan, J.; Mandrus, D. G.; Taniguchi, T.; Watanabe, K.; Yao, W.; Xu, X., Directional Interlayer Spin-Valley Transfer in Two-Dimensional Heterostructures. *Nat. Commun.* **2016,** *7*, 13747.

(212) Yan, W.; Wu-Xing, Z.; Le, H.; Congxin, X.; Li-Ming, T.; Hui-Xiong, D.; Yongtao, L.; Ke-Qiu, C.; Jingbo, L.; Zhongming, W., Light Induced Double 'on' State Anti-Ambipolar Behavior and Self-Driven Photoswitching in p-WSe_2/n-SnS_2 Heterostructures. *2D Mater.* **2017,** *4* (2), 025097.

(213) Murali, K.; Dandu, M.; Das, S.; Majumdar, K., Gate-Tunable WSe_2/$SnSe_2$ Backward Diode with Ultrahigh-Reverse Rectification Ratio. *ACS Appl. Mater. Interfaces* **2018,** *10* (6), 5657-5664.

(214) Tongay, S.; Fan, W.; Kang, J.; Park, J.; Koldemir, U.; Suh, J.; Narang, D. S.; Liu, K.; Ji, J.; Li, J.; Sinclair, R.; Wu, J., Tuning Interlayer Coupling in Large-Area Heterostructures with CVD-Grown MoS_2 and WS_2 Monolayers. *Nano Lett.* **2014,** *14* (6), 3185-3190.

(215) Hong, X.; Kim, J.; Shi, S.-F.; Zhang, Y.; Jin, C.; Sun, Y.; Tongay, S.; Wu, J.; Zhang, Y.; Wang, F., Ultrafast Charge Transfer in Atomically Thin MoS_2/WS_2 Heterostructures. *Nat. Nanotechnol.* **2014,** *9*, 682.

(216) Yang, S.; Wu, M.; Wang, B.; Zhao, L.-D.; Huang, L.; Jiang, C.; Wei, S.-H., Enhanced Electrical and Optoelectronic Characteristics of Few-Layer Type-II SnSe/MoS_2 van der Waals Heterojunctions. *ACS Appl. Mater. Interfaces* **2017,** *9* (48), 42149-42155.

(217) Roy, T.; Tosun, M.; Hettick, M.; Ahn, G. H.; Hu, C.; Javey, A., 2D-2D Tunneling Field-Effect Transistors Using WSe_2/$SnSe_2$ Heterostructures. *Appl. Phys. Lett.* **2016,** *108* (8), 083111.

(218) Yan, X.; Liu, C.; Li, C.; Bao, W.; Ding, S.; Zhang, D. W.; Zhou, P., Tunable $SnSe_2/WSe_2$ Heterostructure Tunneling Field Effect Transistor. *Small* **2017,** *13* (34), 1701478.

(219) Zhou, X.; Hu, X.; Zhou, S.; Song, H.; Zhang, Q.; Pi, L.; Li, L.; Li, H.; Lü, J.; Zhai, T., Tunneling Diode Based on WSe_2/SnS_2 Heterostructure Incorporating High Detectivity and Responsivity. *Adv. Mater.* **2018,** *30* (7), 1703286.

(220) Tan, H.; Xu, W.; Sheng, Y.; Lau, C. S.; Fan, Y.; Chen, Q.; Tweedie, M.; Wang, X.; Zhou, Y.; Warner, J. H., Lateral Graphene-Contacted Vertically Stacked WS_2/MoS_2 Hybrid Photodetectors with Large Gain. *Adv. Mater.* **2017,** *29* (46), 1702917.

(221) Cheng, R.; Li, D.; Zhou, H.; Wang, C.; Yin, A.; Jiang, S.; Liu, Y.; Chen, Y.; Huang, Y.; Duan, X., Electroluminescence and Photocurrent Generation from Atomically Sharp WSe_2/MoS_2 Heterojunction p–n Diodes. *Nano Lett.* **2014,** *14* (10), 5590-5597.

(222) Furchi, M. M.; Pospischil, A.; Libisch, F.; Burgdörfer, J.; Mueller, T., Photovoltaic Effect in an Electrically Tunable van der Waals Heterojunction. *Nano Lett.* **2014,** *14* (8), 4785-4791.

(223) Luo, Y. K.; Xu, J.; Zhu, T.; Wu, G.; McCormick, E. J.; Zhan, W.; Neupane, M. R.; Kawakami, R. K., Opto-Valleytronic Spin Injection in Monolayer MoS_2/Few-Layer Graphene Hybrid Spin Valves. *Nano Lett.* **2017,** *17* (6), 3877-3883.

(224) Yang, T.; Zheng, B.; Wang, Z.; Xu, T.; Pan, C.; Zou, J.; Zhang, X.; Qi, Z.; Liu, H.; Feng, Y.; Hu, W.; Miao, F.; Sun, L.; Duan, X.; Pan, A., Van der Waals Epitaxial Growth and Optoelectronics of Large-Scale WSe_2/SnS_2 Vertical Bilayer p–n Junctions. *Nat. Commun.* **2017,** *8* (1), 1906.

(225) Zhou, X.; Zhou, N.; Li, C.; Song, H.; Zhang, Q.; Hu, X.; Gan, L.; Li, H.; Lü, J.; Luo, J.; Xiong, J.; Zhai, T., Vertical Heterostructures Based on $SnSe_2/MoS_2$ for High Performance Photodetectors. *2D Mater.* **2017,** *4* (2), 025048.

(226) Li, B.; Huang, L.; Zhong, M.; Li, Y.; Wang, Y.; Li, J.; Wei, Z., Direct Vapor Phase Growth and Optoelectronic Application of Large Band Offset SnS_2/MoS_2 Vertical Bilayer Heterostructures with High Lattice Mismatch. *Adv. Electron. Mater.* **2016,** *2*, 1600298.

Chapter 3

Methodology

3.1 Introduction

This chapter introduces the basic principles and operation details for experimental synthesis of the 2D materials and major characterisation techniques. This is based on the understanding of previous work from other group members combined with personal practical experience. All the fabrication processes including growing individual 2D materials such as hBN and SnS_2, post-growth treatment such as doping of 2D WS_2 layers, transfer of 2D materials, as well as the device manufacturing procedures will be covered. A series of characterisation techniques such as microscopy and spectroscopy characterisation techniques will also be included. With the provided details, it is expected that all the experiments and analysis performed in this thesis can be reproducible.

3.2 Chemical Vapour Deposition Synthesis of 2D Materials

3.2.1 Synthesis of Hexagonal Boron Nitride (hBN)

Figure 3.1(a) shows the chemical vapour deposition (CVD) system for the synthesis of hBN, containing the quartz tube reactor (**Figure 3.1**(b)) installed in a tube furnace (Carbolite model HST 12/400), a small heating chamber for providing the hBN gaseous precursors (**Figure 3.1**(c)), and mass flow controllers for controlling the carrier gas flow rate (**Figure 3.1**(d)). A piece of 1 cm by 1 cm Cu substrate (Alfa Aesar, 99.8%) with the thickness of 25 μm

was mechanically polished using commercially available Brasso for least 15 minutes to decrease the surface roughness.

For conventional CVD growth, the polished Cu substrate was immersed in hydrochloric acid at room temperature for 5 min to remove the native surface oxide, followed by acetone and isopropyl alcohol (IPA) cleaning for 5 min in each step. After loading the Cu substrate, the quartz reactor was flushed with 500 sccm Ar gas for 30 min and then raised to 1000°C under 425 sccm Ar and 75 sccm hydrogen mix gas (~25% hydrogen) flow. The Cu substrate was then annealed at 1000°C for 60 min to remove the residual surface organics and enlarge the grain size of Cu foil. By contrast, during the OCVD growth process the Cu foil was firstly oxidised at 180°C for 5 min in the ambient atmosphere prior to hBN growth, leading to the formation of a thin oxide passivating layer on Cu surface. After loading the Cu substrate, the quartz reactor was flushed with 500 sccm Ar gas for 30 min and then raised to 1000°C under 500 sccm Ar flow. Both of the conventional CVD and OCVD growths of hBN were conducted at the atmospheric condition. 8 mg of ammonia borane powder used as a precursor was then heated up in a heating chamber. The hBN growth was carried out with the typical temperatures for the precursor and the substrate being at about 120°C and 1050°C, respectively, under the 120 sccm hydrogen mix gas flow. After growth, the furnace was slid away from the sample to the other end of the runners, which allows the sample to be fast cooled to room temperature.

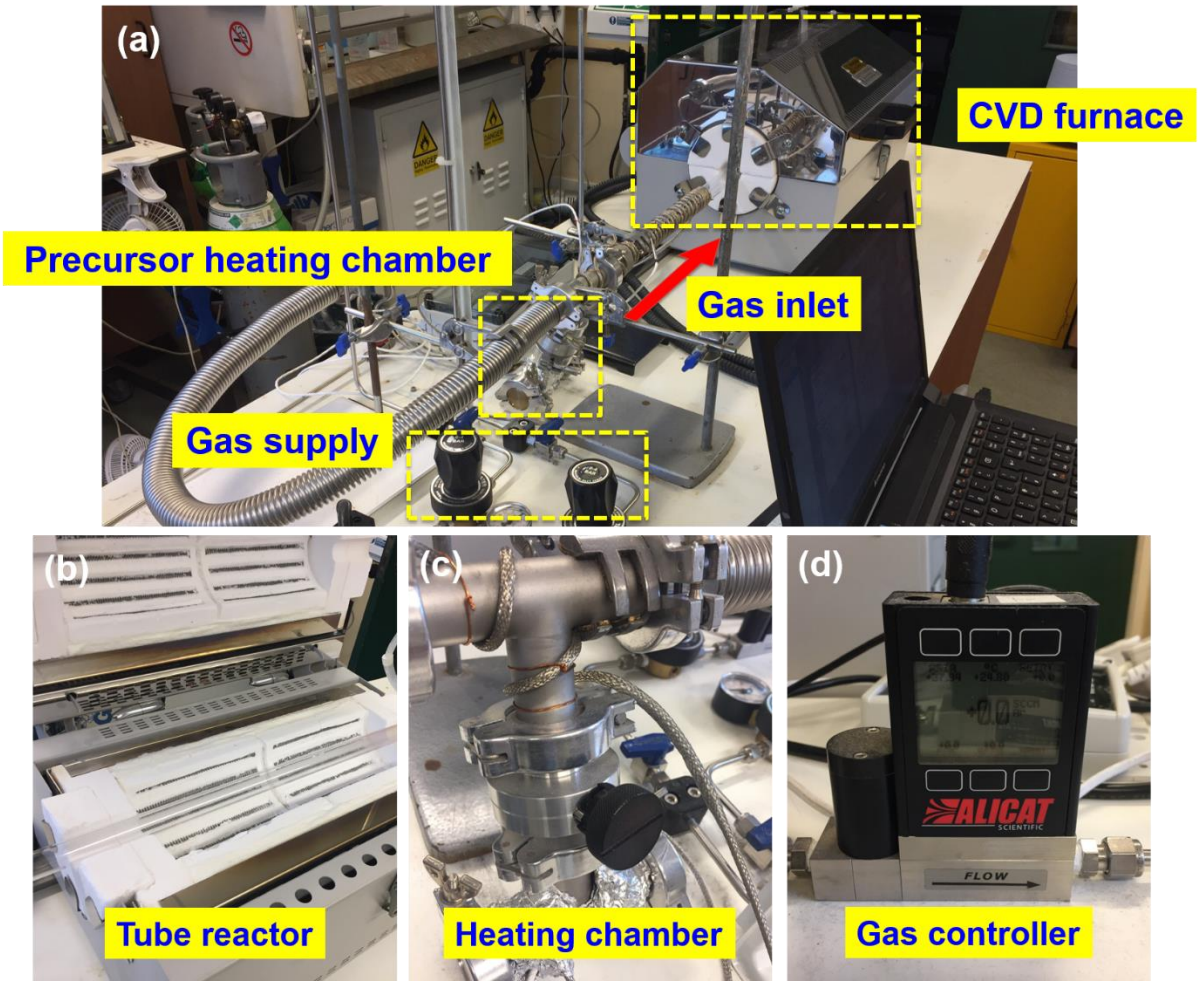


Figure 3.1. CVD experimental setup for the hBN growth. (a) Photograph of the entire CVD system for the hBN growth, including the (b) quartz tube reactor, (c) precursor heating chamber, and (d) mass flow gas controller, respectively.

3.2.2 Synthesis of Tin Disulfide (SnS_2)

A two-furnace CVD system was adopted for the synthesis of SnS_2 to provide a better temperature control, as demonstrated in **Figure 3.2**. 100 mg of sulfur powders was loaded at the centre of furnace 1 in the outer 1 inch quartz tube, while 20 mg of tin sulfide (SnS) was placed at the centre of furnace 2, in an inner tube with smaller diameter of 1 cm. The SiO_2 substrate was then placed downstream in the furnace 2, about 6 cm away from the SnS precursor. The CVD growth of SnS_2 was conducted at the atmospheric condition. After loading

the precursors and growth substrate, the whole system was flushed with 500 sccm Ar gas for 30 min to remove the residual air and then the furnace 1 and 2 were raised to 160°C and 220°C, respectively, under the 100 sccm Ar flow to create a sulfur sufficient atmosphere. After introducing sulfur vapour for 15 min, the temperature of furnace 2 was increased to 550°C and the temperature of furnace 1 was increased to 180°C to conduct the SnS_2 growth. After 15 min growth, the Ar flow rate was first decreased to 10 sccm, enabling the S molecules in the outer tube to diffuse into the inner tube and sulphurising the SnS powder to reduce the supplied amount of SnS gaseous precursor, followed by fast cooling process with 500 sccm Ar gas flow to remove the residual gas precursors and stop the reaction.

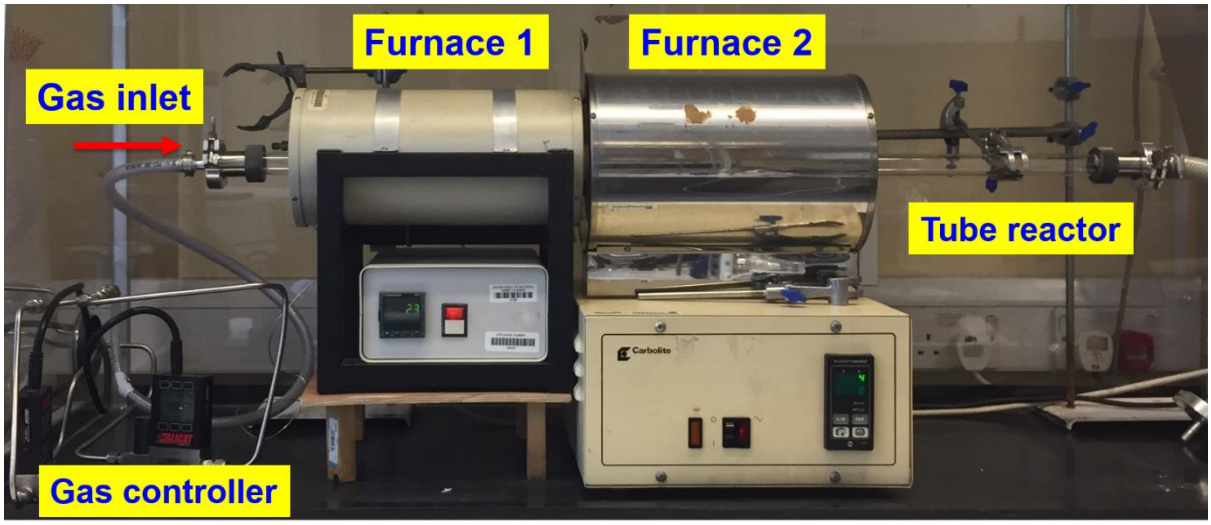


Figure 3.2. Photograph of the CVD experimental setup for the 2D semiconductors growth.

3.2.3 Synthesis of Graphene

Monolayer graphene was grown in the 4 inch CVD system demonstrated in **Figure 3.3** with aid of Dr. Yuewen Sheng. The Cu substrate was the same as that for the hBN growth, with Brasso polishing and cleaned under acid as well as organic solvents before the growth. After loading the Cu substrate into the CVD furnace, the whole system was firstly flushed with 1000 sccm Ar, 500 sccm H_2 and 50 sccm CH_4 for 30 min to remove the residual air. The CVD growth

was performed at atmospheric pressure and started with raising furnace temperature to 1060°C with the ramping rate of 50°C/min under a flow of 500 sccm Ar and 100 sccm H_2, followed by 1 hour annealing under the same condition of carrier gas flow. Graphene growth was then carried out by adjusting the gas flow into 500 sccm Ar, 100 sccm H_2 and 10 sccm CH_4 at 1060°C for 1 hour. After growth, the CH_4 supply was immediately stopped and the CVD furnace was slid away from the sample to the other end of the runners, which allows the sample to be fast cooled to room temperature.

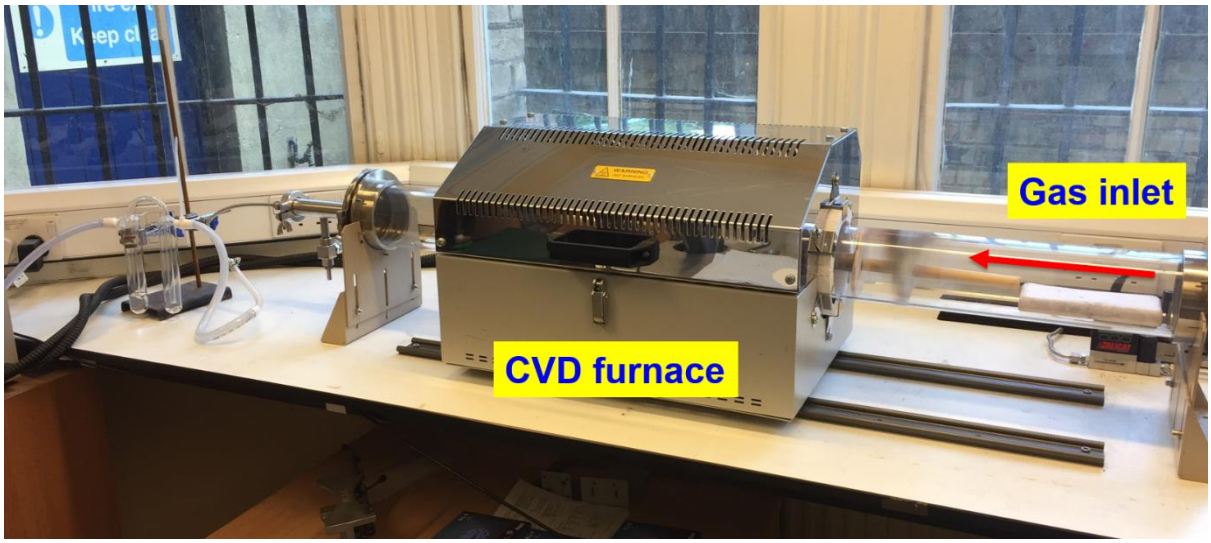


Figure 3.3. Photograph of the CVD experimental setup for the graphene growth.

3.2.4 Synthesis of Tungsten Disulfide (WS_2)

The CVD experimental setup for the WS_2 growth using S and WO_3 as precursors was similar to that of the SnS_2 growth with a two-furnace system. Before growth, the substrate was cleaned in acetone and isopropanol (IPA) for 10 min each, followed by a 5 min oxygen plasma treatment. 200 mg of sulfur powder was loaded at the centre of furnace 1 in the outer 1 in. quartz tube, while 100 mg of WO_3 powder was placed at the centre of furnace 2, in an inner quartz tube with a smaller diameter of 1 cm. The SiO_2 substrate was then placed downstream

in furnace 2, about 8.5 cm away from the WO_3 powder. The growth system was first flushed with 500 sccm Ar for 30 min to drive off the oxygen, followed by a pre-introduction of sulfur by heating the sulfur powder up to 180 °C to create a sulfur-rich environment. After which furnace 2 was ramped to 1050 °C and the reaction was then conducted under the temperature of 1150 °C for 3 min with H_2 gas flow of 25 sccm and Ar gas flow of 225 sccm. After that, furnace 2 was set down to room temperature with an Ar flow of 10 sccm, while furnace 1 was heated up to 400°C. The flow rate was set back to 500 sccm when furnace 2 reached 950 °C to purge the abundant sulfur away from the system. Finally, the growth synthesis ended up with fast cooling process by sliding the furnace and away from the sample when furnace 2 decreased under 850 °C.

3.2.5 Synthesis of Molybdenum Disulfide (MoS_2)

The CVD experimental setup for the MoS_2 growth was similar to that of the SnS_2 growth with a two-furnace system. The growth occurred with the precursors of molybdenum trioxide and sulfur in APCVD using Ar as the carrier gas. 500 mg of S powder was loaded in the outer 1 inch quartz tube at the central area of furnace 1, while 20 mg of MoO_3 was placed in the inner quartz tube at the upstream of furnace 2, being around 12 cm away from its left opening. The substrate was placed vertically in the centre of furnace 2. After the system was flushed for 60 min with argon, sulfur vapour was pre-introduced into the growth region for 15 min by heating furnace 1 to 180°C. Then the temperature of the second furnace was increased to ~800°C and kept for 15 min under 150 sccm Ar flow, and at the same time, the location where MoO_3 powder was placed reached a temperature of around 300°C. Next, the Ar flow rate was reduced to 10 sccm and maintained for 25 min, followed by a fast cooling process.

3.2.6 Thermal Doping of Tin in TMDs

The single-crystalline monolayer TMDs such as WS_2 was firstly synthesised by atmospheric CVD using sulfur and tungsten trioxide as precursors and followed by the second step of Sn thermal doping. During the Sn doping stage, 3 mg of SnS was loaded at the centre of the furnace and the as-grown WS_2 was placed in the downstream of furnace in the 1 inch quartz tube, about 5 cm away from the SnS. The Sn thermal doping of WS_2 was conducted at the atmospheric condition. After loading the precursors and monolayer WS_2, the whole system was flushed with 500 sccm Ar gas for 30 min to remove the residual air. The temperature in the furnace was then raised to 550 °C in 30 min with 100 sccm Ar flow and maintained for some time (5-20 min) to conduct the doping of Sn before cooling down to room temperature.

3.3 Transfer of 2D Materials

3.3.1 2D Materials on Cu Substrates

For the 2D materials grown on Cu substrates such as graphene and hBN, after the CVD growth the sample was firstly coated with a supporting polymer film, polymethylmeth-acrylate (PMMA) at 4500 rpm for 60 seconds on top to protect the as-grown 2D layered sample from mechanical damage. The original copper substrate was then etched in 0.3 M aqueous ammonium persulfate solution. After the copper substrate was removed by etchant solution, the PMMA/2D sample stack was then floated on DI water three times to eliminate the residual ions from etchant solution. The 2D layer sample supported by PMMA was then pasted on to a clean oxidized silicon wafer. After placing the PMMA/2D sample stack on the clean oxidized silicon wafer, the sample was left in the fume hood overnight to slowly evaporate the water trapped between the film and the substrate followed by baked on the hot plate at 180°C for 15

min to enhance the interface contact. Finally, the PMMA supporting layer was removed by placing the sample in acetone for more than 12 hours.

3.3.2 2D Materials on SiO_2 Substrates

For the 2D materials grown on SiO_2 substrates including SnS_2, WS_2, Sn-doped WS_2, MoS_2 in this work, the as-synthesised sample was first spin-coated with PMMA at 4500 rpm for 60 seconds after completion of the synthesis. The substrate was then floated on 1 M aqueous potassium hydroxide solution to etch the SiO_2. After the SiO_2 had been removed by the etchant solution, the PMMA/2D sample stack was then rinsed by transferring on deionized water three times to eliminate the residual ions from the etchant solution. The rinsed stack was subsequently transferred onto the target substrate and dried in air overnight, followed by baking at 180 °C for 30 min to enhance the adhesion at the interface. Finally, the PMMA supporting layer was removed by submerging the sample in acetone for more than 12 hours.

3.4 Microscopy Characterisation

3.4.1 Optical Microscopy

The domain size, morphology, surface cleanliness and layer number of 2D materials over large areas can be quickly and easily examined by optical microscopy (OM). In the SiO_2 substrate, when the thickness of the oxide layer satisfies certain thickness conditions, the optical path difference of two neighbouring interfering lights results in the colour changes and optical contrast.[1] **Figure 3.4** illustrates an example of contrast difference between a variety of MoS_2 layer number, indicating that the optical contrast is sensitive to the layer number for 2D materials. This makes the OM characterisation a fast and non-destructive way to evaluate the

sample qualities. The resulted images were frequently enhanced by adjusting brightness/contrast to show information of interest using the image processing tool, "ImageJ".

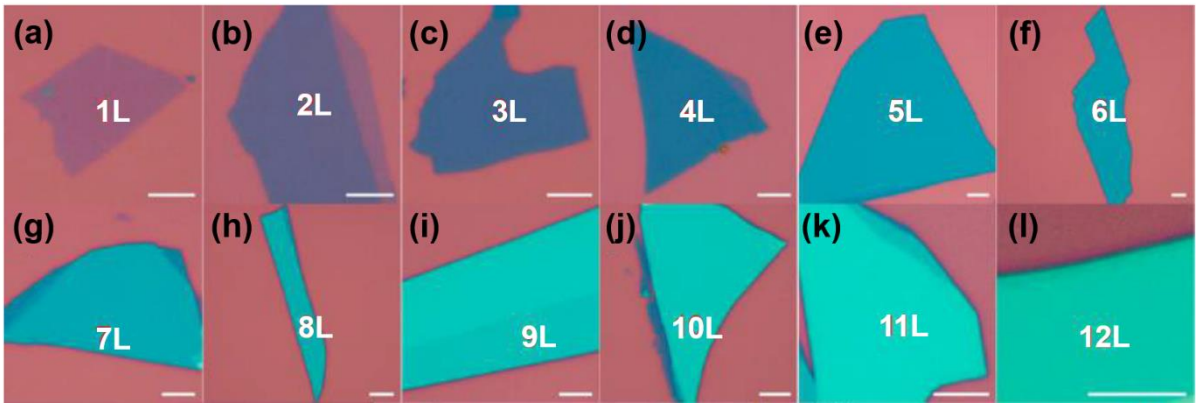


Figure 3.4. Optical microscopy image of MoS_2 with different layer thicknesses on SiO_2 substrates. The samples thickness in (a-l) increases from monolayer (1L) to 12L, respectively. Reproduced with permission from ref. [1]. © 2013 American Chemical Society.

3.4.2 Scanning Electron Microscopy

Similar to OM characterisation, scanning electron microscopy (SEM) is another typical microscope technique to study the crystal structure and surface morphology of 2D materials, but with higher magnification to inspect the nanoscale objects. In the SEM, electrons are emitted from an electron gun by thermionic or field emission under ultrahigh vacuum conditions. When the specimen is excited with an incident electron beam, secondary electrons are emitted from the specimen surface and collected by an Everhart-Thornley detector located aside. Due to the surface sensitivity, the second electrons can therefore reveal the topography and morphology of the specimen surface. It is noted that the ultrathin nature of 2D materials requires a low accelerating voltage to reduce the penetration depth and collect more information from the surface structures. In this work, the SEM characterisation was performed using a Hitachi-4300 field emission gun (FEG) with an accelerating voltage of 3.0 kV and

beam current of 10 μA (**Figure 3.5**). The resolution can be reached down to 100 nm. During the SEM characterisation, the specimen was mounted onto the sample stub firmly using carbon sticky pads to prevent unwanted charging.

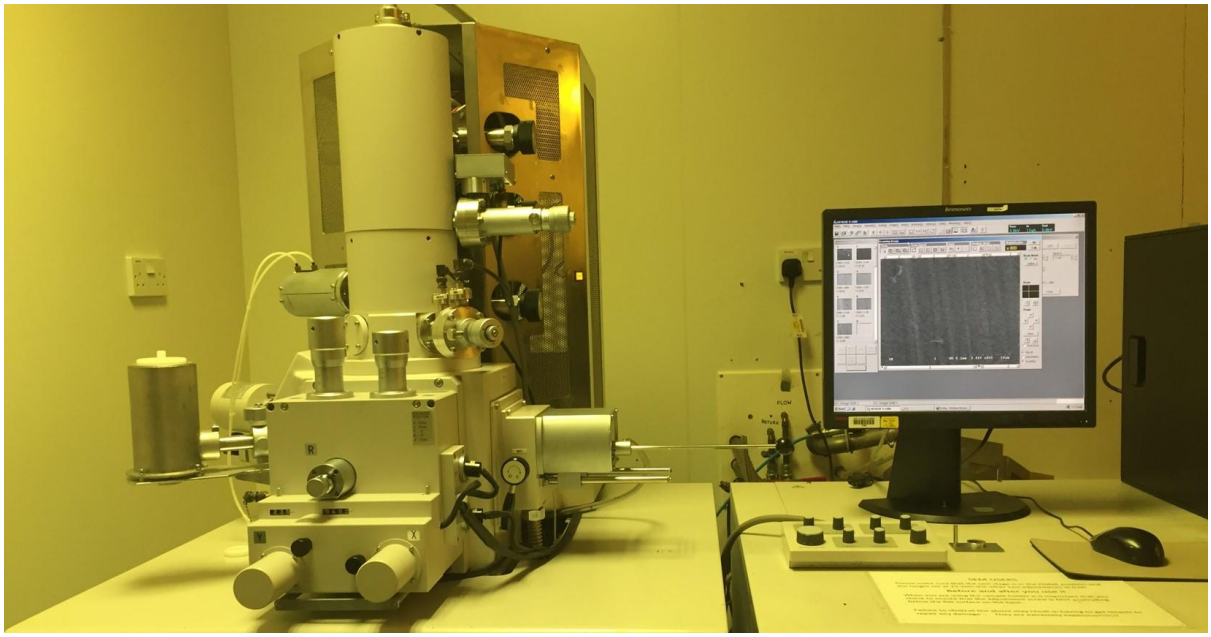


Figure 3.5. Photograph of scanning electron microscopy.

3.4.3 Transmission Electron Microscopy

Transmission electron microscopy (TEM) is the characterisation tool that analyses the crystalline information and microstructure of materials from micron scale down to atomic resolution. The electron beam source of TEM is similar to that of SEM, but with much higher accelerating voltages between 60 kV and 300 kV. The high resolution capability of TEM originates from the interaction of the incident accelerated electrons transmitted through nanometre thin specimen. When the electrons passes the specimen, they are scattered by the electrostatic potential of its atoms both coherently and incoherently, contributing to the image contrast. In addition, the wavelength of incident high-energy electrons is typically a few thousandths nanometre, which is about hundreds to thousands times larger than the specimen

thickness. The atoms of the specimen hence act as a diffraction grating to the incident electrons, which are diffracted according to the crystal structure of specimen forming a specific diffraction pattern. In this work, TEM characterisation was performed on the JEOL 2100 LaB_6 operated at an accelerating voltage of 80 kV with the help of Dr. Shanshan Wang and Dr. Ja Kyung Lee. The TEM imaging was utilised to determine the layer number of 2D materials through counting lines of contrast along the cross-sectional view of back-folded edges resulted from the transfer process. Selected area electron diffraction (SAED) was adopted to examine the crystallinity of 2D materials.

3.4.4 Annular Dark Field Scanning Transmission Electron Microscopy

In contrast to conventional TEM imaging, where a large area of the specimen is subjected to a parallel beam of electrons, scanning transmission electron microscopy (STEM) utilises a very small probe of electrons scanning across the specimen by deflection coils, the electron beam is focused to a fine spot. By taking on an annular dark-field (ADF) detector, which is able to collect scattered electrons that are strongly dependent on atomic weight, the ADF-STEM imaging acquires strong atomic contrast and is particularly useful for identifying different atoms in 2D materials, where the heavier atoms appear brighter than light atoms. In this work, ADF-STEM imaging was performed with the help of Dr. Gyeong Hee Ryu and Jun Chen in the electron Physical Sciences Imaging Centre (ePSIC) at Diamond Light Source. An aberration-corrected JEOL ARM300CF STEM equipped with a JEOL ETA corrector was operated under an accelerating voltage of 60 kV for the ADF-STEM images shown in Chapter 7. The spherical aberration (Cs) and chromatic aberration (Cc) were 0.4 μm and 0.89 mm, respectively. Dwell times of 5–20 μs and a pixel size of 0.006 nm $pixel^{-1}$ were used for imaging. Conditions were a 30 μm CL aperture with a convergence semiangle of 31.5 mrad and a beam current of 44 pA. The acquisition angles for these images were 49.5–198 mrad.

3.4.5 Atomic Force Microscopy

Atomic force microscopy (AFM) utilises a cantilever with a very sharp tip to scan over the specimen surface and measure the subtle changes of van der Waals forces between the tip and specimen. As the tip approaches the specimen surface, the van der Waals interaction between the tip and specimen leads to an attractive force. However, when the cantilever is brought even closer to the specimen surface, the repulsive force increases rapidly and becomes dominant, resulting in the cantilever deflecting away from the surface. The output signal is based on the degree of cantilever deflection. According to surface conditions and application demands, the operation of AFM can be divided into three primary modes: contact, tapping and non-contact modes. In the characterisation of 2D materials, because of their susceptibility to surface adsorbates, the AFM measurements are generally conducted under the tapping mode, where the cantilever is mounted into a piezoelectric holder and oscillates at its resonant frequency to tap the specimen periodically. In this work, AFM was performed by Dr. Benjamin Porter and Nhlakanipho Mkhize using an Asylum Research MFP-3D in AC mode with a silicon AC-160TS cantilever (Olympus, spring constant ~42 N/m and resonant frequency ~300 kHz) to examine the surface smoothness at sub-nanometre resolution and layer thickness of as-synthesised 2D materials. The AFM mappings and the corresponding height profiles were generated by using the 'Gwyddion' software.

3.5 Spectroscopy Characterisation

Spectroscopy is utilised to study the interactions between matter and electromagnetic radiation and is a field that encompasses a wide range of techniques. In the field of 2D materials, Raman spectroscopy and photoluminescence (PL) spectroscopy are the most

common characterisation tools for analysing the electronic structure and vibrational properties of 2D materials.

3.5.1 Raman Spectroscopy

Raman spectroscopy provides a quick and non-invasive method for investigating the interaction between photons and lattice vibrations as well as characterising the chemical composition and layer number of 2D materials. It employs the inelastic scattering of incident light in the material, where the material releases a different quantity of energy after the photon excitation. The energy of scattered light can either decrease through releasing phonons or increase through absorbing phonons resulted from the lattice vibration of the material.[2] The characteristic peaks in the Raman spectrum, corresponding to intensity of this inelastic scattered light and its frequency, are strongly dependent on different vibrational modes of the material as well as the incident light source. **Figure 3.6**(a) and (b) present two examples of typical Raman spectra from monolayer WS_2 under different excitation laser wavelengths. It can be seen that the WS_2 monolayers exhibit two prominent first-order vibrational modes, E^1_{2g} and A_{1g} vibrational modes.[3] The E^1_{2g} mode corresponds to the in-plane vibration of S and W atoms moving in opposite directions, whereas the A_{1g} mode is associated with the out-of-plane vibration of S atoms moving perpendicular to the atomic plane in opposite directions. It is noted that additional two peaks are also revealed in the Raman spectra, *LA(M)* and *2LA(M)*, corresponding to the first-order and second-order longitudinal acoustic modes at the M point of the Brillouin zone.[4]

In this work, Raman spectroscopy was carried out using a JY Horiba LabRAM Aramis spectrometer with an imaging confocal Raman microscope (**Figure 3.7**). The excitation source was a green light with wavelength of 532 nm generated by a frequency-doubled Nd:YAG laser

and the spot size was around 1 μm. The full power of the laser was 12.5 mW, but different filters can be applied to avoid sample damage or signal saturation. There are two types of grating, 600 mm^{-1} (slits per mm grating) and 1800 mm^{-1}, in the system for the use of different purposes. Before taking the measurement, the system was firstly calibrated by a standard Si chip with a characteristic peak at 520.7 cm^{-1} to eliminate the instrumental errors. During the Raman measurement, the 1800 mm^{-1} grating was selected for the better spectral resolution.

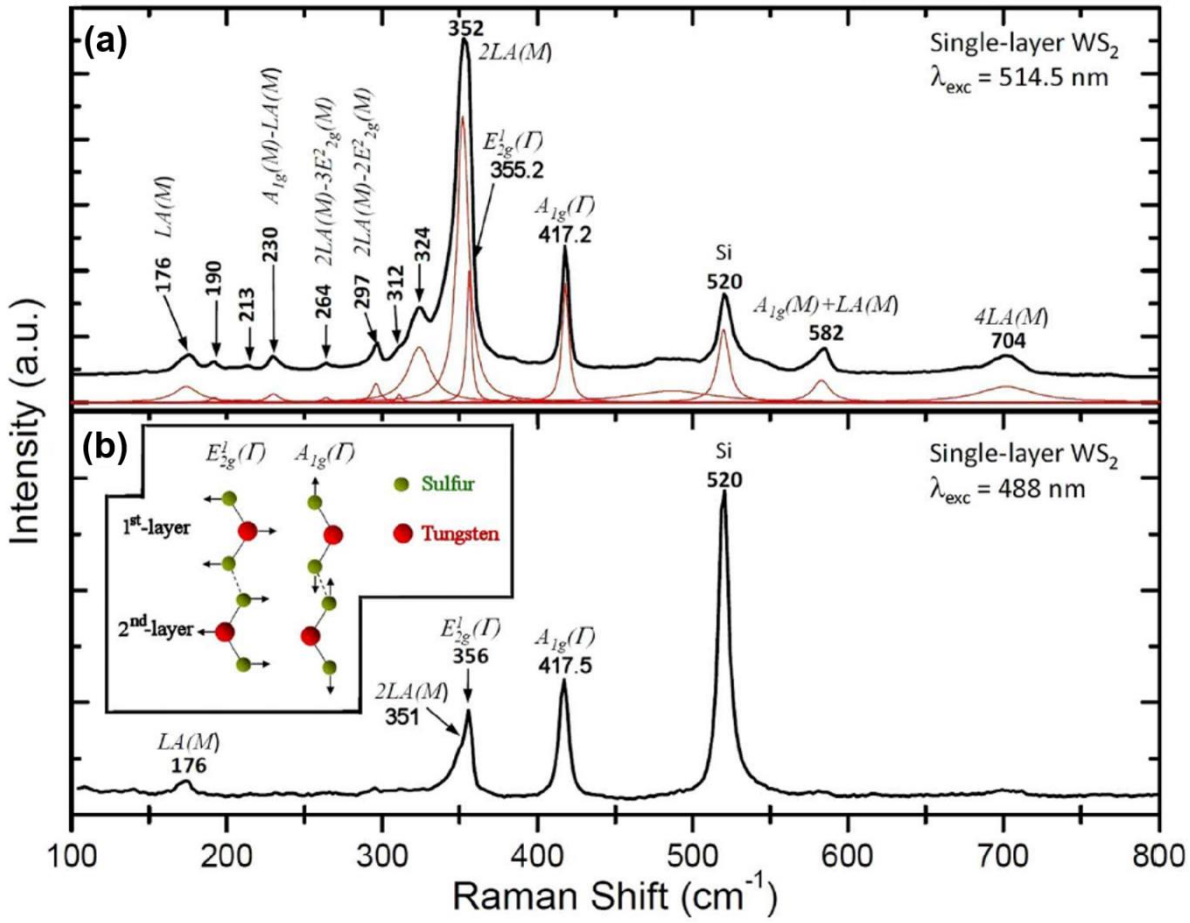


Figure 3.6. Raman spectra of monolayer WS_2 using lasers with different wavelength. (a) Raman spectrum using a laser excitation of 514.5 nm and the multi-Lorentzian fitting for individual mode contributions of the monolayer WS_2. (b) Raman spectrum using a laser excitation of 514.5 nm. The inset illustrates the atomic displacements for the two primary modes of WS_2 layers, in-plane E_{2g}^1 vibrational mode and out-of-plane A_{1g} vibrational mode. Reproduced with permission from ref. [4]. © 2013 Nature Publishing Group.



Figure 3.7. Photograph of Raman and photoluminescence spectroscopy system.

3.5.2 Photoluminescence Spectroscopy

Photoluminescence (PL) involves exciting a sample optically by a laser source and measuring the wavelength (energy) of the resulted output photons. For the semiconducting materials, under the laser excitation excitons are generated when the excitation energy is larger than the optical bandgap, the energy difference between the calculated electronic bandgap and excitonic binding energy of the semiconductors. PL spectroscopy measures the optical emission originating from exciton recombination or exciton-exciton annihilation and directly correlates to the excitonic energy levels of the semiconductors (**Figure 3.8**(a)).[5] It is therefore an adequate method for characterising the optical bandgap, doping level, lattice strain and interlayer interaction of 2D semiconductors. In the example of 2D WS_2 layers demonstrated in **Figure 3.8**(b), the monolayer WS_2 exhibits strong PL emission because of the direct exciton recombination, while the PL intensity dramatically decreases about 100 times in multilayer WS_2 because of the direct-to-indirect bandgap transition.[6]

In this work, PL spectroscopy was employed within the same system as Raman spectroscopy since the laser excitation also induced photoluminescence. Switching between Raman and PL measurement mode was accessible from the software package installed. In the PL measurement, the PL intensity as a function of wavelength (i.e., 500-800 nm) was captured by using the coarse resolution 600 mm^{-1} grating. To investigate the uniformity of as-grown 2D semiconductors, the instrument was able to provide multi-point measurement for both Raman and PL spectra across lateral dimensions in a fixed step size and produce mapping images.

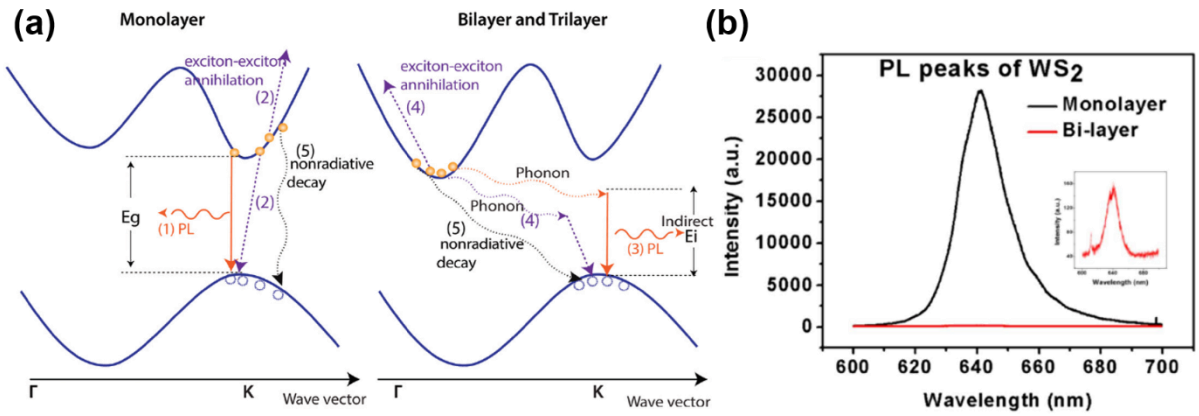


Figure 3.8. Photoluminescence emission characteristics of WS_2 layers. (a) Schematic summary of the pathways for photoluminescence emission of WS_2, including (1) direct exciton recombination; (2) direct exciton-exciton annihilation; (3) indirect exciton recombination; (4) indirect exciton-exciton annihilation; (5) other non-radiative pathways. Reproduced with permission from ref. [5]. © 2015 The Royal Society of Chemistry. (b) PL spectra of monolayer and bilayer WS_2 with the inset of bilayer WS_2 spectral details. Reproduced with permission from ref. [6]. © 2015 Nature Publishing Group.

3.6 Device Measurement

3.6.1 Fabrication Process

To fabricate the devices based on 2D materials, electron-beam lithography (EBL) was utilised to pattern the device features over a large area (**Figure 3.9**(a)). This technique exploits

a focused beam of electrons to write a customised pattern on the sample covered with electron-sensitive film. The electron-sensitive films can be classified into positive resists and negative resists. In the positive resists, the chemical reaction takes place under the electron exposure and weakens the bonding. The resists therefore become more soluble by the developer. In the case of negative resists, the electron exposure promotes crosslinking of the resists and makes them more difficult to dissolve in the developer. As a consequence, the developer removes the exposed area when utilising positive resists, whereas negative resists remain on the substrate surface where it is exposed.

The device fabrication process starts with the metal bond pad patterning by utilising the bilayer PMMA positive resist. A PMMA-495K in anisole solvent was first spin-coated on a 300 nm SiO_2/Si substrate, followed by the second layer spin-coating of PMMA-950K. Since the resist with light molecular weight (PMMA-495K) has higher rate of dissolving in developer, the bilayer configuration exhibits an undercut structure after developing, enabling the effective lift-off after metal deposition. Both PMMA-495K and PMMA-950K resists were spin-coated at 4500 rpm for 45 seconds, and baked at 180°C for 90 seconds before the electron beam exposure. The JEOL JBX-5500FS EBL system was used to pattern bond pads in a bilayer PMMA resist. After the EBL patterning, developing treatment was performed for 45 seconds using the conventional 1:3 MIBK/IPA developer. After which the samples were put into the thermal evaporator (Edward 360) for depositing Cr/Au (10 nm/80 nm) metal bond pads (**Figure 3.9**(b)). In the thermal evaporation, metal vapours were provided through Joule heating in a vacuum environment and gradually deposited onto the target substrates. This was followed by a lift-off process, where the samples were subsequently soaked in acetone at 45°C overnight to remove the unwanted regions of metal film lying on top of the resist.

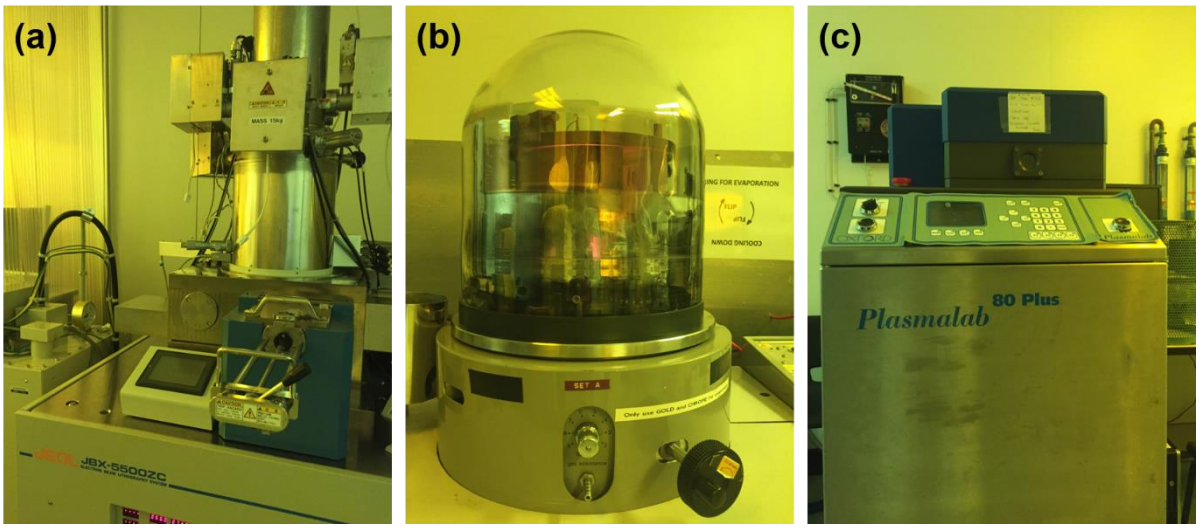


Figure 3.9. Cleanroom equipment for the device fabrication process. (a) Electron beam lithography for the patterning of devices features. (b) Thermal evaporator for the metal bond pad deposition. (c) Reactive ion etching for the fabrication of graphene ribbons.

In contrast to the metal bond pads patterning, a negative resist (maN-2403) was adopted for the graphene ribbon patterning. The continuous graphene film was firstly transferred onto the SiO_2/Si substrate with pre-patterned metal bond pads, followed by spin-coating of maN-2403 at 3000 rpm for 30 seconds on the substrate and baked at 90°C for 90 seconds before the exposure to the electron. The graphene film was then patterned again using EBL with a length and width of 100 and 25 µm, respectively. The 1 µm gaps between graphene channels were fabricated using the same process. The samples were developed in ma-D525 for 150 seconds after the electron exposure, then exposed to reactive ion etching (RIE) treatment (Plasmalab 80 Plus) to remove the excess graphene area using oxygen plasma generated by the RF electromagnetic field (**Figure 3.9**(c)). Lastly, the 2D semiconductors were transferred to the sample with patterned metal bond pads and graphene ribbons. In this work, the EBL process was performed with the help from Dr Haijie Tan and Tongxin Chen.

3.6.2 Electrical and Opto-Electrical Measurement

The electrical and opto-electrical measurements of the devices based on 2D materials were performed using a custom-built probe station (**Figure 3.10**(a)). Two Keithley 2400 source meters were used for I-V characteristics and I-V_g transfer curve measurements of the 2D transistors placed on a stage, which can be adjusted in X, Y and Z directions through a digital controller (**Figure 3.10**(b)). The gate voltage was applied through the p-doped silicon substrate from the back side with silver paste. For illumination during the photoresponse measurements, a 532 nm diode-pumped solid-state laser (Thorlabs, DJ532-40), which was coupled into a confocal microscope to form a beam with spot size of ~150 μm^2 as a light source. The power values of the output laser were measured by a digital power meter (Thorslab Optics PM100D) placed above the devices before each I-V measurement. Two tungsten tips (Signatone SE-T) were used to connect the source and drain metal bond pads of each device to the source meter and to apply a potential sweeping from negative to positive bias. Measurements were all done at room-temperature under ambient pressure.

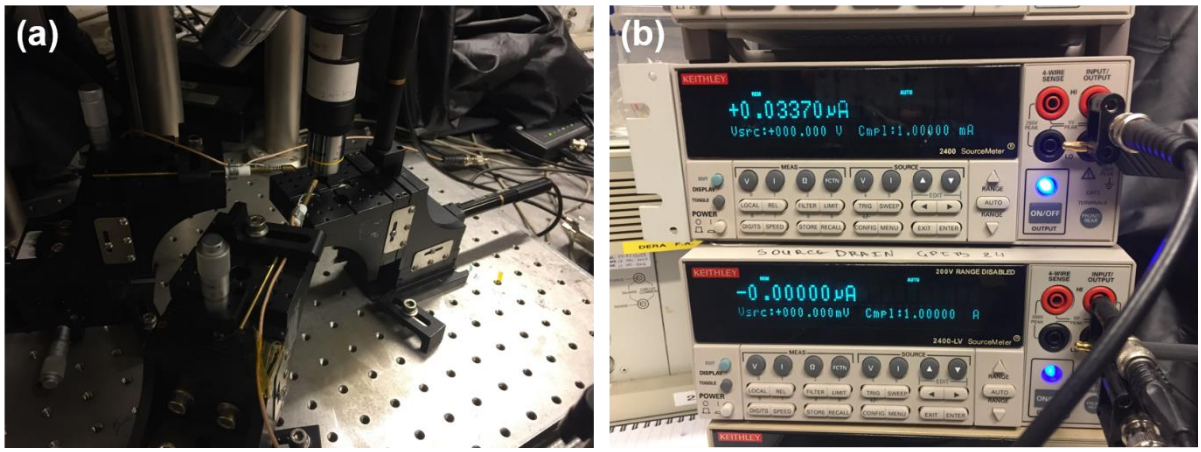


Figure 3.10. Measurement setup for devices based on 2D materials. (a) Probe station for the device measurement. (b) Source meters for the voltage and current measurement.

3.7 Reference

(1) Li, H.; Wu, J.; Huang, X.; Lu, G.; Yang, J.; Lu, X.; Xiong, Q.; Zhang, H., Rapid and Reliable Thickness Identification of Two-Dimensional Nanosheets Using Optical Microscopy. *ACS Nano* **2013,** *7* (11), 10344-10353.

(2) Saito, R.; Tatsumi, Y.; Huang, S.; Ling, X.; Dresselhaus, M. S., Raman Spectroscopy of Transition Metal Dichalcogenides. *J. Phys. Condens. Matter* **2016,** *28* (35), 353002.

(3) Tonndorf, P.; Schmidt, R.; Böttger, P.; Zhang, X.; Börner, J.; Liebig, A.; Albrecht, M.; Kloc, C.; Gordan, O.; Zahn, D. R. T.; Michaelis de Vasconcellos, S.; Bratschitsch, R., Photoluminescence Emission and Raman Response of Monolayer MoS_2, $MoSe_2$, and WSe_2. *Opt. Express* **2013,** *21* (4), 4908-4916.

(4) Berkdemir, A.; Gutiérrez, H. R.; Botello-Méndez, A. R.; Perea-López, N.; Elías, A. L.; Chia, C.-I.; Wang, B.; Crespi, V. H.; López-Urías, F.; Charlier, J.-C.; Terrones, H.; Terrones, M., Identification of Individual and Few Layers of WS_2 Using Raman Spectroscopy. *Sci. Rep.* **2013,** *3*, 1755.

(5) Yuan, L.; Huang, L., Exciton Dynamics and Annihilation in WS_2 2D Semiconductors. *Nanoscale* **2015,** *7* (16), 7402-7408.

(6) Kang, K. N.; Godin, K.; Yang, E.-H., The Growth Scale and Kinetics of WS_2 Monolayers under Varying H_2 Concentration. *Sci. Rep.* **2015,** *5*, 13205.

Chapter 4

Growth of Large Single-Crystalline Monolayer Hexagonal Boron Nitride by Oxide-Assisted Chemical Vapour Deposition

4.1 Introduction

The bottom-up vapour phase growth of hexagonal boron nitride (hBN) has been reported for a range of transition catalyst metals (including Cu,[1] Ni,[2] Pt,[3-4] Fe,[5] Co,[6] Ir,[7] Ru,[8] Rh,[9] and Ag[10]) and other insulating substrate such as SiO_2 and sapphire that allow the direct growth of other 2D materials on hBN without any additional transfer process.[11-12] The precursors used for hBN growth range from gas (diborane and ammonia),[13] liquid (borazine),[4] to solid (ammonia borane, trimethylamine borane and oligomeric aminoborane).[14-16] A variety of growth techniques for achieving atomically thin hBN films over large distance have been obtained through chemical vapour deposition (CVD), physical vapour deposition (PVD) and molecular beam epitaxy (MBE).[17-20] CVD is an attractive method for the growth of hBN because of its low cost, simple design, and simple operation. The domain size for hBN to date, however, is still much smaller than that of graphene grown on commonly used Cu substrates. This is attributed to the much smaller adsorption energies of the B-N pair in hBN crystal on the Cu surface compared to that of a pair of graphene carbon atoms on the basis of density function theory (DFT) calculations.[21-22] The nucleation of hBN on Cu can consequently be achieved with much lower levels of surface supersaturation of precursors. The domain sizes of CVD grown hBN were typically on the orders of micrometres.

Similar to the improvement of graphene films quality, several works have sought to control the nucleation density and increase the domain size by electrochemical polishing,[23] melting and re-solidifying of the Cu substrates.[24-25] Other common strategies, including controlling the amount of precursors,[1] the orientation of the Cu substrates,[26-29] the annealing time and flowrate of catalytic hydrogen gas,[30] changing the growth substrate into Cu-Ni alloy, Fe and Ge are also beneficial for the enhancement of hBN domain size.[28, 31-32] Most recently, it was shown that oxygen plays a critical role in modulating the growth behaviour of the graphene on Cu. The presence of oxygen on Cu surface can not only decrease the density of graphene nuclei but also can accelerate the growth rate.[33-36] However, the study of the influence of oxygen on hBN growth is still in its nascent stage. Only a few reports show that introducing oxygen during hBN growth can lower the energy barrier of precursor dehydrogenation and suppress the growth selectivity.[37] Thus, further investigation of the role of oxygen is still important. In this chapter, the growth of highly-crystalline monolayer hBN was realised by introducing a thin oxide layer onto the Cu substrate prior to the growth stage. This CVD approach assisted by the preformed oxide layer, denoted as OCVD, yields a decrease in hBN nucleation density at the initial growth stage and can reach a continuous film with an increase in growth time. The whole OCVD process is performed under atmospheric pressure using Cu foils that are only briefly mechanically polished, eliminating the need for electrochemical polishing. In addition, the highly aligned orientation of triangular hBN domains over a large area indicates the epitaxial relationship between hBN and Cu substrate. The as-grown hBN monolayers were also characterised by using Raman spectroscopy, atomic force microscopy (AFM), scanning electron microscopy (SEM) and transmission electron microscopy (TEM).

4.2 Results and Discussion

4.2.1 Oxide-Assisted CVD Growth of hBN

Figure 4.1(a) schematically shows the experimental setup for the CVD growth of hBN with the Cu catalytic substrate placed on the ceramic crucible. The synthesis of monolayer hBN was performed using a custom-built 1-inch CVD system with quartz tube and gas flow rates controlled by digital mass flow controllers. Ammonia borane (BH_3NH_3) powder was used as the hBN growth source and placed into a small chamber with the heating belt upstream of the CVD furnace. The two separated heating systems provide better temperature control, and the amounts of the feedstocks can be controlled by the needle valve between the small chamber and the quartz tube. Prior to hBN growth, the ammonia borane powder was heated to 120°C with the needle valve closed. The growth of hBN commences when the needle valve is open, allowing the precursors to diffuse to Cu substrate surface at high-temperature regime.

The elementary surface processes involved in the CVD growth of monolayer hBN on Cu substrate are schematically shown in **Figure 4.1**(b). First, ammonia borane used as a precursor is thermally decomposed in the temperature range from 70°C to 140°C. The decomposition of ammonia borane produces gaseous hydrogen, borazine and aminoborane. These gaseous molecules are adsorbed on the Cu surface when they are carried to the Cu substrate by argon gas. Second, the adsorbed hydrogen atoms dehydrogenate the aminoborane molecules and generate active species such as BN dimers that contribute to hBN growth. Because these active species are thermally unstable, they tend to agglomerate to form a stable hBN nucleus when their levels of supersaturation are sufficiently high. Here, the surface irregularities such as grain boundaries and the rough surface of Cu are known to stimulate hBN nucleation. Third, the rest of the active species attach to the existing hBN nuclei and enlarge the domain through surface diffusion that is driven by a concentration gradient. Finally, the

continual supply of active species gives rise to the coalescence of adjacent hBN domains into a continuous film when the hBN domain is sufficiently large. It is also noted that in the experiments, the CVD growth is conducted under ambient pressure, so that the evaporation of Cu atoms that resulted from the high growth temperature (1050°C), which is close to the melting point of Cu (1083°C), has a weaker impact on hBN growth than on low-pressure CVD.

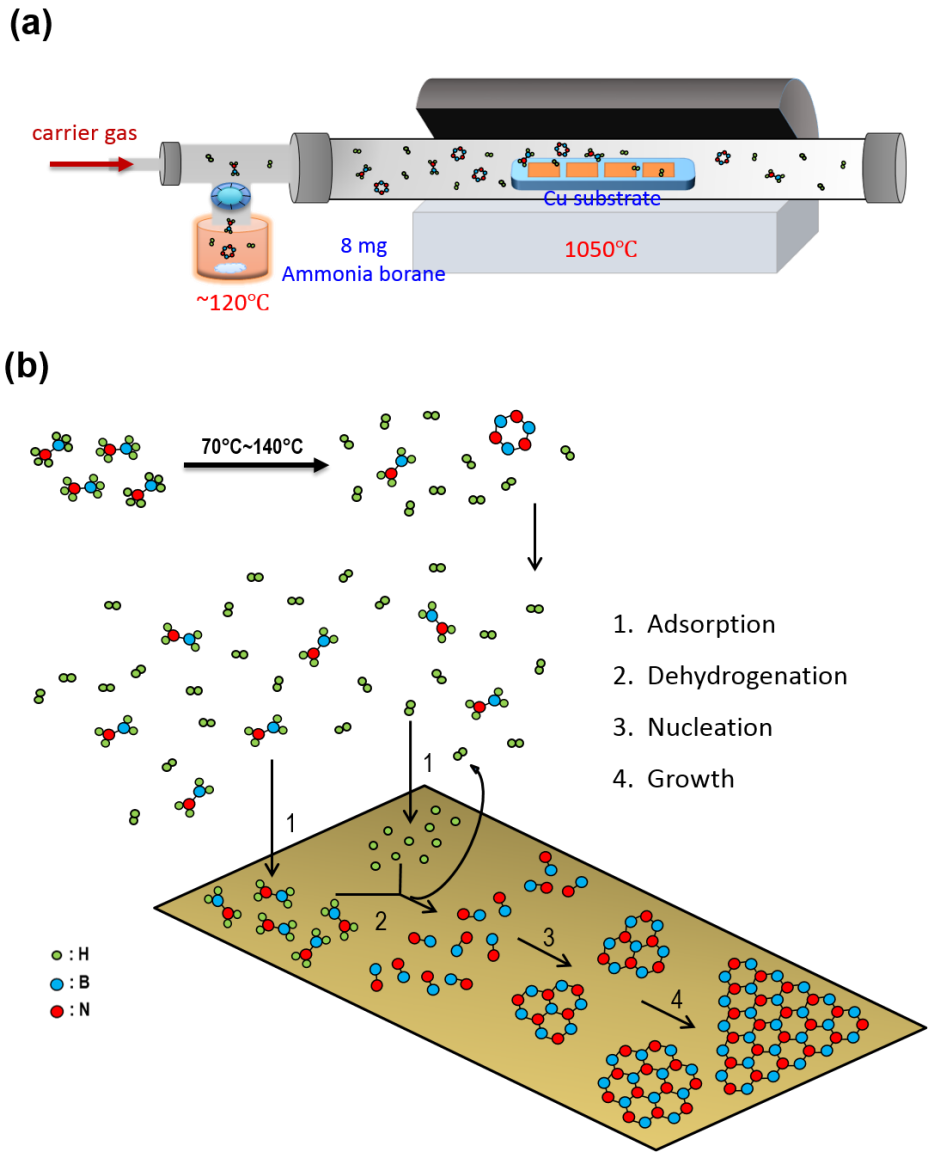


Figure 4.1. Atmospheric-pressure CVD synthesis of hBN on copper. (a) Schematic illustration of the CVD experimental setup with Cu foils in a ceramic crucible. (b) Schematic illustration of the mechanisms in the growth of hBN on the Cu surface by CVD.

The surface roughness of the Cu substrate plays a critical role in reducing the nucleation density of hBN crystals. **Figure 4.2** demonstrates the effect of substrate polishing on the hBN nucleation density. Because of the rolling process from the fabrication of Cu foils, the as-purchased Cu substrate contains surface parallel textures. The hBN domains tend to nucleate along these textures because of the existence of dense surface irregularities and dangling bonds of the substrate around these textures (**Figure 4.2**(a-c)). In comparison, the hBN domains grown on mechanically polished Cu substrates show a suppression of nucleation density (**Figure 4.2**(d-f)) because of the smoothed surface. The lower nucleation density on polished Cu substrates also reveals a decreasing surface coverage under the same growth condition. This allows the production of hBN crystals with larger domains and higher quality.

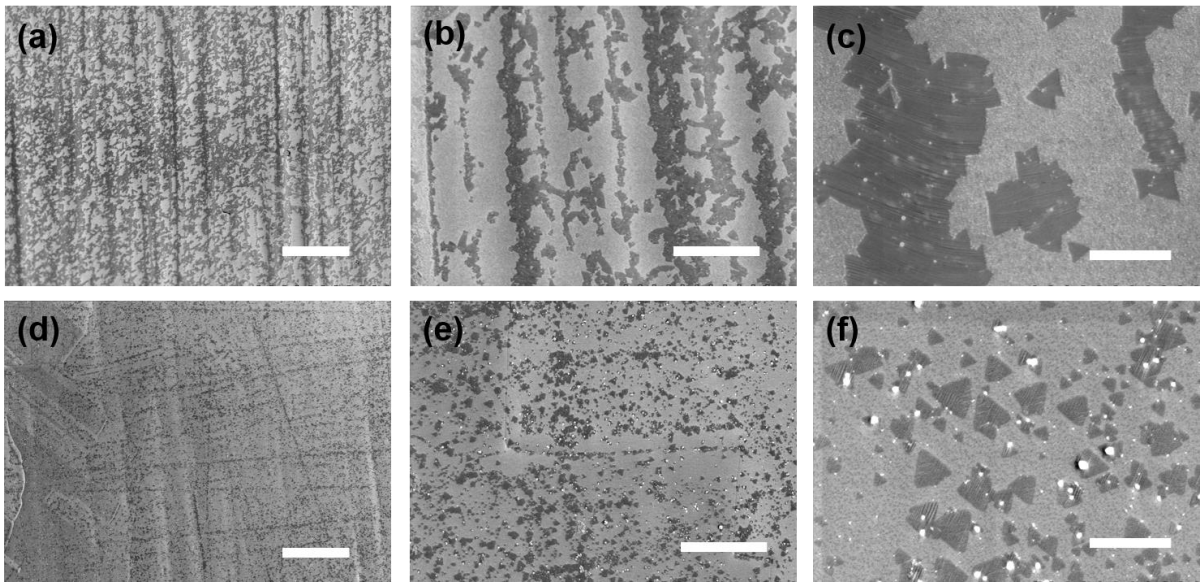


Figure 4.2. Influence of surface texture of Cu substrate on the hBN domain density. (a-c) SEM images of hBN grown by regular CVD process on unpolished Cu substrates. (d-f) SEM images of hBN grown by regular CVD process on mechanical polished Cu substrates. The scale bar is 100 μm in (a) and (d), 30 μm in (b), (e), 5 μm in (c) and (f).

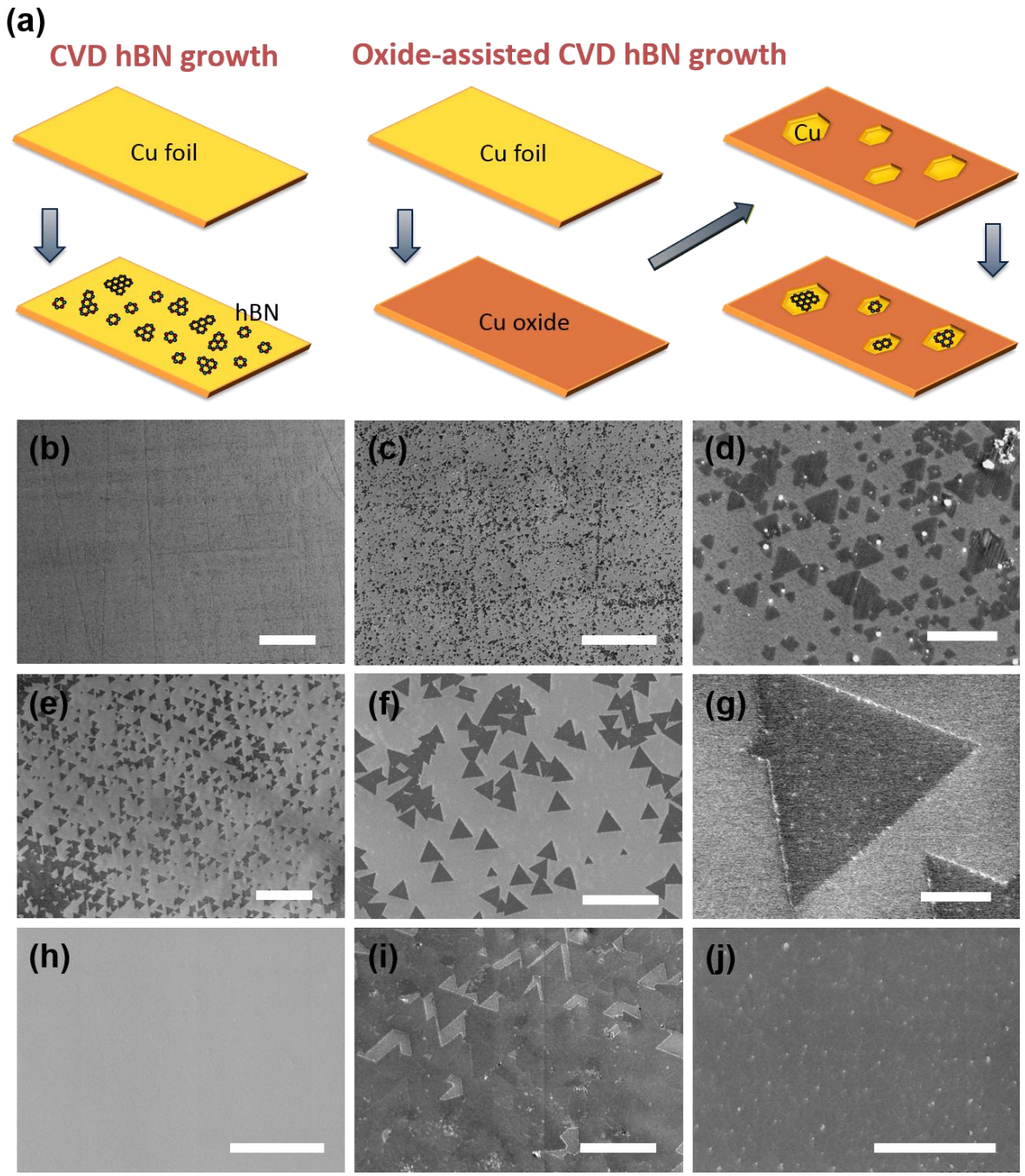


Figure 4.3. OCVD growth of large hBN domains on the Cu substrate from sporadic to continuous film. (a) Schematic illustrations showing the hBN growth mechanism by conventional CVD process and OCVD process with a preformed oxide layer on Cu substrates. (b-d) SEM images of hBN grown for 10 min via the conventional CVD process. (e-g) SEM images of hBN grown for 30 min via the OCVD process. (h-j) SEM images of hBN grown via OCVD process in 10, 45 and 60 minutes, respectively. The scale bar is 100 μm in (b) and (e), 30 μm in (c), (f), (h-j) and 5 μm in (d) and (g).

Figure 4.3(a) schematically explains the growth mechanism in reducing the initial nucleation density of hBN through the OCVD growth. In conventional CVD growth process the active species are generated from the decomposition of the ammonia borane precursor, leading to boron- and nitrogen-containing species nucleating and forming small domains. Because the Cu surface contains dense surface irregularities, including surface steps, dislocation threads, and impurities that could be the preferred nucleation sites, hBN nucleates randomly on the Cu surface during the initial growth stage, and the domain boundaries inevitably exist when the domains become coarser and eventually form a continuous hBN film. By contrast, during the OCVD growth process, the Cu substrate is first oxidised, forming a thin oxide layer on the surface. Because the boron- and nitrogen-containing species have a higher binding energy for the nucleation on the oxide layer, the preformed oxide layer passivates the nucleation sites of Cu surfaces before hBN growth. In the following hBN growth stage, the oxide layer gradually decomposes under the reducing hydrogen atmosphere, and only the limited fresh Cu surface can absorb the active species and form a stable nucleus. This allows the subsequent active species absorbed on the Cu substrate to attach the initial hBN nuclei by surface diffusion, so that the number of preferred nucleation sites is reduced.

The reduced nucleation density due to the surface oxide passivating layer is shown in the SEM images in **Figure 4.3**(b-g). The nucleation density could be reduced from 10^6 to 10^3 mm^{-2}. As a result, the hBN domains grown via the conventional CVD process are randomly nucleated on Cu surface ranging from 0.5 to 5 μm (**Figure 4.3**(b-d)), while the hBN domain size grown via the OCVD process is about 20 μm (**Figure 4.3**(e-g)). Because hBN nucleation occurs only after the passivating Cu oxide layer decomposes, the growth of hBN is slower in the OCVD process. In conventional CVD process, it takes about 10 min of growth time to reach 50% surface coverage for hBN domains (**Figure 4.3**(b-d)), but in the OCVD process, no distinct hBN domains are observed within the 10 min growth period (**Figure 4.3**(h)). The hBN

growth proceeds when the growth time is increased to 45 min (**Figure 4.3**(i)) and monolayer hBN growth is almost completed after growth for 60 min (**Figure 4.3**(j)). It is also noted that several white particles and wrinkles are usually observed on the hBN surface. The white particles might be associated with the stable by-products such as borazine decomposed from the ammonium borane precursors, and the wrinkles are attributed to the negative thermal expansion coefficient of hBN, resulting in shrinkage of hBN but expansion of the underlying Cu substrate during the cooling stage.

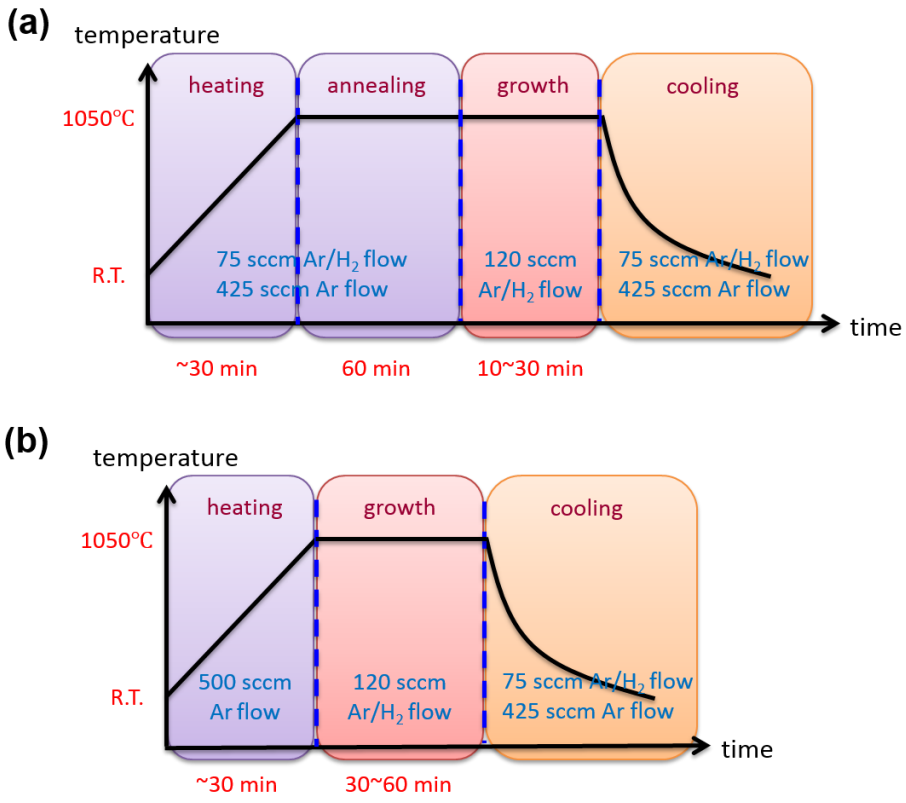


Figure 4.4. Comparison of the temperature curves as a function of growth conditions between regular CVD and OCVD hBN process. (a) The heating profile and growth conditions for the regular CVD process. (b) The heating profile and growth conditions for the OCVD process.

The comparison between heating profiles for the furnace as a function of time and the gas flow rate used to grow hBN during each timeline in conventional CVD and OCVD

processes are demonstrated in **Figure 4.4**. In the conventional CVD process, the whole system was first flushed with argon gas and then ramped up to a high temperature in a reducing atmosphere. The copper was annealed for at least 1 hour after the furnace had reached the desired growth temperature. The growth of hBN then proceeded on Cu via the introduction of the decomposed ammonia borane precursors. By contrast, because the oxide layer is prone to decomposition at high temperature, the annealing was cancelled and hydrogen was turned off before the growth stage to stabilise the oxide layer on Cu surface during the OCVD hBN growth process. The thickness of the oxide layer is found to be influential in suppressing the nucleation density. As the decomposition of the oxide layer could still occur at high temperatures during the heating stage, the OCVD growth of hBN (**Figure 4.5**(a)) would be similar to conventional CVD growth if the oxide layer is not sufficiently thick and starts to reveal bare Cu surface prior to the growth. Once the oxide layer can maintain the full coverage before the growth starts, further increasing the oxide layer thickness only results in a longer time to initiate the growth rather than a decrease in nucleation density (**Figure 4.5**(b-c)).

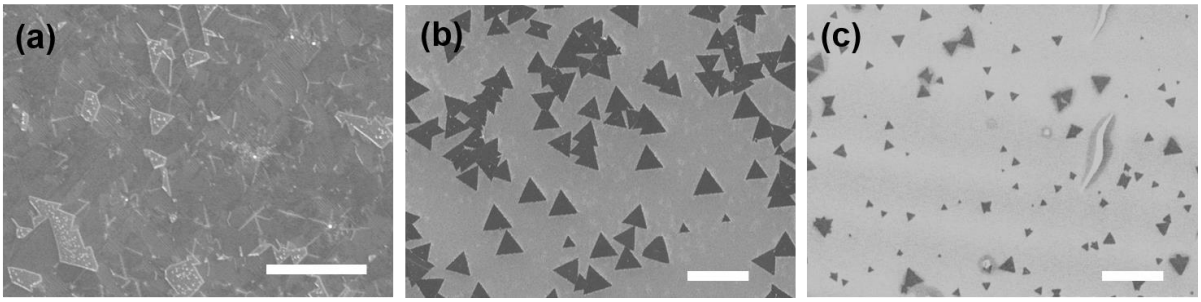


Figure 4.5. Effect of the surface oxide layer on the hBN nucleation density in the OCVD growth. (a-c) SEM images of hBN grown by OCVD process in 30 min on the Cu substrates oxidized at 180°C for (a) 2 min, (b) 5 min, and (c) 10 min before the growth. All the scale bars are 20 μm.

The OCVD-grown hBN also exhibited different morphologies in different Cu substrates. **Figure 4.6** shows the different domain shape of hBN obtained from each Cu

substrate in our OCVD setup. This is attributed to the misbalance between B and N atoms. Although the ammonia borane precursor has equimolar stoichiometry (B/N ratio of 1/1), it is reported that the edge with N-termination is energetically favourable versus that with B-termination,[38] resulting in a triangular hBN domain with all N-terminated edges for the first two Cu substrates (position 1 and 2). The higher nucleation density of hBN on the first piece of Cu is attributed to the dense borazine particles that instigate heterogeneous nucleation, but the amount could be reduced for the subsequent Cu substrates farther away. To further study the growth behaviour of hBN, including the orientation dependence and layer number, the following analysis was mainly focused on the triangular hBN grown by OCVD.

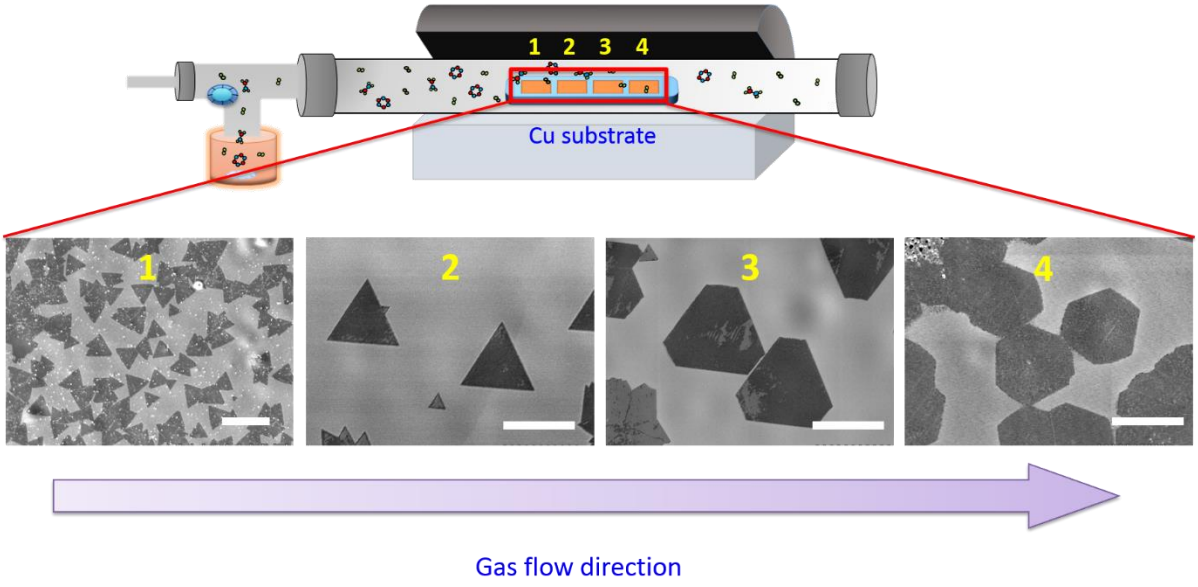


Figure 4.6. SEM images of hBN growth with Cu substrates placed at the position 1 to 4 in the CVD setup, demonstrating the morphology variation along the Ar gas flow direction. All the scale bars are 20 μm.

4.2.2 Characterisation and Orientation Analysis of hBN

Figure 4.7 displays the orientation dependence of hBN domains on Cu surface. In the SEM image shown in **Figure 4.7**(a), triangular hBN domains can be observed on three different Cu grains; the grain boundary of Cu is marked by the red dashed line. Close-ups of each Cu grain marked by the dashed orange, green, and blue rectangles are shown in **Figure 4.7**(c-e), respectively. The hBN domains in different Cu grains have preferred growth directions, and the measurement of the edge orientation for each hBN domain produces histograms of the total number of edges at a given angle. The statistical distributions of the orientations of hBN triangles in **Figure 4.7**(c-e) are shown in **Figure 4.7**(f-h), respectively, revealing a propensity of edges separated from one another by 60°. This indicates that most of the dominant triangular hBN domains within the same Cu grain, as outlined in red, within individual Cu grains are well aligned in the same orientation, indicating an epitaxial relationship between the hBN domain and the underlying Cu substrate. Only a few triangular domains are on the different orientations with inversion symmetry or rotation symmetry, as outlined in yellow and purple, respectively. Some of the hBN domains contain additional facets with several 3- or 6-fold symmetric orientations forming a variety of complex structures, which may be attributed to the merging of neighbouring triangular hBN domains with rotations of 30° and 60° when the nucleation sites are sufficiently close to one another.

The different orientations for hBN triangles could lead to different types of domain boundaries. As illustrated in **Figure 4.7**(b), when two well-orientated triangular domains merge together they can stitch seamlessly and preserve the single-crystalline structure. In comparison, when two misaligned hBN triangles with different rotations merge together, a domain boundary is formed by pentagon-heptagon pairs or square-octagon pairs. These few misaligned hBN domains might be attributed to the disturbance arising from an impurity like a borazine by-product on Cu surface or the dislocations on Cu surface generated by mechanical polishing.

When two oppositely orientated domains merge together, a defect line with B-B or N-N bonding might be generated at the interface. The percentages of these three different orientations of triangular hBN domains in **Figure 4.7**(c-e) are listed in **Figure 4.7**(i-k), demonstrating that around 70% of the hBN triangles are aligned.

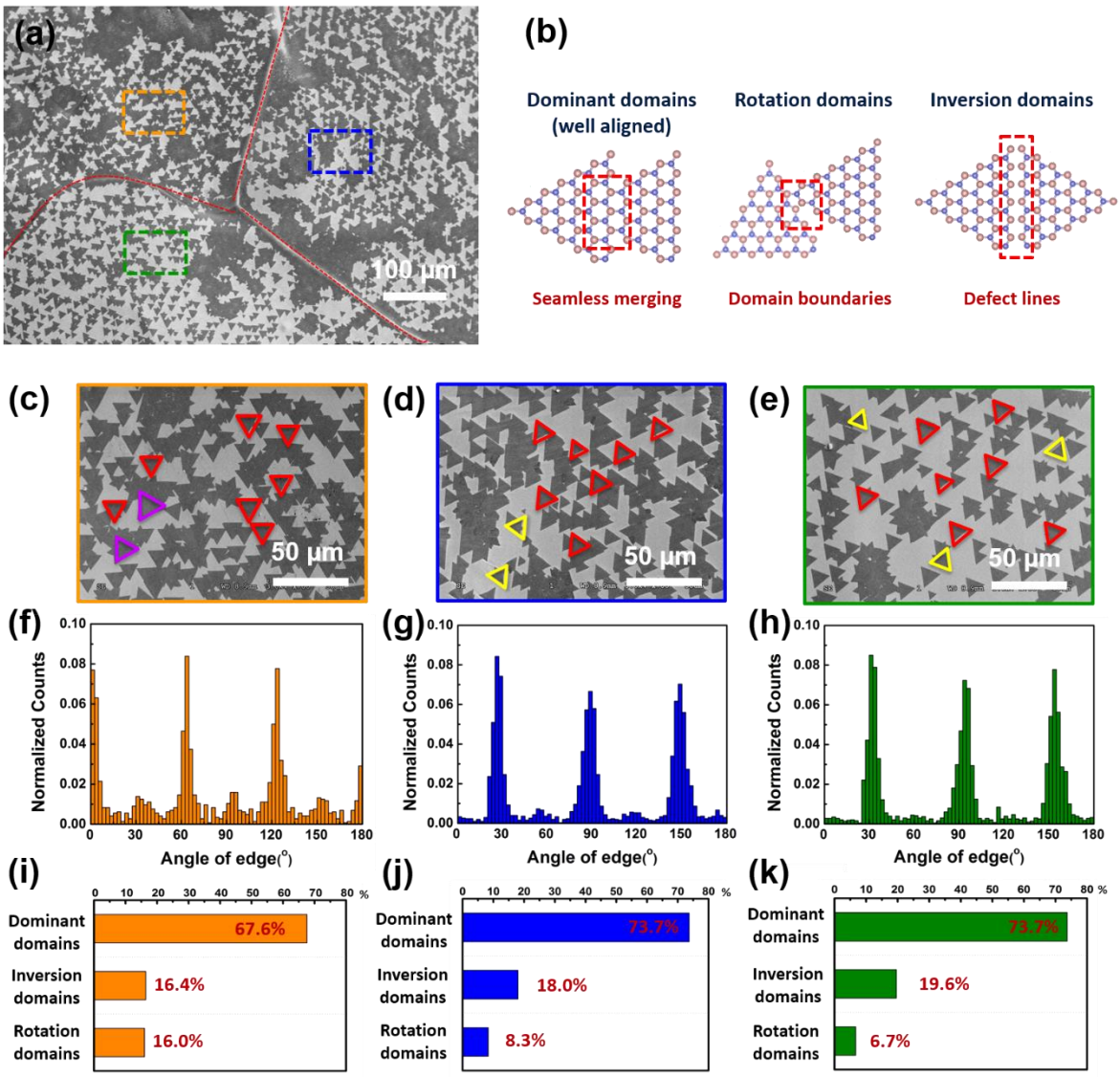


Figure 4.7. Orientation dependence of triangular hBN domains grown on Cu. (a) Low-magnification SEM image demonstrating the growth of hBN crystals on polycrystalline Cu foil by OCVD with a growth time of 40 min. (b) Schematic illustration of the atomic configuration for merged between triangular hBN domains that have different orientations. (c-e) Magnified SEM images chosen from panels denoted by different dashed lines (orange dashed line for (c), green dashed line for (d), and

blue dashed line for (e)) in (a), showing the different preferred growth directions of hBN triangular domains within each Cu grain. (f-h) Statistical distributions of the edge angles of individual OCVD-grown triangular hBN domains within each Cu grain shown in (c-e), respectively. (i-k) Percentages of different types of triangular hBN domains merging within each Cu grain shown in (c-e), respectively.

To further study the characteristics of the OCVD-grown hBN, both the as-grown triangular hBN domains and continuous hBN film were transferred to a Si substrate with a 300 nm oxide layer. The SEM image in **Figure 4.8**(a) shows the triangular hBN domain grown for 40 min on a Cu substrate by OCVD. Increasing the growth time could lead to the continuous hBN film (**Figure 4.8**(d)). It is observed that the wrinkles on the hBN surface that resulted from the different thermal expansion coefficients between hBN and Cu during the cooling process were stretched across the Cu grain boundaries, indicating that the hBN is grown uniformly over the entire Cu substrate surface. **Figure 4.8**(b) and (e) show the optical image of the hBN domains in **Figure 4.8**(a) and hBN film in **Figure 4.8**(d) after the transfer to SiO_2/Si substrate. The optical contrast indicates uniformity and cleanliness of the hBN surface. **Figure 4.8**(c) and (f) show the AFM analysis of the edge for the transferred hBN domain sample from **Figure 4.8**(b) and (e), respectively. The step height for the domain edge is estimated to be about 0.54 and 0.58 nm, both consistent with the equivalent thickness of a single layer in bulk hBN (~0.4 nm). The slightly larger measured value may be attributed to the trapping of the adsorbed molecules (e.g., H_2O) between the hBN and SiO_2/Si substrate. It is also noted that there are several white dots distributed around the domain edge, which may come from the PMMA residual left on the hBN surface after the transfer process.

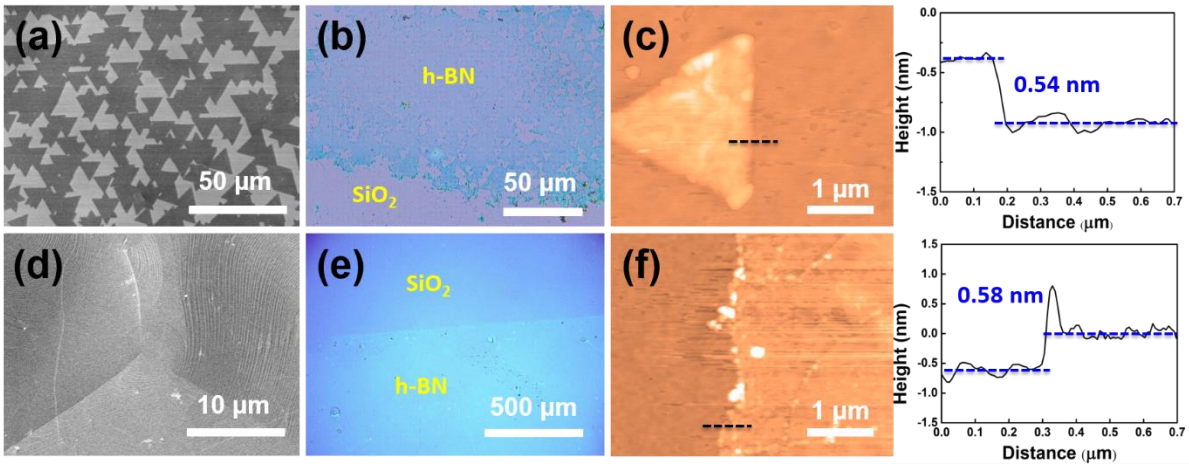


Figure 4.8. Number of layer characterisation for a triangular hBN domain and continuous film grown on Cu by OCVD. (a) SEM image of triangular hBN domains grown for 40 min on a Cu substrate. (b) Optical image of triangular hBN domains in (a) transferred to a SiO_2/Si substrate. (c) AFM image with the scanned line over the corner of triangular hBN domain edge. (d) SEM image of continuous hBN films grown for 60 min on a Cu substrate. (e) Optical image of continuous hBN films in (d) transferred to a SiO_2/Si substrate. (f) AFM image with the scanned line over the corner of a continuous hBN film edge.

To elucidate the uniformity of monolayer hBN, the OCVD-grown hBN films were further characterised by Raman spectroscopy. The characteristic peak of hBN results from the E_{2g} vibration mode, and its peak position is related to the layer number. For the bulk hBN layers, the Raman peak is centred at around 1365 cm^{-1} and shifts to a higher frequency when the number of layers is reduced. **Figure 4.9**(a) shows the photograph of a continuous hBN film transferred onto a SiO_2/Si substrate. Because the opacity of hBN layers is nearly zero, the optical contrast of hBN domains is very weak. The differentiation between monolayer hBN domains and SiO_2/Si substrate relies on the surface impurities like PMMA residuals from the transfer process left on the film edges. The additional contrast is helpful in distinguishing the hBN boundaries. **Figure 4.9**(b) shows the Raman spectra of each position indicated in **Figure 4.9**(a) to examine the uniformity of the continuous film. The histograms of the measured E_{2g} peak

position and full width at half-maximum (FWHM) are displayed in **Figure 4.9**(c) and (d), respectively. Each Raman peak measured at different positions on the hBN film is located around 1369-1371 cm^{-1}, with the FWHM ranging from 14 to 22 cm^{-1}. All of the measured E_{2g} peaks are consistent with previous reports on the Raman signature of mechanical exfoliated monolayer hBN, indicating that the continuous hBN film has a uniform layer number. It is noted that there is a small peak located around 1450 cm^{-1} in the Raman spectra that is caused by the third-order scattering of Si.

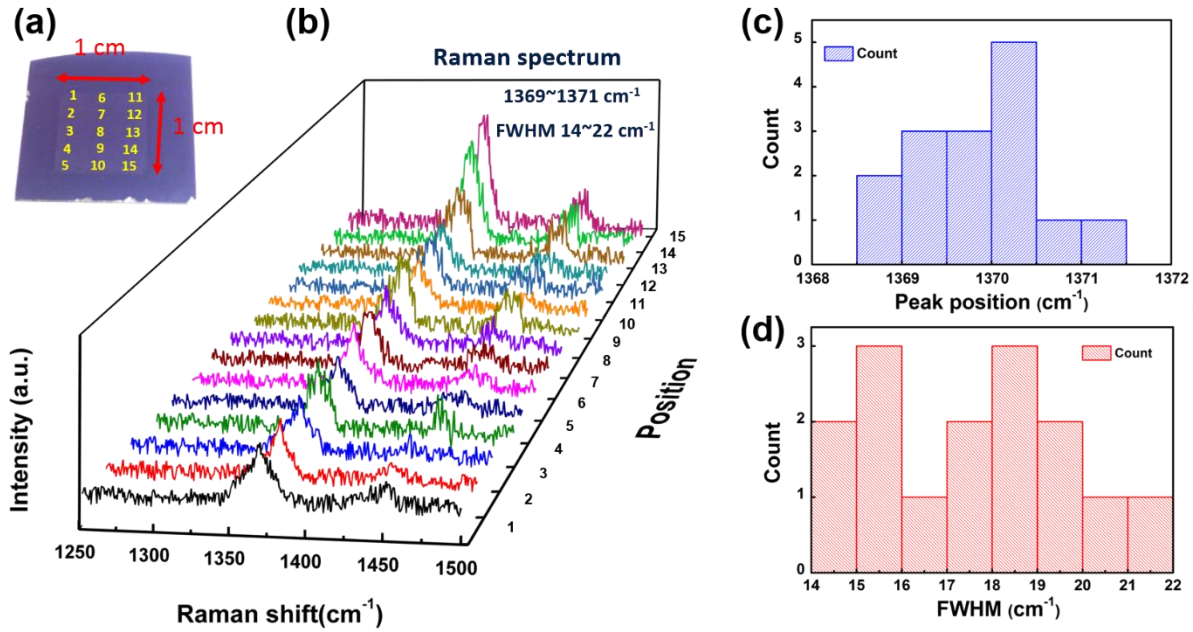


Figure 4.9. Raman characterisation of a continuous hBN film on a Si substrate with a 300 nm oxide layer. (a) Photograph of 1cm*1cm hBN film transferred onto a SiO_2/Si substrate. (b) Raman spectrum of hBN on a SiO_2/Si substrate at different positions indicated in (a). (c) Histogram of the characteristic peak position of the hBN film. (d) Histogram of the full width at half-maximum (FWHM) of the hBN film.

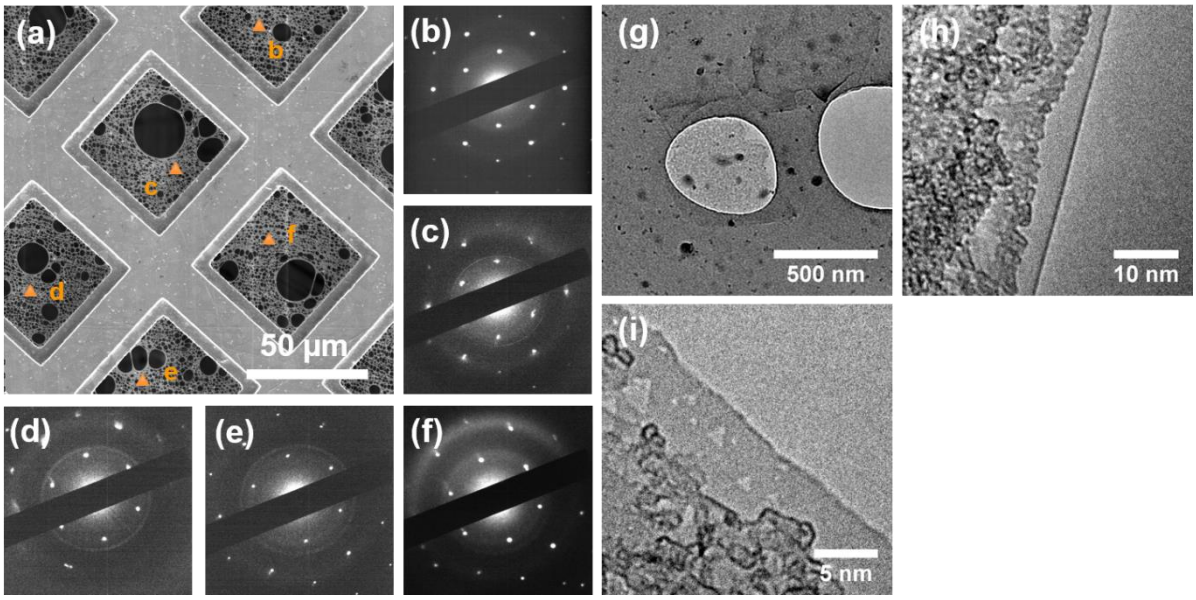


Figure 4.10. TEM characterisation of continuous hBN films. (a) SEM image of a suspended OCVD-grown hBN film supported by a lacey carbon, Cu mesh TEM grid. (b-f) Selected area electron diffraction (SAED) patterns recorded at different locations in the copper mesh marked in (a). (g) Low-magnification TEM image of an OCVD-grown hBN. (h-i) High-magnification TEM images of OCVD-grown hBN on the folded (h) and open (i) edges, respectively.

The atomic structure of OCVD-grown hBN was further studied by high–resolution (HR) TEM. **Figure 4.10**(a) and (g) show the SEM and low-magnification TEM images, respectively, of hBN on a lacey carbon coated Cu TEM grid. All the selected area electron diffraction (SAED) patterns, shown in **Figure 4.10**(b-f), correspond to locations marked by orange triangles in **Figure 4.10**(a) and reveal 6-fold symmetric diffraction spots, indicating the high crystallinity for the as-grown hBN. The 2D mapping of SAED patterns in **Figure 4.10**(a), shows single-crystal orientations are maintained among the locations d-f, giving a domain size for the continuous film of about 100 μm, which is much larger than that of an individual triangular hBN nucleated domain in the **Figure 4.7**(c-e). This could be explained from **Figure 4.7**(b), where seamless coalescence occurs when the individual domains have the same orientation. Because most of the as-grown triangular hBN domains are well-aligned in the

specific directions as shown in **Figure 4.7**(i-k), they could stitch together when merging into a continuous film without generating grain boundary defects. Locations b and c in **Figure 4.10**(a) show a rotation of the SAED pattern compared to the lower region and indicate the presence of a domain boundary or folded section. Imaging back-folded edge regions provides a line of contrast for counting the number of layers. There is only one line being observed at the folded edge region (**Figure 4.10**(h)), confirming the hBN grown by OCVD is monolayer. It is also noted that well-orientated triangular holes with various size are observed within the monolayer hBN region with an open edge (**Figure 4.10**(i)). These triangular holes were produced by electron beam irradiation and are in agreement with previous reports of TEM imaging of monolayer hBN films.[39-40] In addition to the monolayer hBN, TEM images show small nanoscale regions containing bilayer and multilayer domains, as shown in **Figure 4.11**(a-b). Further SEM observation (**Figure 4.11**(c)) indicates that the continuous hBN film is composed of 91.8% monolayer regions and 8.2% multilayer regions.

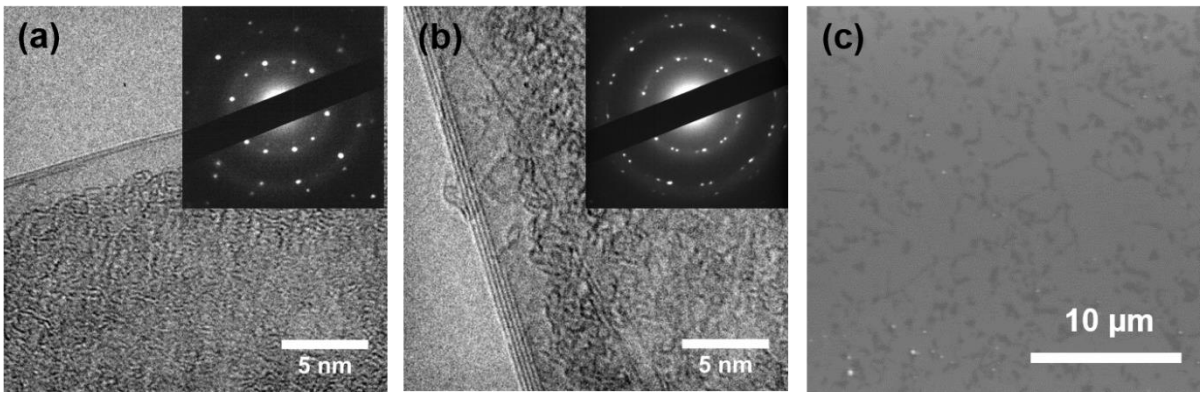


Figure 4.11. TEM characterisation of hBN films containing more than one layer. (a) TEM image of the folded edges for bilayer hBN. The inset shows its corresponding electron diffraction pattern. (b) TEM image of the folded edges for multilayer hBN. The inset shows its corresponding electron diffraction pattern. (c) SEM image of the continuous hBN film on a SiO_2 substrate with the multilayer area.

4.2.3 Employing hBN for the Growth of MoS_2/hBN Vertical Heterostructures

To further evaluate the quality of the as-grwon hBN, the hBN film was adopted as an insulating substrate for the subsequent growth of semiconducting 2D MoS_2. By prolonging the growth time, the obtained hBN continuous films was firstly transferred to the SiO_2 substrate to avoid the reaction between Cu substrate and sulphur precursor. **Figure 4.12**(a) and (b) demonstrates the experimental setup of CVD growth for the MoS_2 on the transferred hBN surface and the resulted atomic structure of the MoS_2/hBN heterostructure. In the growth of MoS_2, two separate furnaces were adopted for better temperature control of both precursors and substrate. In addition, two concentric quartz tubes were used to separate the gaseous precursors before they reached to SiO_2 growth substrate. This helps to avoid the unnecessary reactions between two different precursors during the transport of vaporised molecules to the SiO_2 substrate.

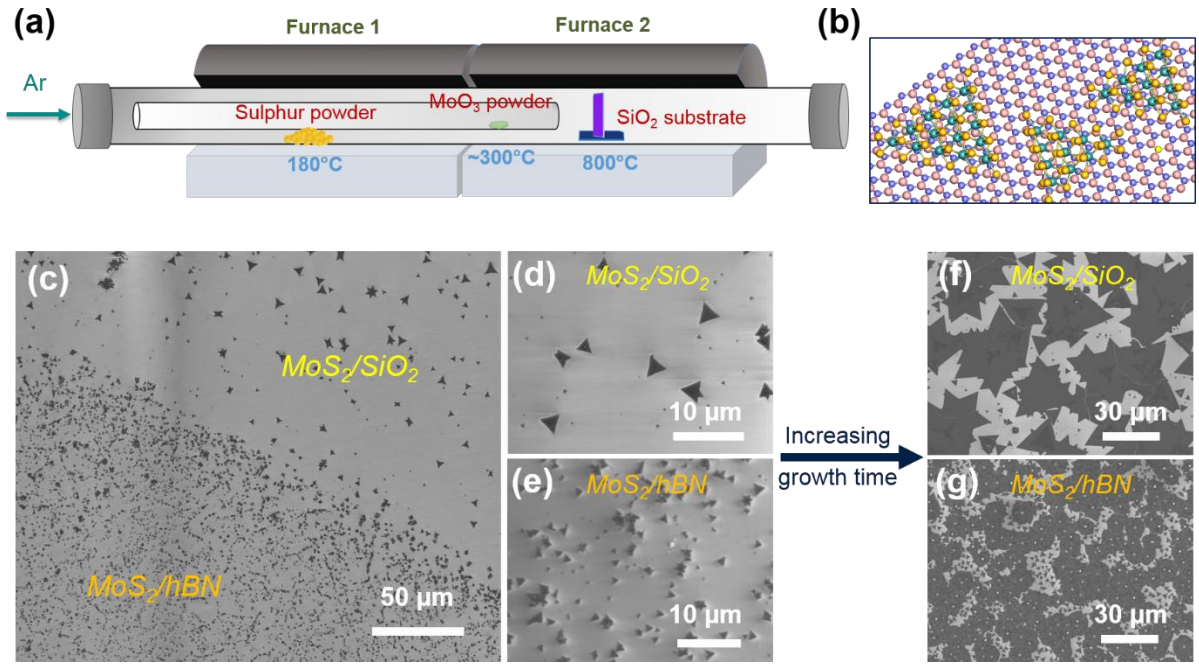


Figure 4.12. Direct growth of MoS_2 layers on the hBN continuous films obtained from OCVD process. (a) Schematic illustration of the CVD experimental setup for the growth of MoS_2 on hBN layers transferred onto a SiO_2 substrate. (b) Schematic illustration showing the atomic model of resulted

MoS_2/hBN vertical heterostructures after MoS_2 growth. (c) Low magnification SEM image of as-grown MoS_2 crystals around the edge region of a hBN continuous film. (d) SEM image of MoS_2 crystals grown on the SiO_2 surface with the growth time of 20 min. (e) SEM image of MoS_2 crystals grown on the hBN surface with the growth time of 20 min. (f) SEM image of MoS_2 crystals grown on the SiO_2 surface with the growth time of 60 min. (g) SEM image of MoS_2 crystals grown on the hBN surface with the growth time of 60 min.

Figure 4.12(c) displays the low magnification SEM image of the MoS_2 grown on the region around the transferred boundary between hBN and SiO_2. The zoomed-in images of MoS_2 grown on SiO_2 and hBN are shown in **Figure 4.12**(d) and (e), respectively. It can be seen that MoS_2 on both hBN and SiO_2 surface exhibits triangular shape with sharp edges and smooth sides and the domain size on both surfaces is around 1~2 μm. Besides, the nucleation density of the MoS_2 grown on hBN is much higher than that grown on SiO_2 surfaces. This may be attributed to the polymer PMMA residual left on the hBN surfaces caused by the transfer process. By increasing the growth time from 20 min to 60 min, the MoS_2 with higher surface coverage could be obtained, shown in **Figure 4.12**(f) and (g). It is noted that higher amount of small MoS_2 nuclei aggregate around the particles from PMMA residual at the hBN surface because of the higher roughness on the substrate surface (**Figure 4.12**(g)), leading to smaller lateral size of MoS_2 crystals compare to that grown on SiO_2 surfaces (**Figure 4.12**(f)). Developing the new transfer process of hBN films with better surface cleanliness in the future is a key role in improving the growth behaviour of MoS_2 and obtaining larger crystals.

Raman and photoluminescence (PL) spectroscopy analysis were useful tools to evaluate the thickness, quality and uniformity of the as-grown MoS_2. **Figure 4.13**(a) provides the Raman spectra of MoS_2 grown on hBN and SiO_2 surface with an excitation wavelength of 532 nm. Two characteristic Raman vibration modes of MoS_2 can be seen in the spectra, the E^1_{2g}

mode and the A_{1g} mode, which are the representation of the in-plane vibration of Mo and S atoms and the out-of-plane vibration of S atoms respectively.[41] The E^1_{2g} mode and the A_{1g} mode of the MoS_2 grown on SiO_2 are located at around 382.9 cm^{-1} and 403.5 cm^{-1}, respectively; while those characteristic peaks of MoS_2 grown on hBN are centred at around 384.7 cm^{-1} and 404.4 cm^{-1}, respectively. The frequency difference of MoS_2 on the both SiO_2 and hBN surface in Raman spectrum is about 20 cm^{-1}, which is consistent with the CVD-grown monolayer MoS_2 in previous works. Besides, the slightly blueshift of E^1_{2g} and A_{1g} peaks from MoS_2 grown on hBN may arise from the lower lattice mismatch and the lattice strain.

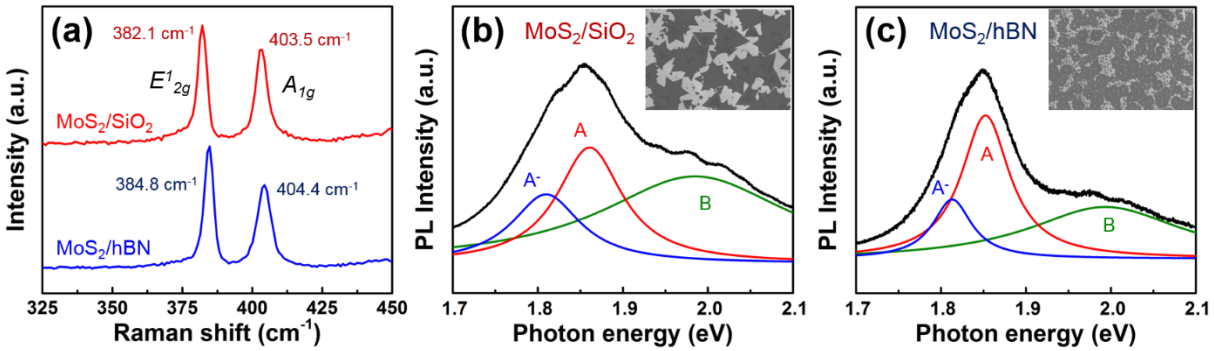


Figure 4.13. Raman and PL characterisation of MoS_2/hBN vertical heterostructures. (a) Raman spectrum of MoS_2 crystals grown on the hBN and SiO_2 surfaces. (b) PL spectrum of MoS_2 crystals grown on the SiO_2 surface with the fitting of the three subpeaks corresponding to the A, A^- and B excitonic transition. (c) PL spectrum of MoS_2 crystals grown on the hBN surface with the fitting of the three subpeaks corresponding to the A, A^- and B excitonic transition.

The characteristic peak of MoS_2 in the PL spectrum shown in **Figure 4.13**(b-c) contains three subpeaks, located at about 625, 670, 680 nm, corresponding to the A1 exciton emission, B1 exciton emission, and recombination of trions, respectively.[42] The A1 and B1 emissions arise from the direct excitonic transitions at the Brillouin zone K point with the energy difference due to the spin-orbital splitting of the valence band. Through the fitting with the

three subpeaks of MoS_2, the intensity ratio between A and A^- subpeaks could be extracted. It can be seen that the A/A^- intensity ratio of MoS_2 grown on hBN surface is around 2.62 (**Figure 4.13**(c)), which is 53% higher than that on SiO_2 surface where the A/A^- intensity ratio is around 1.71 (**Figure 4.13**(b)). This is attributed to the less amount of charge impurities and lower doping level for MoS_2 grown on hBN than SiO_2. The as-grown hBN film could be therefore regarded as an ideal substrate for the growth of other 2D materials when compared to the conventional SiO_2 substrate.

4.3 Conclusion

In summary, this chapter demonstrates the significant decrease in nucleation density through the OCVD growth of hBN, in which the formation of a passivating oxide layer on the Cu surface is preceded by the growth of hBN. The domain size of hBN can therefore be enhanced from 1 to 20 μm, and the merger of aligned domains leads to single-crystal domains at least 100 μm in size. Both AFM and Raman analysis show that the as-grown hBN is monolayer with high quality and uniformity. The orientation of hBN grown by OCVD exhibits a strong dependence on the crystallographic orientation of the underlying Cu substrate. Most of the hBN domains are well-aligned within the same Cu grain, making the grain size of the continuous hBN film possibly equal to that of the grain in the Cu substrate. This work is an alternative approach to those already reported for growing hBN films with large domain sizes because this work utilises the oxide surface of Cu to suppress nucleation density. The substrates used are cheap and easily prepared by a rapid mechanical polishing before oxidation, both of which are easy to scale up and are safe.

4.4 Reference

(1) Kim, K. K.; Hsu, A.; Jia, X.; Kim, S. M.; Shi, Y.; Hofmann, M.; Nezich, D.; Rodriguez-Nieva, J. F.; Dresselhaus, M.; Palacios, T.; Kong, J. Synthesis of Monolayer Hexagonal Boron Nitride on Cu Foil Using Chemical Vapor Deposition. *Nano Lett.* **2012,** *12*, 161-166.

(2) Shi, Y.; Hamsen, C.; Jia, X.; Kim, K. K.; Reina, A.; Hofmann, M.; Hsu, A. L.; Zhang, K.; Li, H.; Juang, Z.-Y.; Dresselhaus, M. S.; Li, L.-J.; Kong, J. Synthesis of Few-Layer Hexagonal Boron Nitride Thin Film by Chemical Vapor Deposition. *Nano Lett.* **2010,** *10*, 4134-4139.

(3) Kim, G.; Jang, A. R.; Jeong, H. Y.; Lee, Z.; Kang, D. J.; Shin, H. S. Growth of High-Crystalline, Single-Layer Hexagonal Boron Nitride on Recyclable Platinum Foil. *Nano Lett.* **2013,** *13*, 1834-1839.

(4) Park, J.-H.; Park, J. C.; Yun, S. J.; Kim, H.; Luong, D. H.; Kim, S. M.; Choi, S. H.; Yang, W.; Kong, J.; Kim, K. K.; Lee, Y. H. Large-Area Monolayer Hexagonal Boron Nitride on Pt Foil. *ACS Nano* **2014,** *8*, 8520-8528.

(5) Kim, S. M.; Hsu, A.; Park, M. H.; Chae, S. H.; Yun, S. J.; Lee, J. S.; Cho, D.-H.; Fang, W.; Lee, C.; Palacios, T.; Dresselhaus, M.; Kim, K. K.; Lee, Y. H.; Kong, J. Synthesis of Large-Area Multilayer Hexagonal Boron Nitride for High Material Performance. *Nat. Commun.* **2015,** *6*, 8662.

(6) Orofeo, C. M.; Suzuki, S.; Kageshima, H.; Hibino, H. Growth and Low-Energy Electron Microscopy Characterization of Monolayer Hexagonal Boron Nitride on Epitaxial Cobalt. *Nano Res.* **2013,** *6*, 335-347.

(7) Farwick zum Hagen, F. H.; Zimmermann, D. M.; Silva, C. C.; Schlueter, C.; Atodiresei, N.; Jolie, W.; Martínez-Galera, A. J.; Dombrowski, D.; Schröder, U. A.; Will, M.; Lazić, P.; Caciuc, V.; Blügel, S.; Lee, T.-L.; Michely, T.; Busse, C. Structure and Growth of Hexagonal Boron Nitride on Ir(111). *ACS Nano* **2016,** *10*, 11012-11026.

(8) Sutter, P.; Lahiri, J.; Albrecht, P.; Sutter, E. Chemical Vapor Deposition and Etching of High-Quality Monolayer Hexagonal Boron Nitride Films. *ACS Nano* **2011,** *5*, 7303-7309.

(9) Corso, M.; Auwärter, W.; Muntwiler, M.; Tamai, A.; Greber, T.; Osterwalder, J. Boron Nitride Nanomesh. *Science* **2004,** *303*, 217-220.

(10) Müller, F.; Grandthyll, S. Monolayer Formation of Hexagonal Boron Nitride on Ag(001). *Surf. Sci.* **2013,** *617*, 207-210.

(11) Behura, S.; Nguyen, P.; Che, S.; Debbarma, R.; Berry, V. Large-Area, Transfer-Free, Oxide-Assisted Synthesis of Hexagonal Boron Nitride Films and Their Heterostructures with MoS_2 and WS_2. *J. Am. Chem. Soc.* **2015,** *137*, 13060-13065.

(12) Jang, A. R.; Hong, S.; Hyun, C.; Yoon, S. I.; Kim, G.; Jeong, H. Y.; Shin, T. J.; Park, S. O.; Wong, K.; Kwak, S. K.; Park, N.; Yu, K.; Choi, E.; Mishchenko, A.; Withers, F.; Novoselov, K. S.; Lim, H.; Shin, H. S. Wafer-Scale and Wrinkle-Free Epitaxial Growth of Single-Orientated Multilayer Hexagonal Boron Nitride on Sapphire. *Nano Lett.* **2016,** *16*, 3360-3366.

(13) Ismach, A.; Chou, H.; Ferrer, D. A.; Wu, Y.; McDonnell, S.; Floresca, H. C.; Covacevich, A.; Pope, C.; Piner, R.; Kim, M. J.; Wallace, R. M.; Colombo, L.; Ruoff, R. S. Toward the Controlled Synthesis of Hexagonal Boron Nitride Films. *ACS Nano* **2012,** *6*, 6378-6385.

(14) Jaehyun, H.; Jun-Young, L.; Heemin, K.; Jong-Souk, Y. Synthesis of Wafer-Scale Hexagonal Boron Nitride Monolayers Free of Aminoborane Nanoparticles by Chemical Vapor Deposition. *Nanotechnology* **2014,** *25*, 145604.

(15) Tay, R. Y.; Li, H.; Tsang, S. H.; Zhu, M.; Loeblein, M.; Jing, L.; Leong, F. N.; Teo, E. H. T. Trimethylamine Borane: A New Single-Source Precursor for Monolayer hBN Single Crystals and h-BCN Thin Films. *Chem. Mater.* **2016,** *28*, 2180-2190.

(16) Wang, X.; Hooper, T. N.; Kumar, A.; Priest, I. K.; Sheng, Y.; Samuels, T. O. M.; Wang, S.; Robertson, A. W.; Pacios, M.; Bhaskaran, H.; Weller, A. S.; Warner, J. H. Oligomeric Aminoborane Precursors for the Chemical Vapour Deposition Growth of Few-Layer Hexagonal Boron Nitride. *CrystEngComm* **2017,** *19*, 285-294.

(17) Sutter, P.; Lahiri, J.; Zahl, P.; Wang, B.; Sutter, E. Scalable Synthesis of Uniform Few-Layer Hexagonal Boron Nitride Dielectric Films. *Nano Lett.* **2013,** *13*, 276-281.

(18) Wang, H.; Zhang, X.; Meng, J.; Yin, Z.; Liu, X.; Zhao, Y.; Zhang, L. Controlled Growth of Few-Layer Hexagonal Boron Nitride on Copper Foils Using Ion Beam Sputtering Deposition. *Small* **2015,** *11*, 1542-1547.

(19) Glavin, N. R.; Jespersen, M. L.; Check, M. H.; Hu, J.; Hilton, A. M.; Fisher, T. S.; Voevodin, A. A. Synthesis of Few-Layer, Large Area Hexagonal-Boron Nitride by Pulsed Laser Deposition. *Thin Solid Films* **2014,** *572*, 245-250.

(20) Nakhaie, S.; Wofford, J. M.; Schumann, T.; Jahn, U.; Ramsteiner, M.; Hanke, M.; Lopes, J. M. J.; Riechert, H. Synthesis of Atomically Thin Hexagonal Boron Nitride Films on Nickel Foils by Molecular Beam Epitaxy. *Appl. Phys. Lett.* **2015,** *106*, 213108.

(21) Kim, H.; Mattevi, C.; Calvo, M. R.; Oberg, J. C.; Artiglia, L.; Agnoli, S.; Hirjibehedin, C. F.; Chhowalla, M.; Saiz, E. Activation Energy Paths for Graphene Nucleation and Growth on Cu. *ACS Nano* **2012,** *6*, 3614-3623.

(22) Stehle, Y.; Meyer, H. M.; Unocic, R. R.; Kidder, M.; Polizos, G.; Datskos, P. G.; Jackson, R.; Smirnov, S. N.; Vlassiouk, I. V. Synthesis of Hexagonal Boron Nitride Monolayer: Control of Nucleation and Crystal Morphology. *Chem. Mater.* **2015,** *27*, 8041-8047.

(23) Tay, R. Y.; Griep, M. H.; Mallick, G.; Tsang, S. H.; Singh, R. S.; Tumlin, T.; Teo, E. H. T.; Karna, S. P. Growth of Large Single-Crystalline Two-Dimensional Boron Nitride Hexagons on Electropolished Copper. *Nano Lett.* **2014,** *14*, 839-846.

(24) Khan, M. H.; Huang, Z.; Xiao, F.; Casillas, G.; Chen, Z.; Molino, P. J.; Liu, H. K. Synthesis of Large and Few Atomic Layers of Hexagonal Boron Nitride on Melted Copper. *Sci. Rep.* **2015,** *5*, 7743.

(25) Tay, R. Y.; Park, H. J.; Ryu, G. H.; Tan, D.; Tsang, S. H.; Li, H.; Liu, W.; Teo, E. H. T.; Lee, Z.; Lifshitz, Y.; Ruoff, R. S. Synthesis of Aligned Symmetrical Multifaceted Monolayer Hexagonal Boron Nitride Single Crystals on Resolidified Copper. *Nanoscale* **2016,** *8*, 2434-2444.

(26) Song, X.; Gao, J.; Nie, Y.; Gao, T.; Sun, J.; Ma, D.; Li, Q.; Chen, Y.; Jin, C.; Bachmatiuk, A.; Rümmeli, M. H.; Ding, F.; Zhang, Y.; Liu, Z. Chemical Vapor Deposition Growth of Large-Scale Hexagonal Boron Nitride with Controllable Orientation. *Nano Res.* **2015,** *8*, 3164-3176.

(27) Grace, E. W.; Alexander, J. M.; James, J. M.; Marc, W.; Maria, A.; Jose, A.; Kai, C.; Gavin, R. B.; Neil, R. W. Van der Waals Epitaxy of Monolayer Hexagonal Boron Nitride on Copper Foil: Growth, Crystallography and Electronic Band Structure. *2D Mater.* **2015,** *2*, 025003.

(28) Yin, J.; Liu, X.; Lu, W.; Li, J.; Cao, Y.; Li, Y.; Xu, Y.; Li, X.; Zhou, J.; Jin, C.; Guo, W. Aligned Growth of Hexagonal Boron Nitride Monolayer on Germanium. *Small* **2015,** *11*, 5375-5380.

(29) Li, J.; Li, Y.; Yin, J.; Ren, X.; Liu, X.; Jin, C.; Guo, W. Growth of Polar Hexagonal Boron Nitride Monolayer on Nonpolar Copper with Unique Orientation. *Small* **2016,** *12*, 3645-3650.

(30) Wu, Q.; Park, J.-H.; Park, S.; Jung, S. J.; Suh, H.; Park, N.; Wongwiriyapan, W.; Lee, S.; Lee, Y. H.; Song, Y. J. Single Crystalline Film of Hexagonal Boron Nitride Atomic Monolayer by Controlling Nucleation Seeds and Domains. *Sci. Rep.* **2015,** *5*, 16159.

(31) Lu, G.; Wu, T.; Yuan, Q.; Wang, H.; Wang, H.; Ding, F.; Xie, X.; Jiang, M. Synthesis of Large Single-Crystal Hexagonal Boron Nitride Grains on Cu–Ni Alloy. *Nat. Commun.* **2015,** *6*, 6160.

(32) Caneva, S.; Weatherup, R. S.; Bayer, B. C.; Brennan, B.; Spencer, S. J.; Mingard, K.; Cabrero-Vilatela, A.; Baehtz, C.; Pollard, A. J.; Hofmann, S. Nucleation Control for Large, Single Crystalline Domains of Monolayer Hexagonal Boron Nitride via Si-Doped Fe Catalysts. *Nano Lett.* **2015,** *15*, 1867-1875.

(33) Zhou, H.; Yu, W. J.; Liu, L.; Cheng, R.; Chen, Y.; Huang, X.; Liu, Y.; Wang, Y.; Huang, Y.; Duan, X. Chemical Vapour Deposition Growth of Large Single Crystals of Monolayer and Bilayer Graphene. *Nat. Commun.* **2013,** *4*, 2096.

(34) Hao, Y.; Bharathi, M. S.; Wang, L.; Liu, Y.; Chen, H.; Nie, S.; Wang, X.; Chou, H.; Tan, C.; Fallahazad, B.; Ramanarayan, H.; Magnuson, C. W.; Tutuc, E.; Yakobson, B. I.; McCarty, K. F.; Zhang, Y.-W.; Kim, P.; Hone, J.; Colombo, L.; Ruoff, R. S. The Role of Surface Oxygen in the Growth of Large Single-Crystal Graphene on Copper. *Science* **2013,** *342*, 720-723.

(35) Hao, Y.; Wang, L.; Liu, Y.; Chen, H.; Wang, X.; Tan, C.; Nie, S.; Suk, J. W.; Jiang, T.; Liang, T.; Xiao, J.; Ye, W.; Dean, C. R.; Yakobson, B. I.; McCarty, K. F.; Kim, P.; Hone, J.; Colombo, L.; Ruoff, R. S. Oxygen-Activated Growth and Bandgap Tunability of Large Single-Crystal Bilayer Graphene. *Nat. Nanotechnol.* **2016,** *11*, 426-431.

(36) Chang, R.-J.; Lee, C.-H.; Lee, M.-K.; Chen, C.-W.; Wen, C.-Y. Effects of Surface Oxidation of Cu Substrates on the Growth Kinetics of Graphene by Chemical Vapor Deposition. *Nanoscale* **2017,** *9*, 2324-2329.

(37) Li, X.; Li, Y.; Wang, Q.; Yin, J.; Li, J.; Yu, J.; Guo, W. Oxygen-Suppressed Selective Growth of Monolayer Hexagonal Boron Nitride on Copper Twin Crystals. *Nano Res.* **2017,** *10*, 826-833.

(38) Liu, Y.; Bhowmick, S.; Yakobson, B. I. BN White Graphene with "Colorful" Edges: The Energies and Morphology. *Nano Lett.* **2011,** *11*, 3113-3116.

(39) Jin, C.; Lin, F.; Suenaga, K.; Iijima, S. Fabrication of a Freestanding Boron Nitride Single Layer and Its Defect Assignments. *Phys. Rev. Lett.* **2009,** *102*, 195505.

(40) Warner, J. H.; Rümmeli, M. H.; Bachmatiuk, A.; Büchner, B. Atomic Resolution Imaging and Topography of Boron Nitride Sheets Produced by Chemical Exfoliation. *ACS Nano* **2010,** *4*, 1299-1304.

(41) Tonndorf, P.; Schmidt, R.; Böttger, P.; Zhang, X.; Börner, J.; Liebig, A.; Albrecht, M.; Kloc, C.; Gordan, O.; Zahn, D. R. T.; Michaelis de Vasconcellos, S.; Bratschitsch, R.,

Photoluminescence Emission and Raman Response of Monolayer MoS_2, $MoSe_2$, and WSe_2. *Opt. Express* **2013,** *21*, 4908-4916.

(42) Splendiani, A.; Sun, L.; Zhang, Y.; Li, T.; Kim, J.; Chim, C.-Y.; Galli, G.; Wang, F., Emerging Photoluminescence in Monolayer MoS_2. *Nano Lett.* **2010,** *10*, 1271-1275.

Chapter 5

Chemical Vapour Deposition Growth of 2D Layered Tin Disulfide and its Optoelectronic Characteristics with Graphene Electrodes

5.1 Introduction

For the purpose of optoelectronic devices with greater selectivity in wavelength, it is essential to develop other 2D layered semiconductors with bandgaps that could cover the entire visible spectrum. The 2D semiconducting materials with blue and green light absorption have therefore been exploited in the past few years. For example, metal monochalcogenide gallium sulfide (GaS) has reported to exhibit a bandgap of 2.5 eV when reducing to monolayer,[1] which is appropriate for blue-light channel. In comparison, 2D indium selenide (InSe), gallium selenide (GaSe) and tin disulfide (SnS_2) are ideal candidates for green-light channel, with the bandgap of 2.4 eV,[2] 2.1 eV and 2.2 eV,[3-4] respectively.

Photodetector is one of the application of SnS_2 that shows promising potential. Huang *et al.* first used the mechanical exfoliated few-layer SnS_2 to fabricate photodetecting transistors and demonstrated a photoresponsivity of ~100 A/W.[5] Similarly, Tao *et al.* later developed a chemical hot bath method for the synthesis of SnS_2, and the resulting photodetector showed a high spectral selectivity. However, the lack of scalability hinders these top-down approaches from industrial mass production.[6] In comparison, chemical vapour deposition (CVD) is the effective way to achieve large area growth of atomically thin 2D materials for successful device applications. The CVD growth of MoS_2 and WS_2 has been well-investigated, the domain size

could be at the scale of 100 μm and the growth of continuous films with high uniformity could also be achieved.[7-9] In light of this, Su *et al.* reported a controlled CVD growth of SnS_2 on SiO_2 with a patterned seed array. The as-fabricated photodetectors exhibit a short response time ~5 μs, which is much faster than other layered 2D semiconductors.[10] The CVD-grown SnS_2 with different morphologies has been subsequently demonstrated on other growth substrates and integrated on polymer film for flexible photodetectors.[11-12] Photodetecting devices incorporating van dew Waals (vdW) crystals with SnS_2 layers and other 2D materials, however, have not been reported yet. This may be ascribed to the complex fabrication process including multiple lift-off and etching procedures to pattern 2D materials without damaging their adjacent layers.

In this chapter, the use of combination of SnS_2 with graphene (Gr) to fabricate Gr-SnS_2-Gr lateral heterostructures as well as the estimation of their photodetecting performance are demonstrated. All the 2D materials are obtained from CVD growth, which has the advantages for scalable production in the future compared to previous reports using mechanical exfoliation.[13] The adjustable Fermi level of Gr could modulate the Schottky barrier height and lower the contact resistance at the Gr-SnS_2 interface, giving rise to high photoresponsivity (~ 20 A/W) and detectivity (4×10^{14} Jones). The thickness of the SnS_2 channel is also found to be influential on the detection behaviour- turning from interface dominant to bulk dominant as the thickness of SnS_2 increases. These appealing features of SnS_2-based photodetectors offer a bright future for the applications in flexible optoelectronics.

5.2 Results and Discussion

5.2.1 Synthesis and Characterization of SnS_2 Crystals

Figure 5.1(a) schematically illustrates the CVD setup for the CVD growth of SnS_2 with a SiO_2 substrate placed on the ceramic crucible. SnS_2 was grown by using tin sulfide (SnS) and sulfur precursors. Sulfur and SnS precursors are placed in the centre of furnace 1 and 2, respectively, whereas the SiO_2 substrate is put at the downstream of furnace 2, around 6 cm away from the SnS powders. Compared to conventional tin precursors of tin dioxide (SnO_2) for the synthesis of SnS_2, the SnS precursor could reduce the thermal budget of CVD growth as the bonding energy of Sn-S is lower than that of Sn-O bonding.[14] Besides, the absence of oxygen in the precursor is also beneficial for the growth of high crystallinity without oxygen defects. The SnS_2 growth was carried out using a custom-designed 1-inch CVD system with quartz tube and gas flow rates controlled by digital mass flow controllers. The two separate furnaces provide better control of both precursors and substrate. With a view to avoiding unnecessary reactions between two different precursors during vaporised atoms' transportation to the substrate, two concentric quartz tubes were used to separate the gaseous precursors before they reached the substrate surface.

The detailed growth parameter setting is displayed in **Figure 5.1**(b). At the beginning of the growth, both of the furnace temperatures were raised over 180°C for 15 min with 100 sccm Ar carrier gas to provide sulfur-rich environment for the whole CVD reactor. The furnace 2 was then heated up to 550°C, followed by a 15 min SnS_2 growth. After the growth, the flow rate of Ar was set down to 10 sccm, and the furnace 1 was raised to 400°C to evaporate the residual sulfur powders. Those excess sulfur vapours were purged away by turning back the flow rate of Ar to 500 sccm when the temperature of furnace 2 was lower than 500°C. The fast cooling was carried out after the purging of sulfur vapour to stop the CVD growth process. By

optimising the growth parameters, which will be discussed later, the high-quality of layered SnS_2 crystals with different thicknesses could be obtained. **Figure 5.1**(c) and (d) are the low-magnification and high-magnification optical images of the as-grown SnS_2 crystals, respectively. It is noted that except growing along the planar directions (**Figure 5.1**(e)), part of the SnS_2 crystals are grown in out-of-plane directions and stand semi-vertically (**Figure 5.1**(f)). This may be attributed to the large amount of dangling bonds on the SiO_2 surface, resulting in larger energy barrier for surface diffusion and shorter diffusion length of the Sn-S active species.

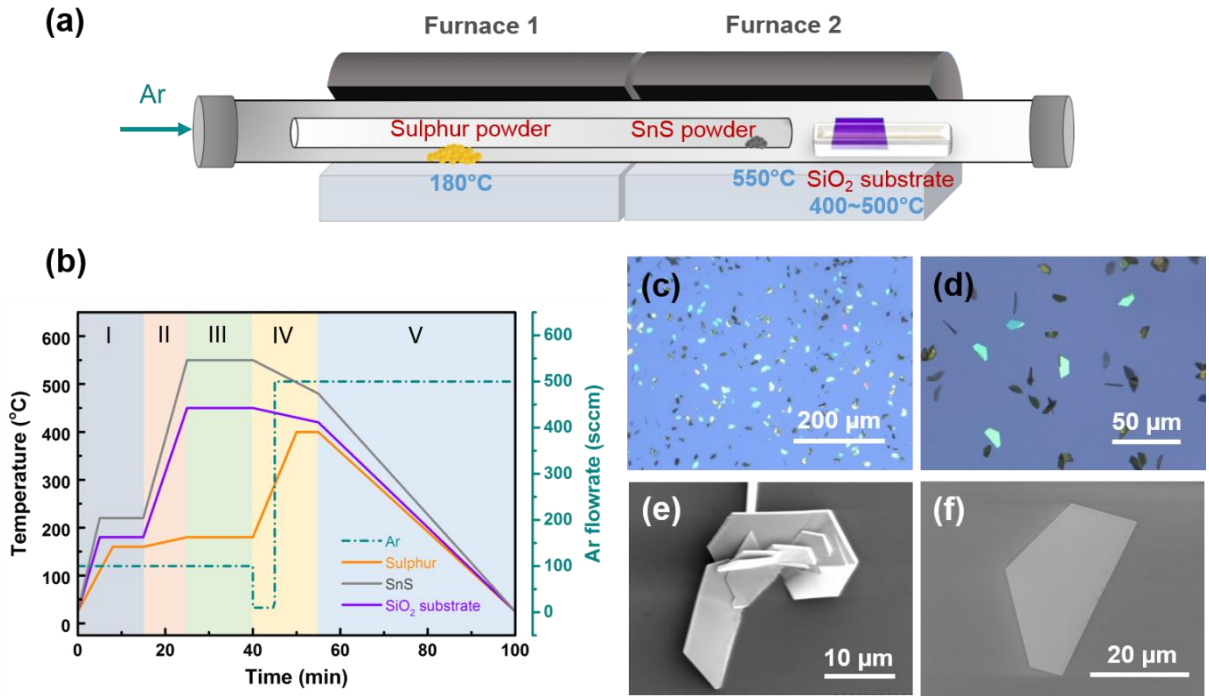


Figure 5.1. Atmospheric-pressure CVD synthesis of SnS_2 crystals on SiO_2 substrate. (a) Schematic illustration of the CVD experimental setup for synthesising SnS_2 crystals. (b) Temperature and carrier gas profile for the CVD growth. There are five stages included in the whole process: (I) Sulfur pre-introduction, (II) heating, (III) growth, (IV) slow cooling, and (V) fast cooling. (c) Low-magnification optical image to show the large-scale production of as-grown SnS_2 crystals. (d) Enlarged optical image showing the details of thin and thick SnS_2 crystals. (e-f) SEM images of SnS_2 crystals grow in the (e) perpendicular and (f) horizontal directions to the SiO_2 substrates, respectively.

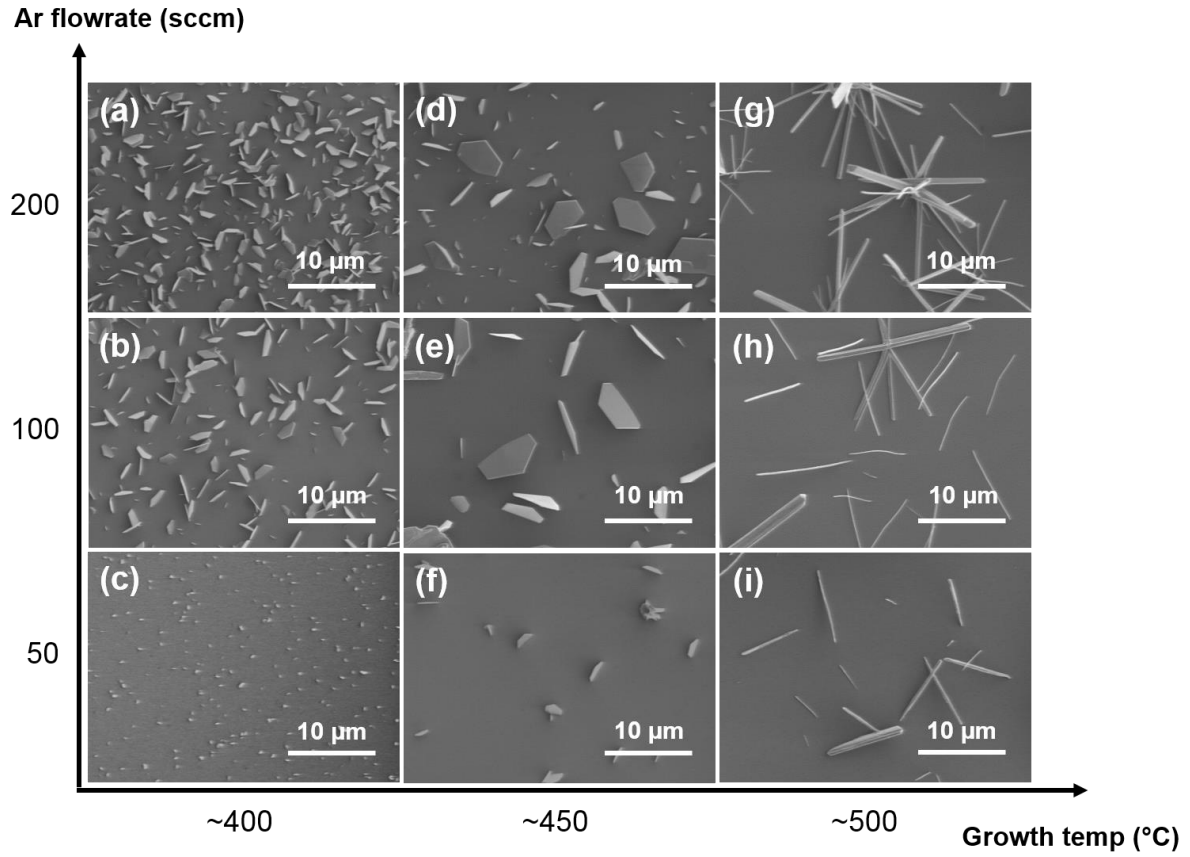


Figure 5.2. SEM images demonstrating the morphology control of SnS_2 growth under different growth conditions in terms of T (°C)/J_{Ar} (sccm): (a) 400/200, (b) 400/100, (c) 400/50, (d) 450/200, (e) 450/100, (f) 450/50, (g) 500/200, (h) 500/100, and (i) 500/50.

In the typical CVD growth, there are five elementary steps including (1) the sublimation of precursors and the transport of gas molecules to the substrate, (2) diffusion of the molecules through the boundary layer and adsorption of molecules onto the substrate surface, (3) surface diffusion of the active species, (4) attachment to the growth sites that are thermally stable, and (5) desorption of the excess active species. Generally, the rate-limiting step in the whole growth process could be either diffusion (step (2)) or reaction on the substrate surface (step (3) and (4)), which is strongly affected by the flow rate of the carrier gas and reaction temperature, respectively. To obtain SnS_2 crystals with high quality, the growth of SnS_2 was systematically optimised through tuning these crucial parameters, as reported in **Figure 5.2**. As shown in

Figure 5.2(g-i), the growth begins to transfer from nanoplatelets to nanowires when the growth temperature is above 500°C. The Raman spectrum for these nanowires shown in **Figure 5.3** exhibits the characteristic peaks located at 153.5, 235.2, and 309.1 cm^{-1}. These peaks were observed in other reports of Sn_2S_3 growth, indicating the existence of Sn_2S_3 under higher growth temperature.[15] The growth of SnS_2 is preferential under the growth temperature below 500°C, leading to the growth in the planar direction where the crystal morphology becomes trapezoid, which is similar to previous reports. The low rate of Ar carrier gas is found to be influential to the growth direction. As shown in **Figure 5.2**(d-f), a high Ar flow rate produces a larger percentage of the SnS_2 crystals growing along out-of-plane directions, whereas a low Ar flow rate could lower the reaction rate of the tin and sulfur precursors. This phenomenon could be ascribed to the different mass transfer rates in the CVD growth. Under the high Ar flow rate, the adsorbed species on the SiO_2 substrate may not have enough time to incorporate into the lattice site that is most thermodynamically stable. The SnS_2 crystals therefore have higher tendencies to grow with out-of-plane directions. The low Ar flow rate, in comparison, results in larger boundary layer thickness for mass transport and restricts the precursor supplies. Through the growth parameter optimisation, the moderate growth temperature and the Ar carrier flow rate could lead to a better growth of SnS_2 crystals. The SnS_2 crystals with domain size around 20 μm and thickness of 10-30 nm could be obtained under 450°C and Ar flow rate of 100 sccm.

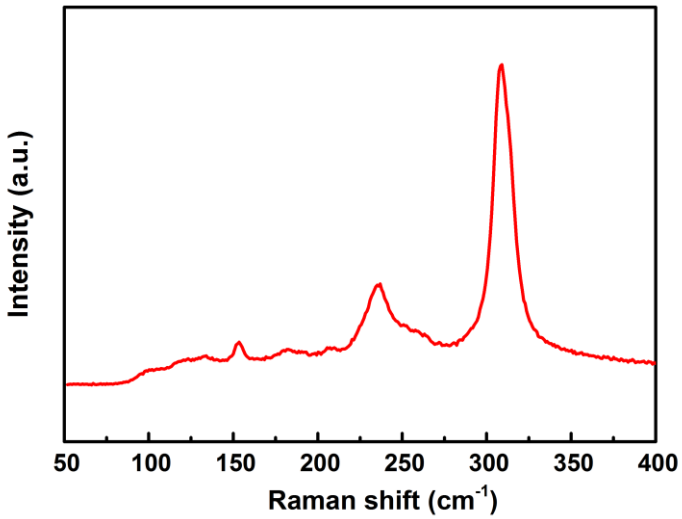


Figure 5.3. Raman spectrum of Sn_2S_3 obtained from the higher growth temperature regime.

To determine the thickness of individual SnS_2 crystals, atomic force microscopy (AFM) was performed. **Figure 5.4**(a) shows the as-grown SnS_2 crystals with a variety of thickness. The measured AFM thicknesses of the crystals marked by the blue and green dashed circle are listed in **Figure 5.4**(b) and (c). The Raman spectrum was further used to characterise the SnS_2 crystals with different thicknesses. As shown in **Figure 5.4**(d), there are two Raman characteristic peaks of SnS_2, A_{1g} at 314 cm^{-1} and E_g at 207 cm^{-1}, corresponding to the out-of-plane vibrational phonon mode and the intra-layer vibrational phonon mode.[16] The E_g peak disappears with decreasing the number of layers because of the reduction in the number of scattering centres for the in-plane scattering. In addition, the absence of the A_g and B_{3g} peaks confirms that the SnS precursor was fully converted into SnS_2 on the SiO_2 substrates.[17]

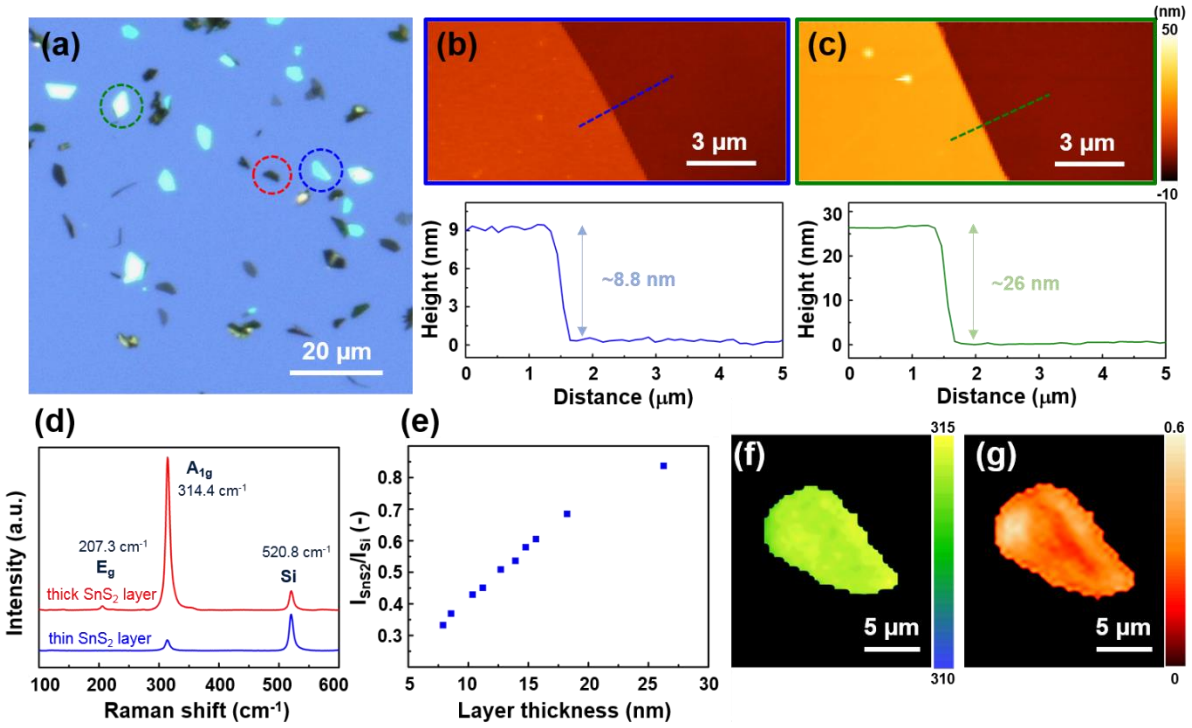


Figure 5.4. Raman analysis and AFM study of SnS_2 crystals. (a) Optical image displaying the distribution of SnS_2 crystals with different thicknesses. (b-c) AFM images and height profiles of SnS_2 crystals with different thicknesses indicated by the blue and green dashed circle, respectively, in (a). (d) Raman spectrum of SnS_2 crystals with different thicknesses indicated by the blue and red dashed circle, respectively, in (a). (e) Relationship between the intensity ratio of SnS_2 A_{1g} peak and Si characteristic peak from Raman spectrum and the layer thickness measured by AFM. (f) Raman mapping for the peak position of A_{1g} mode from SnS_2 crystal indicated in the blue dashed circle in (a). (g) Raman mapping for the peak intensity ratio between A_{1g} mode from the same SnS_2 crystal and Si substrate.

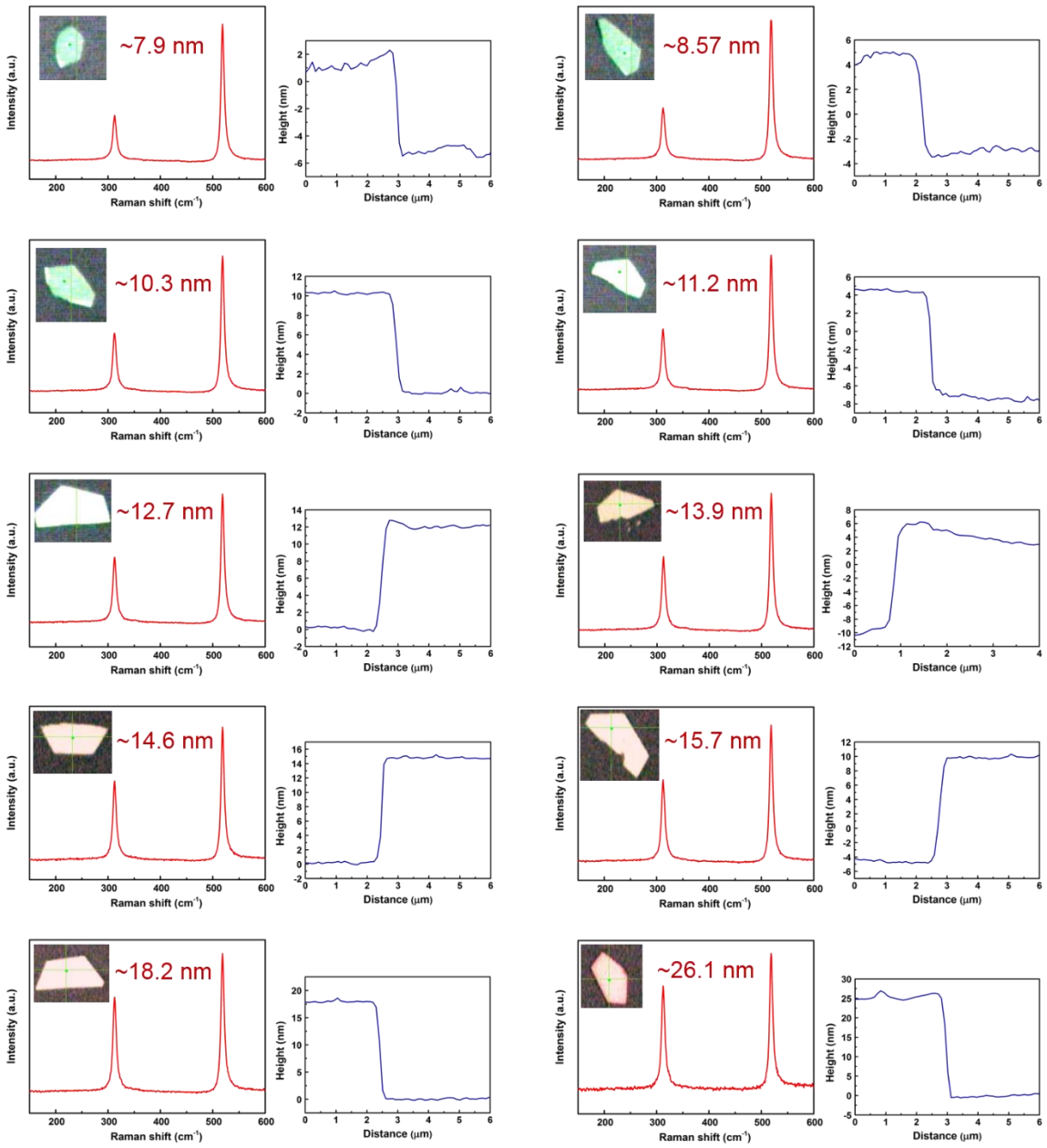


Figure 5.5. Raman spectrum and corresponded step height profiles measured from AFM for SnS_2 crystals with different thicknesses.

To quantify the thickness dependence, the AFM measurement is further combined with Raman analysis (**Figure 5.5**). As shown in **Figure 5.4**(e), each SnS_2 characteristic peak from the Raman spectrum was normalised by the intensity of the Si peak. It can be seen from **Figure 5.4**(e) that the intensity ratio of A_{1g} peak and Si peak increases approximately linearly with

thickness, which is consistent with the previous simulation report using a first-principles calculation method.[18] This enables Raman analysis to serve as a simple approach for measuring the layer number. To elucidate the uniformity of individual SnS_2 domains, the SnS_2 crystal marked by the blue dashed circle in **Figure 5.4**(a) was further analysed by Raman mapping. The A_{1g} peak position mapping from **Figure 5.4**(f) shows that all the SnS_2 crystal positions exhibit a characteristic peak centred around 313.5 to 314.5 cm^{-1}, indicating the composition uniformity. From **Figure 5.4**(g) demonstrating the mapping for the intensity ratio of the A_{1g} peak to the Si characteristic peak, it can be seen that the area near the crystal edge has slightly larger value. This could result from the defects near the SnS_2 crystal edges that accelerate the adlayer growth.

5.2.2 Photodetecting Transistors Based on Gr-SnS_2-Gr

To further evaluate the quality of as-grown SnS_2 crystals, the SnS_2 photodetector was fabricated using a PMMA supporting layer to transfer the as-grown SnS_2 onto Gr ribbons; the detail is described in Chapter 3. **Figure 5.6**(a) schematically shows the top view and the side view of the SnS_2 photodetector with the Gr electrodes connected to the Cr/Au bond pads. **Figure 5.6**(b) shows the optical image of such a device that includes the SnS_2 crystals bridging between the Gr electrodes. The gap between the Gr electrodes is measured to be 1 μm. The quality of the Gr electrodes is identified by the Raman spectrum shown in **Figure 5.7**(a). The intensity of the 2D peak is twice larger than the G peak, and the absence of the D peak indicates a monolayer Gr with high quality.

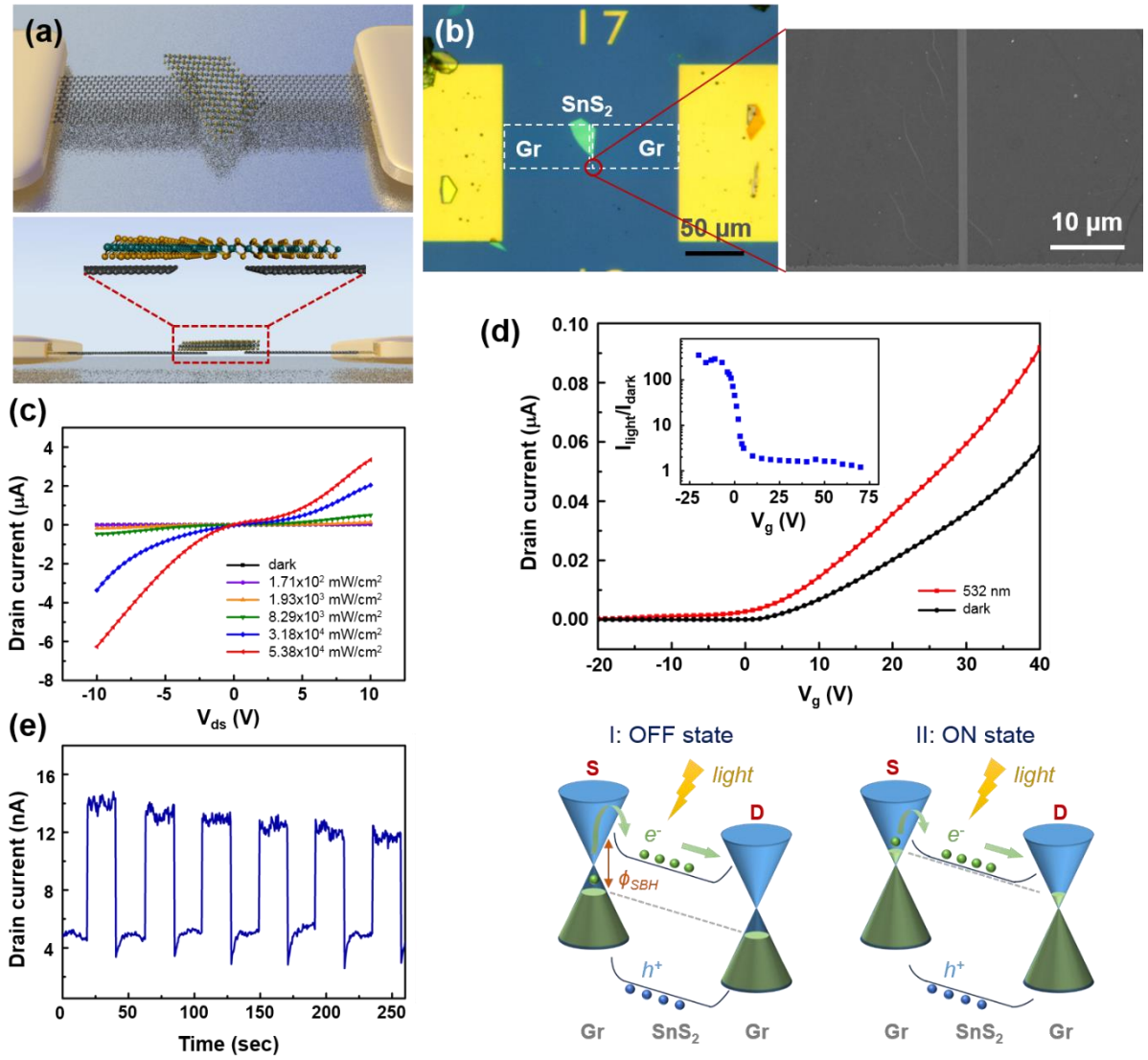


Figure 5.6. Characteristics of SnS_2-based photodetectors. (a) Schematic illustrations of the fabricated photodetector with SnS_2 crystals on patterned Gr ribbons. (b) Optical image of a fabricated single Gr-SnS_2-Gr photodetector. The magnified SEM image shows that the gap between Gr electrodes is 1 μm. (c) I-V curve of the Gr-SnS_2-Gr device in the dark and in the presence of laser illumination with different intensities. (d) Comparison of the transfer curves for a Gr-SnS_2-Gr photodetector measured in the dark and under the illumination at 171 mW/cm^2 and under 5 V biased voltage. The inset shows the photoresponse ratio of the illumination current and dark current as a function of the gate bias. The bottom illustration displays the band diagram of the SnS_2 photodetector at the Gr electrode contacts when tuning the gate voltage in the ON and OFF state. (e) Photoswitching behaviour of the

device resulted from the incident pulsed laser light with an intensity 2.55×10^4 mW/cm^2 under bias of 2 V.

Figure 5.6(c) displays the output characteristics of the device. The IV measurement both under the dark state (**Figure 5.7**(b)) and laser illumination is notably nonlinear and asymmetric with respect to the bias polarity, indicating the Schottky contact between the Gr electrode and the SnS_2 channel. The dependence of the current on the back-gate voltage is also investigated. As shown in **Figure 5.7**(c), the transfer characteristics of the device demonstrate the n-type behaviour with higher conductance at high gate voltage. The device retains its n-type characteristics under the laser illumination, and the drain current is larger than that in the dark for all applied gate voltages and increases significantly when sweeping the gate voltage to the on state, shown in **Figure 5.6**(d). This indicates that the photocurrent dominates over thermionic and tunnelling current in the entire operation of the device. It should be noted that in our device geometries the Gr ribbons are also affected by the back gate potential (e.g., change of conductivity with different gate voltages). To improve this drawback, the top-gate design, where the metal oxide gate electrodes can be selectively deposited on the SnS_2 surface, is suggested to utilise to precisely measure the characteristics of SnS_2 channel.

The influence of the gate voltage on the photoresponse ratio (I_{light}/I_{dark}), demonstrated in the inset of **Figure 5.6**(d), is further investigated. On switching the gate voltage to the OFF state, the ratio is much higher than that in the ON state, indicating that more tunnelling and thermionic current participate in the SnS_2 channel with the increase of gate voltage. Therefore, the photocurrent predominates the channel current when the device is in the OFF state. The principle was also explained by the energy band diagram of the SnS_2 photodetector, shown in the bottom of **Figure 5.6**(d). The work function of Gr is estimated around 4.6 eV and the electron affinity of SnS_2 is about 4.1 eV,[19-20] resulting in the formation of a Schottky barrier at

the interface between Gr and SnS_2. When the device is in the depletion region, the down-shifted Fermi level of SnS_2 results in a large energy barrier between the conduction band of SnS_2 and the Fermi level of Gr. As a consequence, upon illumination, the photocurrent in the SnS_2 channel outnumbers the tunnelling and thermionic current. By contrast, when the device is operated in the accumulation region, the tunnelling and thermionic current can easily overcome the barrier because the Fermi level approaches its conduction band.[21] The reduction of the energy barrier also allows a more efficient generation of photocurrent and stronger photoresponse.

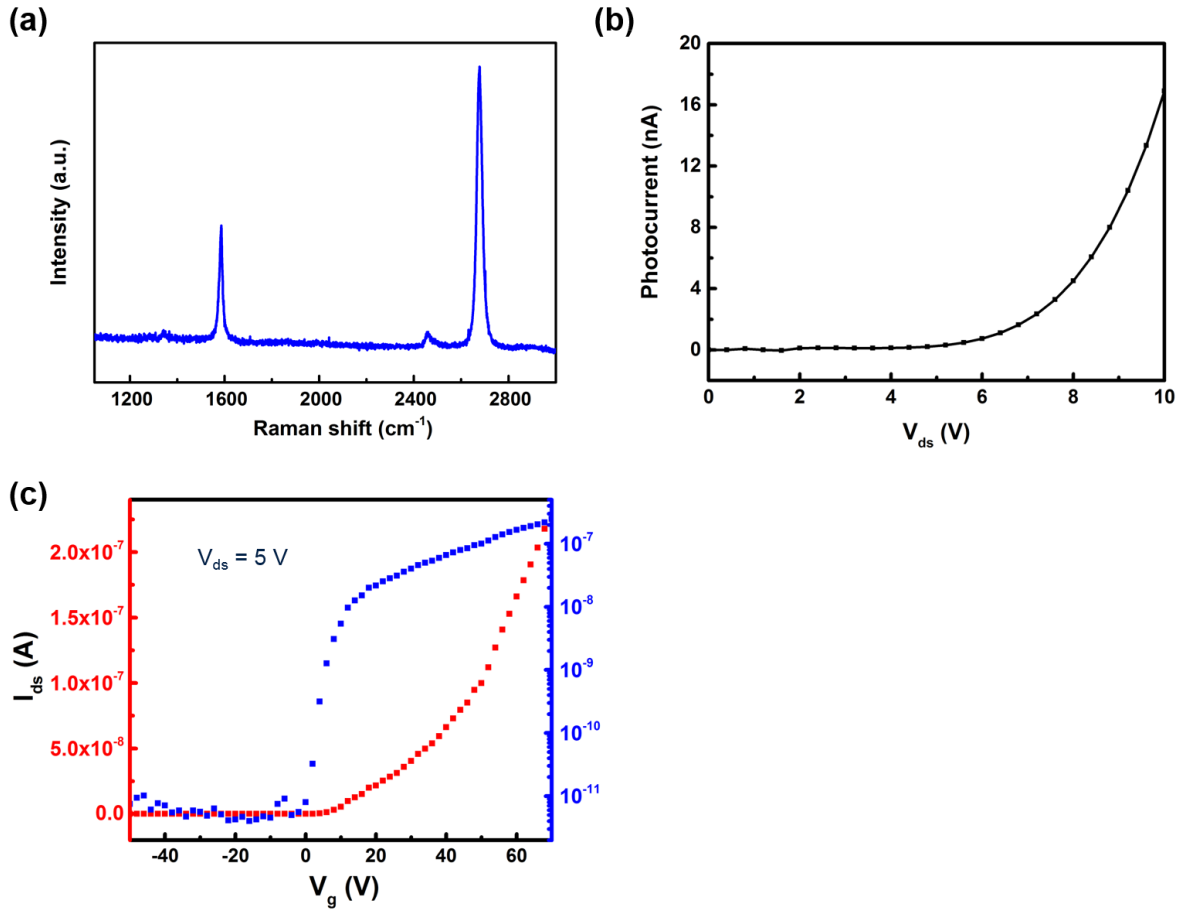


Figure 5.7. Gr-SnS_2-Gr lateral heterostructure. (a) Raman spectrum of Gr electrodes. (b) I-V characteristics of the Gr-SnS_2-Gr photodetector in the dark. (c) Transfer curves of Gr-SnS_2-Gr photodetector in logarithmic and linear coordinates under 5 V bias voltage.

In addition, the photoswitching characteristics demonstrated in **Figure 5.6**(e) shows that the SnS_2 photodetector exhibits a stable and reproducible photoresponse in a series of periodical light stimulation. The slight degradation of photocurrent with time may be attributed to the additional defects in the SnS_2 generated by light or heat, as well as the adsorbates on the SnS_2 surface. Besides, because of the negative temperature coefficient in conductivity, the mobility of graphene and SnS_2 is slightly decreased under the heating induced by photon absorption and leads to reducing photocurrent.[22-23] It is also noted that the high off current and low on-off current ratio could stem from the lower contact resistance between Gr and SnS_2 layers; further improvement via revising device configuration may be adopted in the future.

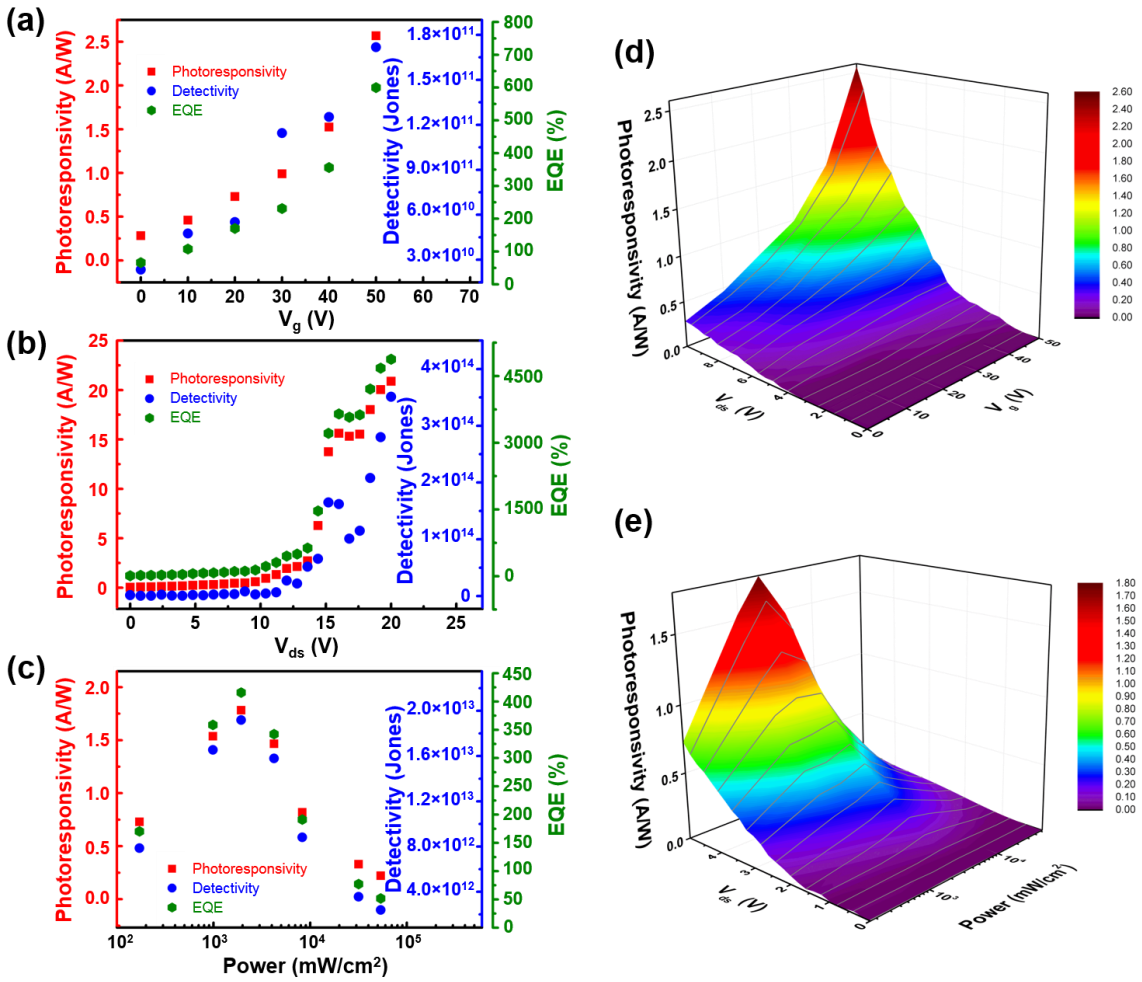


Figure 5.8. Photodetection performance of Gr-SnS_2-Gr under the influence of gate, illumination power and source-drain bias. (a) Influence of gate bias on photoresponsivity, detectivity and external

quantum efficiency (EQE) for the SnS_2 device. (b) Influence of source-drain bias on photoresponsivity, detectivity and EQE for the SnS_2 device. (c) Influence of illumination power on photoresponsivity, detectivity and EQE for the SnS_2 device. (d) The 3D view of photoresponsivity mapping for the Gr-SnS_2-Gr photodetector under different source-drain and gate biases. (e) The 3D view of photoresponsivity mapping for the Gr-SnS_2-Gr photodetector under different source-drain bias and laser illumination.

To further characterise the performance of the device, other three main figures of merit that are used to evaluate the photodetector were also discussed. The photoresponsivity (R) is defined as the ratio of the output photocurrent to the input optical power, representing the device electrical response to the incident light at a certain wavelength. In **Figure 5.8**(a), the photoresponsivity rises with the gate voltage sweeping to the positive side. The calculated photoresponsivity at V_G = 50 V is about 10 times greater than that at V_G = 0 V. The external quantum efficiency (EQE) is the ratio between the number of photogenerated carriers and the number of incident photons; it can be expressed by using the following formula

$$EQE = hcR/e\lambda \quad (1)$$

where h is the Plank's constant, c is the light velocity, R is the photoresponsivity, e is the elementary charge, and λ is the wavelength of incident light. In addition, taking the bandwidth, geometry, and noise of the device into consideration, the specific detectivity (D*) reflects the sensitivity of the device. It is defined by $D^*=R\times(Af)^{1/2}/i_N$, where A is the effective area of the detector, f is the bandwidth, and i_N is the noise current of the device. By considering the shot noise as the main noise source with $i_N = (2eI_{dark})^{1/2}$, D^* can be consequently expressed as

$$D^*=RA^{1/2}/(2eI_{dark})^{1/2} \quad (2)$$

where I_{dark} is the measured dark current.[24] It is worthwhile noting that the device based on 2D materials contains a *1/f* noise component resulting from the non-Ohmic contacts and defects that are non-negligible.[25-26] Similar to photoresponsivity, both EQE and detectivity increase when sweeping the gate voltage towards the ON state because of the enhanced carrier mobility. As shown in **Figure 5.8**(b), all the photoresponsivity, EQE and detectivity values increase with the enhancement of source-drain bias; this is because of the higher drift velocity of the photogenerated carriers. Under the 20 V source-drain bias, the detectivity can reach the value of 4×10^{14} Jones (Jones = cm $Hz^{1/2}$ W^{-1}), which is the highest value to date compared to other reports shown in **Table 5.1**.[10-12, 27-30] The photoresponsivity and EQE are also increased to 20 A/W and 4600%, respectively. Interestingly, unlike other reports showing the decrease with the increase of laser power for the phototransistor made by 2D materials, all of the figures of merit initially increase with the enhanced illumination power and start to decrease when the power is larger than 2000 mW/cm^2, shown in **Figure 5.8**(c). Besides, the 3D photoresponsivity maps shown in the **Figure 5.8**(d) and (e) indicate the notable control of photoresponse through systematically tuning the excitation power, source-drain bias and gate voltage.

Table 5.1. Comparison of figures of merit with other reported photodetectors using CVD-grown 2D materials as semiconducting channels.

Device	Measurement condition				Photoresponsivity	EQE	Detectivity	I_{on}/I_{off}	Reference
	λ	P	V_{ds}	V_g	R		D		
FL MoS_2	532 nm	2000 mW/cm^2	10 V	0 V	0.57 A/W	-----	10^{10} Jones	---	27
1L WSe_2	650 nm	0.38 mW/cm^2	2 V	-60 V	1.8 x 10^5 A/W	3.5 x 10^5 %	3 x 10^{14} Jones	---	28
1L SnS_2	390 nm	157 mW/cm^2	15 V	0 V	-----	150 %	-----	~1.36	29
FL SnS_2	457 nm	2400 mW/cm^2	2 V	0 V	8.8 x 10^{-3} A/W	2.4 %	2 x 10^9 Jones	~2.17	10
FL SnS_2	450 nm	1 mW/cm^2	10 V	0 V	2 A/W	-----	-----	~2	11
FL SnS_2	350 nm	6.93 mW/cm^2	1 V	0 V	261 A/W	93000 %	1.9 x 10^{10} Jones	~13	12
FL SnS_2	473 nm	2.04 mW/cm^2	3 V	50 V	100 A/W	33000 %	-----	~3.08	30
FL SnS_2	532 nm	171 mW/cm^2	20 V	0 V	20 A/W	4500 %	3.5 x 10^{14} Jones	~2.92	This work

To further explain the relationship between the photoresponsivity and illumination power, the charge transfer at the interface between the SnS_2 channel and Gr electrodes was further investigated. The SnS_2 crystals were transferred onto the continuous Gr ribbons. **Figure 5.9**(a) schematically shows the top view and the side view of the SnS_2 on the continuous Gr ribbon connected to the Cr/Au bond pads. **Figure 5.9**(b) shows the optical image of such SnS_2/Gr vertical heterostructure. Because Gr is much more conductive than the SnS_2 layers, the transfer curve of the heterostructure in **Figure 5.9**(c) shows a typical ambipolar field-effect characteristic. The Dirac point at 22 V indicates the p-doping of Gr because of the exposure in the air and the PMMA transfer residue. When exposed to laser illumination, the Dirac point of the heterostructure shifts to 16 V, indicating that Gr is less p-doped and its Fermi level is increased. This negative shift of the Dirac point results from the photogenerated holes that are trapped in the SnS_2, acting as an additional positive gate voltage to Gr.[31]

Figure 5.9(d) illustrates a schematic of the band structure at the interface of Gr and SnS_2, explaining that the increase of Gr Fermi level results from the surface charge transfer at the heterostructure interface. Under the laser excitation, the excitons are generated in SnS_2 crystals with electrons injected into Gr and holes staying in SnS_2. This results in a decrease of work function for Gr because of its limited density of states, and the Schottky barrier height at the Gr-SnS_2 junction is therefore reduced, which could lower the contact resistance at the junction and enhance the photoresponsivity of Gr-SnS_2-Gr devices.[32-33]

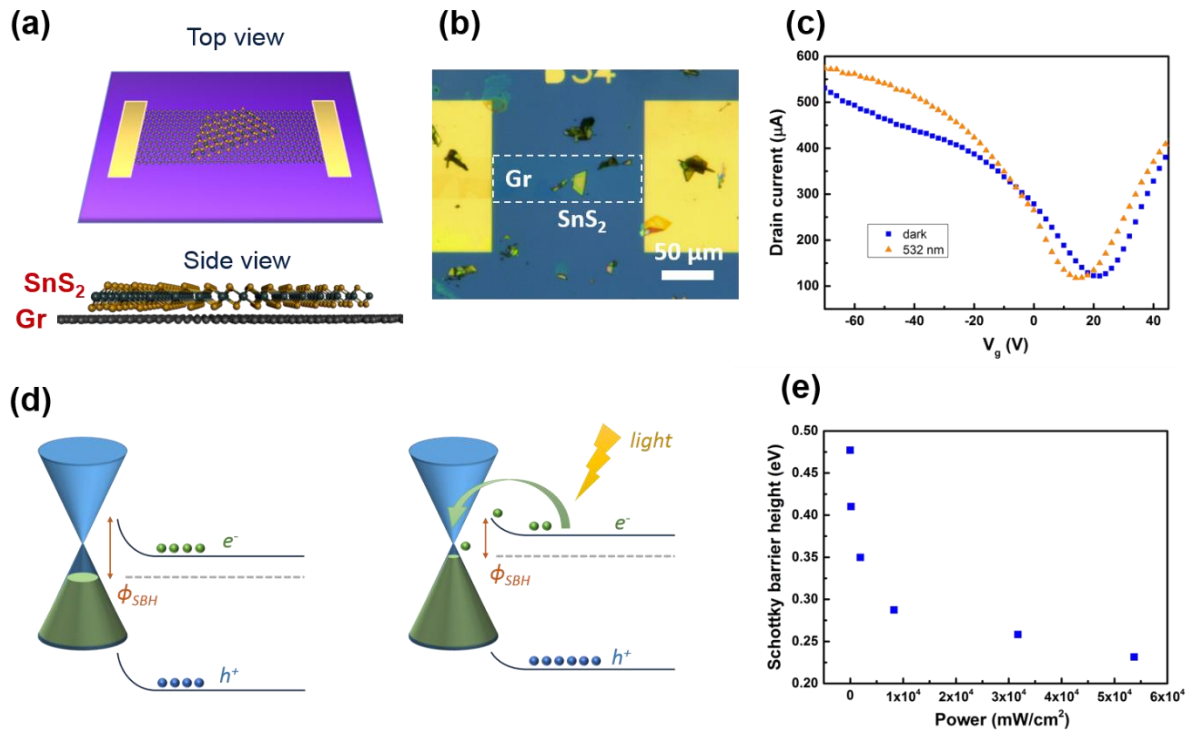


Figure 5.9. Mechanism for the positive dependence on photoresponsivity with the increase of laser illumination. (a) Schematic illustration of the device based on Gr electrodes and SnS_2. (b) Optical image of the device with SnS_2 crystals on continuous Gr channels. (c) Transfer curves of the Gr-SnS_2 device measured in the dark and under illumination at 8290 mW/cm^2. (d) Schematic band diagram of the Gr-SnS_2 heterostructure under equilibrium and illumination, depicting the change of Schottky barrier height. (e) The calculated Schottky barrier height at the Gr-SnS_2 interface as a function of laser excitation.

To further study the influence of the excitation power on the Schottky barrier height at the interface of Gr and SnS_2, the modified thermionic emission equation was used to extract the Schottky barrier height from the I-V measurements under different laser power intensities. Given the semi-metal and semiconductor properties of Gr and SnS_2, the output characteristics of the Gr-SnS_2-Gr (MSM) device can be understood with a simple representation of a back-to-back Schottky diode pair in series.[34-36] The current of the device can be expressed as:

$$I = I_0 \exp\left[-\left(1-\frac{1}{n}\right)e\beta V_1\right][\exp(e\beta V_1) - 1] \quad (1)$$

$$I = \frac{V_2}{R} \quad (2)$$

$$I = -I_0 \exp\left[-\left(1-\frac{1}{n}\right)e\beta V_3\right][\exp(e\beta V_3) - 1] \quad (3)$$

$$U = V_1 + V_2 + V_3 \quad (4)$$

By solving equation (1)-(4), we can get:

$$I = I_0\left[\frac{cohs\left(\frac{1}{2}\left(1-\frac{1}{n}\right)e\beta(U-IR)\right)}{cohs\left(\frac{1}{2n}e\beta(U-IR)\right)}\right]^{-\left(1-\frac{1}{n}\right)}\frac{sinh\left(\frac{1}{2}e\beta(U-IR)\right)}{cosh\left(\frac{1}{2n}e\beta(U-IR)\right)}\ , \quad (5)$$

where I is the source-drain current, U is the source-drain bias, n is the ideality factor, e is the elementary charge unit, $\beta = 1/k_BT$ is the Boltzmann factor, R is the internal resistance, and V_i (i = 1,2,3) is the voltage drop across the left diode, middle resistance, and right diode. I_0 is a constant related to the Schottky barrier height, which can be further expressed as:

$$I_0 = wA_{2D}T^{\frac{3}{2}} * exp(-\beta e\Phi_{SB})\ , \quad (6)$$

where w is the contact width of Gr and A_{2D} is the two-dimensional equivalent of Richardson constant,[37] T is the temperature, and Φ_{SB} is the effective Schottky barrier height. By using I_0 as fitting parameter in equation (5), the effective Schottky barrier can be extracted.

As shown in **Figure 5.9**(e), it is found that the effective Schottky barrier height decreases with increasing light power in the low power density regime. When the power is larger than 2000 mW/cm^2, the effective Schottky barrier height remains nearly constant with a value of around 0.25 V. Thus, the photoresponsivity increases when increasing the excitation power at low power densities because of the largely reduced effective Schottky barrier height, whereas at high-power illumination, the saturation of trap states and the increasing

recombination rate could lead to a decrease of photoresponsivity with increasing excitation power.[38]

5.2.3 Effect of SnS_2 Channel Thickness on Device Characteristics

To elucidate the SnS_2 crystal quality, the photoresponse on different SnS_2 channel thicknesses was furthered measured. The measured I-V characteristics and the influence of the excitation power and source-drain bias on the photoresponsivity for different SnS_2 channel thicknesses are shown in the **Figure 5.10**. **Figure 5.11**(a) shows the calculated photocurrent under different excitation laser powers. It can be seen that the photocurrent increases as the channel thickness becomes larger. By fitting the plot through a simple power-law, $I_{ph} \propto P^{\alpha}$, the factor α can be extrapolated. The sublinear dependence of photocurrent on illumination power indicates the existence of trap states, which could result from the sulfur vacancies or edge defects in SnS_2 layers and the charge impurities from adsorbed molecules on the SnS_2 surface, confirming the photogating effect for the sensing mechanism with the schematic illustration demonstrated in **Figure 5.11**(b).[39] In the photogating effect, one of the two carrier types is trapped in the localised states located at defects or surface adsorbates; these trapped carriers act as local gates and effectively modulate the conductance of the semiconductor. As the power density increases, more surface traps may be filled by the carriers generated under illumination, thus resulting in the saturation of photocurrent. Another evidence for the presence of photogating was the substantial current spikes after turning off the laser illumination from the time-resolved curve, as shown in **Figure 5.6**(e). This is because of the relaxation of excessive holes staying in the trap states after switching off the laser light; a similar phenomenon has also been found by other reports.[40]

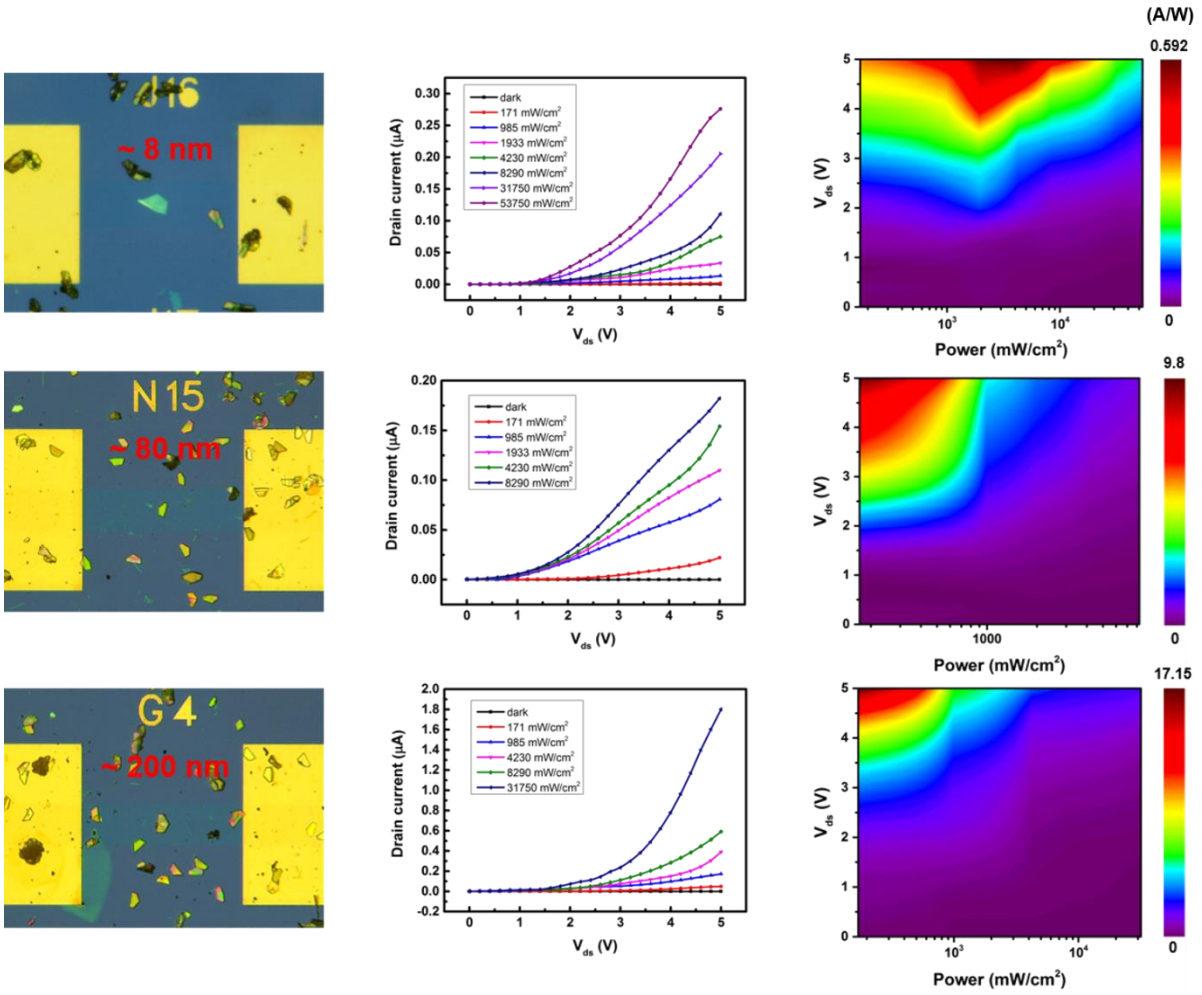


Figure 5.10. Thickness dependence of the source-drain current and photoresponsivity under different source-drain bias and laser illumination.

In **Figure 5.11**(c), the dependence on the laser power of the photoresponsivity shows that the photoresponsivity increases as the SnS_2 channel becomes thicker under all laser powers. This may stem from the mobility enhancement of SnS_2 as thickness increases because of the mitigated charge impurities. Also, the number of photogenerated carriers is expected to be larger in the thicker SnS_2 channel. Besides, the relationship between the photoresponsivity and laser powers was found to be dependent on the different SnS_2 channel thicknesses. For thin SnS_2 crystals, the photoresponsivity first increases with the enhancement of laser power and begins to drop at higher power density. This is because of the charge transfer at the interface

of SnS_2 channel and the Gr electrodes that was explained earlier. For thick SnS_2 crystals, however, the photoresponsivity decreases monotonously with increasing laser power.

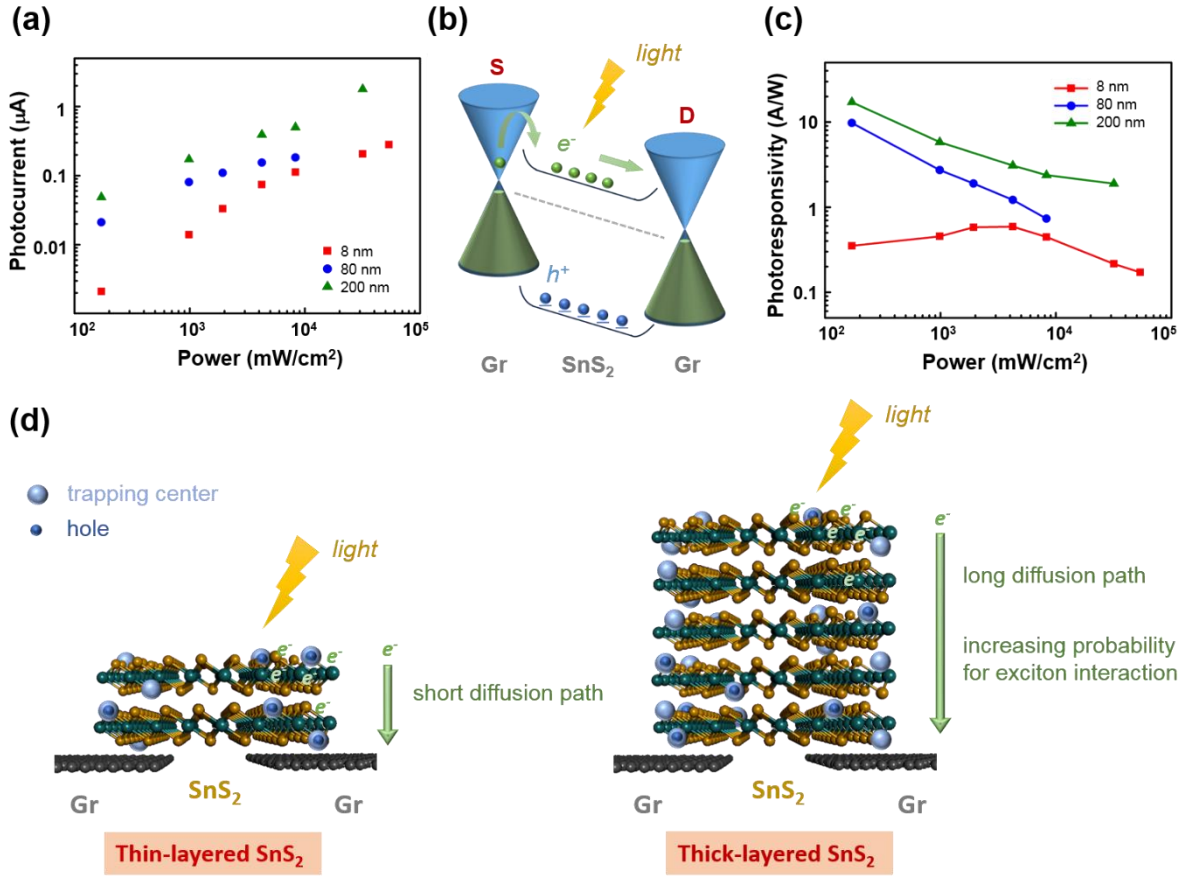


Figure 5.11. Influence of SnS_2 channel thickness on the photoresponse. (a) Power dependence of the photocurrent for different SnS_2 crystal thicknesses under 5 V source-drain bias. (b) Energy band diagram demonstrating the photogating mechanism of the SnS_2 channel with Gr electrodes. (c) Power dependence of the photoresponsivity for different SnS_2 crystal thicknesses under 5 V source-drain bias. (d) Schematic illustration explaining the transport mechanism of photoinduced carriers within SnS_2 channels of different thicknesses.

The reason for this different relationship between the photoresponsivity and laser powers is schematically explained in **Figure 5.11**(d). For the thin-layered SnS_2 channel, the photoresponse is dominant by the interface between graphene and SnS_2. The reducing Schottky

barrier height leads to the increase of photoresponsivity along with enhanced laser illumination at low powers. In contrast, as SnS_2 layers become thicker, the photogenerated carriers have longer diffusion path to transport from the SnS_2 channel to Gr ribbons under laser illumination. This results in the increasing probability of exciton interaction and the shortening lifetime of photogenerated carriers. The benefits of lowering Schottky barrier height are suppressed, and the photoresponsivity shows the negative correlation with laser intensity at low illumination powers. The photoresponse of thick-layered SnS_2 becomes bulklike and is similar to traditional phototransistors using metals as electrodes.

5.3 Conclusion

This chapter demonstrates how CVD growth of SnS_2 on a SiO_2 substrate can be achieved using a combination of tin sulfide (SnS) and S powder. The as-grown SnS_2 crystals with different thicknesses were also stamped onto Gr electrodes grown by CVD for the fabrication of 2D photodetectors; the photodetecting behaviour of Gr-SnS_2-Gr lateral heterostructures was then investigated. For thin SnS_2 crystals, the reducing Schottky barrier height resulting from the charge transfer at the Gr-SnS_2 interface could increase the photoresponsivity with the increasing illumination power. As the SnS_2 layers become thicker, the influence turns from interface-dominant into bulk-dominant because of the increasing exciton interaction and the diffusion path for carriers in the SnS_2 layers. This Gr-SnS_2-Gr 2D photodetector shows that semiconducting SnS_2 has performance comparable to other 2D TMD systems such as MoS_2 in the green spectral region when combined with Gr electrodes. This demonstrates reliable sensing properties of SnS_2 of great potential for future applications in ultrathin 2D optoelectronics with high performance.

5.4 Reference

(1) Hu, P.; Wang, L.; Yoon, M.; Zhang, J.; Feng, W.; Wang, X.; Wen, Z.; Idrobo, J. C.; Miyamoto, Y.; Geohegan, D. B.; Xiao, K., Highly Responsive Ultrathin GaS Nanosheet Photodetectors on Rigid and Flexible Substrates. *Nano Lett.* **2013,** *13* (4), 1649-1654.

(2) Bandurin, D. A.; Tyurnina, A. V.; Yu, G. L.; Mishchenko, A.; Zólyomi, V.; Morozov, S. V.; Kumar, R. K.; Gorbachev, R. V.; Kudrynskyi, Z. R.; Pezzini, S.; Kovalyuk, Z. D.; Zeitler, U.; Novoselov, K. S.; Patanè, A.; Eaves, L.; Grigorieva, I. V.; Fal'ko, V. I.; Geim, A. K.; Cao, Y., High Electron Mobility, Quantum Hall Effect and Anomalous Optical Response in Atomically Thin InSe. *Nat. Nanotechnol.* **2016,** *12*, 223-227.

(3) Li, X.; Lin, M.-W.; Puretzky, A. A.; Idrobo, J. C.; Ma, C.; Chi, M.; Yoon, M.; Rouleau, C. M.; Kravchenko, I. I.; Geohegan, D. B.; Xiao, K., Controlled Vapor Phase Growth of Single Crystalline, Two-Dimensional GaSe Crystals with High Photoresponse. *Sci. Rep.* **2014,** *4*, 5497.

(4) Mutlu, Z.; Wu, R. J.; Wickramaratne, D.; Shahrezaei, S.; Liu, C.; Temiz, S.; Patalano, A.; Ozkan, M.; Lake, R. K.; Mkhoyan, K. A.; Ozkan, C. S., Phase Engineering of 2D Tin Sulfides. *Small* **2016,** *12* (22), 2998-3004.

(5) Huang, Y.; Sutter, E.; Sadowski, J. T.; Cotlet, M.; Monti, O. L. A.; Racke, D. A.; Neupane, M. R.; Wickramaratne, D.; Lake, R. K.; Parkinson, B. A.; Sutter, P., Tin Disulfide—An Emerging Layered Metal Dichalcogenide Semiconductor: Materials Properties and Device Characteristics. *ACS Nano* **2014,** *8* (10), 10743-10755.

(6) Tao, Y.; Wu, X.; Wang, W.; Wang, J., Flexible Photodetector from Ultraviolet to Near Infrared Based on a SnS_2 Nanosheet Microsphere Film. *J. Mater. Chem. C* **2015,** *3* (6), 1347-1353.

(7) Rong, Y.; Fan, Y.; Leen Koh, A.; Robertson, A. W.; He, K.; Wang, S.; Tan, H.; Sinclair, R.; Warner, J. H., Controlling Sulphur Precursor Addition for Large Single Crystal Domains of WS_2. *Nanoscale* **2014,** *6* (20), 12096-12103.

(8) Shanshan, W.; Merce, P.; Harish, B.; Jamie, H. W., Substrate Control for Large Area Continuous Films of Monolayer MoS_2 by Atmospheric Pressure Chemical Vapor Deposition. *Nanotechnology* **2016,** *27* (8), 085604.

(9) Sheng, Y.; Tan, H.; Wang, X.; Warner, J. H., Hydrogen Addition for Centimeter-Sized Monolayer Tungsten Disulfide Continuous Films by Ambient Pressure Chemical Vapor Deposition. *Chem. Mater.* **2017,** *29* (11), 4904-4911.

(10) Su, G.; Hadjiev, V. G.; Loya, P. E.; Zhang, J.; Lei, S.; Maharjan, S.; Dong, P.; M. Ajayan, P.; Lou, J.; Peng, H., Chemical Vapor Deposition of Thin Crystals of Layered Semiconductor SnS_2 for Fast Photodetection Application. *Nano Lett.* **2015,** *15* (1), 506-513.

(11) Xia, J.; Zhu, D.; Wang, L.; Huang, B.; Huang, X.; Meng, X.-M., Large-Scale Growth of Two-Dimensional SnS_2 Crystals Driven by Screw Dislocations and Application to Photodetectors. *Adv. Funct. Mater.* **2015,** *25* (27), 4255-4261.

(12) Zhou, X.; Zhang, Q.; Gan, L.; Li, H.; Zhai, T., Large-Size Growth of Ultrathin SnS_2 Nanosheets and High Performance for Phototransistors. *Adv. Funct. Mater.* **2016,** *26* (24), 4405-4413.

(13) Song, H. S.; Li, S. L.; Gao, L.; Xu, Y.; Ueno, K.; Tang, J.; Cheng, Y. B.; Tsukagoshi, K., High-Performance Top-Gated Monolayer SnS_2 Field-Effect Transistors and Their Integrated Logic Circuits. *Nanoscale* **2013,** *5* (20), 9666-9670.

(14) Hu, Y.; Chen, T.; Wang, X.; Ma, L.; Chen, R.; Zhu, H.; Yuan, X.; Yan, C.; Zhu, G.; Lv, H.; Liang, J.; Jin, Z.; Liu, J., Controlled Growth and Photoconductive Properties of Hexagonal SnS_2 Nanoflakes with Mesa-Shaped Atomic Steps. *Nano Res.* **2017,** *10* (4), 1434-1447.

(15) Price, L. S.; Parkin, I. P.; Hardy, A. M. E.; Clark, R. J. H.; Hibbert, T. G.; Molloy, K. C., Atmospheric Pressure Chemical Vapor Deposition of Tin Sulfides (SnS, Sn_2S_3, and SnS_2) on Glass. *Chem. Mater.* **1999,** *11* (7), 1792-1799.

(16) Smith, A. J.; Meek, P. E.; Liang, W. Y., Raman Scattering Studies of SnS_2 and $SnSe_2$. *J. Phys. C: Solid State Phys.* **1977,** *10* (8), 1321-1323.

(17) Xia, J.; Li, X.-Z.; Huang, X.; Mao, N.; Zhu, D.-D.; Wang, L.; Xu, H.; Meng, X.-M., Physical Vapor Deposition Synthesis of Two-Dimensional Orthorhombic SnS Flakes with Strong Angle/Temperature-Dependent Raman Responses. *Nanoscale* **2016,** *8* (4), 2063-2070.

(18) Gonzalez, J. M.; Oleynik, I. I., Layer-Dependent Properties of SnS_2 and $SnSe_2$ Two-Dimensional Materials. *Phys. Rev. B* **2016,** *94* (12), 125443.

(19) Yu, Y.-J.; Zhao, Y.; Ryu, S.; Brus, L. E.; Kim, K. S.; Kim, P., Tuning the Graphene Work Function by Electric Field Effect. *Nano Lett.* **2009,** *9* (10), 3430-3434.

(20) Burton, L. A.; Whittles, T. J.; Hesp, D.; Linhart, W. M.; Skelton, J. M.; Hou, B.; Webster, R. F.; O'Dowd, G.; Reece, C.; Cherns, D.; Fermin, D. J.; Veal, T. D.; Dhanak, V. R.; Walsh, A., Electronic and Optical Properties of Single Crystal SnS_2: an Earth-Abundant Disulfide Photocatalyst. *J. Mater. Chem. A* **2016,** *4* (4), 1312-1318.

(21) Lopez-Sanchez, O.; Lembke, D.; Kayci, M.; Radenovic, A.; Kis, A., Ultrasensitive Photodetectors Based on Monolayer MoS_2. *Nat. Nanotechnol.* **2013,** *8* (7), 497-501.

(22) Heo, J.; Chung, H. J.; Lee, S.-H.; Yang, H.; Seo, D. H.; Shin, J. K.; Chung, U. I.; Seo, S.; Hwang, E. H.; Das Sarma, S., Nonmonotonic Temperature Dependent Transport in Graphene Grown by Chemical Vapor Deposition. *Phys. Rev. B* **2011,** *84* (3), 035421.

(23) Patil, S. G.; Tredgold, R. H., Electrical and Photoconductive Properties of SnS_2 Crystals. *J. Phys. D Appl. Phys.* **1971,** *4* (5), 718.

(24) Xie, C.; Mak, C.; Tao, X.; Yan, F., Photodetectors Based on Two-Dimensional Layered Materials Beyond Graphene. *Adv. Funct. Mater.* **2017,** *27* (19), 1603886.

(25) Renteria, J.; Samnakay, R.; Rumyantsev, S. L.; Jiang, C.; Goli, P.; Shur, M. S.; Balandin, A. A., Low-Frequency 1/f Noise in MoS_2 Transistors: Relative Contributions of the Channel and Contacts. *Appl. Phys. Lett.* **2014,** *104* (15), 153104.

(26) Kufer, D.; Konstantatos, G., Highly Sensitive, Encapsulated MoS_2 Photodetector with Gate Controllable Gain and Speed. *Nano Lett.* **2015,** *15* (11), 7307-7313.

(27) Tsai, D.-S.; Liu, K.-K.; Lien, D.-H.; Tsai, M.-L.; Kang, C.-F.; Lin, C.-A.; Li, L.-J.; He, J.-H., Few-Layer MoS_2 with High Broadband Photogain and Fast Optical Switching for Use in Harsh Environments. *ACS Nano* **2013,** *7* (5), 3905-3911.

(28) Zhang, W.; Chiu, M.-H.; Chen, C.-H.; Chen, W.; Li, L.-J.; Wee, A. T. S., Role of Metal Contacts in High-Performance Phototransistors Based on WSe_2 Monolayers. *ACS Nano* **2014,** *8* (8), 8653-8661.

(29) Ye, G.; Gong, Y.; Lei, S.; He, Y.; Li, B.; Zhang, X.; Jin, Z.; Dong, L.; Lou, J.; Vajtai, R.; Zhou, W.; Ajayan, P. M., Synthesis of Large-Scale Atomic-Layer SnS_2 Through Chemical Vapor Deposition. *Nano Res.* **2017,** *10* (7), 2386-2394.

(30) Huang, Y.; Deng, H.-X.; Xu, K.; Wang, Z.-X.; Wang, Q.-S.; Wang, F.-M.; Wang, F.; Zhan, X.-Y.; Li, S.-S.; Luo, J.-W.; He, J., Highly Sensitive and Fast Phototransistor Based on Large Size CVD-grown SnS_2 Nanosheets. *Nanoscale* **2015,** *7* (33), 14093-14099.

(31) Zhang, W.; Chuu, C.-P.; Huang, J.-K.; Chen, C.-H.; Tsai, M.-L.; Chang, Y.-H.; Liang, C.-T.; Chen, Y.-Z.; Chueh, Y.-L.; He, J.-H.; Chou, M.-Y.; Li, L.-J., Ultrahigh-Gain Photodetectors Based on Atomically Thin Graphene-MoS_2 Heterostructures. *Sci. Rep.* **2014,** *4*, 3826.

(32) Tan, H.; Fan, Y.; Rong, Y.; Porter, B.; Lau, C. S.; Zhou, Y.; He, Z.; Wang, S.; Bhaskaran, H.; Warner, J. H., Doping Graphene Transistors Using Vertical Stacked

Monolayer WS_2 Heterostructures Grown by Chemical Vapor Deposition. *ACS Appl. Mater. Interfaces* **2016,** *8* (3), 1644-1652.

(33) Tan, H.; Fan, Y.; Zhou, Y.; Chen, Q.; Xu, W.; Warner, J. H., Ultrathin 2D Photodetectors Utilizing Chemical Vapor Deposition Grown WS_2 With Graphene Electrodes. *ACS Nano* **2016,** *10* (8), 7866-7873.

(34) Adenilson, J. C.; Cleber, A. A.; Olivia, M. B.; Luana, S. A.; Eric, P. B.; Edson, R. L., Back-to-Back Schottky Diodes: the Generalization of the Diode Theory in Analysis and Extraction of Electrical Parameters of Nanodevices. J. Phys.: Condens. Matter 2012, 24 (22), 225303.

(35) Ohta, Y.; Kubozono, Y.; Fujiwara, A., Transport Properties in C60 Field-Effect Transistor with a Single Schottky Barrier. Appl. Phys. Lett. 2008, 92 (17), 173306.

(36) Fan, Y.; Zhou, Y.; Wang, X.; Tan, H.; Rong, Y.; Warner, J. H., Photoinduced Schottky Barrier Lowering in 2D Monolayer WS_2 Photodetectors. *Adv. Opt. Mater.* **2016,** *4* (10), 1573-1581.

(37) Anwar, A.; Nabet, B.; Culp, J.; Castro, F., Effects of Electron Confinement on Thermionic Emission Current in a Modulation Doped Heterostructure. J. Appl. Phys. 1999, 85 (5), 2663-2666.

(38) Zhang, W.; Huang, J.-K.; Chen, C.-H.; Chang, Y.-H.; Cheng, Y.-J.; Li, L.-J., High-Gain Phototransistors Based on a CVD MoS_2 Monolayer. *Adv. Mater.* **2013,** *25* (25), 3456-3461.

(39) Island, J. O.; Blanter, S. I.; Buscema, M.; van der Zant, H. S. J.; Castellanos-Gomez, A., Gate Controlled Photocurrent Generation Mechanisms in High-Gain In_2Se_3 Phototransistors. *Nano Lett.* **2015,** *15* (12), 7853-7858.

(40) Ma, S.; Zeng, L.; Tao, L.; Tang, C. Y.; Yuan, H.; Long, H.; Cheng, P. K.; Chai, Y.; Chen, C.; Fung, K. H.; Zhang, X.; Lau, S. P.; Tsang, Y. H., Enhanced Photocatalytic Activity of WS_2 Film by Laser Drilling to Produce Porous WS_2/WO_3 Heterostructure. *Sci. Rep.* **2017,** *7* (1), 3125.

Chapter 6

Morphology Control of Two-Dimensional Tin Disulfide on Transition Metal Dichalcogenides Using Chemical Vapour Deposition

6.1 Introduction

To construct the 2D vdW heterostructures, several approaches have been developed over the past few years. Multiple step layer-by-layer stacking using mechanical transfer techniques is the most common way to date because of its simple fabrication process.[1-2] In spite of this, the lack of scalability and stacking orientation control restrict their applications, and the unavoidable introduction of interfacial contamination is detrimental to the performance of the resulting devices. A direct chemical vapour deposition (CVD) growth strategy, in comparison, offers great advantages of size control and clean interface. It is therefore considered as a practical solution for the future large-scale industrial applications.[3-5] Furthermore, compared to the vapour phase growth of conventional semiconductor-based heterojunctions, it is possible to build 2D vdW heterostructures without the restrictions of lattice-matching because of the lack of dangling bonds at the interfaces.[6]

To date, there are several reports demonstrating the successful CVD growth of vdW vertical heterostructures combining 2D layered semiconductors including WS_2/MoS_2,[7] MoS_2/WS_2,[8] MoS_2/WSe_2,[9] $WSe_2/MoSe_2$,[10] and ReS_2/WS_2.[11] Most of these 2D semiconductor components are Mo and W based chalcogenides, whose physical properties have been widely investigated in the past. The photoresponse performance of SnS_2-based devices has shown to

be comparable to other 2D layered semiconductors such as MoS_2 and WS_2.[12-15] However, in previous reports the CVD SnS_2 grown on commercial SiO_2 substrate exhibits high percentage of crystals with random growth directions or even stacked vertically without any order,[16-17] which is detrimental for the device applications. The growth of single crystalline SnS_2 with well-defined shape still remains challenging.

In this chapter, the improved synthesis by switching the SnS_2 growth from SiO_2 to other 2D transition metal dichalcogenides, such as WS_2 and MoS_2 via two-step CVD process is reported. The atomically flat surface of WS_2 and MoS_2 enables the control of SnS_2 morphology from irregular shapes to truncated triangles or hexagons with well-defined alignment. Another benefit for this is the realization of SnS_2-based heterostructures using a direct growth method, which has great potential for the future device applications. The growth mechanism and the explanation of morphological differences are proposed. The morphology, crystal structure, and chemical composition were also examined by using scanning electron microscopy (SEM), as well as Raman and PL spectroscopy analysis.

6.2 Results and Discussion

6.2.1 CVD Growth of SnS_2 on WS_2 Monolayers

Figure 6.1(a) schematically illustrates the growth of the SnS_2/WS_2 vdW vertical heterostructure via a two-step strategy. The monolayer WS_2 was grown by CVD in the first step; the growth details and the analysis of the resulted WS_2 crystals are shown in **Figure 6.2**. The schematic illustration in **Figure 6.1**(b) demonstrates the experimental setup for the second step CVD growth of SnS_2 with the pre-grown WS_2 placed on the ceramic crucible where the growth temperature is set to be around 450°C. The two furnaces are provided for the better control of temperature to generate the vapour of precursors. Sulfur and SnS precursors are

placed in the centre of furnace 1 and 2, respectively, whereas the pre-grown WS_2 is put at the downstream of furnace 2, around 6 cm away from the SnS powders. With a view to avoiding unnecessary reactions between two different precursors during the transport of vaporized atoms to the substrate, two concentric quartz tubes were used to separate the gaseous precursors before they reached the substrate surface.

To further elucidate the two-step CVD growth process, the characterization and comparison of WS_2 domains before and after the second step of SnS_2 growth are adopted. As demonstrated by the optical and SEM images in **Figure 6.1**(c) and (d), the WS_2 grown in the first step is fairly uniform, over 90% of which is monolayer with a triangular shape and a typical lateral size of ~15 μm. After the second step of SnS_2 growth, shown in **Figure 6.1**(e) and (f), the WS_2 remains intact and the triangular domain is partially covered by SnS_2 with the domain size of ~10 μm. In addition, it can be seen that SnS_2 crystals are preferentially grown on the WS_2 surface rather than SiO_2/Si substrate, suggesting a strong selectivity for the growth. It is therefore manifested that the WS_2 layers could be superior templates for the growth of high quality SnS_2 layers when compared with the SiO_2/Si substrates, where in previous work pure SnS_2 layers synthesized by CVD tend to form thick multilayers and some of them are not flat. The control of layer number uniformity for SnS_2 growth, however, still remains challenging. As shown in **Figure 6.1**(e), some of the SnS_2 layers display a monolayer to few-layer thickness with light blue colour, while those yellowish SnS_2 crystals indicate thicker layers. The elemental analysis of thicker SnS_2 layers is also presented in **Figure 6.3**.

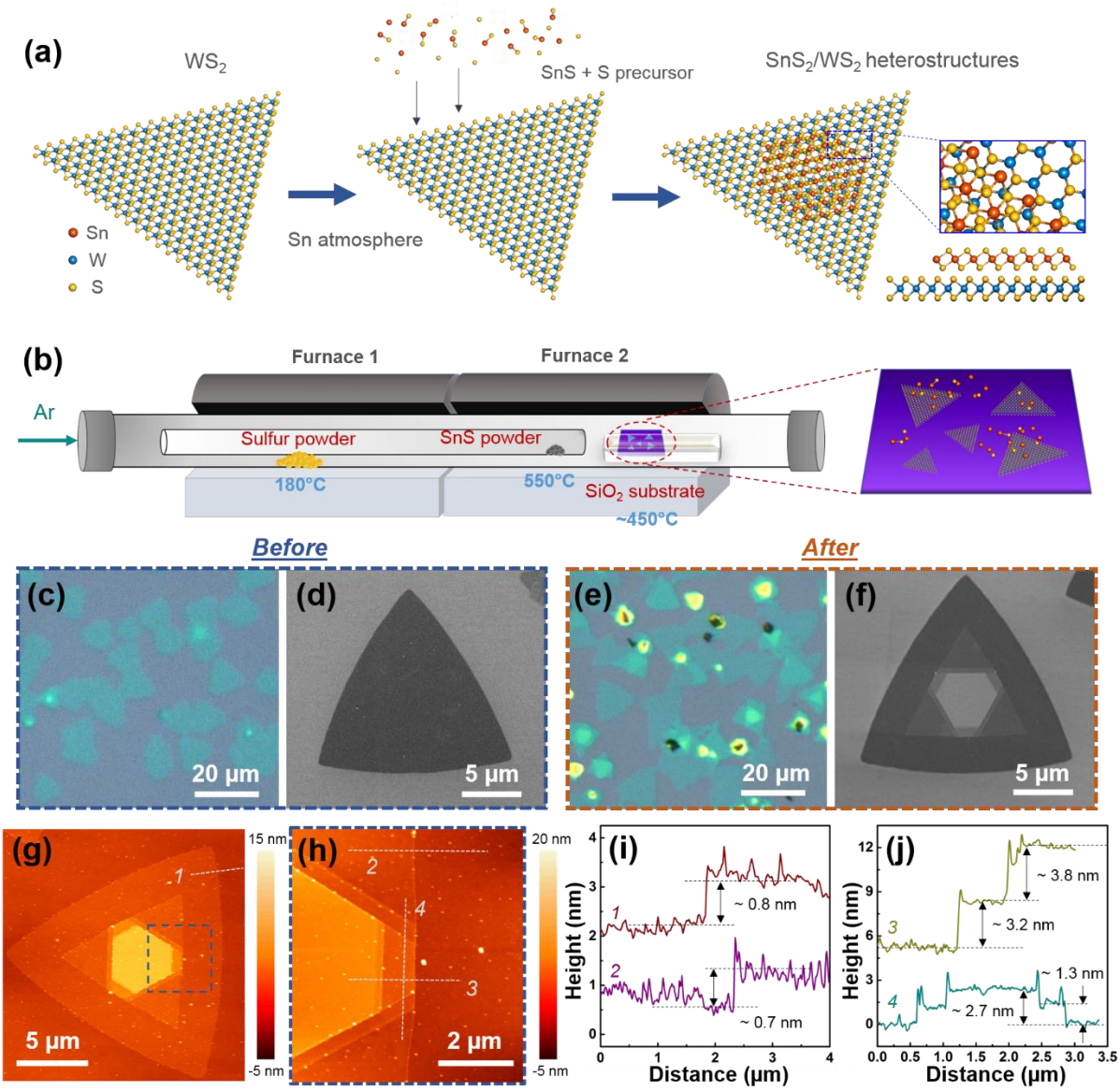


Figure 6.1. Direct growth of SnS_2/WS_2 vertical vdW heterostructures via two-step CVD synthesis. (a) Schematics of atomic configuration showing the two-step synthesis of SnS_2/WS_2 heterostructures. (b) Schematic illustration of the CVD experimental setup for growing SnS_2 on WS_2 layers. (c) Optical image of CVD-grown monolayer WS_2 before the growth of SnS_2. (d) SEM image showing the monolayer WS_2 triangle before the growth of SnS_2. (e) Optical image of the WS_2 after the growth of SnS_2 showing the growth preference of the SnS_2 on the WS_2 surface rather than SiO_2. (f) SEM image of the monolayer WS_2 triangle after the growth of SnS_2 forming a vertical vdW heterostructure. (g) AFM image of the same heterostructure in (f) showing the thickness of the WS_2 triangle. (h) Zoomed-

in AFM image of the blue dashed square in (g), showing the thickness of the as-grown SnS_2. (i-j) Height profile of the WS_2 triangle and SnS_2 layers indicated by the dashed lines in (g) and (h).

Figure 6.1(g) demonstrates the corresponding AFM image of the same SnS_2/WS_2 heterostructure in **Figure 6.1**(f), and an enlarged AFM image showing the area marked by blue dashed square in **Figure 6.1**(g) is also presented in **Figure 6.1**(h). The line profiles across different edges indicated by the dashed lines in **Figure 6.1**(g) and (h) are consequently measured, showing the details on layer number of both WS_2 and SnS_2. As shown in **Figure 6.1**(i), the step heights across the WS_2 and first triangular layer of SnS_2 edges are estimated to be 0.8 and 0.7 nm, respectively, suggesting a monolayer thickness. The hexagonal multilayer SnS_2 region (**Figure 6.1**(j)) is measured to be 7 nm, which is around 8 layers of SnS_2.

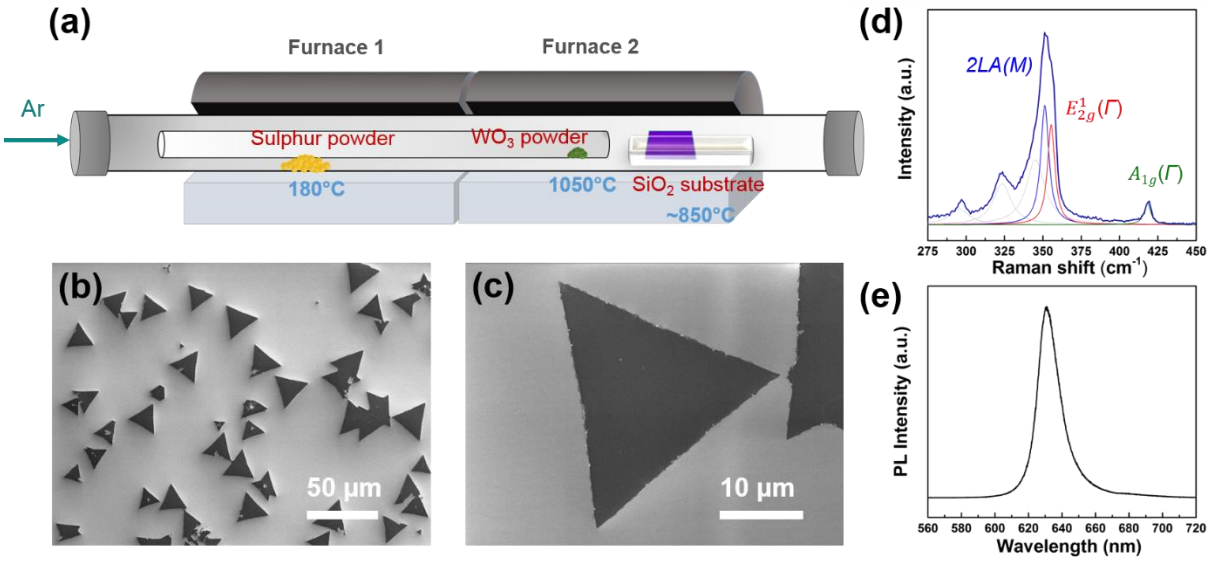


Figure 6.2. Atmospheric-pressure CVD synthesis of WS_2 domains on the SiO_2 substrate. (a) Schematic illustration of the experimental setup for the CVD growth of WS_2. (b) Low magnification SEM image demonstrating the overall coverage of monolayer WS_2. (c) SEM image of triangular monolayer WS_2. (d) Raman spectra of the as-grown monolayer WS_2 with the Lorentz peaks fitting. (e) PL characterization of the as-grown monolayer WS_2.

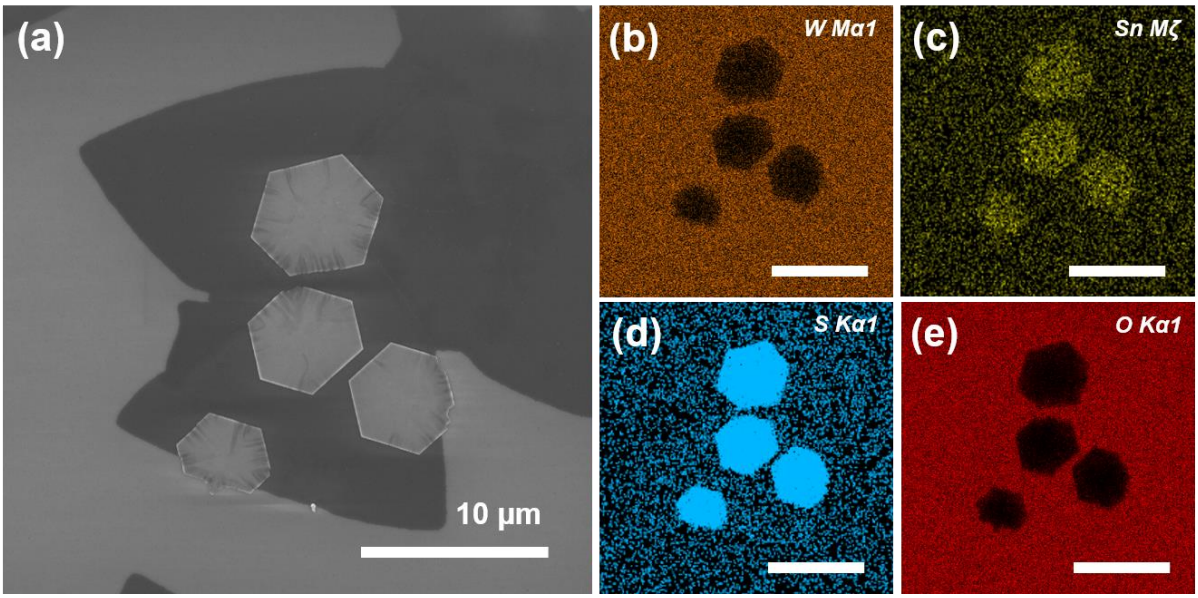


Figure 6.3. EDX elemental analysis of the multilayer SnS_2 in the SnS_2/WS_2 vertical van der Waals (vdW) heterostructure. (a) SEM image of the hexagonal SnS_2 platelets deposited on the monolayer WS_2. (b) EDX elemental mapping of area in (a) showing the distribution of W. (c) EDX elemental mapping of area in (a) showing the distribution of Sn. (d) EDX elemental mapping of area in (a) showing the distribution of S. (e) EDX elemental mapping of area in (a) showing the distribution of O. All the scale bars in (b-e) are 10 μm.

To further characterize the optical properties, the SnS_2/WS_2 heterostructures are studied by Raman and PL spectroscopy. **Figure 6.4**(a) shows the corresponding optical image of the SnS_2/WS_2 heterostructure in **Figure 6.1**(f). **Figure 6.4**(b) shows the Raman spectrum of the WS_2 monolayer and SnS_2/WS_2 heterostructures with different SnS_2 thicknesses, corresponding to the red, blue, and green spots, respectively, in **Figure 6.4**(a). To compare with the SnS_2/WS_2 heterostructure, a 10 nm-thick SnS_2 crystal on SiO_2 was also measured as a reference, whose morphology and AFM measurement are evidenced in **Figure 5.5**. By use of a Lorentz fitting, Raman signals for monolayer WS_2 (i) ranging from 280 to 380 cm^{-1} can be deconvolved into five separated peaks shown in the **Figure 6.4**(d). Two of which can be attributed to the second order longitudinal acoustic (*2LA*) vibration mode and in-plane (E^1_{2g}) vibrational mode located

at ~351 and ~355 cm^{-1}, respectively. Another characteristic peak of monolayer WS_2 is the out-of-plane (A_{1g}) vibrational mode at ~418 cm^{-1}.[18] The Raman spectrum of SnS_2, in contrast, only shows one characteristic peak at ~314 cm^{-1}, corresponding to the out-of-plane (A_{1g}) vibrational mode.[19] It can be seen that in **Figure 6.4**(b) the Raman signals of both the monolayer SnS_2/WS_2 heterostructure (m-SWH, ii) and the few-layer SnS_2/WS_2 heterostructure (f-SWH, iii) are roughly the superimposition of that in the individual WS_2 and SnS_2 monolayers. The increase of the A_{1g} peak intensity in the SnS_2/WS_2 heterostructures is likely due to a peak convolution between out-of-plane vibration modes of WS_2 and SnS_2. Similarly, Raman signals for both m-SWH and f-SWH ranging from 280 to 380 cm^{-1}, shown in **Figure 6.4**(e) and (f), can be deconvolved by a Lorentzian fitting into six separated peaks including the WS_2 peaks and an additional characteristic A_{1g} peak from pristine SnS_2. It is noted that the intensity of the A_{1g} peak from SnS_2 decreases with reducing layer thickness. Thus, the SnS_2 Raman signal in m-SWH becomes difficult to detect.

The interaction of SnS_2 with WS_2 also affects the PL emission in their vdW heterostructure. As shown in **Figure 6.4**(c), the characteristic PL intensity is greatly quenched in both m-SWH and f-SWH compared to that in monolayer WS_2. The PL mapping of the heterostructure in **Figure 6.4**(a) is shown in **Figure 6.4**(g), revealing the PL quenching on the entire SnS_2/WS_2 region. This significant quenching may be attributed to the indirect bandgap of SnS_2 or the strong charge transfer at the interface of the heterostructure. Additionally, in the few-layer SnS_2 the valence band maximum and conduction band minimum are situated at the *Γ-K* line and *M* point, respectively; while in the monolayer WS_2 both of the valence band maximum and conduction band minimum are located at *K* point. This different band alignment in the reciprocal space also reduces direct exciton recombination, leading to the quenching of PL signal.

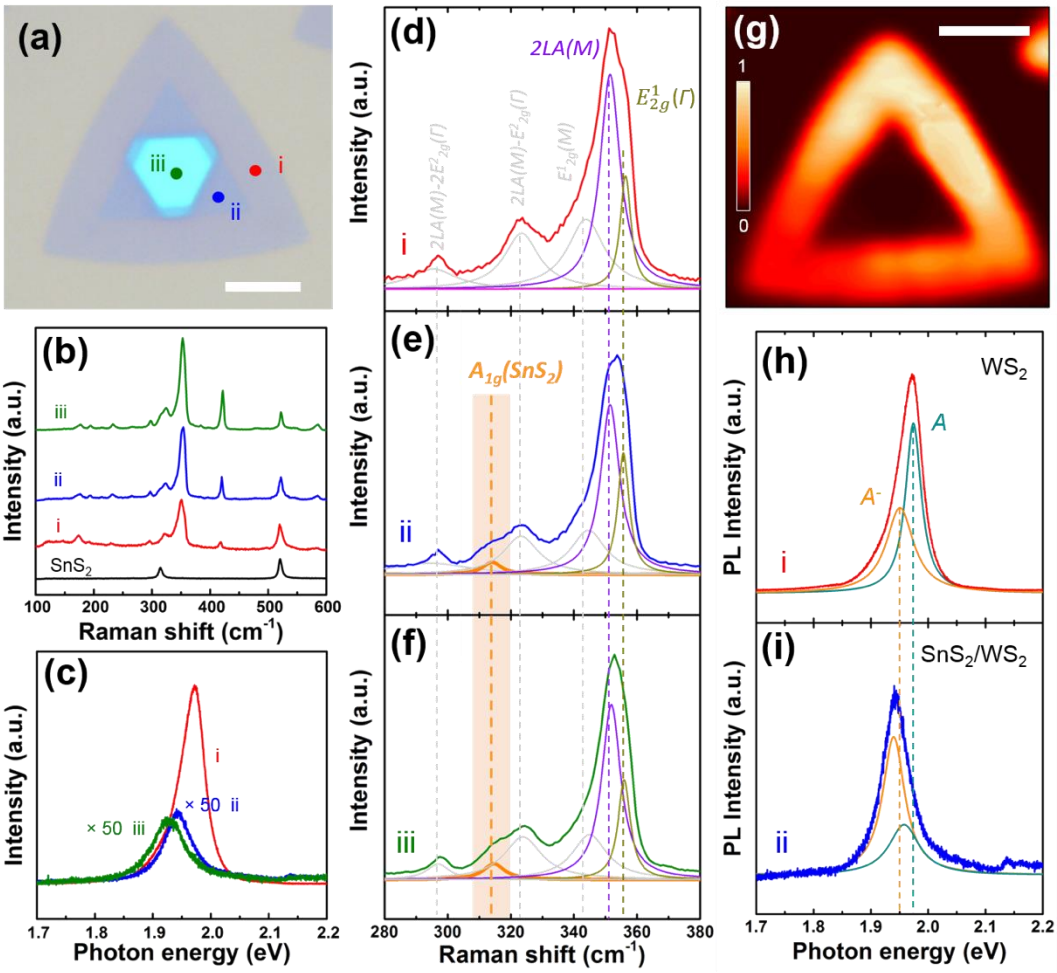


Figure 6.4. Optical characterisation of the SnS_2/WS_2 vdW vertical heterostructure: (a) Optical image of the same heterostructure in Figure 1(f) showing the contrast between WS_2 and SnS_2 layers. (b) Raman spectrum of the SnS_2/WS_2 heterostructures, monolayer WS_2, and SnS_2 marked in (a). (c) PL spectrum of monolayer WS_2 and the SnS_2/WS_2 heterostructures marked in (a). (d) Raman spectrum of monolayer WS_2 with the Lorentzian fitting to extract E_{2g} and A_{1g} peaks. (e) Raman spectrum of a monolayer SnS_2/WS_2 heterostructure (m-SWH) with the Lorentzian fitting to extract E_{2g} and A_{1g} peaks. (f) Raman spectrum of few-layer SnS_2/WS_2 heterostructure (f-SWH) with the Lorentzian fitting to extract E_{2g} and A_{1g} peaks. (g) PL mapping of the SnS_2/WS_2 heterostructure in (a). (h) PL spectrum of monolayer WS_2 with the Lorentzian fitting to extract the exciton and trion emission. (i) PL spectrum of m-SWH with the Lorentzian fitting to extract the exciton and trion emission. The scale bars in (a) and (g) are 5 µm.

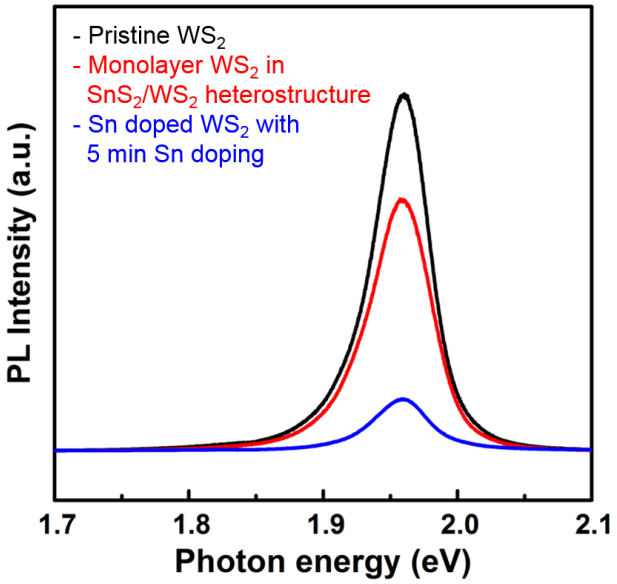


Figure 6.5. Comparison of PL characterisation peak intensity between the pristine monolayer WS_2, monolayer WS_2 in the SnS_2/WS_2 heterostructure and Sn-doped WS_2 monolayer obtained from 5 min Sn doping of the WS_2 layer.

To further analyse the interlayer interaction at the interface of the heterostructure, the PL signal in the monolayer WS_2 and SnS_2/WS_2 heterostructure were then deconvoluted into separate peaks by fitting with two Lorentzian curves, as shown in the **Figure 6.4**(h) and (i). These two Lorentzian curves are attributed to the exciton (A) and trion (A^-) emissions. The corresponding photon energies for A and A^- in monolayer WS_2 are 1.951 eV and 1.974 eV, whereas those in the SnS_2/WS_2 heterostructure are 1.939 eV and 1.958 eV, respectively. The red-shift of both exciton and trion peak in the heterostructure could stem from the tensile strain introduced by SnS_2. Because the lattice constant of monolayer WS_2 is 0.31 nm, whereas that of the SnS_2 is 0.36 nm, this would introduce a tensile strain for monolayer WS_2 after the SnS_2 growth.[20-21] The observed A^-/A peak ratio of the heterostructure (**Figure 6.4**(i)) is much higher than that of the WS_2 monolayer (**Figure 6.4**(h)), indicating an efficient charge separation at the interface of the heterostructure after the photon excitation. This charge transfer is the main reason for the PL emission quenching: part of the charges in WS_2 layers transfer to the adjacent

SnS_2 layers and reduce the excitonic emission. This is consistent with the inferred type II band offset according to previous density functional theory (DFT) calculation results.[22-23] According to the calculation, the conduction band minimum of SnS_2 is -4.16 eV, which is 0.32 eV lower than that of WS_2; while the valance band maximum of WS_2 is -5.82 eV, which is 0.62 eV higher than that of SnS_2. As a consequence, most of the electrons tend to reside in SnS_2 while holes are inclined to stay in WS_2 in the SnS_2/WS_2 vdW heterostructures. Besides, it is noted that the intensity of the PL characteristic peak for monolayer WS_2 without the cover of SnS_2 in the heterostructure is still comparable to the pristine monolayer WS_2. Also, it is much larger than that of monolayer WS_2 with 5 min Sn doping shown in **Figure 6.5**, suggesting little substitution of Sn in the monolayer WS_2 after the SnS_2 growth for the synthesis of the SnS_2/WS_2 heterostructure.

6.2.2 Growth Mechanism

Figure 6.6(a) further explains the details on the growth of SnS_2 on the WS_2 monolayers, which involves several sequential steps. After convective and diffusive transport to the reaction zone, the precursor gas molecules first diffuse into the boundary layer near the SiO_2 substrate and are adsorbed onto the substrate surface. Second, the adsorbed species often migrate some distance on the substrate through surface diffusion. After the migration of the adsorbed species to the growth sites, the adsorbed species are incorporated into the crystal lattice and form chemical bonds through edge attachment. The adsorbed species, in addition, could also desorb from the substrate into the gas phase during these growth stages because of the high reaction temperature.

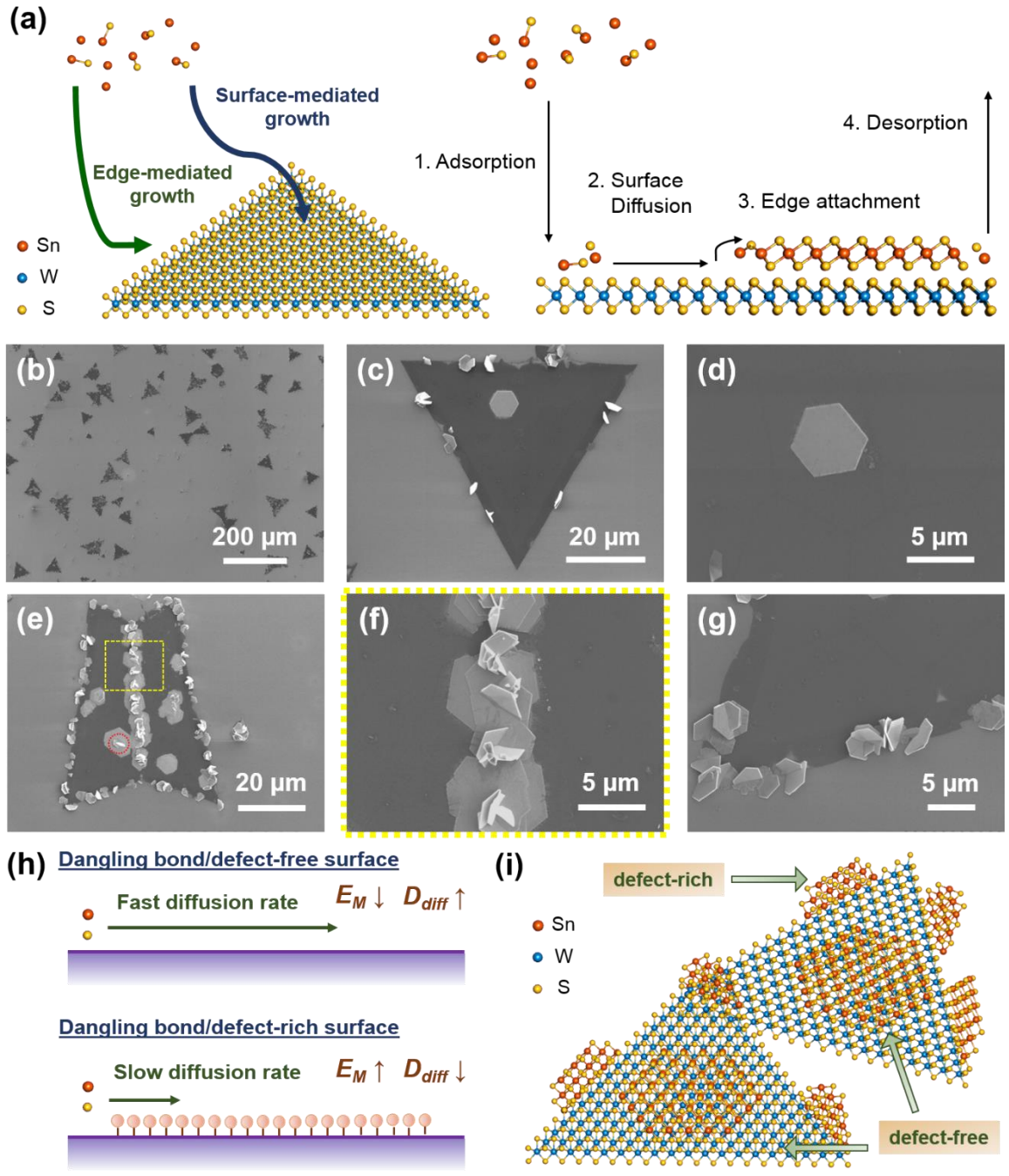


Figure 6.6. Surface-mediated growth and edge-mediated growth of SnS_2 on WS_2 monolayers: (a) Schematic illustrations explaining the growth mechanism and each step during the second step SnS_2 growth on the pre-grown monolayer WS_2. (b) Low magnification SEM image demonstrating the growth of SnS_2 crystals on WS_2 monolayers under the 470°C growth temperature. (c) SEM image demonstrating the difference of SnS_2 growth mediated by the edge and surface of monolayer WS_2. (d) Enlarged SEM image showing the horizontal growth of SnS_2 on WS_2 surface. (e) SEM image

demonstrating the morphology of SnS_2 grown on the mirror tilt WS_2 domains. (f) Enlarged SEM image from the yellow dashed rectangular area in (e) showing the cluster growth of SnS_2 on the domain boundary of WS_2. (g) SEM image showing the SnS_2 growth mediated by the edges of pre-grown WS_2. (h) Schematic illustration explaining the surface diffusion rate of adsorbed species on different types of surface during the growth of SnS_2. (i) Atomic configuration demonstrating the growth difference of SnS_2 grown on defect-rich and defect-free area in monolayer WS_2.

When the temperature increases from 450°C to 470°C, the growth of SnS_2 becomes more reactive and could be both mediated by the surface and edges of WS_2 monolayers. The SEM images in **Figure 6.6**(b) and (c) shows the morphological difference between SnS_2 grown on the WS_2 surface and the edge of WS_2. The surface-mediated growth of SnS_2 shows a stable lateral growth resulting in crystalline hexagons (**Figure 6.6**(d)). In contrast, the edge-mediated growth of SnS_2 exhibits irregular shapes with a random growth direction (**Figure 6.6**(g)). The growth of SnS_2 on multiple monolayer WS_2 domains with domain boundaries between each other, shown in **Figure 6.6**(e), was also examined and displayed a similar morphological difference. The SEM image in **Figure 6.6**(f) shows the domain boundary area marked by the yellow dashed square in **Figure 6.6**(e). It can be seen that on domain boundaries on WS_2 the SnS_2 layers grow vertically in a random manner, which is similar to the edge-mediated growth. The vertical SnS_2 crystals on the WS_2 edges and domain boundaries were further characterised by Raman spectroscopy, and both exhibited strong signals of the SnS_2 characteristic peaks (**Figure 6.7**), indicating the growth of thicker crystals.

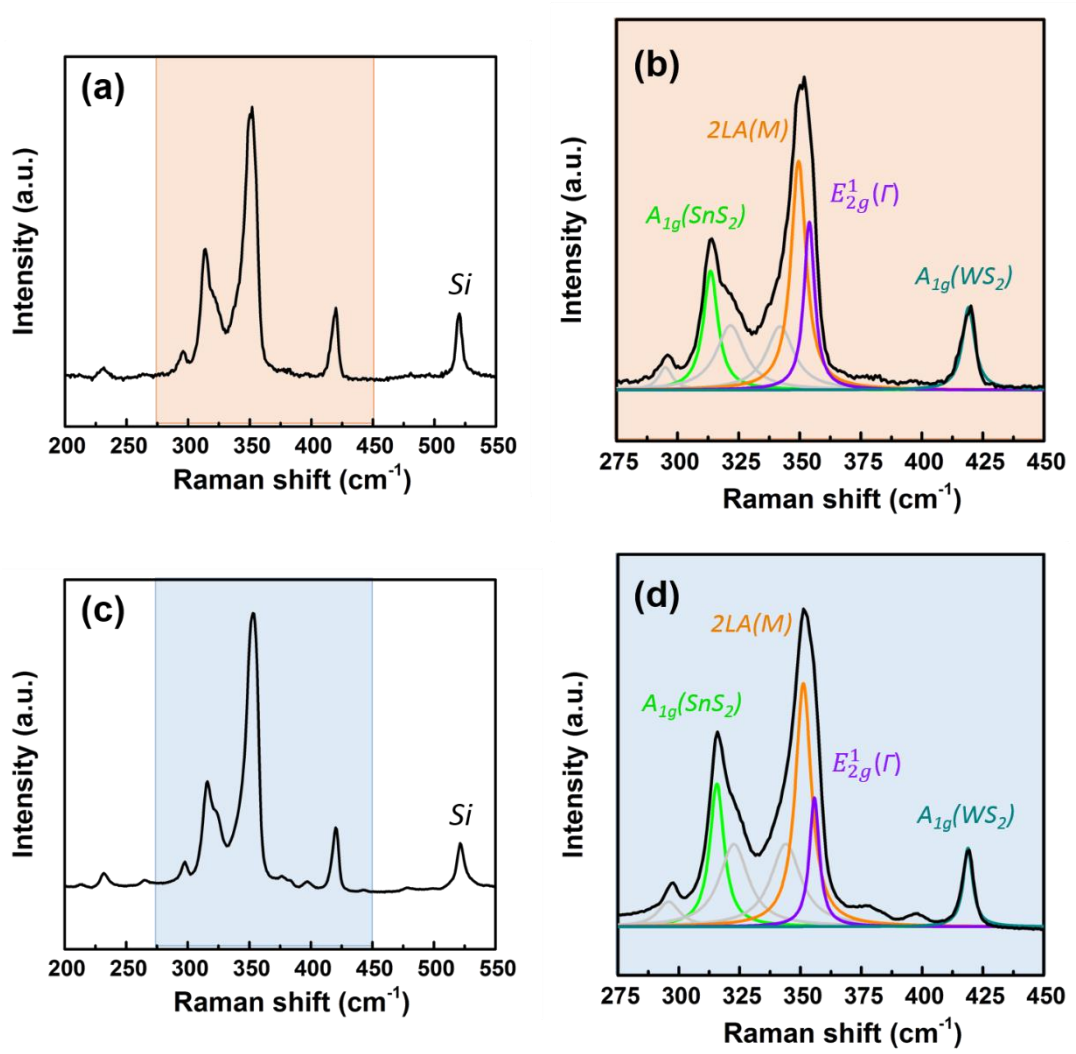


Figure 6.7. Raman characterisation of the vertical SnS_2 crystals on the WS_2. (a-b) Raman spectra of the SnS_2 crystals grown on the edges of WS_2. The enlarged spectrum in (b) shows the Lorentzian fitting to extract the A_{1g} peak of SnS_2 and the E_{2g} and A_{1g} peaks of WS_2. (c-d) Raman spectra of the SnS_2 crystals grown on the domain boundaries of WS_2. The enlarged spectrum in (d) shows the Lorentzian fitting to extract the A_{1g} peak of SnS_2 and the E_{2g} and A_{1g} peaks of WS_2.

The observed morphological difference of SnS_2 could be further explained by the different migration coefficients of adatoms on the WS_2 surface and edges, which leads to horizontal growth on WS_2 surface and cluster growth at the edge of WS_2. Unlike graphene and hBN, the vapour deposition growth of 2D layered SnS_2 is non-catalytic. Without the dominance

of catalysts, the growth is subject to the influence of the interaction between the adsorbed adatoms and the substrate surface. For example, the initial nucleation bonding may affect the eventual morphology. The surface that is abundant of dangling bonds has higher chance to grow 3D structures. The surface diffusion of these adsorbed species hence plays a vital role in determining the final crystal morphology. The surface diffusion coefficient D_{diff} can be expressed as

$$D_{diff} = A*exp(-E_M/k_BT) , \quad (1)$$

where the E_M is the energy barrier of migration for adsorbed species on the substrate surface, k_B is the Boltzmann constant, A is the pre-exponential factor, and T is the temperature. The energy barrier of migration, which increases linearly with the number of surface dangling bonds, drastically affects the surface diffusion of the adsorbed species.[24] As shown in **Figure 6.6**(h), the atomically flat surface of WS_2 that is free of dangling bonds and defects could facilitate the surface diffusion with the longer diffusion length of adsorbed species because of the lower E_M and higher D_{diff}. The adsorbed species on the WS_2 surface therefore have much higher tendency to incorporate into the ideal growth sites with the lowest surface free energy. In contrast, the adsorbed species on the surface with a high density of dangling bonds or defects such as WS_2 edges have slower surface diffusion rate and shorter diffusion length because of the higher E_M and lower D_{diff}. The domain boundaries of WS_2 consist of several pentagon-heptagon (5-7) or square-octagon (6-8) pairs.[25] Although they can be fully reconstructed without unsaturated bonding, the reconstruction is unlikely to be completed ideally, especially for the domain boundaries that arise from stitching of individual domain growing into each other. In addition, the domain boundaries may cause the uneven or undulating surface in the surrounding lattice because of the inherent strain. This would also affect the growth behaviour of SnS_2, and results in the random nucleation or edge attachment forming 3D or irregular microstructures on defect-rich WS_2 edges and domain boundaries during the SnS_2 growth. In

contrast, on the defect-free WS_2 surface the as-grown SnS_2 crystals could show a well-defined hexagonal shape (**Figure 6.6**(i)). The large E_M and lower diffusion rate in WS_2 edges could also promote the nucleation and lead to the thicker SnS_2 crystals. The SiO_2 substrates, likewise, are three-dimensionally bonded and have a high density of dangling bonds at the surfaces, resulting in a high energy barrier of migration for adsorbed species. This hinders the free migration of adsorbed species and the morphology of SnS_2 grown on SiO_2 often exhibits clusters or a non-hexagon crystal shape.[15] A similar growth dependence on the substrate has also been observed in the case of other 2D materials such as NbS_2 and ReS_2,[26-29] which demonstrate the importance of substrate selection on the growth of 2D crystals with high quality. It is noted that some of the SnS_2 crystals could also grow in the out-of-plane direction on the WS_2 surface, which is indicated by the red dashed circle in **Figure 6.6**(e). This is ascribed to the high growth temperature of SnS_2, which could possibly introduce local defects on the WS_2 surfaces.

In addition to the microstructural difference for the SnS_2 growth, most of the SnS_2 crystals grown on the WS_2 surface are well aligned in one orientation, which is demonstrated in **Figure 6.8**(a) and (b). The stacking angle between the WS_2 and SnS_2, illustrated in **Figure 6.8**(c), can be assigned to the angle between the $\{11\bar{2}0\}$ plane of SnS_2 crystals and the $\{11\bar{2}0\}$ plane of WS_2 monolayers. Counting of ~1000 different SnS_2 crystals under the SEM yielded the stacking angle distribution shown in **Figure 6.8**(d), which revealed a preferred stacking angle of near 0°. This indicates the epitaxial relationship between the SnS_2 layers and WS_2 monolayers. In fact, the lattice constants of WS_2 and SnS_2 are 0.31 and 0.36 nm, respectively, and the calculated lattice mismatch is around 16.1%. Though the lattice mismatch between SnS_2 and WS_2 is larger than that in epitaxial III-IV semiconductor heterostructures, it can be relaxed for the growth of vdW heterostructures because of the weak interaction at the interface. The growth of SnS_2 on WS_2 is therefore attributed to the weak vdW interaction instead of

chemical bonding, which is advantageous for the epitaxial growth because of a similar crystallographic order.

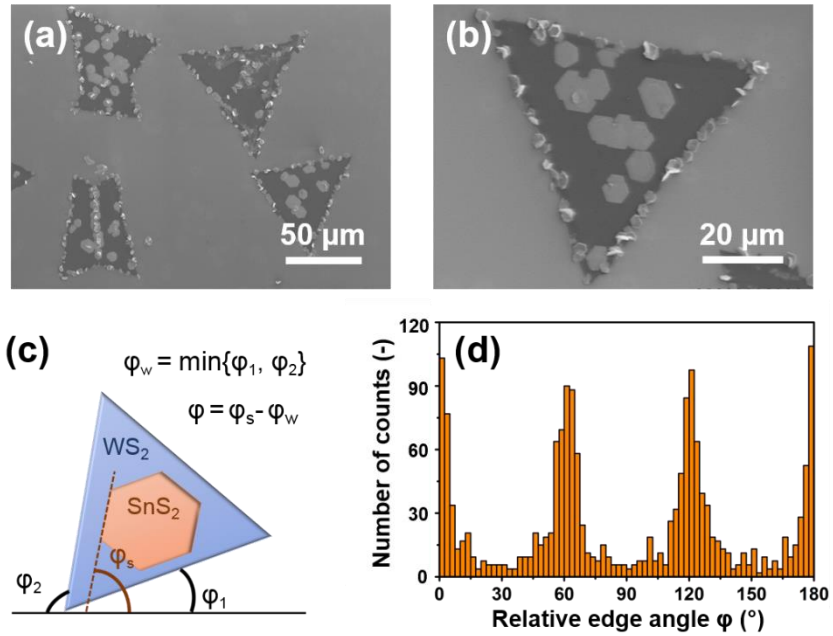


Figure 6.8. Orientation relationship between the SnS_2 crystals and WS_2 monolayers: (a) Low magnification SEM displaying the orientation distribution of SnS_2 crystals within each monolayer WS_2. (b) Enlarged SEM image demonstrating the orientation preference of SnS_2 crystals within the same WS_2 domain. (c) Schematic illustration for the definition of the relative edge angle between the SnS_2 and WS_2 monolayers. (d) Statistical distribution of the relative edge angles of SnS_2 domains within WS_2 monolayers.

6.2.3 CVD Growth of SnS_2 on Other 2D Materials

To confirm the morphological difference of SnS_2 resulting from the density of the surface defects, other 2D materials such as MoS_2 and hBN have also been adopted as the substrates for the SnS_2 growth. **Figure 6.9**(a) and (b) shows the morphology of CVD-grown monolayer MoS_2 prior to the growth of SnS_2. The details of the CVD MoS_2 growth are shown in **Figure 6.10**.

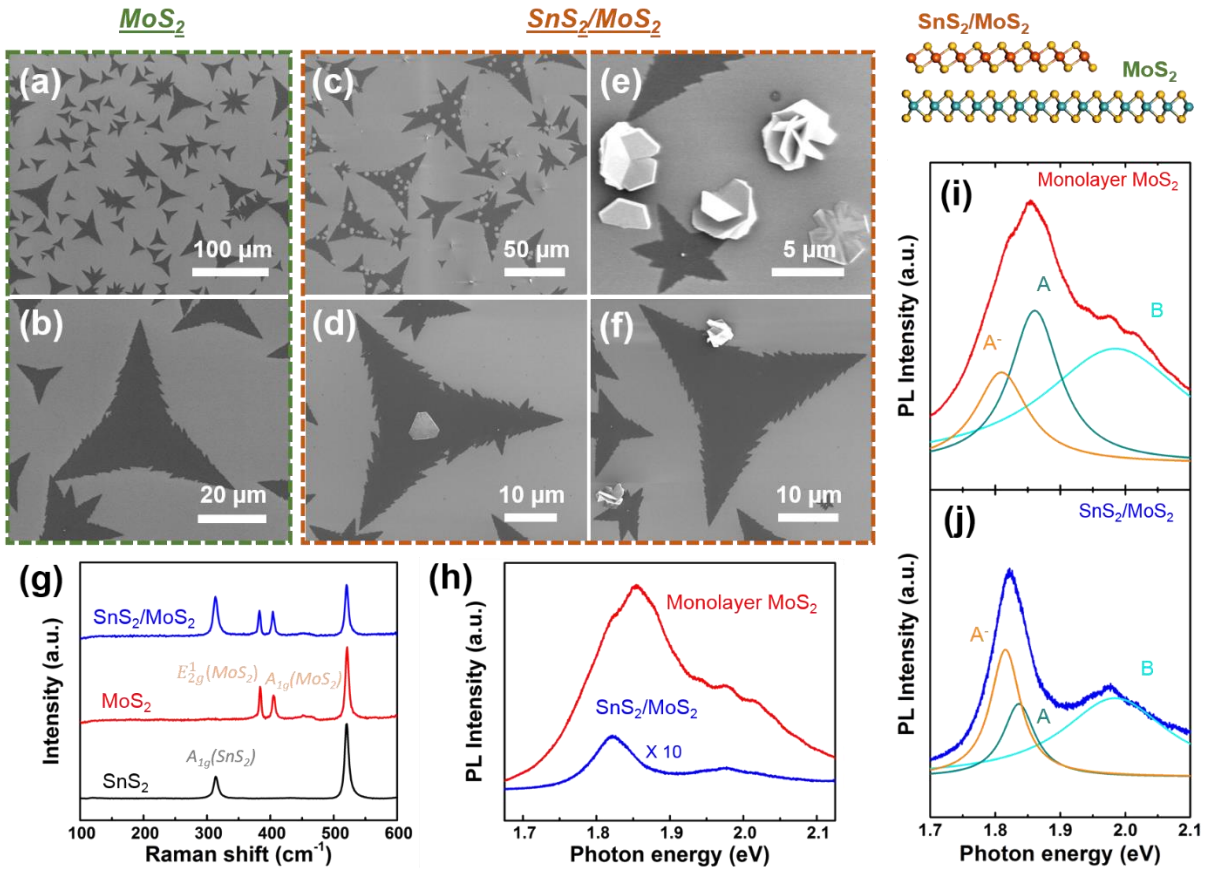


Figure 6.9. Direct CVD growth of SnS_2 on monolayer MoS_2 and the optical analysis of the SnS_2/MoS_2 vertical vdW heterostructures. (a) SEM image of as-grown MoS_2 showing the overall coverage before the SnS_2 growth. (b) SEM image of the monolayer MoS_2 showing the triangular star crystal shape with dendritic edges. (c) Low-magnification SEM image of monolayer MoS_2 after the growth of SnS_2 layers. (d) SEM image showing the horizontal growth of SnS_2 on MoS_2 surface. (e) SEM image of SnS_2 grown on the surface of SiO_2 showing the preference of growing in the out-of-plane directions. (f) SEM image showing the cluster growth of SnS_2 on the edges of MoS_2. (g) Raman spectrum of the SnS_2/MoS_2 heterostructure, monolayer MoS_2, and SnS_2. (h) PL spectrum of monolayer MoS_2 and the SnS_2/MoS_2 heterostructure. (i) PL spectrum of monolayer MoS_2 with the Lorentzian fitting to extract exciton and trion emissions. (j) PL spectrum of the SnS_2/MoS_2 heterostructure with the Lorentzian fitting to extract exciton and trion emissions.

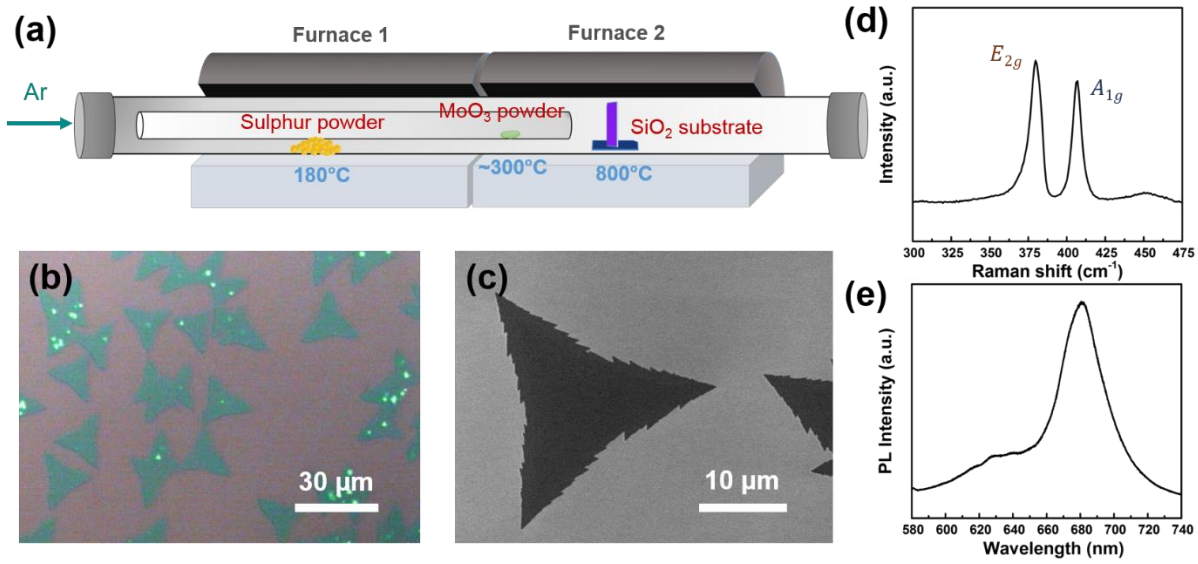


Figure 6.10. Atmospheric-pressure CVD synthesis of MoS_2 domains on the SiO_2 substrate. (a) Schematic illustration of the experimental setup for the CVD growth of MoS_2. (b) Optical image demonstrating the uniformity and overall coverage of monolayer MoS_2. (c) SEM image of star-shaped monolayer MoS_2 with thorns at the edges. (d) Raman spectra of the as-grown monolayer MoS_2 with the Lorentz peaks fitting. (e) PL characterization of the as-grown monolayer MoS_2.

The growth of SnS_2 on monolayer MoS_2 in **Figure 6.9**(c-f) exhibits a similar trend to that on monolayer WS_2. Lateral growth of SnS_2 could be stabilized on the defect-free MoS_2 surface because of the smaller energy barrier of migration and larger diffusion coefficient (**Figure 6.9**(d)), whereas the cluster growth of SnS_2 is observed on the dangling-bond-rich SiO_2 surface (**Figure 6.9**(e)) and MoS_2 edges (**Figure 6.9**(f)). The Raman spectrum in **Figure 6.9**(g) displays both the characteristic signals of the individual SnS_2 A_{1g} peak as well as MoS_2 E^1_{2g} and A_{1g} peak in the SnS_2/MoS_2 heterostructure. There is no obvious peak shift in SnS_2/MoS_2 heterostructure compared to that of MoS_2, indicating that the MoS_2 monolayer remains high quality with little damage after the growth of SnS_2. The quenching of PL signals shown in **Figure 6.9**(h) in the SnS_2/MoS_2 heterostructure is attributed to the interlayer interaction and effective charge separation at the interface between MoS_2 and SnS_2. This is also evidenced by

the increased intensity ratio of trion to exciton peak after the Lorentz fitting, as demonstrated in **Figure 6.9**(i) and (j).

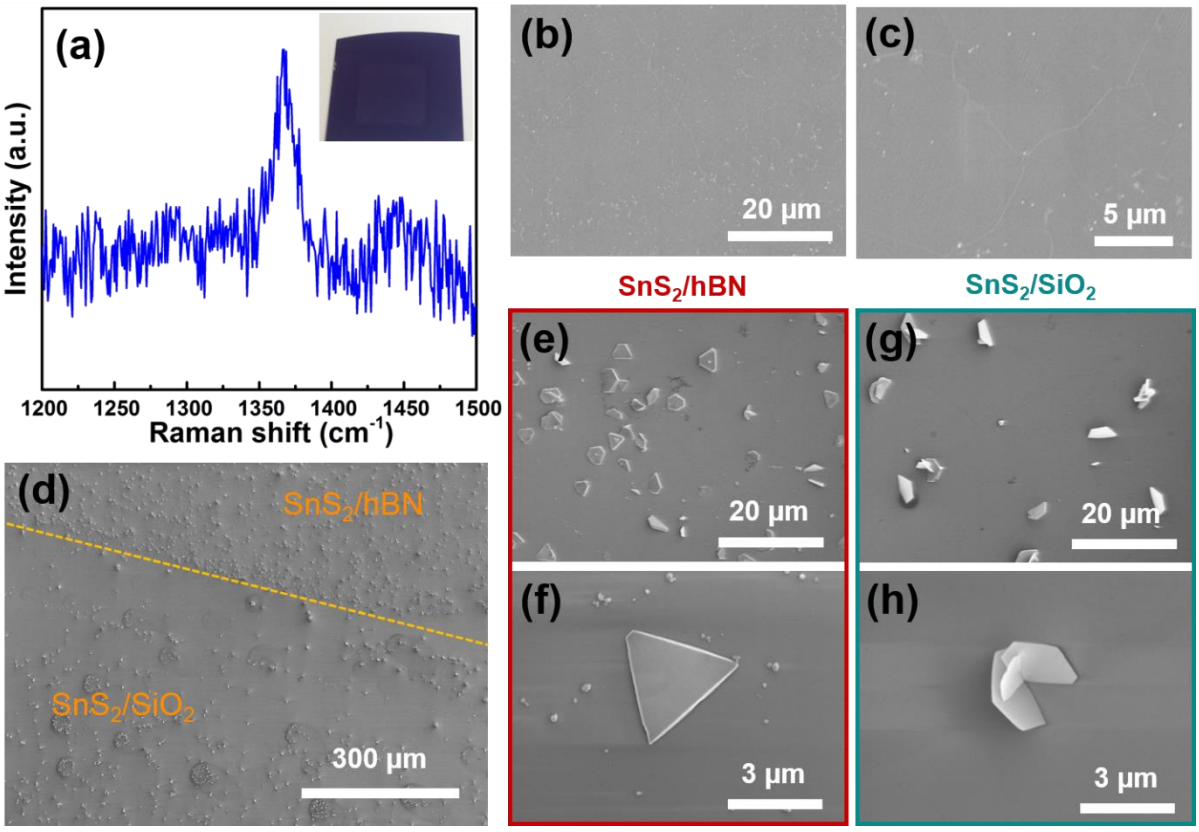


Figure 6.11. CVD growth of SnS_2 on the transferred hBN layers: (a) Raman spectra of the CVD-grown hBN layers after transfer onto a SiO_2 substrate. (b) SEM image of continuous hBN layers on Cu substrate showing the uniformity of the hBN films. (c) Enlarged SEM image of continuous hBN layers on Cu substrate showing the surface cleanliness. (d) SEM image of the edge of transferred hBN continuous films after the growth of SnS_2. (e) SEM image of the SnS_2 crystals grown on the surface of hBN film. (f) Enlarged SEM image showing the individual triangular SnS_2 crystal grown on the hBN surface. (g) SEM image showing the distribution of SnS_2 crystals on the SiO_2 area. (h) Enlarged SEM image showing the growth of SnS_2 crystal on the SiO_2 area.

Likewise, the growth of SnS_2 on hBN through a two-step CVD strategy has also been investigated. In the first step, continuous monolayer hBN films were grown by the OCVD

method described in Chapter 4, using the ammonia borane as the growth precursor, then followed by transfer from Cu surface to SiO_2 substrate (**Figure 6.11**(a-c)). In the second step, employing the as-grown hBN as the growth substrate, SnS_2 crystals were subsequently synthesized on the continuous hBN film. The difference between growth behaviours of SnS_2 crystals is demonstrated in **Figure 6.11**(d). The SnS_2 crystals grown on the hBN film exhibit a higher nucleation density, compared to those grown on the SiO_2, which may result from the higher roughness of transferred hBN film on SiO_2 because of the PMMA residual. Besides, it can be seen that SnS_2 crystals grown on hBN tend to exhibit more like trigonal and hexagonal shape (**Figure 6.11**(e) and (f)), whereas on SiO_2 surfaces SnS_2 crystals exhibit trapezoidal shape (**Figure 6.11**(g) and (h)). On the basis of these SnS_2 growth results in both transition metal dichalcogenides and hBN, it is inferred that the presence of a clean and continuous film of 2D materials without additional transfer process is beneficial for the growth of 2D crystalline SnS_2. These surfaces are completely passivated without any dangling bonds at the atomically clean and ultra-smooth surface and could change the interface energy of SnS_2 and the growth substrate, therefore stabilizing the lateral growth of SnS_2.

6.3 Conclusion

In summary, this chapter demonstrates the successful synthesis of ultrathin SnS_2 crystals by employing 2D WS_2 triangles as the vdW growth substrates. The surface structure of underlying WS_2 layers is found to be critical in determining the growth behaviour of SnS_2. During the growth stage, the atomically flat and inert surface of the WS_2 layers could lower the energy barrier of migration for adsorbed active species and accelerate the surface diffusion compared to the area nearby edges and domain boundaries, which are often with a high density of unsaturated dangling bonds. This results in SnS_2 growth well aligned to the WS_2 lattice and forms crystalline hexagons on the flat WS_2 surface, whereas at the edge and domain boundaries

of WS_2 the SnS_2 grows vertically in a random manner. A similar phenomenon is also observed on other 2D materials such as MoS_2 and hBN, proving the growth behaviour is universal and implying the significance of employing substrates that are free from dangling bonds or defects for the SnS_2 growth. This enables the controllable synthesis of flat 2D SnS_2 with high quality, improving the applicability in future nanoelectronic applications.

6.4 Reference

(1) Huang, Y.; Sutter, E.; Shi, N. N.; Zheng, J.; Yang, T.; Englund, D.; Gao, H.-J.; Sutter, P., Reliable Exfoliation of Large-Area High-Quality Flakes of Graphene and Other Two-Dimensional Materials. *ACS Nano* **2015,** *9* (11), 10612-10620.

(2) Frisenda, R.; Navarro-Moratalla, E.; Gant, P.; Perez De Lara, D.; Jarillo-Herrero, P.; Gorbachev, R. V.; Castellanos-Gomez, A., Recent Progress in the Assembly of Nanodevices and van der Waals Heterostructures by Deterministic Placement of 2D Materials. *Chem. Soc. Rev.* **2018,** *47* (1), 53-68.

(3) Chen, T.; Zhou, Y.; Sheng, Y.; Wang, X.; Zhou, S.; Warner, J. H., Hydrogen-Assisted Growth of Large-Area Continuous Films of MoS_2 on Monolayer Graphene. *ACS Appl. Mater. Interfaces* **2018,** *10* (8), 7304-7314.

(4) Lu, Y.; Chen, T.; Ryu, G. H.; Huang, H.; Sheng, Y.; Chang, R.-J.; Warner, J. H., Self-Limiting Growth of High-Quality 2D Monolayer MoS_2 by Direct Sulfurization Using Precursor-Soluble Substrates for Advanced Field-Effect Transistors and Photodetectors. *ACS Appl. Nano Mater.* **2019,** *2* (1), 369-378.

(5) Chen, T.; Sheng, Y.; Zhou, Y.; Chang, R.-j.; Wang, X.; Huang, H.; Zhang, Q.; Hou, L.; Warner, J. H., High Photoresponsivity in Ultrathin 2D Lateral Graphene:WS_2:Graphene Photodetectors Using Direct CVD Growth. *ACS Appl. Mater. Interfaces* **2019,** *11* (6), 6421-6430.

(6) Tan, C.; Chen, J.; Wu, X.-J.; Zhang, H., Epitaxial Growth of Hybrid Nanostructures. *Nat. Rev. Mater.* **2018,** *3*, 17089.

(7) Gong, Y.; Lin, J.; Wang, X.; Shi, G.; Lei, S.; Lin, Z.; Zou, X.; Ye, G.; Vajtai, R.; Yakobson, B. I.; Terrones, H.; Terrones, M.; Tay, Beng K.; Lou, J.; Pantelides, S. T.; Liu, Z.; Zhou, W.; Ajayan, P. M., Vertical and in-Plane Heterostructures from WS_2/MoS_2 Monolayers. *Nat. Mater.* **2014,** *13*, 1135-1142.

(8) Shi, J.; Tong, R.; Zhou, X.; Gong, Y.; Zhang, Z.; Ji, Q.; Zhang, Y.; Fang, Q.; Gu, L.; Wang, X.; Liu, Z.; Zhang, Y., Temperature-Mediated Selective Growth of MoS_2/WS_2 and WS_2/MoS_2 Vertical Stacks on Au Foils for Direct Photocatalytic Applications. *Adv. Mater.* **2016,** *28* (48), 10664-10672.

(9) Lin, Y.-C.; Ghosh, R. K.; Addou, R.; Lu, N.; Eichfeld, S. M.; Zhu, H.; Li, M.-Y.; Peng, X.; Kim, M. J.; Li, L.-J.; Wallace, R. M.; Datta, S.; Robinson, J. A., Atomically Thin Resonant Tunnel Diodes Built from Synthetic van der Waals Heterostructures. *Nat. Commun.* **2015,** *6*, 7311.

(10) Gong, Y.; Lei, S.; Ye, G.; Li, B.; He, Y.; Keyshar, K.; Zhang, X.; Wang, Q.; Lou, J.; Liu, Z.; Vajtai, R.; Zhou, W.; Ajayan, P. M., Two-Step Growth of Two-Dimensional WSe_2/$MoSe_2$ Heterostructures. *Nano Lett.* **2015,** *15* (9), 6135-6141.

(11) Zhang, T.; Jiang, B.; Xu, Z.; Mendes, R. G.; Xiao, Y.; Chen, L.; Fang, L.; Gemming, T.; Chen, S.; Rümmeli, M. H.; Fu, L., Twinned Growth Behaviour of Two-Dimensional Materials. *Nat. Commun.* **2016,** *7*, 13911.

(12) Huang, Y.; Sutter, E.; Sadowski, J. T.; Cotlet, M.; Monti, O. L. A.; Racke, D. A.; Neupane, M. R.; Wickramaratne, D.; Lake, R. K.; Parkinson, B. A.; Sutter, P., Tin Disulfide—An Emerging Layered Metal Dichalcogenide Semiconductor: Materials Properties and Device Characteristics. *ACS Nano* **2014,** *8* (10), 10743-10755.

(13) Xia, J.; Zhu, D.; Wang, L.; Huang, B.; Huang, X.; Meng, X.-M., Large-Scale Growth of Two-Dimensional SnS_2 Crystals Driven by Screw Dislocations and Application to Photodetectors. *Adv. Funct. Mater.* **2015,** *25* (27), 4255-4261.

(14) Ahn, J.-H.; Lee, M.-J.; Heo, H.; Sung, J. H.; Kim, K.; Hwang, H.; Jo, M.-H., Deterministic Two-Dimensional Polymorphism Growth of Hexagonal n-Type SnS_2 and Orthorhombic p-Type SnS Crystals. *Nano Lett.* **2015,** *15* (6), 3703-3708.

(15) Chang, R.-J.; Tan, H.; Wang, X.; Porter, B.; Chen, T.; Sheng, Y.; Zhou, Y.; Huang, H.; Bhaskaran, H.; Warner, J. H., High-Performance All 2D-Layered Tin Disulfide: Graphene Photodetecting Transistors with Thickness-Controlled Interface Dynamics. *ACS Appl. Mater. Interfaces* **2018,** *10* (15), 13002-13010.

(16) Su, G.; Hadjiev, V. G.; Loya, P. E.; Zhang, J.; Lei, S.; Maharjan, S.; Dong, P.; M. Ajayan, P.; Lou, J.; Peng, H., Chemical Vapor Deposition of Thin Crystals of Layered Semiconductor SnS_2 for Fast Photodetection Application. *Nano Lett.* **2015,** *15* (1), 506-513.

(17) Zhou, X.; Zhang, Q.; Gan, L.; Li, H.; Zhai, T., Large-Size Growth of Ultrathin SnS_2 Nanosheets and High Performance for Phototransistors. *Adv. Funct. Mater.* **2016,** *26* (24), 4405-4413.

(18) Sheng, Y.; Wang, X.; Fujisawa, K.; Ying, S.; Elias, A. L.; Lin, Z.; Xu, W.; Zhou, Y.; Korsunsky, A. M.; Bhaskaran, H.; Terrones, M.; Warner, J. H., Photoluminescence Segmentation within Individual Hexagonal Monolayer Tungsten Disulfide Domains Grown by Chemical Vapor Deposition. *ACS Appl. Mater. Interfaces* **2017,** *9* (17), 15005-15014.

(19) Smith, A. J.; Meek, P. E.; Liang, W. Y., Raman Scattering Studies of SnS_2 and $SnSe_2$. *J. Phys. C: Solid State Phys.* **1977,** *10* (8), 1321-1323.

(20) Pak, S.; Lee, J.; Lee, Y.-W.; Jang, A. R.; Ahn, S.; Ma, K. Y.; Cho, Y.; Hong, J.; Lee, S.; Jeong, H. Y.; Im, H.; Shin, H. S.; Morris, S. M.; Cha, S.; Sohn, J. I.; Kim, J. M., Strain-Mediated Interlayer Coupling Effects on the Excitonic Behaviors in an Epitaxially Grown MoS_2/WS_2 van der Waals Heterobilayer. *Nano Lett.* **2017,** *17* (9), 5634-5640.

(21) Tweedie, M. E. P.; Sheng, Y.; Sarwat, S. G.; Xu, W.; Bhaskaran, H.; Warner, J. H., Inhomogeneous Strain Release during Bending of WS_2 on Flexible Substrates. *ACS Appl. Mater. Interfaces* **2018,** *10* (45), 39177-39186.

(22) Burton, L. A.; Whittles, T. J.; Hesp, D.; Linhart, W. M.; Skelton, J. M.; Hou, B.; Webster, R. F.; O'Dowd, G.; Reece, C.; Cherns, D.; Fermin, D. J.; Veal, T. D.; Dhanak, V. R.; Walsh, A., Electronic and Optical Properties of Single Crystal SnS_2: an Earth-Abundant Disulfide Photocatalyst. *J. Mater. Chem. A* **2016,** *4* (4), 1312-1318.

(23) Kang, J.; Tongay, S.; Zhou, J.; Li, J.; Wu, J., Band Offsets and Heterostructures of Two-Dimensional Semiconductors. *Appl. Phys. Lett.* **2013,** *102* (1), 012111.

(24) Kangawa, Y.; Akiyama, T.; Ito, T.; Shiraishi, K.; Nakayama, T., Surface Stability and Growth Kinetics of Compound Semiconductors: An Ab Initio-Based Approach. *Materials* **2013,** *6* (8), 3309-3360.

(25) Ji, H. G.; Lin, Y.-C.; Nagashio, K.; Maruyama, M.; Solís-Fernández, P.; Sukma Aji, A.; Panchal, V.; Okada, S.; Suenaga, K.; Ago, H., Hydrogen-Assisted Epitaxial Growth of Monolayer Tungsten Disulfide and Seamless Grain Stitching. *Chem. Mater.* **2018,** *30* (2), 403-411.

(26) Huang, L.; Yu, Y.; Li, C.; Cao, L., Substrate Mediation in Vapor Deposition Growth of Layered Chalcogenide Nanoplates: A Case Study of $SnSe_2$. *J. Phys. Chem. C* **2013,** *117* (12), 6469-6475.

(27) Ge, W.; Kawahara, K.; Tsuji, M.; Ago, H., Large-Scale Synthesis of NbS_2 Nanosheets with Controlled Orientation on Graphene by Ambient Pressure CVD. *Nanoscale* **2013,** *5* (13), 5773-5778.

(28) Li, X.; Cui, F.; Feng, Q.; Wang, G.; Xu, X.; Wu, J.; Mao, N.; Liang, X.; Zhang, Z.; Zhang, J.; Xu, H., Controlled Growth of Large-Area Anisotropic ReS_2 Atomic Layer and its Photodetector Application. *Nanoscale* **2016,** *8* (45), 18956-18962.

(29) Wu, R.; Tao, Q.; Dang, W.; Liu, Y.; Li, B.; Li, J.; Zhao, B.; Zhang, Z.; Ma, H.; Sun, G.; Duan, X.; Duan, X., van der Waals Epitaxial Growth of Atomically Thin 2D Metals on Dangling-Bond-Free WSe_2 and WS_2. *Adv. Funct. Mater.* **2019,** *29* (12), 1806611.

Chapter 7

Metal Exchange Driven Post-Growth Substitutional Tin Doping of 2D WS_2 Crystals Using Chemical Vapour Deposition

7.1 Introduction

In light of Si and III-IV semiconductor technologies over the past few decades, doping engineering of 2D materials appears to be the key technique to effectively modify the physical properties and expand their functionalities.[1-2]

With a view to obtaining stable 2D structures for future nanoelectronic applications, substitutional doping was considered as an effective way to modulate the properties of 2D semiconductors among the current doping strategies. This type of doping has often been accomplished by adopting the powder vaporisation chemical vapour deposition (CVD) approach and putting all the precursors together at the same time in the CVD quartz tube during the growth phase of the crystals.[3-4] This all-in-one method can lead to the stable substitutional doping structure, but is challenging to produce high quality dopants and control their uniformity because of the different crystallisation temperatures of materials and precursor evaporation rates.

A two-step strategy where the host 2D materials are first synthesised with high quality and followed by gentle post treatments is a more promising method to integrate different 2D elements together and obtain a stable products with controllable properties. Because chalcogen

atoms are generally exposed to the outer surface in 2D TMDs, it is easier to replace them with other anionic heteroatoms such as halogen in the post treatment processes.[5] For example, plasma treatment of TMDs under N_2 or PH_3 exposure results in the implantation of nitrogen and phosphorus, respectively, in the chalcogen vacancies.[6-7] Likewise, thermal annealing of CVD-grown MoS_2 under the Se atmosphere gives rise to the selenide formation via substitutional doping.[8] In contrast, little reports have explored the metal substitution using post-growth treatments, as it is difficult to dope extrinsic metal atoms in the lattice of 2D TMDs after CVD growth. This is because transition metal atoms are generally more stable than chalcogens in TMDs, and the encapsulating chalcogen atoms act as blocking layers, prohibiting the incorporation of the extrinsic metal element in the post-growth treatments.

In this chapter, the post-growth modification of CVD-grown WS_2 with metallic Sn dopants was reported using SnS precursor to achieve a range of Sn/W/S composite 2D materials. This post-growth doping method not only preserves the advantages of scalability from traditional CVD approach,[9-11] but also provides a better uniformity control for dopant spatial distribution. The analysis of annular dark-field scanning transmission electron microscopy (ADF-STEM) on monolayer and bilayer regions reveals that the substitutional doping of Sn takes place only in the the top surface. These results provide an improved route to post-growth doping of pre-formed 2D materials (i.e., WS_2 crystals) with other elements (i.e., Sn) to modulate their structures, broadening doping strategies beyond traditional methods where all precursors are included at the same time during the growth process. This allows the realization of direct selective layer doping in bilayer crystals and could even expand into more chemically complicated structures.

7.2 Results and Discussion

7.2.1 Thermal Doping of Sn in the CVD-Grown WS_2 Layers

The synthesis of tin-doped WS_2 was realised through a two-step strategy. As shown in **Figure 7.1**(a), the WS_2 monolayers were first grown by the chemical vapour deposition (CVD) method employing tungsten trioxide (WO_3) and sulfur powders at 1050°C. The presence of WS_2 crystals and their optical properties were examined by Raman and photoluminescence (PL) spectroscopy, as shown in **Figure 6.2**, after which the samples were then reintroduced to the CVD chamber for the Sn treatment. In the second step, the as-grown WS_2 layers were subsequently put under the Sn-rich atmosphere using the SnS as a precursor. It is noted that compared to the traditional method using tin dioxide (SnO_2) for the growth of tin-rich 2D materials, the SnS precursor is advantageous for providing an environment with less oxygen contamination. The doping temperature was found to play a critical role in the control of the substitution reaction of Sn, which will be discussed later.

Figure 7.1(b) schematically shows the experimental setup for the synthesis of Sn-doped WS_2 crystals using the post thermal treatment method. The doping of Sn was carried out using a homebuilt 1-inch CVD system with a quartz tube, and gas flow rates were controlled by digital mass flow controllers. Both the SnS precursor and the pre-grown WS_2 crystals were placed on the ceramic crucible, separated by around 7 cm with the SnS precursor placed in the centre of the furnace. **Figure 7.1**(c) and (d) shows a comparison of the optical images for the as-grown triangular WS_2 before and after 10 min of the second Sn doping stage, demonstrating that there is no significant damage or change of morphology during the thermal doping process. Besides, both WS_2 before and after Sn doping were further characterized by atomic force microscopy (AFM), as shown in the **Figure 7.1**(e) and (f), respectively. From the dark yellow dashed line in **Figure 7.1**(e) and (f) across the step edge at the corner of the WS_2 crystal, the

line profiles (**Figure 7.1**(g)) are acquired. These reveal that the step height at the WS_2 edge are measured to be 0.77 nm before Sn doping and 0.81 nm after doping, respectively. This confirms that the thickness of WS_2 remains monolayer after the doping of Sn.

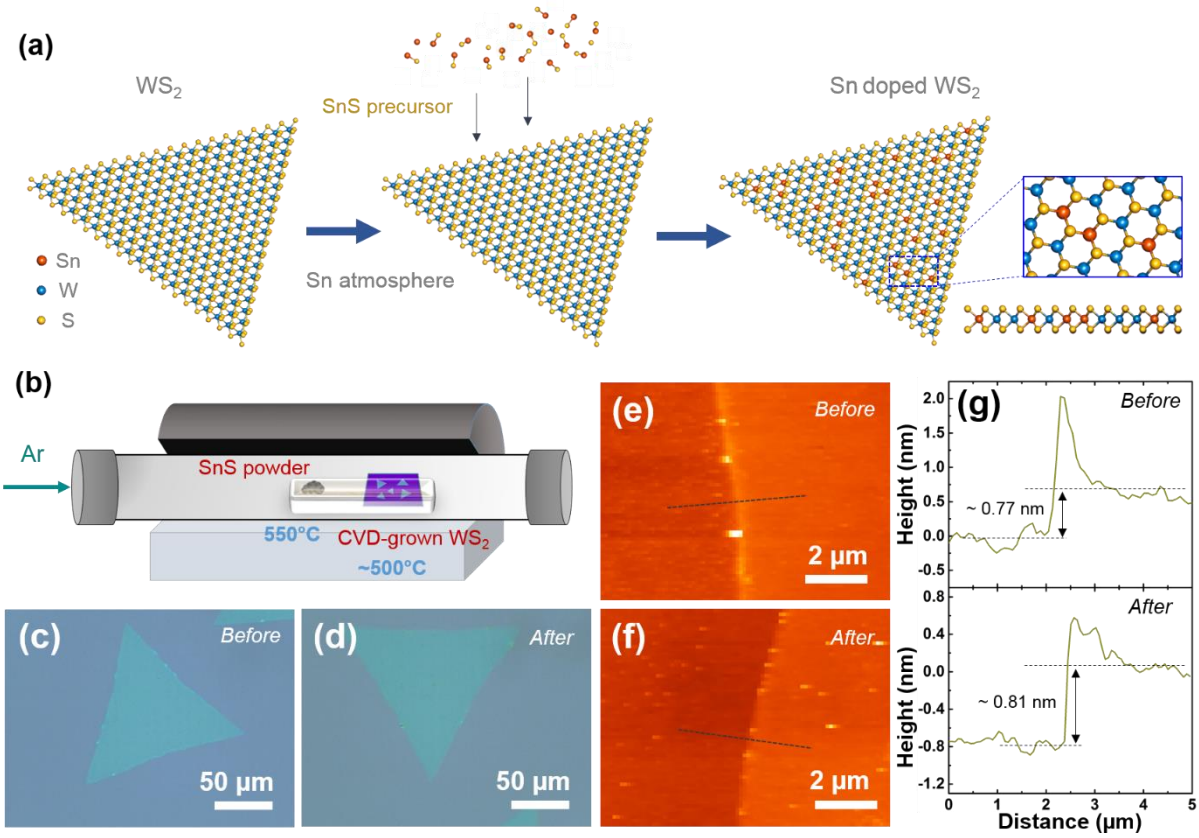


Figure 7.1. Doping of Sn in the CVD-grown WS_2. (a) Schematics of atomic configuration showing the formation of Sn-doped WS_2 monolayers. (b) Schematic illustration of the experimental setup for the thermal doping of Sn in WS_2. (c-d) Optical image of monolayer WS_2 before and after 10 of min Sn doping, respectively. (e-f) Atomic force microscopy (AFM) image of monolayer WS_2 before and after 10 min of Sn doping, respectively. (g) Line profile from the dark yellow dashed line in (e-f) at the edge corner showing the thickness of WS_2 layers before and after the Sn doping, respectively.

To further demonstrate the property change with the amount of Sn dopants, the Sn-doped WS_2 crystals were synthesized with different Sn doping times and further characterised by spectroscopy. The Raman spectrum from **Figure 7.2**(a) demonstrates that there is no

apparent peak shift between the pristine WS_2 and the WS_2 crystals after different Sn doping times (5, 10, 15, and 20 min), indicating that the WS_2 monolayers remain with high quality with little damage after the doping of Sn. This is also evidenced by the comparison of SEM images between Sn-doped WS_2 monolayers with different Sn doping times and the corresponding pristine WS_2, as shown in **Figure 7.3**. In addition, only the two subtle peaks at 383 cm^{-1} and 397 cm^{-1} in the Raman spectrum are observed in the Sn-doped WS_2 layers. These peaks are due to the Raman resonance effect that resulted from the extrinsic substitutional dopants, which was also found in a previous report.[12]

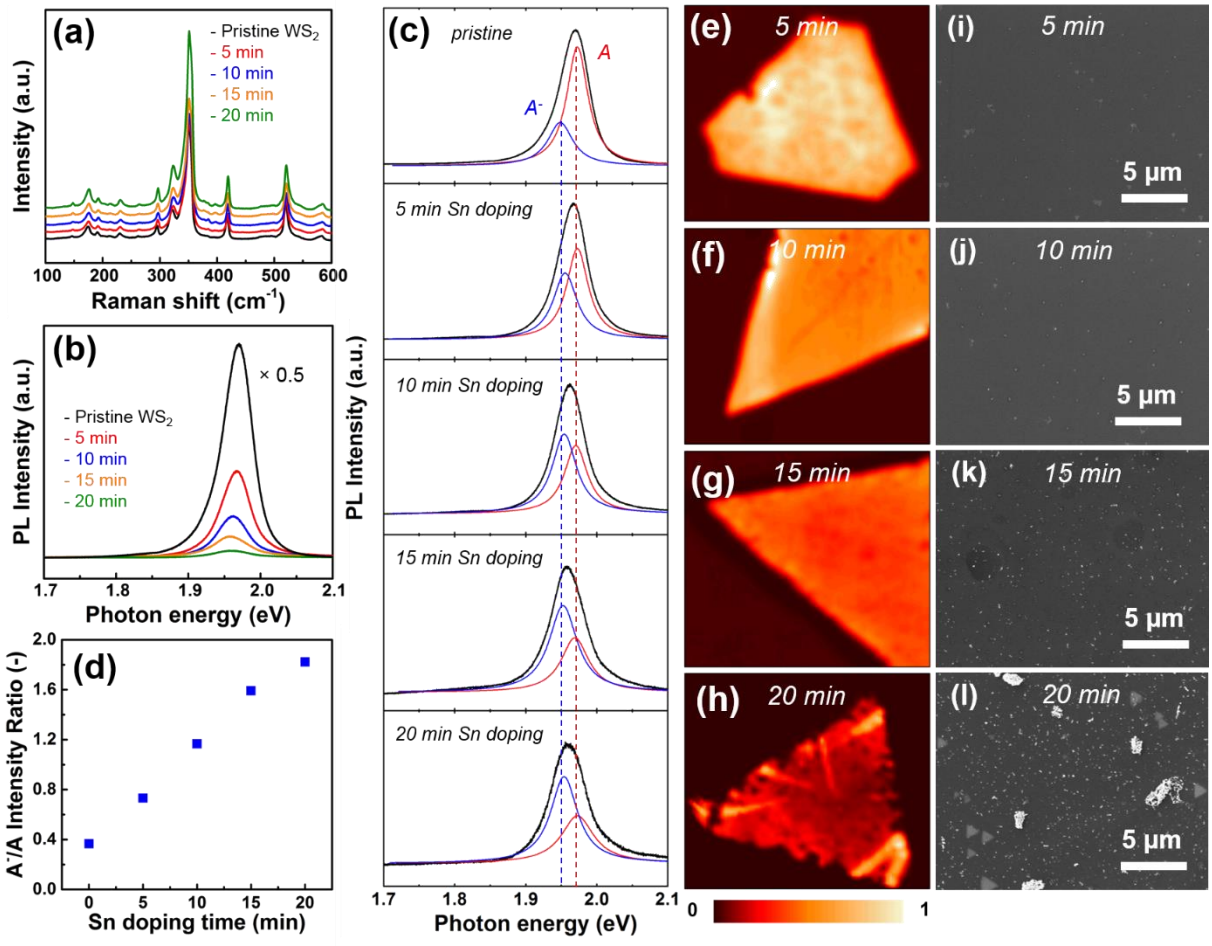


Figure 7.2. Characterisation of Sn-doped WS_2 with different Sn doping times. (a) Raman spectrum of monolayer WS_2 before and after 5, 10, 15, and 20 min of Sn doping. (b) PL spectrum of monolayer WS_2 before and after 5, 10, 15, and 20 min of Sn doping. (c) PL spectra of the pristine monolayer WS_2

and after each Sn doping time with the Lorentzian fitting by excitonic and trionic peaks. (d) Plot of the intensity ratio between the excitonic and trionic peaks versus the Sn doping time. (e-h) PL mapping of the WS_2 after (e) 5, (f) 10, (g) 15, and (h) 20 min of Sn doping. (i-l) SEM images of the surface of monolayer WS_2 after (i) 5, (j) 10, (k) 15, and (l) 20 min of Sn doping.

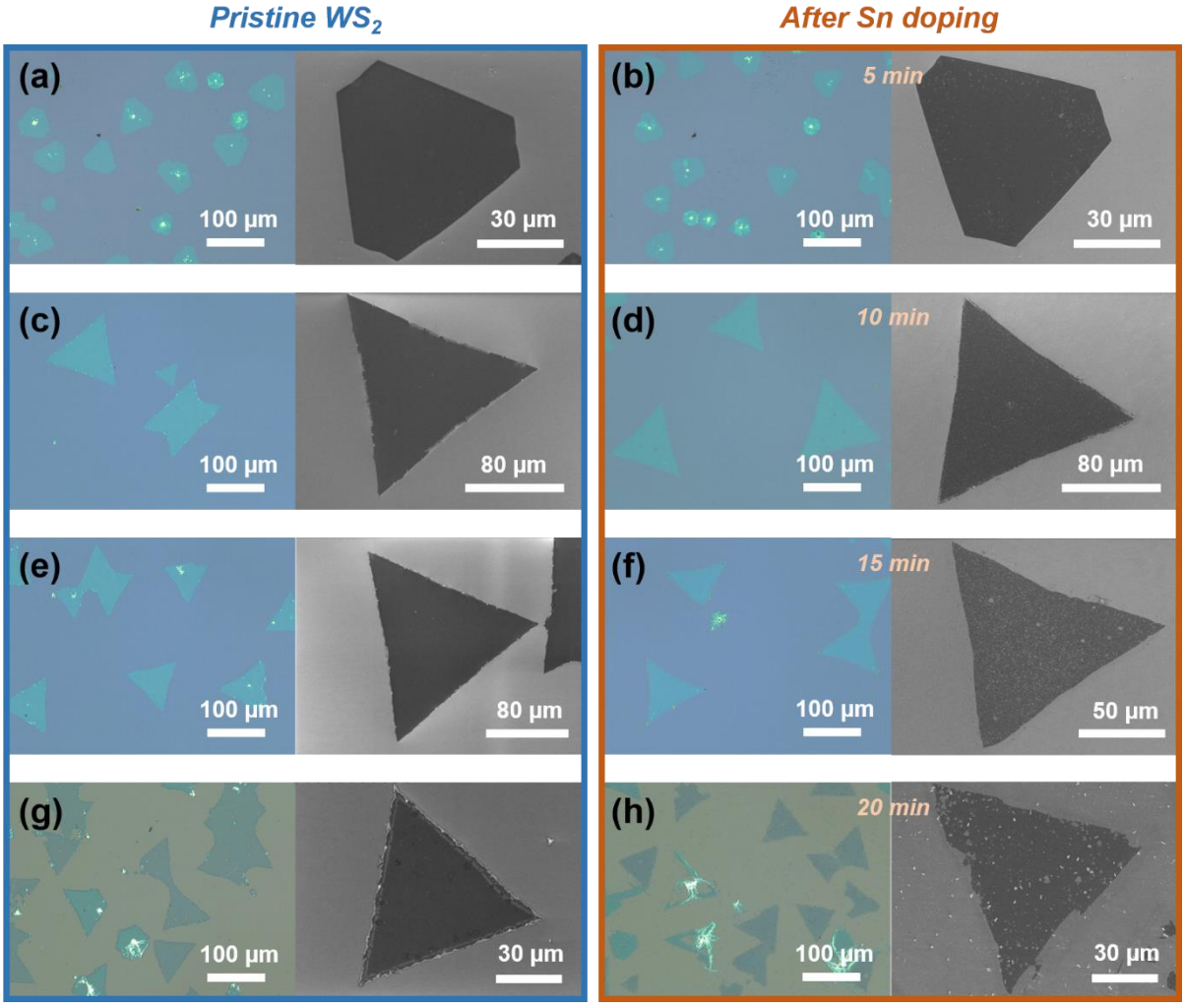


Figure 7.3. Morphology comparison of WS_2 before and after Sn doping. (a) Optical and SEM image of pristine WS_2 showing the overall coverage and individual crystals before Sn doping. (b) Optical and SEM image of a WS_2 crystal after 5 min of Sn doping. (c) Optical and SEM image of pristine WS_2 showing the overall coverage and an individual crystal before Sn doping. (d) Optical and SEM image of a WS_2 crystal after 10 min of Sn doping. (e) Optical and SEM image of pristine WS_2 showing the overall coverage and an individual crystal before Sn doping. (f) Optical and SEM image of a WS_2 crystal

after 15 min of Sn doping. (g) Optical and SEM image of pristine WS_2 showing the overall coverage and an individual crystal before Sn doping. (h) Optical and SEM image of a WS_2 crystal after 20 min of Sn doping.

The PL characteristic peak of WS_2, shown in **Figure 7.2**(b), reveals a gradual quenching with the increase of the doping time and concentration of Sn dopants. This indicates an increased concentration of electrons due to the Sn dopants that act as electron donors (n-type dopants) when substituting the W atoms in the WS_2 layers.[13] Each PL spectrum was then deconvoluted into two separate peaks, corresponding to the exciton (A) and trion (A^-) emissions, using Lorentzian fitting shown in **Figure 7.2**(c). It can be seen that from **Figure 7.2**(d), the intensity ratio between extracted A^- peak and A peak rises with the increase of the Sn doping time, indicating that more negatively charged excitons resulting from the electron supply of extrinsic Sn atoms. This is also consistent with the measured PL quenching.

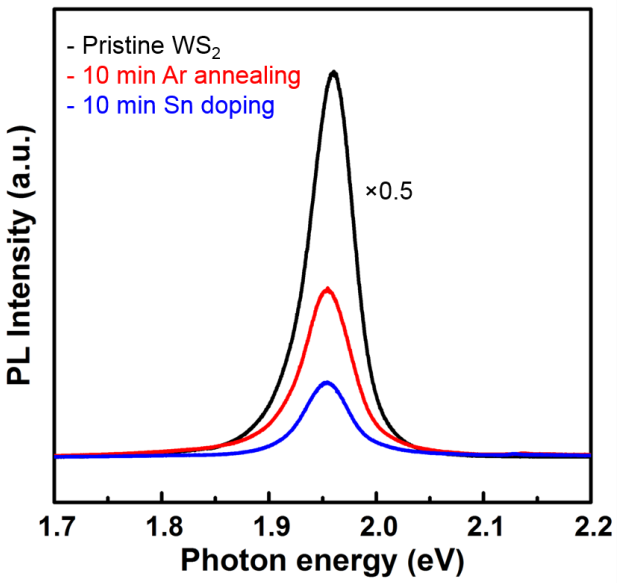


Figure 7.4. Comparison of PL peak intensities between the pristine monolayer WS_2, pristine WS_2 after 10 min Ar annealing and Sn-doped WS_2 monolayer obtained from 10 min Sn doping of WS_2.

It is noted that the Ar annealing of monolayer WS_2 could also lead to the PL quenching because of the introduction of sulfur vacancies at high temperature; however, this effect could be minimized as the SnS precursor could provide additional sulfur during the Sn doping and potentially induce the self-healing of sulfur vacancies. The PL intensity of the resulted WS_2 with Sn doping is much smaller than that with Ar annealing under the same treatment time (**Figure 7.4**). This confirms that the PL quenching comes from the doping of Sn rather than the loss of sulfur atoms. **Figure 7.2**(e-h) shows the corresponding PL mapping of the Sn-doped WS_2 crystal with different Sn doping times. It can be seen that the PL intensities are relatively uniform over the entire Sn-doped WS_2 layers except for the sample after 20 min of Sn doping. This may result from the initiation of the WS_2 degradation as the supply of sulfur from the SnS precursor becomes deficient to fill in the increasing sulfur vacancies. The SEM was employed to further examine the change of the WS_2 surface under different Sn doping times. As shown in **Figure 7.2**(i-l), it can be seen that during the first 15 min of Sn doping, the WS_2 remains a clean surface, whereas after 20 min of doping, bunches of chunky white particles could be observed and the WS_2 starts to degrade and reveal triangular holes on the surfaces. For the further characterisation of Sn-doped WS_2 monolayers, the analysis was focused on the monolayer WS_2 after 10 min of Sn doping and its comparison with the pristine monolayer WS_2 crystals.

7.2.2 ADF-STEM Characterisation of Sn-Doped WS_2 Layers

Although both SEM and PL studies provide useful insights into the characterization of the Sn doping of WS_2, they offer limited information for the quantification and distribution of Sn dopants in the WS_2 monolayers. Direct imaging of the Sn dopants using annular dark-field scanning transmission electron microscopy (ADF-STEM) is a powerful technique to further identify the location of the Sn dopants within the WS_2. The SEM image in **Figure 7.5**(a) shows

the triangular Sn-doped WS_2 layers after 10 min of Sn doping, indicated by blue dashed lines, transferred from the SiO_2 substrate to a holy SiN grid for the characterisation of ADF-STEM. The enlarged SEM image in **Figure 7.5**(b) shows details of the central area of the triangular Sn-doped WS_2, marked by a red circle in **Figure 7.5**(a). This shows that the additional adlayer resulting from the overgrowth on monolayer WS_2 during the first step CVD synthesis process. To confirm the existence of Sn, the sample was first examined by EDX analysis, shown in **Figure 7.6**(a). **Figure 7.5**(c) presents the ADF-STEM image of the yellow circle in **Figure 7.5**(b), displaying a clear boundary between the monolayer and bilayer-doped WS_2. **Figure 7.5**(d-f) demonstrates typical ADF-STEM images with different magnifications of the Sn-doped WS_2.

In ADF-STEM imaging, the primary contrast mechanism is the Z-contrast. The collected signal in the ADF-STEM images is directly proportional to $Z^{1.6}$, meaning that the elements with higher atomic numbers (higher Z) exhibit higher intensity in the image. This enables atoms of different elements to be discriminated on the basis of their contrast difference. After introducing the optical aberration system, the imaging technique is capable of identifying and locating different elements. In the Sn-doped WS_2 crystals, W atoms (Z=74) appear with higher intensity than double S (Z=16) columns, and the Sn (Z=50) atom can also be distinguished from double S columns and single W column. From the line intensity scan (**Figure 7.5**(g)) extracted in the blue and yellow columns in **Figure 7.5**(f), it can be clearly seen that the Sn atoms are all situated at the W sites, suggesting the substitutional doping of Sn with W in WS_2. To confirm that the dimmer spot is a Sn atom, the experimental intensity line profile was also compared with the simulated Z-contrast intensity profile. This shows a great match with the Sn simulation result (**Figure 7.6**(b)), better than that for other metal dopants, such as Cr, which could originate from the trace elements of the metal oxide precursors.[14] A higher magnification ADF-STEM image is shown in **Figure 7.5**(j) in false colour to show the

Sn dopant locations (white circles). Besides, the sulfur maintains stacking vertically together based on the line scan along the $[11\bar{2}0]$ direction (blue column in **Figure 7.5**(f)), suggesting that the whole crystal structure remains 2H phase after the doping of Sn. To further determine the composition of the Sn-doped WS_2 sample, a maximum filter (**Figure 7.5**(h)) was first applied on the low magnification ADF-STEM image of **Figure 7.5**(d) to reveal the contrast difference between Sn and W. Statistical counting of the individual W/Sn sites in the **Figure 7.5**(h) was then adopted, and the histogram of intensity of each site is shown in **Figure 7.5**(k). By applying a threshold in the intensity of 3.8 arbitrary units (a.u.), the Sn dopants, highlighted by blue dots, could be identified (**Figure 7.5**(i)). The corresponding atomic percentage of the Sn in Sn-doped WS_2 monolayer is estimated to be around 8.16%. In addition, it can be seen that the arrangement of the Sn dopants in the Sn-doped WS_2 differs from mono-Sn (1-Sn), bi-Sn (2-Sn), and tri-Sn (3-Sn) to tetra-Sn (4-Sn) dopants, whose the atomic structures are illustrated in **Figure 7.5**(m). The statistical distribution in **Figure 7.5**(l) shows that among the Sn dopants, around 80% of them are arranged in 1-Sn. This indicates the little preference for the Sn dopants to cluster in the WS_2 layers, and the doping of Sn is fairly uniform.

In addition, as confirmed by the fast Fourier transform (FFT) of the ADF-STEM image in the inset of **Figure 7.5**(d), the spacing of (100) and (110) lattice plane in the Sn-doped WS_2 is measured to be 0.29 nm and 0.17 nm, respectively, which is slightly larger than the lattice plane spacing of pristine WS_2. This implies the change of lattice parameter of WS_2 after the doping of Sn. In traditional semiconductor doping structure, where the dopant concentration is generally in the order of ppm, the Sn concentration in this work is much larger. It is expected that the alloyed $Sn_xW_{(1-x)}S_2$ with the T phase structure can be acquired when continuing to increase the Sn dopants in the WS_2 layers.

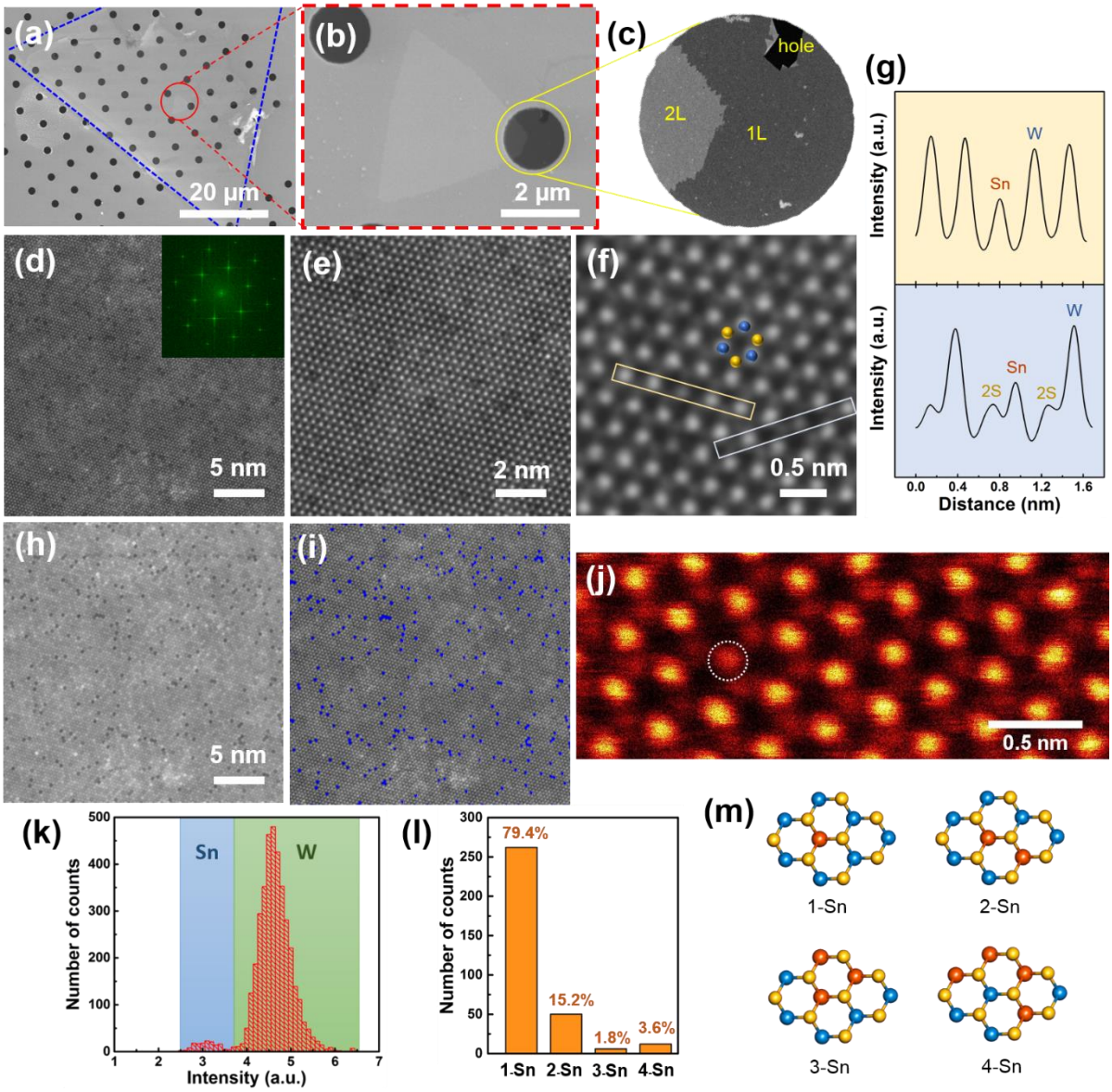


Figure 7.5. Annular dark-field STEM (ADF-STEM) analysis of the monolayer Sn-doped WS_2. (a) SEM image of Sn-doped WS_2 transferred onto the SiN TEM grid. (b) Enlarged SEM image of the red circle indicated in (a) showing the details of the monolayer Sn-doped WS_2 and a small island of bilayer Sn-doped WS_2. (c) ADF-STEM image of the same area in (b). (d-f) ADF-STEM images showing the area of monolayer Sn-doped WS_2 with different magnifications. The inset in (d) shows the fast Fourier transform (FFT) image of (d). (g) Intensity line profiles across the yellow and blue rows in (f) showing the differences in intensity between W and Sn. (h) Maximum filter with the low magnification STEM image (d) displaying the distinct contrast between the Sn dopants and W atoms. (i) Labelled atom image obtained from (d) demonstrating the distribution of Sn dopants (blue dot). (j) High-magnification ADF-

STEM image of a Sn dopant in the WS_2 lattice with false colour LUT (red-hot). The white dashed circle indicates the Sn site. (k) Histogram analysis of image (h) after applying the maximum filter. (l) Histogram analysis showing the percentage of different configurations of Sn dopants. (m) Atomic structure for the four different configurations of Sn dopants.

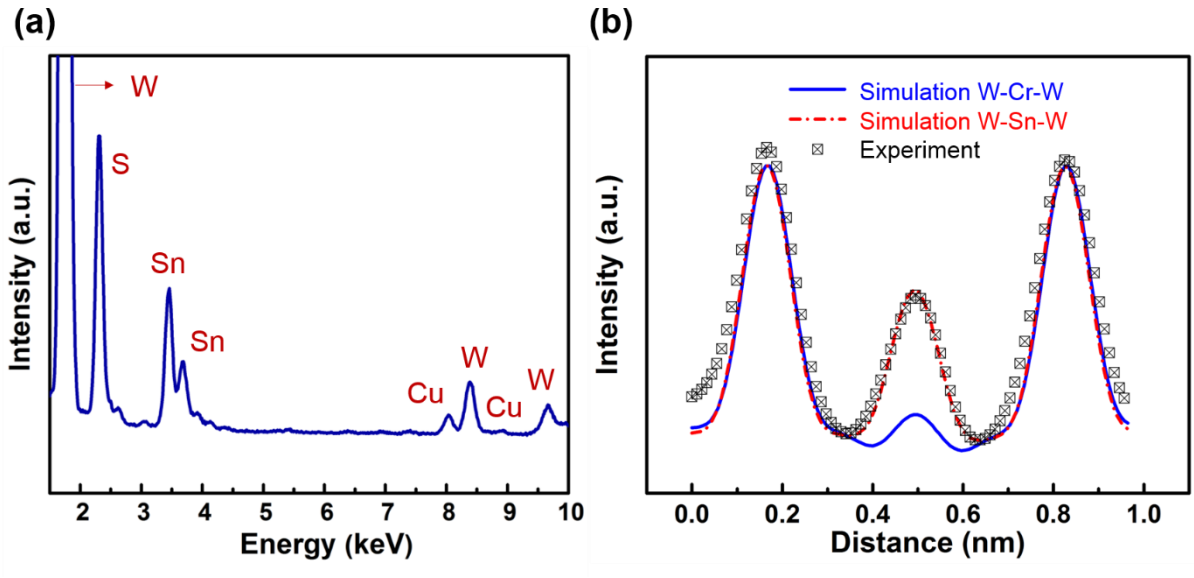


Figure 7.6. Elemental analysis for the confirmation of Sn dopants in WS_2 layers. (a) EDX measurement of the Sn-doped WS_2 monolayer obtained from 10 min doping of Sn. (b) Comparison between the intensity line profile of metal column from the experimental ADF-STEM image in Figure 3(f) and the simulated intensity profile based on W-Sn-W and W-Cr-W.

To further understand the Sn doping, the monolayer-bilayer step edge region of Sn-doped WS_2 was examined using ADF-STEM, as shown in **Figure 7.5**(b). This enables the relative orientation of the two layers and the sub-lattice sites to be determined. **Figure 7.7**(a) illustrates a low magnification ADF-STEM image at the monolayer-bilayer interface. **Figure 7.7**(b) is the magnified ADF-STEM image of the yellow dashed square in **Figure 7.7**(a), demonstrating the intensity details on each lattice site. It can be seen that the bilayer Sn-doped WS_2 follows the 2H stacking sequence, where the single W/Sn (double S) column in one layer

overlaps with the double S (single W/Sn) column in the other layer. The two layers are fully eclipsed with a rotation angle of 60° between each lattice orientation. **Figure 7.7**(c) shows the intensity profile of the line scan along the $[11\bar{2}0]$ direction indicated by the blue column in **Figure 7.7**(b). The lattice sites with the largest intensity correspond to the superimposition of one W atom and two S atoms, and the two lattice sites with lower intensity in **Figure 7.7**(c) correspond to the Sn dopants and sulfur vacancy (SV), respectively. It is noted that the Sn dopants in the bilayer Sn-doped WS_2 are slightly dimmer than the SV because of the smaller Z in total. On the basis of these intensity differences, the Sn dopant sites could be distinguished, which enables the analysis of the dopant distribution in the bilayer Sn-doped WS_2. A high magnification ADF-STEM image of the bilayer region is shown in **Figure 7.7**(e) in false colour to show the Sn dopant locations (white circles) and S vacancy sites (blue circles).

To further locate the Sn dopant site in each layer, a rhombohedral unit cell illustrated in **Figure 7.7**(d) containing one W atom located at the A site and two overlapped S atoms situated at the B sites was extracted from **Figure 7.7**(b). Because of the 2H stacking sequence, it is inferred that on the second layer of Sn-doped WS_2, the W and S atoms swap with each other with S atoms at the A site and the W atom at the B site. After careful examination, it is found that all of the Sn dopants are situated at the B sites rather than the A sites in bilayer Sn-doped WS_2. This indicates that the Sn dopants are only introduced in the secondary layer rather than the bottom layer in the bilayer Sn-doped WS_2, whose atomic configuration is shown in **Figure 7.7**(i). This selective doping of the top surface could potentially establish a vertical heterojunction in bilayer crystals, which has not been reported in previous studies. **Figure 7.7**(f) shows the low magnification ADF-STEM image of the bilayer Sn-doped WS_2. By setting a threshold intensity, each Sn dopant in the bilayer region could be located. The yellow dashed circle in the **Figure 7.7**(g) reveals the contrast of monolayer Sn-doped WS_2, which could probably stem from the electron beam damage. After counting each Sn dopant in the bilayer

region, the statistical distribution in the **Figure 7.7**(h) shows that the 1-Sn remains with a dominant arrangement, around 70% among all the Sn dopants.

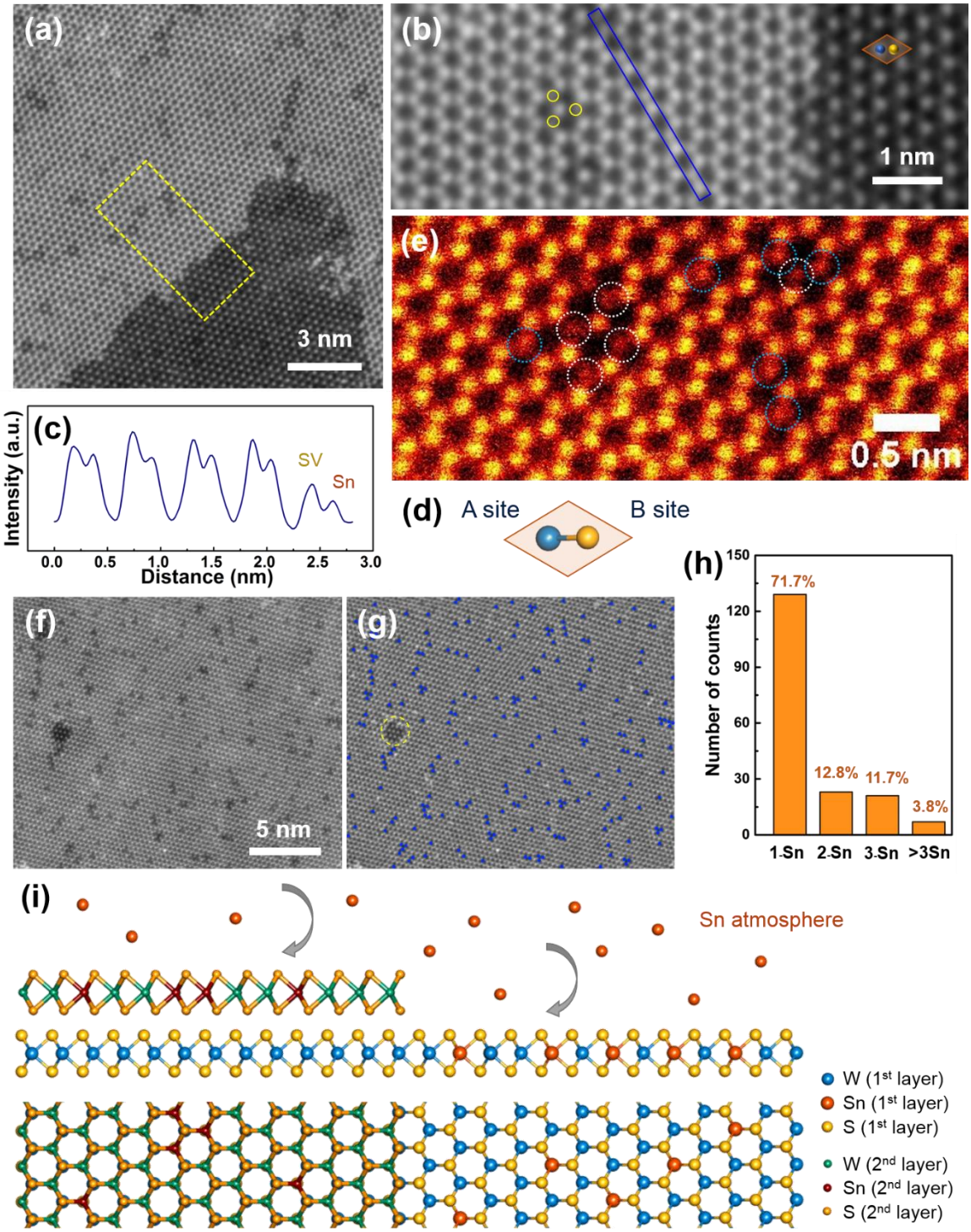


Figure 7.7. ADF-STEM analysis of the bilayer Sn-doped WS_2. (a) Low-magnification ADF-STEM image showing the boundary between the monolayer and bilayer Sn-doped WS_2. (b) Enlarged ADF-

STEM image from the yellow dashed square in (a). (c) Intensity line profile across the blue row in (b) showing the differences in intensity between W and Sn sites and sulfur vacancies in the bilayer regions. (d) Schematic illustration of a unit cell extracted from (b) with a metal atom situated on the A site and two chalcogen atoms on the B site. (e) High-magnification ADF-STEM image of Sn dopants in bilayer WS_2. White dashed circles indicate Sn dopants and blue dashed circles indicate S vacancy sites. (f) Low-magnification ADF-STEM image of bilayer Sn-doped WS_2. (g) Labelled atom image obtained from (f) demonstrating the distribution of Sn dopants (blue dot). (h) Histogram analysis from (g) showing the percentage of different configurations of Sn dopants. (i) Atomic structure illustrations for both the top and side views of the Sn-doped WS_2 showing that the Sn dopants are only introduced in the top layer of WS_2.

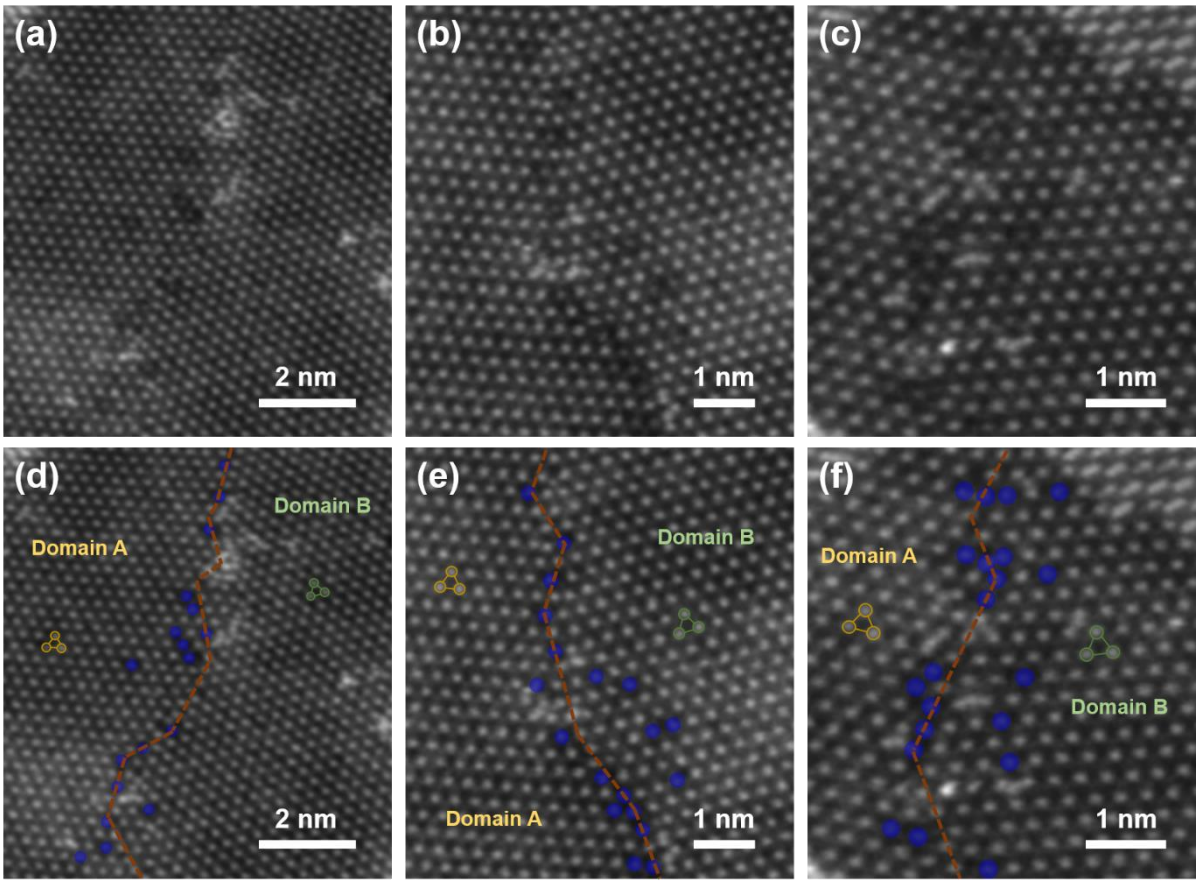


Figure 7.8. ADF-STEM analysis of Sn-doped WS_2 domain boundaries obtained under the low Sn doping temperature. (a-c) ADF-STEM images showing the distribution of Sn dopants near by the WS_2

domain boundaries. (d-f) Corresponding labelled atom image from (a), (b) and (c), respectively, with the Sn dopants marked by blue dots and the boundaries between two individual WS_2 domains indicated by red dashed lines.

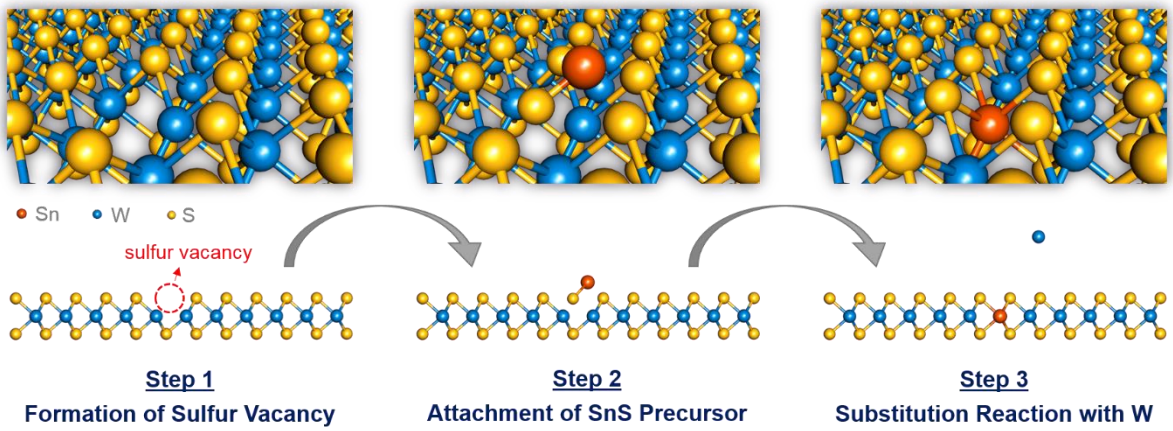


Figure 7.9. Doping mechanism of Sn substituting into W sites in the WS_2 layers.

In addition, the doping temperature is found to be critical in controlling the substitution reaction in the WS_2 layers. As shown in **Figure 7.8**, when decreasing the doping temperature to 450°C, a high density of the Sn dopants are distributed nearby the domain boundaries rather than the entire WS_2 layers. This could be ascribed to the substitution reaction driven by the sulfur vacancies during the doping process. As shown in **Figure 7.9**, during the thermal doping process, the presence of the sulfur vacancies could lower the structural stability of the WS_2 layer (step 1), and the SnS precursors are likely to be first incorporated on the active sites nearby the sulfur vacancies (step 2), after which the SnS tends to substitute the nearest unsaturated W sites; this includes the dissociation of neighbouring five W-S bonding, the formation of new five Sn-S bonding and additional two W-S bonding associated with the original sulfur vacancies (step 3). The bonding energy for W-S and Sn-S are reported to be 648 kJ/mol and 464 kJ/mol, respectively.[15-16] The enthalpy of the Sn substitution reaction is

therefore estimated to be -376 kJ/mol, indicating a more energetically favourable and stable structure of Sn-doped WS_2. The sulfur vacancies also help to lower the formation energy of domain boundaries in WS_2 and could promote the formation of the domain boundaries, which are composed of several pentagon-heptagon pairs with unsaturated bonding.[17] When the doping temperature decreases to 450°C, the thermally induced sulfur vacancies is greatly reduced and most of the remaining sulfur vacancies primarily comes from the area nearby the domain boundaries. As a consequence, the Sn doping is greatly suppressed at the lower doping temperatures, and the Sn atoms tend to accumulate at the imperfection sites that are easier for the creation of sulfur vacancies.

7.2.3 Electrical Properties of Sn-Doped WS_2 Monolayers

For the purpose of characterising the electrical properties, both the pristine WS_2 and Sn-doped WS_2 layers were then utilised to fabricate bottom-gated transistors with a channel length of 1 μm and channel width of 25 μm; the details of the device fabrication are described in Chapter 3. **Figure 7.10**(a) schematically shows the top view and side view of the as-fabricated device, which comprises gapped graphene ribbons with the Sn-doped WS_2 crystal in the middle. **Figure 7.10**(b) shows the optical image of the device, the gap between the graphene ribbons is 1 μm and both of the ribbons are connected to Cr/Au (10 nm/80 nm) bond pads. To compare the doping effect on the electrical properties, both the pristine and Sn-doped WS_2 layers are transferred on top of the gap between two graphene ribbons. The I-V measurement in **Figure 7.10**(c) shows that the monolayer Sn-doped WS_2 exhibits a lower current signal comparing to the pristine WS_2, which could possibly be attributed to the damaging of the WS_2 layer during the Sn substitution reaction. The nonlinear curves indicates the Schottky contact at the interface between both the WS_2 layers and graphene ribbons. When applying the gate voltage of 40 V, the current signal of Sn-doped WS_2 layer becomes four times

larger than that of pristine WS_2 shown in **Figure 7.10**(d). Besides, both the I-V characteristics of pristine WS_2 and Sn-doped WS_2 are more linear compared to those measured without gate bias, indicating the reducing Schottky barrier height at the graphene-WS_2 contacts.

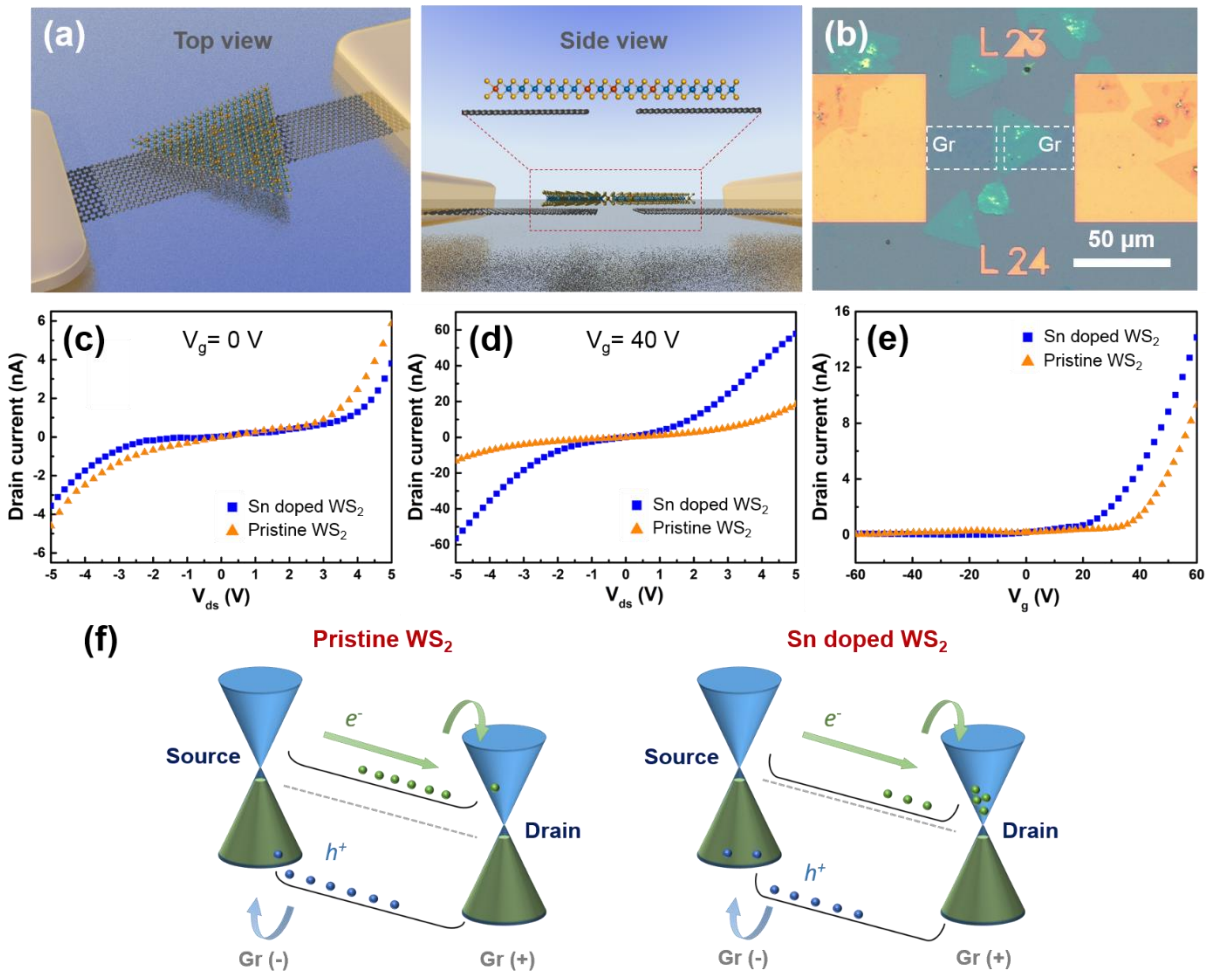


Figure 7.10. Electrical measurement of pristine and Sn-doped WS_2 layers. (a) Schematic illustration of a device based on monolayer Sn-doped WS_2 connected to the patterned Gr ribbons. (b) Optical image of the fabricated device with Sn-doped WS_2 monolayer bridged by graphene ribbons. (c) Output characteristics of the pristine and Sn-doped WS_2 monolayers without applying the gate voltage. (d) Output characteristics of the pristine and Sn-doped WS_2 monolayers under the gate voltage of 40 V. (e) Transfer characteristic curves of the bottom-gated devices based on pristine and Sn-doped WS_2 monolayers under the bias of 2 V. (f) Energy band diagram for the pristine WS_2 and Sn-doped WS_2 monolayer with Gr contacts.

The transfer characteristic curves of pristine WS_2 and Sn-doped WS_2 monolayers are demonstrated in **Figure 7.10**(e), both of which show a typical behaviour of the n-type semiconductor. Besides, it is observed that the doping of Sn significantly affects the threshold voltage (V_{th}), which could be obtained from the extrapolation in the linear region of the transfer characteristic curves, toward the neutral point. For the device based on pristine WS_2 monolayers the V_{th} is found to be around 35 V, which is consistent to our previous report,[9,18] whereas in the device with Sn-doped WS_2 monolayers the V_{th} shifts to 22 V. This indicates that the n-type doping resulting from the Sn substitution, which is consistent with the PL quenching phenomenon. The energy band diagrams in **Figure 7.10**(f) further illustrate that the n-type doping by Sn makes the Fermi level closer to the conduction band of WS_2, resulting in smaller gate voltage to reach the ON-state and the negative shift of the transfer curve. The carrier injection within Sn-doped WS_2 to the external circuit is therefore more efficient under the positive gate.

7.3 Conclusion

In summary, this chapter demonstrates the post-growth modification by Sn substitution in the monolayer and bilayer WS_2 crystals grown by CVD. This method separates the growth stage of the host 2D materials and thermal doping stage of extrinsic atoms, which has a better control of the dopant spatial distribution. The substitution relies on the sulfur vacancies and the bonding between W and Sn, which is more favourable under high doping temperature. In bilayer WS_2 crystals, the Sn substitutional doping only occurs in the top layer, resulting in a selective layer doping and potentially creating vertical heterostructures. The measurement of the transfer characteristics indicates the n-type doping of the WS_2 layers after the Sn substitution, which is consistent with the PL quenching phenomenon. These results provide a new route to the structural modification of 2D materials for various applications.

7.4 Reference

(1) Ning, C.-Z.; Dou, L.; Yang, P., Bandgap Engineering in Semiconductor Alloy Nanomaterials with Widely Tunable Compositions. *Nat. Rev. Mater.* **2017,** *2*, 17070.

(2) Pham, V. P.; Yeom, G. Y., Recent Advances in Doping of Molybdenum Disulfide: Industrial Applications and Future Prospects. *Adv. Mater.* **2016,** *28* (41), 9024-9059.

(3) Kochat, V.; Apte, A.; Hachtel, J. A.; Kumazoe, H.; Krishnamoorthy, A.; Susarla, S.; Idrobo, J. C.; Shimojo, F.; Vashishta, P.; Kalia, R.; Nakano, A.; Tiwary, C. S.; Ajayan, P. M., Re Doping in 2D Transition Metal Dichalcogenides as a New Route to Tailor Structural Phases and Induced Magnetism. *Adv. Mater.* **2017,** *29* (43), 1703754.

(4) Susarla, S.; Kutana, A.; Hachtel, J. A.; Kochat, V.; Apte, A.; Vajtai, R.; Idrobo, J. C.; Yakobson, B. I.; Tiwary, C. S.; Ajayan, P. M., Quaternary 2D Transition Metal Dichalcogenides (TMDs) with Tunable Bandgap. *Adv. Mater.* **2017,** *29* (35), 1702457.

(5) Yang, L.; Majumdar, K.; Liu, H.; Du, Y.; Wu, H.; Hatzistergos, M.; Hung, P. Y.; Tieckelmann, R.; Tsai, W.; Hobbs, C.; Ye, P. D., Chloride Molecular Doping Technique on 2D Materials: WS_2 and MoS_2. *Nano Lett.* **2014,** *14* (11), 6275-6280.

(6) Azcatl, A.; Qin, X.; Prakash, A.; Zhang, C.; Cheng, L.; Wang, Q.; Lu, N.; Kim, M. J.; Kim, J.; Cho, K.; Addou, R.; Hinkle, C. L.; Appenzeller, J.; Wallace, R. M., Covalent Nitrogen Doping and Compressive Strain in MoS_2 by Remote N_2 Plasma Exposure. *Nano Lett.* **2016,** *16* (9), 5437-5443.

(7) Nipane, A.; Karmakar, D.; Kaushik, N.; Karande, S.; Lodha, S., Few-Layer MoS_2 p-Type Devices Enabled by Selective Doping Using Low Energy Phosphorus Implantation. *ACS Nano* **2016,** *10* (2), 2128-2137.

(8) Li, H.; Wu, X.; Liu, H.; Zheng, B.; Zhang, Q.; Zhu, X.; Wei, Z.; Zhuang, X.; Zhou, H.; Tang, W.; Duan, X.; Pan, A., Composition-Modulated Two-Dimensional Semiconductor Lateral Heterostructures via Layer-Selected Atomic Substitution. *ACS Nano* **2017,** *11* (1), 961-967.

(9) Sheng, Y.; Tan, H.; Wang, X.; Warner, J. H., Hydrogen Addition for Centimeter-Sized Monolayer Tungsten Disulfide Continuous Films by Ambient Pressure Chemical Vapor Deposition. *Chem. Mater.* **2017,** *29* (11), 4904-4911.

(10) Chen, T.; Zhou, Y.; Sheng, Y.; Wang, X.; Zhou, S.; Warner, J. H., Hydrogen-Assisted Growth of Large-Area Continuous Films of MoS_2 on Monolayer Graphene. *ACS Appl. Mater. Interfaces* **2018,** *10* (8), 7304-7314.

(11) Lu, Y.; Chen, T.; Ryu, G. H.; Huang, H.; Sheng, Y.; Chang, R.-J.; Warner, J. H., Self-

Limiting Growth of High-Quality 2D Monolayer MoS_2 by Direct Sulfurization Using Precursor-Soluble Substrates for Advanced Field-Effect Transistors and Photodetectors. *ACS Appl. Nano Mater.* **2019,** *2* (1), 369-378.

(12) Sasaki, S.; Kobayashi, Y.; Liu, Z.; Suenaga, K.; Maniwa, Y.; Miyauchi, Y.; Miyata, Y., Growth and Optical Properties of Nb-Doped WS_2 Monolayers. *Appl. Phys. Express* **2016,** *9* (7), 071201.

(13) Mouri, S.; Miyauchi, Y.; Matsuda, K., Tunable Photoluminescence of Monolayer MoS_2 via Chemical Doping. *Nano Lett.* **2013,** *13* (12), 5944-5948.

(14) Robertson, A. W.; Lin, Y.-C.; Wang, S.; Sawada, H.; Allen, C. S.; Chen, Q.; Lee, S.; Lee, G.-D.; Lee, J.; Han, S.; Yoon, E.; Kirkland, A. I.; Kim, H.; Suenaga, K.; Warner, J. H., Atomic Structure and Spectroscopy of Single Metal (Cr, V) Substitutional Dopants in Monolayer MoS_2. *ACS Nano* **2016,** *10* (11), 10227-10236.

(15) Sevy, A.; Huffaker, R. F.; Morse, M. D., Bond Dissociation Energies of Tungsten Molecules: WC, WSi, WS, WSe, and WCl. *J. Phys. Chem. A* **2017,** *121* (49), 9446-9457.

(16) Drowart, J.; Goldfinger, P., The Dissociation Energies of the Group VIA Diatomic Molecules. *Q. Rev. Chem. Soc.* **1966,** *20* (4), 545-557.

(17) Ji, H. G.; Lin, Y.-C.; Nagashio, K.; Maruyama, M.; Solís-Fernández, P.; Sukma Aji, A.; Panchal, V.; Okada, S.; Suenaga, K.; Ago, H., Hydrogen-Assisted Epitaxial Growth of Monolayer Tungsten Disulfide and Seamless Grain Stitching. *Chem. Mater.* **2018,** *30* (2), 403-411.

(18) Tan, H.; Xu, W.; Sheng, Y.; Lau, C. S.; Fan, Y.; Chen, Q.; Tweedie, M.; Wang, X.; Zhou, Y.; Warner, J. H., Lateral Graphene-Contacted Vertically Stacked WS_2/MoS_2 Hybrid Photodetectors with Large Gain. *Adv. Mater.* **2017,** *29* (46), 1702917.

Chapter 8

Conclusion and Future Outlook

8.1 Thesis Summary

The objective of this doctoral thesis involves the contributions to the development of novel 2D materials beyond commonly-investigated graphene and TMDs for next generation nanoelectronics. These novel 2D materials include hexagonal boron nitride (hBN), tin disulfide (SnS_2), and other tin-derivative dichalcogenides obtained through the post-growth treatment under the Sn-rich atmosphere.

In chapter 4, a new oxide-assisted chemical vapour deposition (CVD) synthesis of hBN was demonstrated. This chapter shows how an oxide passivating layer on the Cu surface before the growth of hBN by chemical vapour deposition (CVD) can lead to increased domain sizes from 1 to 20 μm by reducing the nucleation density from 10^6 to 10^3 mm^{-2}. The hBN domains within each Cu grain are well-oriented, indicating an epitaxial relationship between the hBN crystals and the Cu substrates that leads to larger crystal domains within the film of around 100 μm. Continuous films are grown and show a high degree of monolayer uniformity. This CVD approach removes the need for low pressures, electrochemical polishing, and expensive substrates for large-area continuous films of hBN monolayers, which is beneficial for industrial applications that require scalable synthesis.

In chapter 5, SnS_2 crystals with layered 2D sheets are grown by CVD using a novel SnS precursor and integrated into all 2D transistors with graphene (Gr) electrodes. SnS_2 has a

different band structure from WS_2 and MoS_2, offering variance in device performance. The Gr-SnS_2-Gr transistors exhibit excellent photodetector response with high detectivity and photoresponsivity. The response of the all 2D photodetectors is shown to depend upon the charge trapping at the SnS_2-Gr interface and the Schottky barrier modulation. Thickness dependent SnS_2 measurements in devices reveal a transition from interface dominated response for thin crystals to bulk like response for the thicker SnS_2 crystals, showing the sensitivity of devices fabricated using layered materials on the number of layers. These results demonstrate that SnS_2 has photosensing performance when combined with graphene electrodes that is comparable to other 2D transition metal dichalcogenides of MoS_2 and WS_2.

In chapter 6, the CVD growth and morphology control of 2D SnS_2 on CVD-grown WS_2 layers was demonstrated. In addition to the formation of type II van der Waals (vdW) vertical heterostructures with enhanced charge separation, the morphology of SnS_2 is found to be highly dependent on the underlying substrate surface. Lateral growth could be stabilised with epitaxially aligned crystals on the defect-free surface, whereas cluster growth appears on the defect-rich surface. This is attributed to the lower energy barrier of migration for adsorbed active species on the defect-free surface, resulting in facilitated surface diffusion compared to the defect-rich surface. These results show how SnS_2:WS_2 interactions at edges and basal planes influence the final 2D vertical stack. The similar results are obtained when switching the growth substrates to other 2D transition metal dichalcogenides, such as MoS_2 layers, showing the importance of defect-free 2D substrates on the SnS_2 growth for future device applications.

In chapter 7, a new post-growth doping strategy in monolayer and bilayer WS_2 crystals was introduced. This utilizes a metal exchange mechanism, whereby Sn atoms become substitutional dopants in the W sites by energetically favourable replacement. We achieve this using CVD techniques, where high quality grown WS_2 single crystals are first grown and then

subsequently reacted with a SnS precursor. Thermal control of the exchange doping mechanism is revealed, indicating that a sufficiently high enough temperature is required to create the S vacancies that are the initial binding sites for the SnS precursor and metal exchange occurrence. This results in a better control of dopants distribution compared to the traditional all-in-one approach, where dopants are added during the growth phase. The Sn dopants exhibit an n-type doping behaviour in the WS_2 layers, as deduced from the decreased threshold voltage of transistor transfer characteristics. Annular dark-field scanning transmission electron microscopy (ADF-STEM) shows that in bilayer WS_2 the Sn doping occurs only in the top layer, creating vertical heterostructures with atomic layer doping precision. This post-growth modification opens up ways to selectively dope one layer at a time and construct mixed stoichiometry vertical heterojunctions in bilayer crystals.

8.2 Future Outlook

Despite the great effort that have been put over the past few years, large-scale manufacturing of 2D materials is still at the beginning stage. For the purpose of producing 2D materials in industrial scale, employing low pressure system to the CVD could improve the spatial uniformity of the resulted materials and is beneficial for the large-area production. Apart from upscaling the CVD process, a thorough understanding for the underlying mechanism behind the synthesis is also imperative. Several questions are still required to be addressed in this project, including (1) how to control the number of layers for the OCVD growth of multilayer hBN to increase the functionality for applications in nanoelectronic devices, since hBN often serves as the tunnelling barrier and its thickness could greatly affect the tunnel current; (2) how to effectively control the thickness of the SnS_2 during the growth and reach to the monolayer or bilayer crystal; (3) what the difference is between the initial nucleation for SnS_2 grown on WS_2 basal plane and WS_2 edges, which may also influence the eventual

morphologies; (4) how to experimentally correlate the sulfur vacancies to the Sn dopants in Sn-doped WS_2. To further solve these issues, a series of *in-situ* and *ex-situ* characterisation techniques will be required to track the real-time synthesis procedure.

For the aspect of nanoelectronic applications, the influence of the Sn dopant concentration on the bandgap of Sn-doped WS_2 and the resulting electrical properties can be further investigated. If the thickness of SnS_2 can be successfully controlled over large area, it is worthwhile to utilise the SnS_2/WS_2 heterostructures as the building blocks for semiconducting channels as they are expected to exhibit better efficiency for charge separation, which would be advantageous for the light harvesting applications. In addition, incorporating hBN layers into these 2D semiconductors could increase the tuneability of their electronic properties for the design of device structures with improved performance, or even enable the fabrication of light emitting devices that utilise type I heterostructures.